

NASA Tech Briefs

National
Aeronautics and
Space
Administration



Aerospace developments have been adapted commercially to produce heated gloves and ski boots. Rechargeable batteries in the soles of boots and inside the wrists of gloves power heater circuits like those used in the Apollo command module. Monofilament open-mesh material used in lunar space-suit boot liners "wicks away" moisture.

About the NASA Technology Utilization Program

The National Aeronautics and Space Act of 1958, which established NASA and the United States civilian space program, requires that "The Administration shall provide for the widest practicable and appropriate dissemination of information concerning its activities and the results thereof."

To help carry out this objective the NASA Technology Utilization (TU) Program was established in 1962. It offers a variety of valuable services to facilitate the transfer of aerospace technology to nonaerospace applications, thus assuring American taxpayers maximum return on their investment in space research; thousands of spinoffs of NASA research have already occurred in virtually every area of our economy.

The TU Program has worked for engineers, scientists, technicians, and businessmen. And it can work for you.

NASA Tech Briefs

Tech Briefs is published quarterly and is free to any U.S. citizen or organization. It is both a current-awareness medium and a problem-solving tool. Potential products ... industrial processes ... basic and applied research ... shop and lab techniques ... computer software ... new sources of technical data ... concepts ... you will find them all in NASA Tech Briefs. The first section highlights a few of the potential new products contained in Tech Briefs. The remainder of the volume is organized by technical category to help you quickly review new developments in your areas of interest. Finally, a subject index makes each issue a convenient permanent reference file.

Further Information on Innovations

Although many articles are complete in themselves, others are backed up by Technical Support Packages (TSP's). TSP's are available without charge and may be ordered by simply completing the enclosed TSP Request Card. Further information on some innovations is available for a nominal fee from other sources, as indicated at the ends of the articles. In addition, Technology Utilization Officers at NASA Field Centers will assist you directly when necessary. (See page A4.)

Patent Licenses

Many of the inventions described are under consideration for patents or have been patented by NASA. Unless NASA has decided not to apply for a patent, the patent status is described at the end of each article. For further information about the Patent Program see page A8.

Other Technology Utilization Services

To assist engineers, industrial researchers, business executives, city officials, and other potential users in applying space technology to their problems, NASA sponsors six Industrial Applications Centers. Their services are described on page A6. In addition, an extensive library of computer programs is available through COSMIC, the Technology Utilization Program's outlet for NASA-developed software. (See page A5.)

Applications Program

To help solve public-sector problems in such areas as safety, health, transportation, and environmental protection, NASA TU Applications Teams, staffed by professionals from a variety of disciplines, work with Federal agencies, local governments, and health organizations to identify critical problems amenable to technical solutions. Among their many significant contributions are a rechargeable heart pacemaker, a lightweight fireman's breathing apparatus, aids for the handicapped, and safer highways.

Reader Feedback

We hope you find the information in NASA Tech Briefs useful. A reader feedback card has been included because we want your comments and suggestions on how we can further help you apply NASA innovations and technology to your needs. Please use it, or if you need more space, write us a letter.

NASA TU Services

A3

Technology Utilization services that can assist you in learning about and applying NASA technology.



New Product Ideas

A9

A summary of selected innovations of value to manufacturers for the development of new products.



Tech Briefs

469

Electronic Components and Circuits



487

Electronic Systems



505

Physical Sciences



527

Materials



545

Life Sciences



565

Mechanics



589

Machinery



611

Fabrication Technology



623

Mathematics and Information Sciences



Subject Index

631

Items in this issue are indexed by subject; a cumulative index will be published yearly.



COVERS: The photographs on the front and back covers illustrate recent developments by NASA and its contractors that have resulted in commercial and nonaerospace spinoffs. For information about the heated gloves and ski boots, circle 96 on the Reader Service Card; for more facts about laser surveying, circle 97.

About This NASA Publication

NASA Tech Briefs, a quarterly publication, is distributed free to U.S. citizens to encourage commercial application of U.S. space technology. For information on publications and services available through the NASA Technology Utilization Program, write to the Director, Technology Utilization Office, P. O. Box 8757, Baltimore/Washington International Airport, Maryland 21240.

"The Administrator of National Aeronautics and Space Administration has determined that the publication of this periodical is necessary in the transaction of the public business required by law of this Agency. Use of funds for printing this periodical has been approved by the Director of the Office of Management and Budget through December 31, 1979."

This document was prepared under the sponsorship of the National Aeronautics and Space Administration. Neither the United States Government nor any person acting on behalf of the United States Government assumes any liability resulting from the use of the information contained in this document, or warrants that such use will be free from privately owned rights.

Change of Address

Change of Address: If you wish to have NASA Tech Briefs forwarded to your new address, use one of the Subscriptions cards enclosed in the back of this volume of NASA Tech Briefs. Be sure to check the appropriate box indicating change of address.

Communication Concerning Editorial Matter

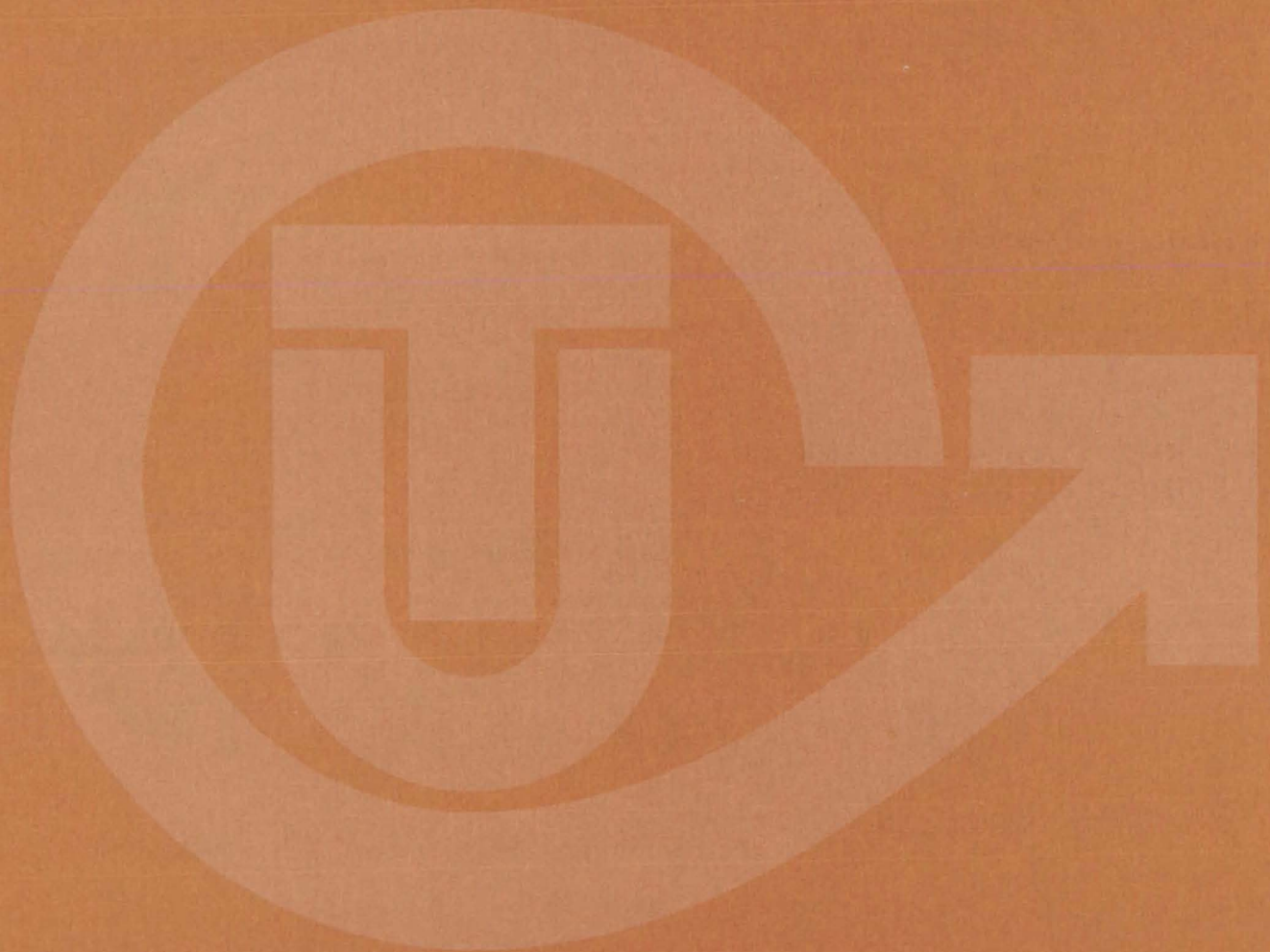
For editorial comments or general communications about NASA Tech Briefs, you may use the self-addressed Feedback card in the back of NASA Tech Briefs, or write to: The Publications Manager, Technology Utilization Office (E TU-6), NASA Headquarters, Washington, DC 20546. Technical questions concerning specific articles should be directed to the Technology Utilization Officer of the sponsoring NASA Center (addresses listed on page A4).

NASA TECH BRIEFS Published quarterly by the National Aeronautics and Space Administration, Technology Utilization Branch, Washington, DC.

Administrator: **Robert A. Frosch**; Chief, Technology Utilization Branch: **Louis Mogavero**; Publications Program Manager: **Judson O. Harrison III**.

Prepared for the National Aeronautics and Space Administration by **Logical Technical Services Corp.**: Editor-in-Chief: **Graham L. Gross**; Art Director: **Ernest Gillespie**; Managing Editor: **Jay Kirschenbaum**; Senior Editor: **Donald Blattner**; Chief Copy Editor: **Oden Browne**; Staff Editors: **Michael Polchaninoff**, **Jonathan Rogers**, **Ted Selinsky**, **George Watson**; Graphics: **Bruce Appel**, **Concetto Auditore**, **Judy Tenenbaum**; Editorial & Production: **Richard Johnson**, **Rose Giglietti**, **Vincent Susinno**, **John Tucker**, **Madeline Tucker**, **Ernestine Walker**, **Carl Woolridge**.

NASA TU SERVICES



THE NASA TECHNOLOGY UTILIZATION OFFICERS

They will help you apply the innovations described in Tech Briefs.



The Technology Utilization Officer (TUO)

Each NASA Center has a Technology Utilization Officer — An applications engineer whose job is to help you make use of new technology developed at his center. He brings you the NASA Tech Briefs and other special publications, sponsors conferences, and arranges for expert assistance in solving technical problems.

Technical Assistance

Working together with NASA Scientists and Engineers and the Industrial Applications Centers, the center TUO's can answer specific questions about innovations and related NASA technology.

Technical Support Package (TSP's)

For many of the innovations described in Tech Briefs, the center TUO has prepared additional material that will help you in detailed evaluation and actual use or construction of the new technology. You may get TSP's free of cost by using the TSP Request Card or writing the center TUO.

Who to Contact. Of course, many technical questions about Tech Briefs are answered in the TSP's, but when no TSP is available, or you have further questions, write the Technology Utilization Officer at the center that sponsored the research at the address listed below.

Charles C. Kubokawa
Ames Research Center
Code AU: 240-2
Moffett Field, CA 94035
(415) 965-5554

Donald S. Friedman
Goddard Space Flight Center
Code 702.1
Greenbelt, MD 20771
(301) 344-6242

John T. Wheeler
Johnson Space Center
Code AT3
Houston, TX 77058
(713) 483-3809

Raymond J. Cerrato
John F. Kennedy Space Center
Code SA-RTP
Kennedy Space Center, FL 32899
(305) 867-2780

John Samos
Langley Research Center
Mail Stop 139A
Hampton, VA 23665
(804) 827-3281

Paul Foster
Lewis Research Center
21000 Brookpark Rd.
Cleveland, OH 44135
(216) 433-4000, Ext. 6832

Aubrey D. Smith
George C. Marshall Space Flight Center
Code AT01
Marshall Space Flight Center, AL 35812
(205) 453-2224

John C. Drane
NASA Resident Legal Office-JPL
4800 Oak Grove Drive
Pasadena, CA 91103
(213) 354-6420

Gilmore H. Trafford
Wallops Flight Center
Wallops Island, VA 23337
(804) 824-3411, Ext 201

Jerry Harrison
NASA Headquarters
Code ETU-6
Washington, DC 20546
(202) 755-2244

COSMIC

(Computer Software Management & Information Center)

AN ECONOMICAL SOURCE OF COMPUTER PROGRAMS DEVELOPED BY THE GOVERNMENT.

COSMIC is sponsored by NASA to give you access to over 1400 computer programs developed by NASA and the Department of Defense, and selected programs from other government agencies. It is one of the Nation's largest software libraries.

COSMIC charges very reasonable fees for programs to help cover part of their expenses—and NASA pays for the remainder. Programs generally cost from \$500 to \$1000, but a few are more expensive and many are less. Documentation is available separately and very inexpensively.

COSMIC collects and stores software packages, insures that they are complete, prepares special announcements (such as Tech Briefs), publishes an indexed software catalog, and reproduces programs for distribution. COSMIC helps customers to identify their software needs, follows up to determine the successes and problems, and provides updates and error corrections. In some cases, NASA engineers can offer guidance to users in installing or running a program.

COSMIC programs range from management (pert scheduling) to information science (retrieval systems) and computer operations (hardware and software). Hundreds of engineering programs perform such tasks as structural analysis, electronic circuit design, chemical analysis, and design of fluid systems. Others determine building energy requirements, optimize mineral exploration, and draw maps of water-covered areas using NASA satellite data. In fact, the chances are, if you use a computer, you can use COSMIC.

COSMIC is eager to help you get the programs you need. For more information about services or software available from COSMIC, fill out and mail the COSMIC Request Card in this issue.

COSMIC: Computer Software Management and Information Center

Suite 112, Barrow Hall, University of Georgia, Athens, Georgia 30602 Phone: (404) 542-3265

WHERE IS THE WORLD'S LARGEST BANK OF TECHNICAL DATA

?



It's in Indianapolis and Pittsburgh, it's in Storrs, Connecticut and Research Triangle Park, North Carolina; and it's in Albuquerque and Los Angeles.

NASA IAC's — INDUSTRIAL

You can get more information and more data on more technical subjects through NASA's network of IAC's than anywhere else in the world. About 8,000,000 documents and growing at the rate of 50,000 more each month!

Major sources include:

- 750,000 NASA Technical Reports
- Selected Water Resources Abstracts
- NASA Scientific and Technical Aerospace Reports
- Air Pollution Technical Information Center
- NASA International Aerospace Abstracts
- Chem Abstracts Condensates
- Engineering Index
- Energy Research Abstracts
- NASA Tech Briefs
- Government Reports Announcements

and many other specialized files on food technology, textile technology, metallurgy, medicine, business, economics, social sciences, and physical science.

The IAC's are one of the most economical ways of staying competitive in today's world of exploding technology. The help available from the network ranges from literature searches through expert technical assistance.

Literature Searches

Help in designing your search, typically from 30 to 300 abstracts in as narrow or broad an area as you need, and complete reports when you need them. The most complete "search before research" available!

Current Awareness

Consult with our applications engineers to design your personal program — selected monthly or quarterly abstracts on new developments in your speciality. It's like having your own journal!

Technical Assistance

Our applications engineers will help you evaluate and apply your literature-search results. They can help find answers to your technical problems and put you in touch with scientists and engineers at NASA Field Centers.

To obtain more information about how NASA's IAC's can help you — Check the IAC box on the TSP Request Card in this issue, Or write or call the IAC nearest you.

APPLICATIONS CENTERS

How to get reports and other documents discussed in this issue of Tech Briefs

Many of the innovations in Tech Briefs are described in detail in reports available at a reasonable cost through one or more of the IAC's. To order a report, call or write the IAC referenced at the end of the Tech Brief article at the address below. Be sure to list the titles and accession numbers (N76-..., N75-..., etc.) of those you wish to purchase.

Aerospace Research Application Center (ARAC)
Indiana University-Purdue University at Indianapolis
1201 E. 38th St.
Indianapolis, IN 46205
E. Guy Buck, Director
(317) 264-4644

Knowledge Availability Systems Center (KASC)
University of Pittsburgh
Pittsburgh, PA 15260
Dr. Edmond Howie, Director
(412) 624-5211

New England Research Application Center (NERAC)
Mansfield Professional Park
Storrs, CT 06268
Dr. Daniel U. Wilde, Director
(203) 486-4533

North Carolina Science & Technology
Research Center (NC/STRC)
P. O. Box 12235
Research Triangle Park, NC 27709
Peter J. Chenery, Director
(919) 549-0671

Technology Application Center (TAC)
University of New Mexico
Albuquerque, NM 87131
Stanley A. Morain, Director
(505) 277-4000

NASA Industrial Application Center
Denney Research Building - 3rd Fl.
University of Southern California
University Park
Los Angeles, CA 90007
Dr. Robert Y. Mixer, Director
(213) 741-6132

NASA INVENTIONS AVAILABLE FOR LICENSING

Over 3,500 NASA inventions are available for licensing in the United States - both exclusive and nonexclusive.

Nonexclusive Licenses

Nonexclusive licenses for commercial use are encouraged to promote competition and to achieve the widest use of inventions. They must be used by a negotiated target date but are usually royalty free.



Exclusive Licenses

An exclusive license may be granted to encourage early commercial development of NASA inventions, especially when considerable private investment is required. These are generally for 5 to 10 years and usually require royalties based on sales or use.

The NASA patent licensing program also provides for licensing of NASA-owned foreign patents. In addition to inventions described in Tech Briefs, "NASA Patent Abstract Bibliography," containing abstracts of all NASA inventions, can be purchased from: National Technical Information Service, Springfield, Va., 22161. This document is updated semi-annually.

Patent Licenses and the NASA Tech Brief

Many of the inventions reported in Tech Briefs are patented or are under consideration for a patent at the time they are published. When this is the case, the current patent status is described at the end of the article; otherwise, there is no statement about patents. **If you want to know more about the patent program or are interested in license for a particular invention, write the Patent Counsel at the NASA Field Center that sponsored the research. Be sure to refer to the NASA reference number in parenthesis at the end of the Tech Brief.**

Robert F. Kempf
NASA Headquarters, Code GP-4
400 Maryland Ave., S.W.
Washington, DC 20546
(202) 755-3932

Darrell G. Brekke
Ames Research Center
Mail Code: 200-11A
Moffett Field, CA 94035
(415) 965-5104

John O. Tresansky
Goddard Space Flight Center
Mail Code: 204
Greenbelt, MD 20771
(301) 344-7351

Marvin F. Matthews
Lyndon B. Johnson Space Center
Mail Code: AM
Houston, TX 77058
(713) 483-4871

James O. Harrell
John F. Kennedy Space Center
Mail Code: SA-PAT
Kennedy Space Center, FL 32899
(305) 867-2544

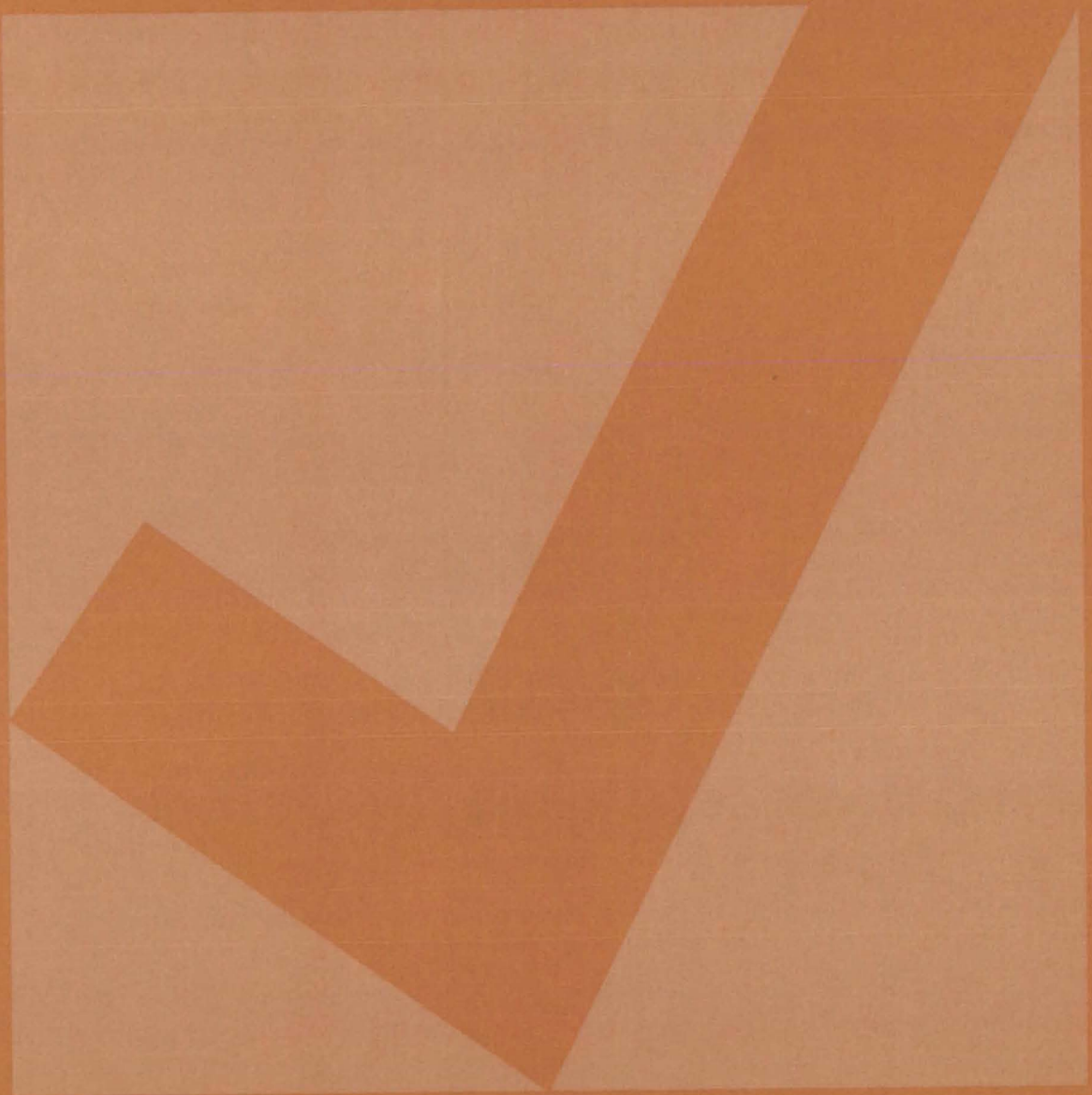
Howard J. Osborn
Langley Research Center
Mail Code: 279
Hampton, VA 23665
(804) 827-3725

Norman T. Musial
Lewis Research Center
Mail Code: 500-311
21000 Brookpark Road
Cleveland, OH 44135
(216) 433-4000

Leon D. Wofford, Jr.
George C. Marshall Space Flight Center
Mail Code: CC01
Marshall Space Flight Center, AL 35812
(205) 453-0020

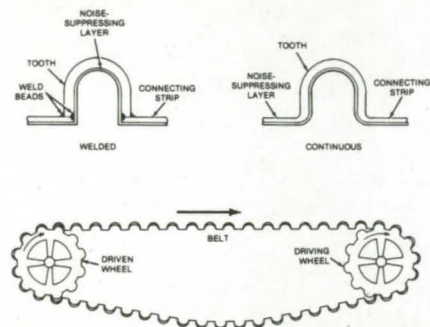
Monte F. Mott
NASA Resident Legal Office
4800 Oak Grove Drive
Pasadena, CA 91103
(213) 354-2700

NEW PRODUCT IDEAS



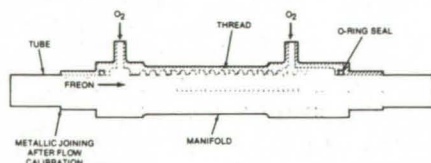
NEW PRODUCT IDEAS are just a few of the many innovations described in this issue of NASA Tech Briefs and having promising commercial applications. Each is discussed further on the referenced page in the appropriate section in this issue. If you are interested in developing a product from these or other NASA innovations, you can receive further technical information by requesting the TSP referenced at the end of the full-length article or by writing the Technology Utilization Office of the sponsoring NASA center (see page A4). NASA's patent-licensing program to encourage commercial development is described on page A8.

Durable, Nonslip, Stainless-Steel Drivebelts



Stainless-steel drivebelts proposed for long-term unattended service in spacecraft could have terrestrial applications where belt replacement is difficult. Unlike belts made of plastic and polymeric fibers, the stainless-steel belts can be used in intense heat or cold, under intense radiation, and under high loads. In one design, cylindrical rods run transverse to the entire belt length to serve as teeth that mesh with the drivewheel sprockets. The rods are secured by steel wires running along the length of the belt. Another proposed belt has U-shaped flexible teeth that engage the wheel sprockets. The teeth are connected by flexible strips. Where the application permits, the belts could be coated with plastic or rubber to reduce noise. (See page 599.)

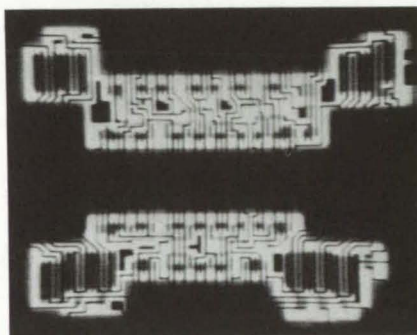
Adjustable Gas-Flow Restrictor



The pressure of a confined gas can be reduced and precisely controlled by a new adjustable flow restrictor. If desired, the gas can also be simultaneously heated or cooled. Developed originally to control oxygen flow in the life-support system of a space vehicle,

the new device can be adapted to other fluid-flow applications, such as petroleum processing or food processing. The gas passes through the annular space between two mating threaded parts. The long, narrow, helical path reduces the pressure within a short axial distance, and the pressure drop can be adjusted simply by screwing or unscrewing the threaded members. A heating fluid or coolant can be circulated through the hollow core of the restrictor to control the gas temperature. (See page 594.)

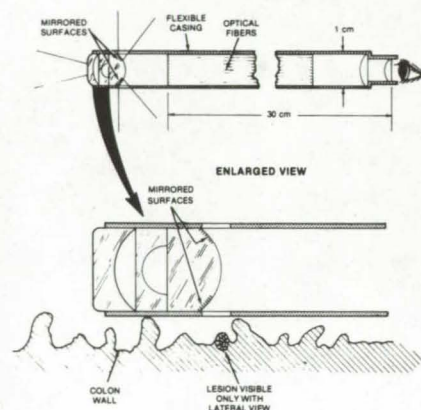
Testing Integrated Circuits by Photoexcitation



Laser light is rapidly scanned over a circuit under test in a new method for rapid production-screening of integrated circuits. In an adaptation of a much slower photoexcitation technique previously used only for developmental tests, the photoresponse of each sub-component of the circuit is recorded as it is clocked through many digital states. The superimposed images form a "signature" of the test circuit, which can be compared with a reference to make a rapid online accept/reject decision. CMOS integrated circuits have already been tested by the procedure, with good results. A He/Ne laser was used, and power delivered to the IC was less than about 0.1 milliwatt. (See page 474.)

Improved Probe for Rectal-Cancer Detection

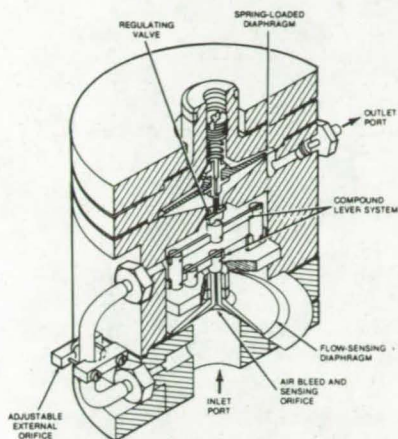
An improved proctosigmoidoscope for inspection of the rectum and colon is able to scan ahead and to the side for viewing around intestinal folds. It will make possible more thorough medical examinations by exposing lesions and other anomalies that could only be seen with a lateral view. The addition of a third lens, which has a mirrored coating along the perimeter of one surface,



distinguishes this instrument from those with conventional two-lens design. The mirrored convex surface reflects the lateral image of the colon wall through a space in the body of the proctosigmoidoscope. A double image is viewed by the operator: He sees a central image of the frontal view and a concentric ring that contains the side view. (See page 562.)

Flow-Compensating Pressure Regulator

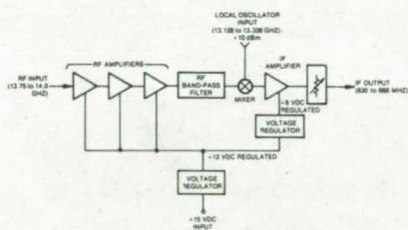
A flow-compensating pressure regulator maintains a constant pressure at its output, despite variations in the infusion flow rate. It can be used with a surgical instrument for the removal of optical cataracts and in other applications where fluid pressure must remain constant. A standard, spring-loaded



diaphragm is the basic pressure-regulating element. A second diaphragm, located a small distance below the first on the same centerline, responds to the pressure drop across an adjustable external orifice and a parallel internal orifice near the flow inlet. The force on this second diaphragm is coupled to the regulator valve through a compound lever. The action of the two diaphragms and the lever exactly compensates for the pressure drop in the surgical instrument that controls the flow rate.

(See page 548.)

Miniature K_U-Band Down Converter

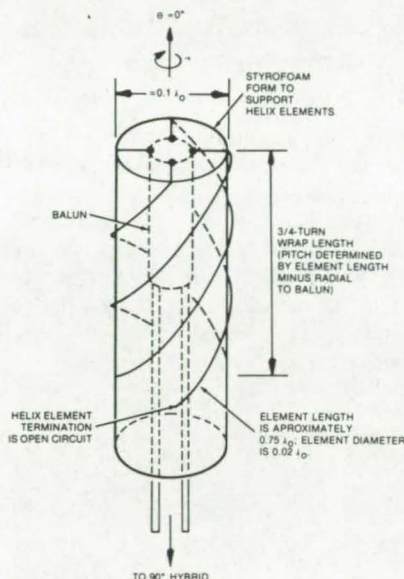


A miniature, hermetically-packaged, thin-film microwave integrated circuit serves as the complete receiver front end (excluding the local oscillator) for compact K_U-band radar and communications systems. The entire circuit is packaged in a small hermetically-welded, nitrogen-filled aluminum case. The circuit consists of three stages of FET amplification, a four-pole Tchebyscheff filter, a balanced mixer, one stage of bipolar transistor IF amplification, and a passive temperature-compensation circuit. Even a voltage regulator is included in the hybrid package. The measured overall noise figure of the converter is approximately 4 dB.

(See page 473.)

Compact Antenna Has Symmetrical Radiation Pattern

A compact, mechanically-stable, quadrifilar-helix antenna, originally developed for outer-planet spacecraft probes, has potential uses in citizens-band radios and other terrestrial communications systems. Its antenna patterns show exceptional uniformity and symmetry, varying by less than 1.5 dB over most of the forward hemisphere,

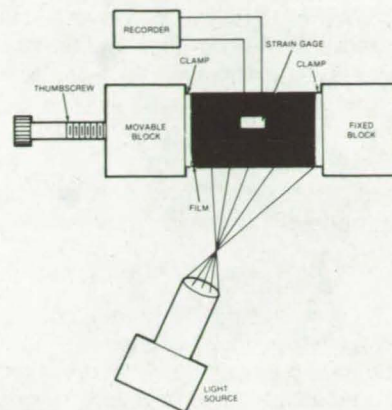


and its gain and VSWR characteristics are also good. A 550-MHz version of the antenna would consist of four wires wound around a dielectric cylinder about 39 cm in length. This design was recently tested successfully on a one-quarter-scale model (2.2 GHz).

(See page 500.)

Ultrathin Films as Photomechanical Transducer

A stretched film approximately 0.1 mil in thickness can detect the presence of light and measure the total light exposure over a period of time. As a new photomechanical transducer, a stretched film could serve as a low-cost, nonelectrical substitute for a photocell in many applications. Discovered during the course of experiments with materials for the solar "sail," the effect is observed as a mechanical stress change (probably caused by heating) when a film is illuminated. The stress is easily monitored with a conventional strain gage. In tests of

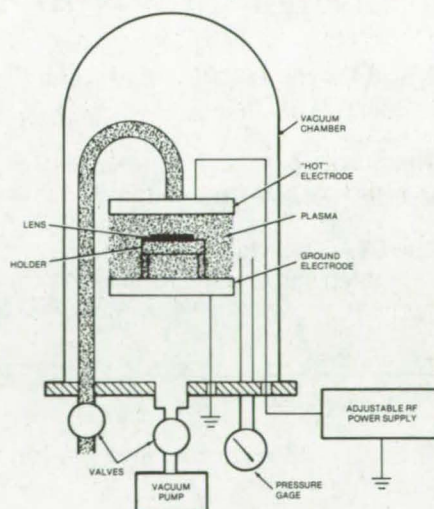


polyimide films, with and without reflective or absorptive coatings, the response varied from -1.5 to -16 g/cm²-W. A practical transducer could be implemented by installing a strain sensor integral with the film and clamping the film between two supported blocks.

(See page 520.)

Scratch-Resistant Plastic Lenses

A three-step, plasma-deposition process deposits a tenacious antiabrasion film on plastic lenses and other plastic components. The process thus eliminates a major problem with optical plastics: their tendency to become scratched under routine cleaning or handling. Each step is carried out in



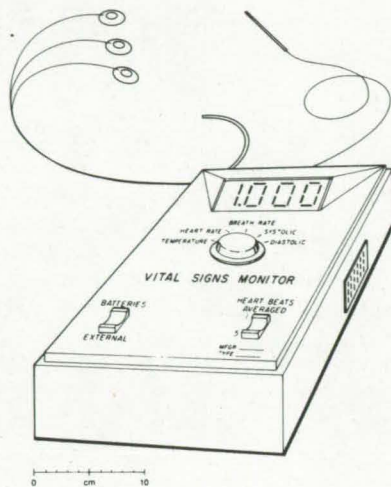
the same vacuum chamber, without removing the lens. The plastic is first exposed to a water-vapor plasma that forms hydroxyl groups on the lens surface. This ensures good adherence of silicon-based monomers, introduced during the second plasma deposition.

Finally, the lens is exposed to an argon plasma that cross-links and stress-relieves the monomer film to create a strong, scratchproof coating. (See page 543.)

Hand-Held Vital-Signs Monitor

Six new hybrid integrated circuits are the basis of a complete physiological vital-signs monitor. Already tested as a prototype, the unit requires only a display, a battery, packaging, and miscellaneous hardware to emerge as a completely-self-contained, hand-held instrument that could be used by doctors on house calls and others in emergency medical applications. The six hybrids, which include

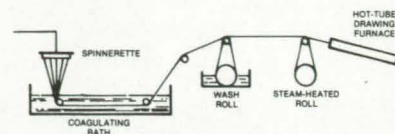
- A Temperature Monitor,
- An ECG Amplifier and Cardiometer Signal Conditioner,
- An Impedance-Pneumograph and Respiration-Rate Signal Conditioner,



- A Heart/Breath-Rate Processor,
 - A Liquid-Crystal Display Driver, and
 - A Clock Circuit,
- evolved from existing conventional-scale circuits. They are based around low-power, CMOS circuitry and can be used independently for other applications.

(See page 551.)

Ultrafine PBI Fibers and Yarns



Ultrathin synthetic fibers, with denier as low as 0.17, are produced by a continuous dry-jet/wet-spinning process. Originally developed to make a light, strong, radiation-resistant fabric for a solar "sail," the new process can produce lightweight textiles with superior physical properties for other applications. A five-hole spinnerette ejects a solution of polybenzimidazole into a water bath, forming five fibers that are then drawn into a tube furnace. By precisely controlling the temperature and the entrance and exit speeds in the furnace, the fibers are drawn to the required thinness without weakening or breaking.

(See page 529.)

ANNOUNCING . . .

A NEW NASA TECHNOLOGY UTILIZATION SERVICE in Cooperation With STATE GOVERNMENTS

NASA recently inaugurated a State Technology Applications Center (STAC) program with the opening of facilities in Florida and Kentucky.

The purpose of the experimental STAC program is to provide technical information services to state and local government agencies as well as to industry within each state.

The STAC's differ from the NASA Industrial Applications Centers (see page A7) primarily in that the STAC's are integrated into existing state technical assistance programs and serve only the host state, whereas the Industrial Applications Centers serve multistate regions.

The STAC's have access to several commercial data bases, as well as the NASA data base, and they normally charge a fee for their services.

Persons wishing **further information** should write to:

In Florida

NASA/Florida State Technology Applications Center (STAC)
311 Weil Hall
University of Florida
Gainesville, Florida 32611

or phone, Gainesville: (904) 392-6760
Orlando: (305) 275-2706
Tampa: (813) 974-2499

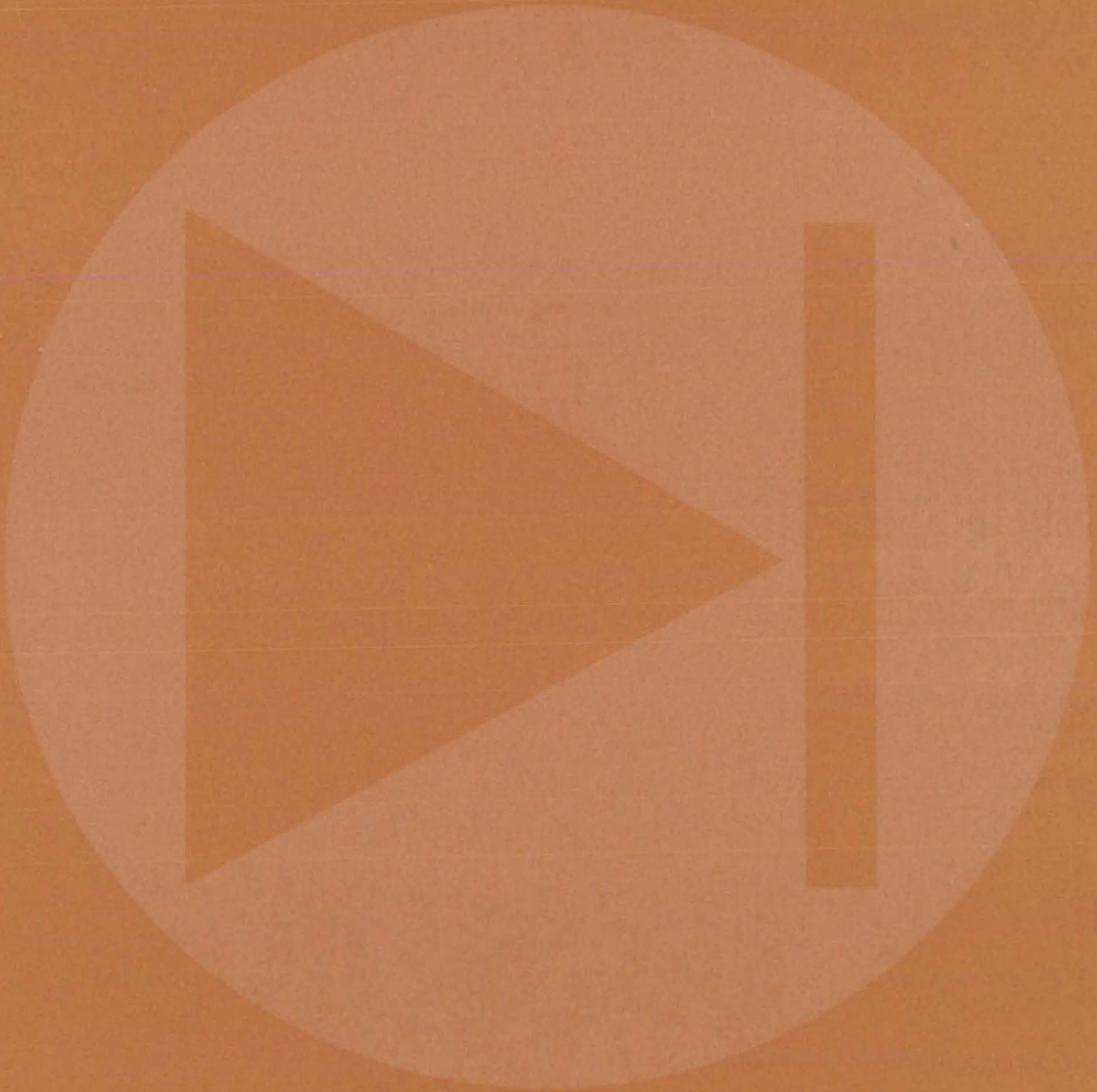
or contact the local State Department of Commerce
Business Development Representative

In Kentucky

NASA/University of Kentucky State Technology Applications Program (STAP)
109 Kinkead Hall
University of Kentucky
Lexington, Kentucky 40506

phone: (606) 258-4632

Electronic Components and Circuits



Hardware, Techniques, and Processes

- 471 Multichannel VCO Needs Only One Reference
- 472 Arc Detector Uses Fiber Optics
- 473 Miniature K_U-Band Down Converter
- 474 Testing Integrated Circuits by Photoexcitation
- 475 Precise Matching of Diodes
- 476 Splicing Shielded Cables
- 477 Modular Ground-Wire Connector
- 477 Electrical-Ground Monitor
- 479 One-Third Selection for Matrix-Addressing Ferroelectrics
- 480 Simplified Phase Detector
- 481 Digital Correlator With Fewer IC's
- 483 Pulse-Width-Modulated Attenuator for AGC
- 484 Overload Protection System
- 485 Load Balancing Multimodule Switching Power Converters

Books and Reports

- 486 Eliminating Gold Migration in Microcircuits

Multichannel VCO Needs Only One Reference

Passband filters and selector logic eliminate the need for separate crystal oscillators in each channel.

Lyndon B. Johnson Space Center, Houston, Texas

A frequency-stabilizing circuit that controls the output of a multichannel microwave oscillator requires only one reference crystal oscillator. Conventional stabilization circuits, in contrast, normally require a separate reference oscillator for each channel.

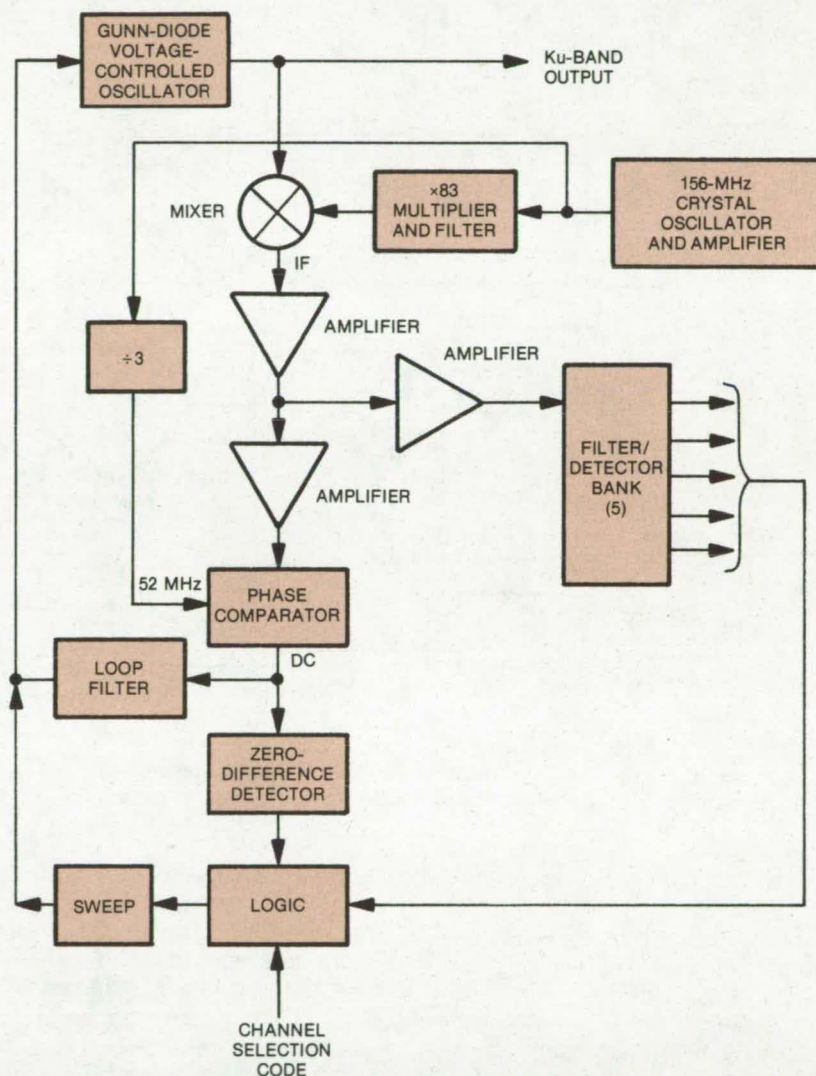
The new circuit was developed to control five K_U-band radar channels for the Space Shuttle, one of which doubles as a communication channel. The circuit stabilizes a Gunn-diode voltage-controlled oscillator (VCO).

As shown in the figure, a single crystal oscillator operates at 156 MHz and supplies a 27-dBm signal to a $\times 83$ multiplier and tuned-cavity filter. The output of the frequency multiplier is mixed with a small portion of the variable-frequency Gunn-diode output to produce an intermediate frequency (IF) of between 156 and 364 MHz at -30 dBm.

Wideband modular amplifiers raise the IF level to drive a phase comparator. The comparator reference input is a 52-MHz signal that is derived by dividing the crystal oscillator output by 3. (Emitter-coupled-logic flip-flops are used in this divider.)

Whenever the Gunn-diode VCO tunes to a frequency for which the IF from the mixer equals an integral multiple of 52 MHz, the phase comparator generates a zero-difference output that is used, via a loop filter, to phase-lock the Gunn diode.

The channel frequency to which the Gunn diode is phase-locked is specified by a digital code applied to logic circuitry. A portion of the mixer IF drives five simple filters, each of which is followed by a radio-frequency detector. The sweep and logic circuitry responds to these detectors, as well as to a zero-difference detection circuit and to the code that specifies the desired channel frequency. The logic ensures that the sweep is stopped, and phase lock occurs only when the IF is



A Voltage-Controlled Oscillator Is Phase-Locked to a selected frequency within any of five channels. The five frequencies are harmonics of a 52-MHz signal derived from a single 156-MHz reference oscillator. Passband filters and channel-selector logic control a sweep circuit to place the VCO in the desired passband.

in a passband that corresponds to the selected channel.

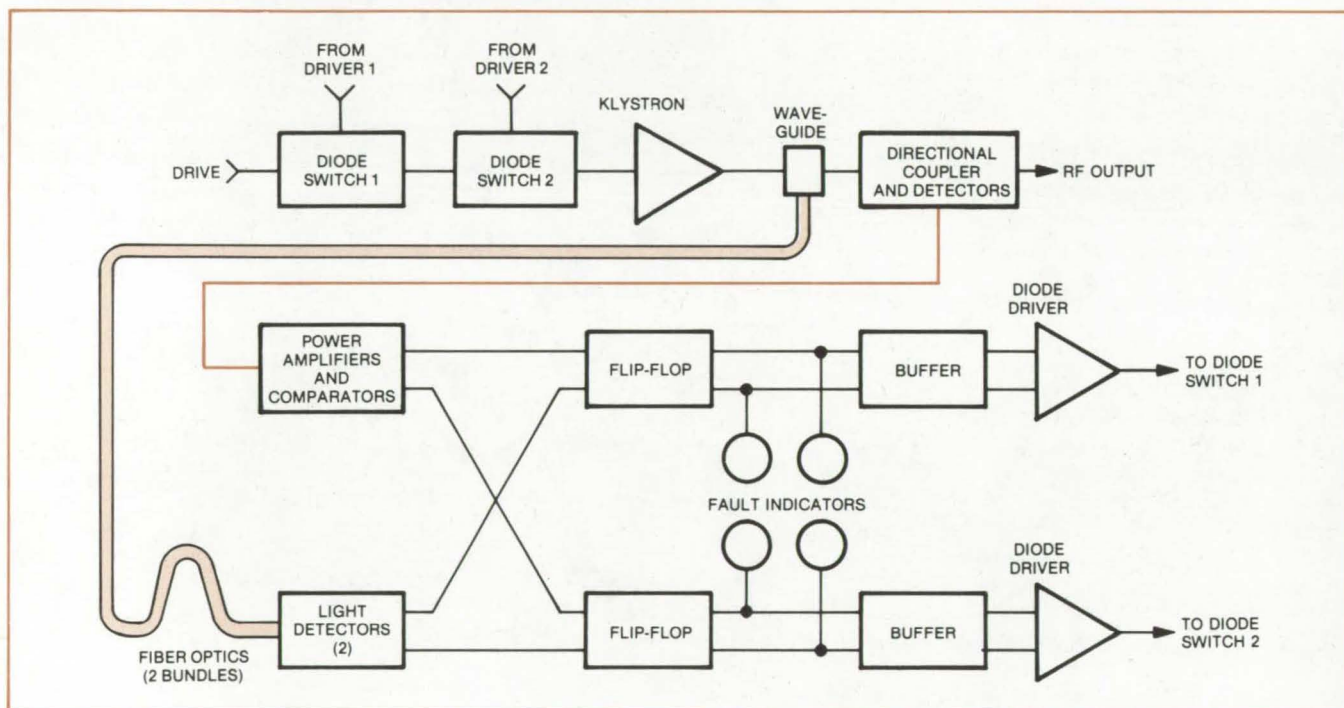
This work was done by Ronald K. Masson and Nicholas P. Morenc of

Hughes Aircraft Co. for Johnson Space Center. No further documentation is available.
MSC-18225

Arc Detector Uses Fiber Optics

A reliable arc detector for high-power microwave circuits uses light pipes and a remote solid-state detector circuit.

NASA's Jet Propulsion Laboratory, Pasadena, California



This **New Arc Detector** uses fiber optics to monitor arcs in the waveguide. The waveguide reflected power is also monitored, using crystal detectors. Both monitoring schemes utilize two channels for improved reliability.

A new arc detector for protecting high-power microwave klystron oscillators uses fiber optics connected to a remote solid-state light-sensing circuit. The fiber optics make it possible to place the sensor (a hybrid photodiode/operational amplifier) away from the RF field and high-temperature areas within the waveguide, preventing false triggering and shutdown of the klystron power supply. The new detector is more reliable, smaller, and more sensitive than many other systems that locate the detector in the waveguide.

The arc detector and sensing circuit, shown in the block diagram, incorporate two parallel fiber-optic bundles. The end of one bundle is aimed at the klystron output window, and the end of the other bundle is directed down the waveguide away from the window. The opposite end of each bundle is coupled to solid-state light detectors. Each light detector has

a silicon photodiode and a low-noise high-speed operational amplifier in a single package. The detector requires only a ± 15 -Volt power supply, as compared to several hundred volts for photomultipliers. The detector sensitivity is determined by selecting the amplifier feedback resistor. The output voltage is proportional to the input light power. It can be periodically checked by placing a small calibrated light source in the waveguide near the fiber optics.

In addition to the light signal, the circuit monitors the reflected power from a waveguide directional coupler. This RF power is divided and drives two crystal detectors. The dc output from each crystal is applied to the input of a voltage comparator. A reference voltage to the comparator is set to the value corresponding to maximum allowable reflected power. When the reference voltage is exceeded, the protective logic circuit is

activated.

The outputs from the light detectors and the reflected-power amplifiers are fed to two edge-triggered flip-flops that feed two pin-diode drivers. The diode drivers control the crystal switches that turn the klystron power supply on or off.

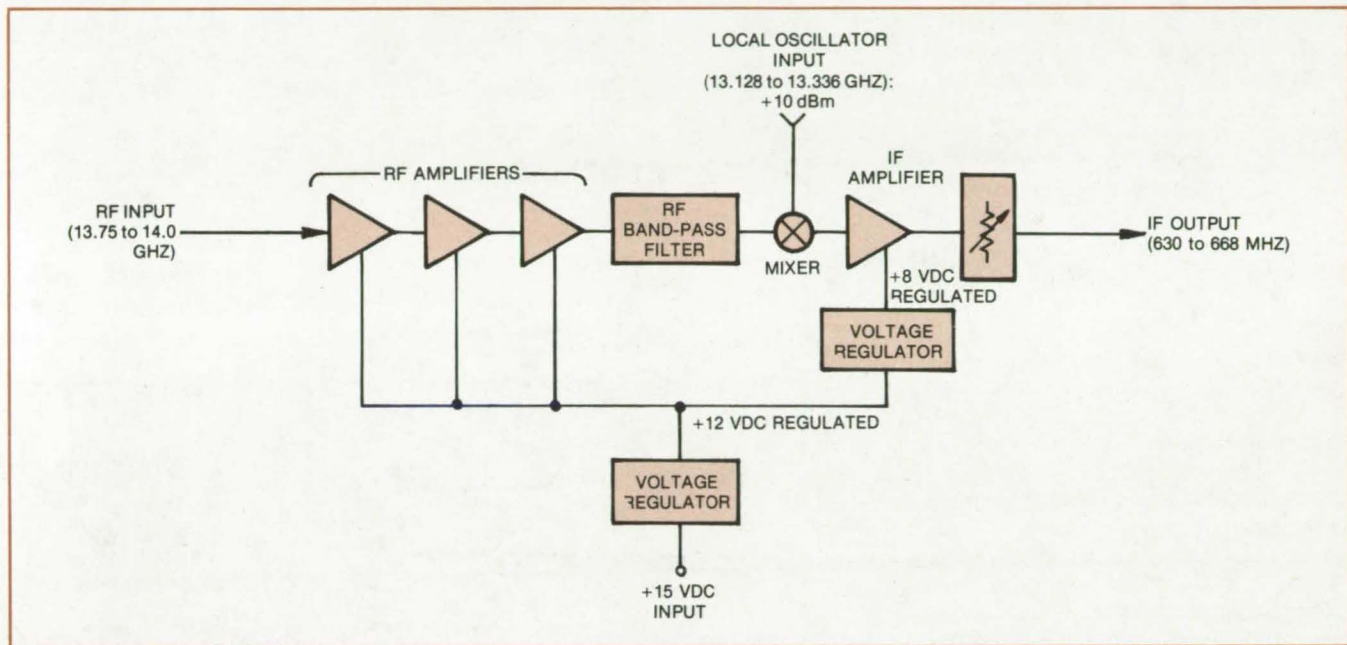
The crystal switches are mounted in a strip-line circuit and are on when they are conducting (forward biased). When both switches are off, they provide 40 dB of attenuation. When one switch is off, it provides 25 dB of attenuation, which is sufficient to reduce the RF klystron output to extinguish an arc or to reduce reflected waveguide power.

This work was done by Edward J. Finnegan and Robert A. Leech of Caltech for NASA's Jet Propulsion Laboratory. For further information, Circle 1 on the TSP Request Card. NPO-13377

Miniature K_U-Band Down Converter

Hybrid circuit can serve as the receiver front end for 13.75- to 14.0-GHz communications and radar systems.

Lyndon B. Johnson Space Center, Houston, Texas



This **Complete K_U-Band Down-Converter Assembly** for 13.75- to 14.0-GHz receivers has been packaged in a hermetically sealed container that measures only 3.25 by 1.425 by 0.62 in. A local oscillator signal is supplied externally.

A miniature, hermetically-packaged, thin-film microwave integrated circuit (MIC) serves as the complete receiver front end (excluding the local oscillator) for compact K_U-band (13.75- to 14.0-GHz) radar and communications systems. The entire MIC assembly is packaged in a small hermetically-welded, nitrogen-filled aluminum case.

The circuit, as shown, consists of three stages of balanced gallium arsenide field-effect-transistor (GaAs FET) amplification, a four-pole Tchebyscheff filter, a balanced mixer, one stage of bipolar transistor IF amplification, and a passive temperature-compensation circuit. An IC voltage regulator is also included.

The amplifiers and other functional elements are fabricated with thin-film

gold circuitry and tantalum nitride resistors on a ceramic substrate. Components, such as transistors and capacitors, are in unpackaged chip form. Each substrate is bonded to a metal carrier that is screwed to the bottom of the case interior.

The measured overall noise figure of the assembly is approximately 4 dB. Each of the three 14-GHz amplifier stages is a balanced module consisting of an input hybrid coupler, two matched GaAs FET channels, and an output coupler. The four-pole Tchebyscheff band-pass filter is deposited as an edge-coupled strip-line layout on an aluminum substrate. A single-balanced mixer is used, and the IF amplifier is a conventional wideband MIC circuit designed around a silicon bipolar transistor.

A "pi" attenuator with a thermistor in the series leg gives the circuit good gain stability over its temperature range. By carefully selecting the resistance values in the shunt legs, the attenuator is made to exhibit a reasonably-good voltage standing-wave ratio (VSWR) and to have a useful attenuation/temperature curve. Although this attenuator does demonstrate some variation in attenuation as a function of temperature and has a higher insertion loss than PIN diode attenuators, its simplicity and small size make it useful for lower-frequency wideband applications.

This work was done by David A. Norbury of Avanteq, Inc., for **Johnson Space Center**. For further information, Circle 2 on the TSP Request Card.

MSC-18313

Testing Integrated Circuits by Photoexcitation

"State superposition" method is a rapid pass/fail check for production-screening of IC's.

Marshall Space Flight Center, Alabama

A system for testing integrated circuits uses photoexcitation to determine the quality of internal elements that are inaccessible to electrical tests. Using a "state superposition" technique, the IC is scanned by a narrow laser beam while being electrically activated through a sequence of operating states. The photocurrent generated in the IC by the light beam is displayed on a CRT in synchronism with the position of the beam. The resulting image is a "signature" of the device under test and could be used to make an accept/reject decision during production screening.

This new approach overcomes a basic problem in using electrical tests to screen integrated circuits: the buffering effect of each succeeding stage on the preceding stages of a digital IC prevents direct monitoring of the internal operation of the circuit by measurements at the external terminals. The photoexcitation method is also superior to electron-beam scanning, since it is completely nondestructive (whereas the electron beam can damage the circuit) and does not require a vacuum chamber.

Although photoexcitation is a known method for testing microcircuits, it has usually not been used for production screening. This is because to be certain that all internal elements (such as transistors and diodes) are active during the tests, many images must be scanned, each with the circuit in a different digital state. This gives detailed information about the circuit operation, but it generates a lot of data that are not easily reduced to a pass/fail criterion.

In the new approach, a set of digital states is selected such that each internal element appears in at least one of the corresponding photoresponse images. Then a test circuit (or program) generates a superposition of the photoresponse images by scanning the device with an optical scanner as it is being clocked repeatedly through the set of selected states. This superposition (the "signature" of the device) can be

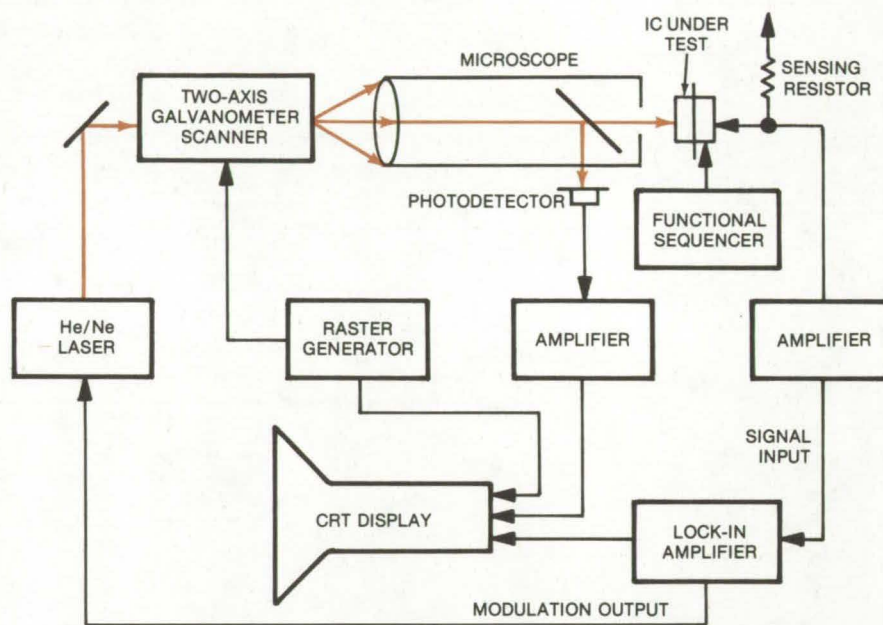


Figure 1. This **Integrated-Circuit Test System** scans a device under test with a modulated laser beam as the circuit is sequenced through a selected group of digital states. The light generates a photocurrent that is sensed, demodulated by a lock-in amplifier, and displayed.

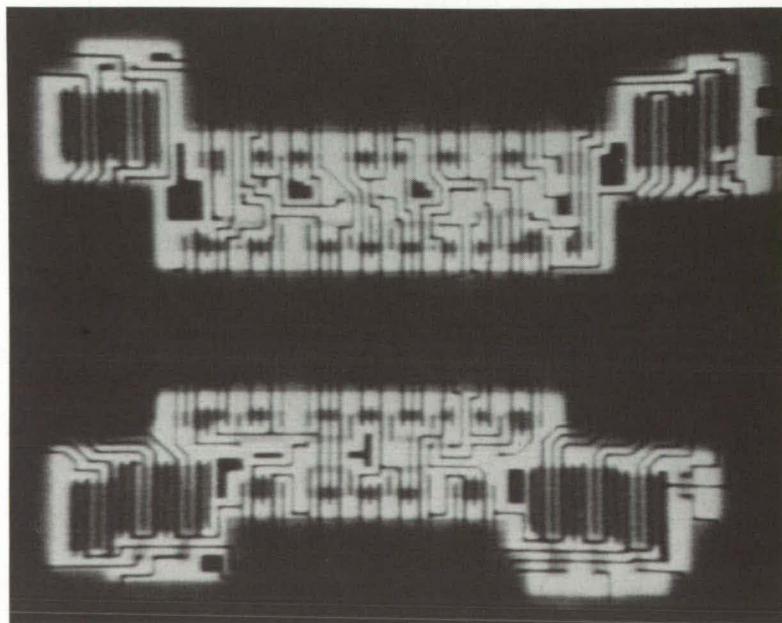


Figure 2. This **Photoresponse Image** was produced by superimposing the images of several digital states. The image is a map of the photocurrent produced when laser light is scanned over the circuit. Bright areas represent regions in which the photocurrent is high; dark areas are regions in which the photocurrent is small. The image is that of a 4028 CMOS microcircuit.

easily compared with the signature of a reference device.

The photoexcitation system — which has been used with good results to test complementary metal-oxide-semiconductor (CMOS) integrated circuits — scans the IC surface with helium/neon laser light that is amplitude-modulated at about 135 kHz (see Figure 1). The laser beam is controlled by lenses and galvanometer/mirror scanners, and the light passes through a neutral density filter that limits the power delivered at the IC surface to less than about 0.1 milliwatt.

The photoresponse signal is sensed by a small resistor in series with the negative voltage (or ground) terminal of the device under test. The voltage drop across the sensing resistor is amplified by an oscilloscope plug-in amplifier and demodulated by a lock-in amplifier.

An important advantage of the modulated laser and lock-in amplifier demodulator is that the zero-reference level of the photoresponse signal is independent of the static power-supply current consumption of the device under test. This is not true when an unmodulated laser is used; in that case, the CRT intensity control must be continually readjusted when the current changes (as a result of changing the digital state, the temperature, or the device).

In the preliminary work, a frame scan time of 50 seconds and a line scan time of 0.1 second were used, producing a 500-line raster with nearly-invisible scan lines (see Figure 2) and a good reflected image.

In practice, the scan time can be much shorter. For very complex or very dense integrated circuits, the functional sequencing of the device

may have to be controlled by the raster generator. This could further reduce the time required to scan the circuit, since only the circuit elements irradiated by the laser beam at any given moment would be activated.

This work was done by J. J. Erickson and Miguel E. Levy of Hughes Aircraft Co. for **Marshall Space Flight Center**. Further information may be found in NASA CR-150474 [N78-13326], "Optical Scanning Tests of Complex CMOS Microcircuits," a copy of which may be obtained at cost from the New England Research Application Center [see page A7].

Inquiries concerning rights for the commercial use of this invention should be addressed to the Patent Counsel, Marshall Space Flight Center [see page A8]. Refer to MFS-23943.

Precise Matching of Diodes

Low-cost method for matching the forward voltage drops of diodes and other semiconductors

NASA's Jet Propulsion Laboratory, Pasadena, California

Two circuit arrangements, one using an ac and the other a dc power source, rapidly select diodes and other semiconductor devices with matched, forward voltage drops. Both circuits are simpler (and less expensive) than conventional, characteristic-curve tracers.

The ac and dc test circuits, which are bridge configurations, are shown in Figure 1. Both versions include two precision equal-value current-limiting resistors R_1 and R_2 in the bridge legs containing the diodes. Each circuit also includes an oscilloscope or other voltmeter to detect bridge imbalance. The dc circuit has precision resistors in the other bridge legs, and the ac circuit includes an additional diode and resistor (R_5) to prevent transformer core saturation during one-half of the ac cycle.

Throughout the tests, any difference in forward voltage drop between the test and the reference diodes is displayed as either a positive or negative voltage across the measuring device. After testing a batch of diodes, those

(continued on next page)

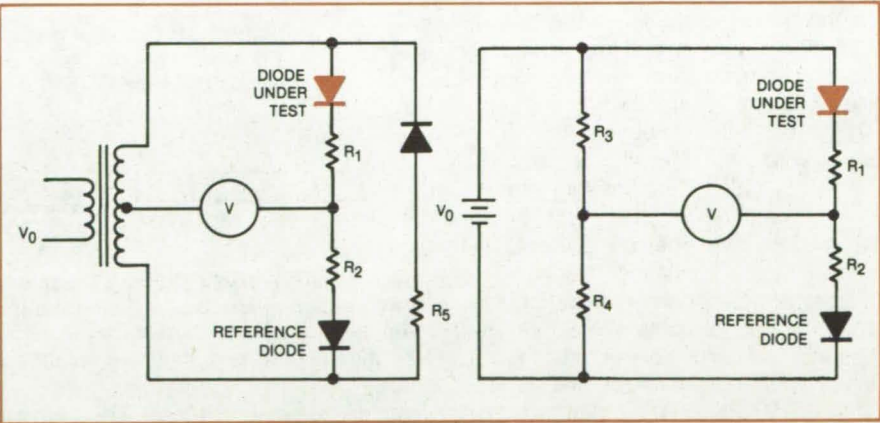


Figure 1. **Circuit for Selecting Matched Diodes** can use either an ac (left) or dc (right) excitation source. Any difference in forward voltage drop between the tested and reference diodes is measured as a voltage imbalance across the bridge.

DEVICE	I_f	V_f	R_1, R_2	R_3, R_4	R_5
SIGNAL DIODE	10 mA	1.0 V	400 Ω (1/2 W)	1,000 Ω (1/2 W)	900 Ω (1/2 W)
RECTIFIER	1.0 A	1.0 V	4 Ω (10 W)	1,000 Ω (1/2 W)	9 Ω (25 W)
POWER RECTIFIER	10.0 A	1.0 V	0.4 Ω (100 W)	1,000 Ω (1/2 W)	0.9 Ω (250 W)

Figure 2. **Representative Resistor Values** are given for the ac test circuit, using a center-tapped 10-volt transformer source.

with identical voltage offsets (within prescribed limits) are easily separated into groups for subsequent use in matched pairs.

For each test, the supply voltage and current can be fixed at levels identical to those encountered by the semiconductor in actual operation. This is controlled by selecting the

correct value of R_1 and R_2 . Figure 2 lists representative resistor values for different current levels supplied by a regulated 10-V center-tapped source. Both power and signal diodes can be tested in the same arrangement because the tested semiconductor is in the upper bridge leg and the reference diode is in the lower leg,

and their temperature coefficients cancel each other.

This work was done by Colonel W. T. McLyman of Caltech for NASA's Jet Propulsion Laboratory. For further information, Circle 3 on the TSP Request Card.
NPO-14293

Splicing Shielded Cables

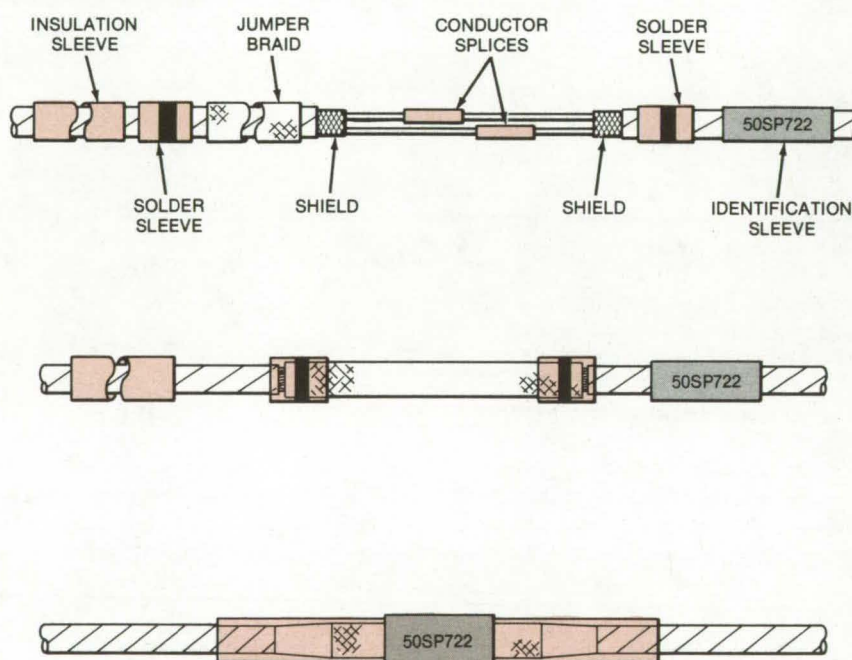
A simple repair technique retains the cable characteristic impedance.

Lyndon B. Johnson Space Center, Houston, Texas

Conventional splicing techniques for shielded cables often cause the cable to bulge at the spliced connection. This changes the separation between the conductors and alters the cable characteristic impedance. However, a new "staggered" splice eliminates this problem. In addition, a jumper braid (instead of a single-wire connection) maintains uniform shielding throughout the length of the cable. (A single-wire jumper is inadequate at all but the very lowest frequencies.) Moreover, the staggered repair can be made without disconnecting the cable ends.

The splice, as shown in the illustration, consists of two crimp-conductor splices and heat-shrinkable insulation sleeves, one jumper braid, two heat-shrinkable solder sleeves, one heat-shrinkable insulation sleeve, and one heatshrinkable identification sleeve. The procedure involves first crimp-splicing the two inner conductors. The splices with insulating sleeves are staggered to prevent cable bulge. Next, a wire braid is fitted over the splices and is connected to the severed shield ends by heat-shrinkable solder sleeves (solder preforms surrounded by shrinkable jackets). After the sleeves are heated to join the ends, an insulation sleeve is slid over the section and heat-shrunk in place. The same procedure, with an identification sleeve, completes the splice.

Two possible insulation materials are modified polyvinylidene fluoride (PVF) and polytetrafluoroethylene (TFE). Since PVF shrinks at a temperature of 350° F (177° C), it is



This **Shielded-Cable Splicing Technique** retains the cable characteristic impedance. The procedure involves splicing the inner conductors in a staggered pattern (top), installing a jumper braid by heat-shrinking two solder sleeves (center), and placing an insulation sleeve over the repaired section and heat-shrinking it (bottom).

easier to install than TFE, which shrinks at 621° F (331° C). TFE, however, is suitable for high-temperature service. Tests on repaired cable sections, using the new splice, showed no significant impedance departures from the original specifications.

This work was done by Wallace P. Lind and William B. McGougan of

Rockwell International Corp. for Johnson Space Center. For further information, Circle 4 on the TSP Request Card.

Inquiries concerning rights for the commercial use of this invention should be addressed to the Patent Counsel, Johnson Space Center [see page A8]. Refer to MSC-18297.

Modular Ground-Wire Connector

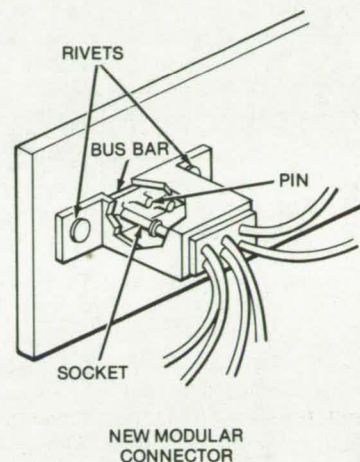
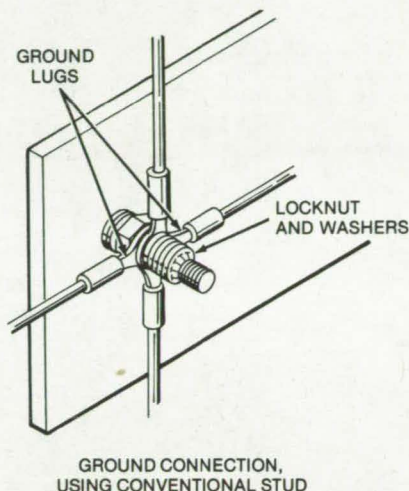
Module makes it easy to remove and attach ground wires.

Lyndon B. Johnson Space Center, Houston, Texas

A chassis-mounted module for ground wires is superior to conventional ground studs (see figure). With the new module, more ground connections can be made in a smaller area, and no terminal lugs, lockwashers, or locknuts are required. Connections are removed or replaced simply by changing wires that have crimped-on connectors. Thus, it is not necessary to remove screws or nuts or to apply a conformal coating. Since the module can accommodate more ground wires than a stud, it reduces the number of holes that must be drilled or punched in a chassis or panel for ground connections.

The module is actually a modified version of a commercially-available pin-and-socket connector that has a one-piece copper bus bar within the housing. One version of this module can handle up to twenty wires.

In the new design, the bus bar is extended to protrude from the sides of the module, and holes are drilled in it so that it can be riveted to the support. The strength of the assembly is therefore improved, as is the load-carrying capacity of the module. This design



Ground Wires Are Inserted into this module (right) that receives crimped-on connectors. A conventional ground lug (left) requires more hardware and the application of a conformal coating.

will be used to make approximately 250 medium-capacity ground-wire connections on the Space Shuttle Orbiter. An alternate version of the module has a single threaded stud, at the center of the bus bar, in place of the riveted connections.

This work was done by William T. Dean and Eugene J. Stringer of Rockwell International Corp. for Johnson Space Center. For further information, Circle 5 on the TSP Request Card. MSC-16633

Electrical-Ground Monitor

Instrument continuously and automatically checks for short circuits between electrical equipment and ground.

Lyndon B. Johnson Space Center, Houston, Texas

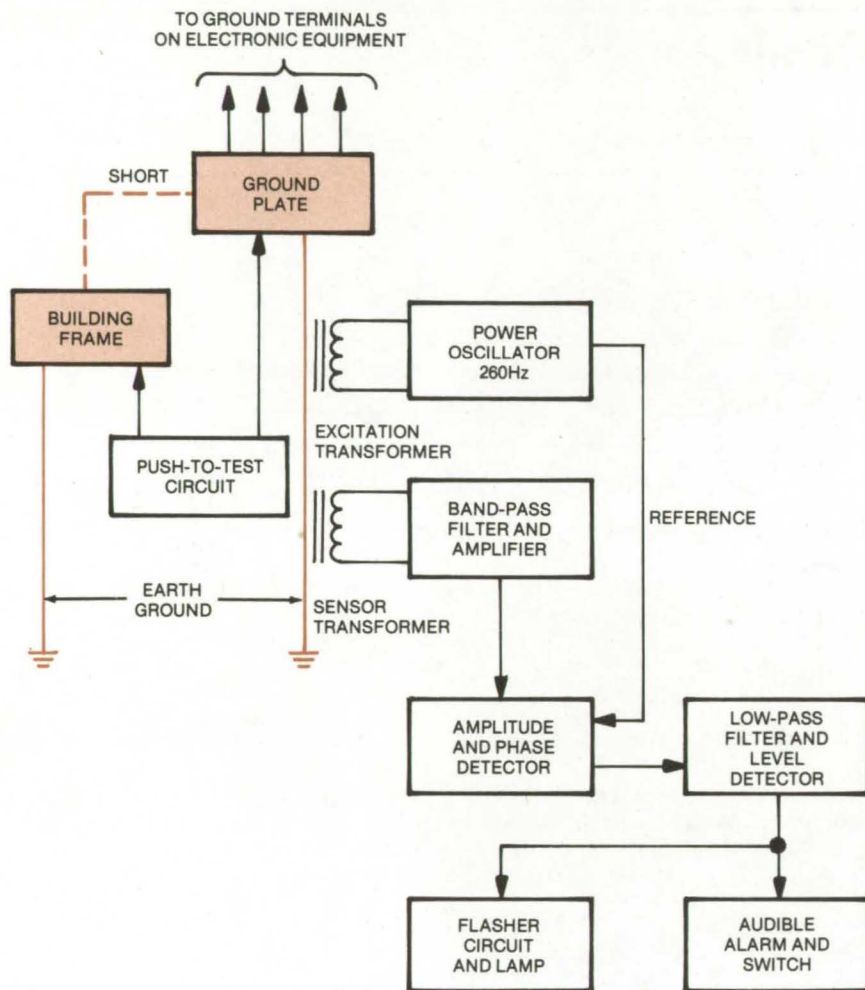
An instrument for detecting short circuits continuously monitors ground connections and sounds an alarm if an out-of-limits condition occurs. The circuit includes electronics that prevent false triggering by high-resistance or capacitive paths and other noise. It is used with a single-point grounding system, in which electrical and electronic equipment are connected locally by cables to a single point, and that point is tied to Earth.

The monitor was developed as a replacement for simple resistance-measuring instruments. These required all equipment connected to the single-point grounding system to be turned off and the cable to the Earth-grounding rod to be disconnected before a ground-fault check could be made.

The new monitor operates from transformers on the single-point grounding cable (see figure). A continuously-running power oscillator

drives the excitation transformer, inducing a low-voltage sinewave in the cable. The voltage and frequency are low to prevent interference with equipment connected to the grounding system; further, a frequency is selected that is not too close to a strong harmonic of the powerline, since a harmonic could falsely trigger the alarm. Reasonable choices for the voltage and frequency are 0.25 volt and 260 hertz.

(continued on next page)



Electrical-Ground Monitoring Instrument detects currents created by short circuits or low-resistance paths between the ground plate and the building frame. The electronics can discriminate between true ground loops and spurious currents caused by capacitive or high-resistance paths.

When a grounding violation occurs, such as a short circuit or low-resistance path between the ground plate and the building frame, a ground loop is formed. The induced voltage causes a current to flow through the ground plate and short circuit, through the building frame to Earth, and up

through both transformers. The current through the sensor transformer induces a voltage that is applied to the input of the band-pass filter and amplifier. Here, noise and powerline harmonics are filtered out so that they do not hamper the operation of the alarm.

The filtered and amplified signal is fed to the amplitude-and-phase detector. By comparing the phase of the signal with the phase of the power oscillator, the phase detector can determine whether the signal is caused by a true short circuit or by a capacitive path. Capacitance between the single ground point and Earth, created by powerline filters and transformers, produces a signal with a leading phase that is rejected by the phase detector. On the other hand, a short circuit produces a signal with a phase that is the same as that of the power oscillator; in this case, the amplitude and phase detector generates a dc output.

The low-pass filter and level detector remove ripple from the dc signal and determine whether the dc level is high enough to sound the alarm. A high resistance, such as that of a worker's body in contact with the building frame, produces a low dc level that is rejected by the level detector. However, a short circuit or low resistance between the ground plate and the building frame produces a high dc level, causing the level detector to send a logic signal to the audible alarm and flasher circuit. A lamp then flashes until the grounding violation has been corrected. The alarm sounds, but it can be turned off while the correction is made.

The monitor contains a push-to-test circuit that can momentarily connect a low resistance between the ground plate and the building. This allows the sensitivity and operation of the grounding alarm to be checked.

This work was done by Thomas D. Lyons of Lockheed Electronics Co., Inc., for Johnson Space Center. For further information, Circle 6 on the TSP Request Card.
MSC-18281

One-Third Selection for Matrix-Addressing Ferroelectrics

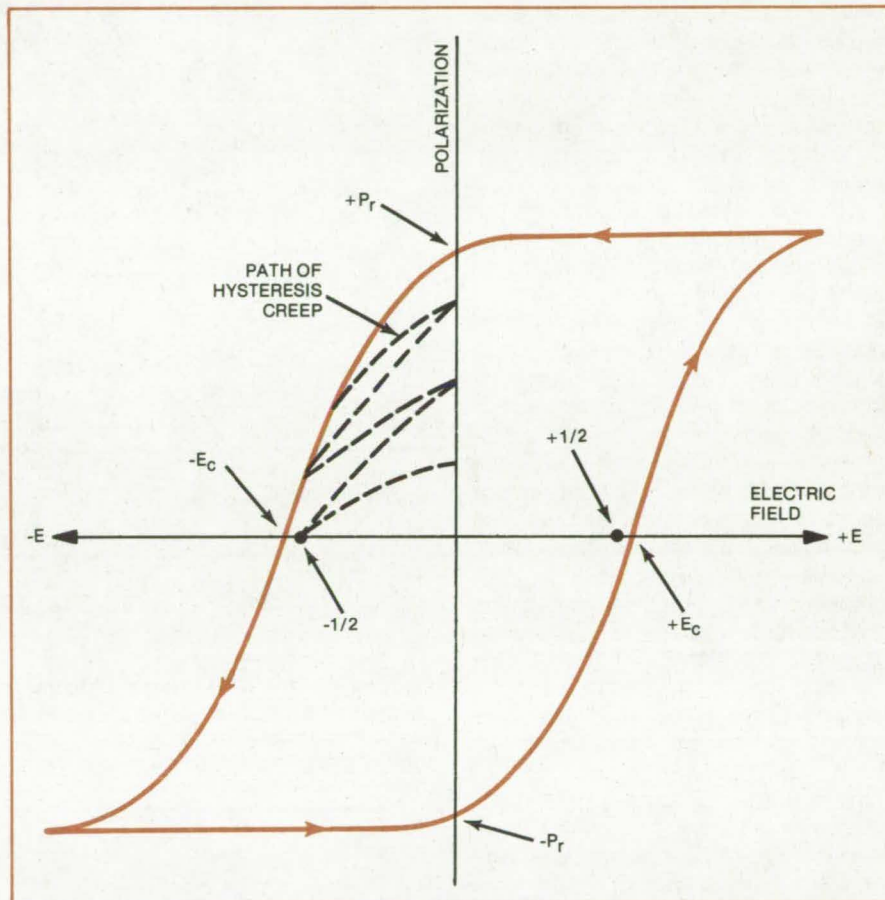
Three-level signal scheme
minimizes hysteresis creep.

Langley Research Center, Hampton, Virginia

The utility of ferroelectrics as memories is limited by electrical cross-coupling that occurs when addressing a ferroelectric device. Data are written into the ferroelectric memory by pulsing orthogonal lines, either sequentially or on a line-at-a-time basis. Writing is very fast; the switching characteristics of the ferroelectric material allow each line to be written within a few microseconds. The standard approach used to address a matrix of orthogonal lines is to use the full voltage on one y line to enable it to accept input data on the x lines or line. One-half voltage is applied to all other y lines to protect them from being influenced by new data on the x lines or line (i.e., $V_y = 1$, $V_x = 1$, $V_y = 1/2$). A high x-line plus voltage would be "no data," and a zero voltage would be "data."

A high poling voltage is required for ferroelectrics, and the hysteresis loops are not as square as with, for example, ferromagnetic materials. A typical hysteresis loop for ferroelectric materials is shown in the diagram. Note that the one-half select voltage is close to the switching voltage E_C . Repetitive application of the minus-one-half select voltage would have the effect of depoling the material from its poled state of $+P_r$ and erasing the information stored at the corresponding juncture of x and y lines. This depoling process is called hysteresis creep, and its electrical path is also plotted in the diagram.

The difference between the x and y voltages at an intersection creates the electric field, E , across the ferroelectric. The electric field is proportional to $(V_y - V_x)$ divided by the thickness of the ferroelectric. If the one-half select voltage resulted in an electrical field greater than E_C , the previous polarization history would be



Hysteresis Loop for a typical ferroelectric memory material is shown along with polarity definitions. With the usual scheme, the select (address) voltage of $1/2$ is close to the switching voltage, E_C . This leads to hysteresis creep upon each application of the select voltage, resulting in the erasure of data.

removed in one pulse. All the line intersections normally are initially set to $-P_r$ with a negative signal.

A three-level signal scheme with a minor change in the voltage levels will minimize the hysteresis creep. By making the voltage levels $V_y = 1$, $V_x = 2/3$, and $V_y = 1/3$ instead of $V_y = 1$, $V_x = 1$, and $V_y = 1/2$, respectively, the cross-coupling voltage levels are reduced significantly. Since hysteresis creep is a function of the number of the voltage pulses and the magnitude of the electric field

relative to E_C , this small improvement in the cross-coupling signal levels greatly relieves hysteresis creep.

This work was done by Lawrence E. Tannas, Jr., of Rockwell International Corp. for **Langley Research Center**. No further documentation is available.

Title to this invention has been waived under the provisions of the National Aeronautics and Space Act [42 U.S.C. 2457(f)], to the Rockwell International Corp., 3370 Miraloma Ave., Anaheim, CA 92803.
LAR-11993

Simplified Phase Detector

Although it has only a few components, a phase detector circuit is linear over 270°.

NASA's Jet Propulsion Laboratory, Pasadena, California

A comparatively simple circuit gives a dc output voltage that is very nearly proportional to the phase difference between an oscillator signal and a reference signal. The region of linearity extends over a phase deviation range of $\pm 135^\circ$.

The new circuit (Figure 1), a modified Tanlock sine-wave phase detector, is intended for systems in which the signal-to-noise ratio is high. Originally, it was designed to demodulate a 500-kilohertz ranging clock signal from the 20.278-megahertz intermediate frequency component in X-band transmitter test equipment.

The detector transforms the oscillator signal into equal, 90° out-of-phase components, transforms the reference into equal, 180° out-of-phase components, and combines the four components in a network containing two matched diodes. The resulting output, E_o , is shown in Figure 1. S is the peak oscillator voltage, ϕ is the phase difference between the oscillator and reference signals. The measured output is shown in Figure 2. The output equation holds if the peak oscillator and peak reference signals are equal, if the phase separation between the oscillator signal components is 90°, and if the diodes are linear (that is, if their characteristic exponent $n = 1$).

If $n = 2$ (a square-law characteristic), the detector output will be sinusoidal instead of a straight line, and it will have a 180° range between peaks instead of the 270° range shown in Figure 2. Also, if the ratio of the oscillator and reference peak voltages is much greater than or less than 1, the range will similarly be limited to 180°.

This work was done by Lloyd M. Hershey of Caltech for NASA's Jet Propulsion Laboratory. For further information, Circle 7 on the TSP Request Card.
NPO-13395

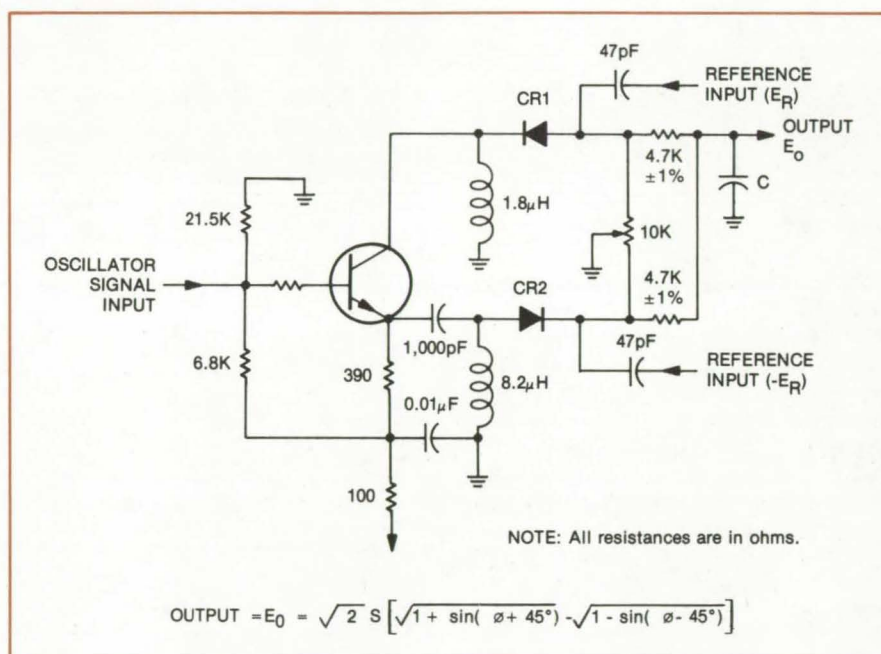


Figure 1. This 270° Phase Detector circuit combines oscillator and reference signals in a matched diode network. The output is linear if the inputs are equal in peak amplitude, the oscillator signal is converted to two quadrature components, and the crystals are linear.

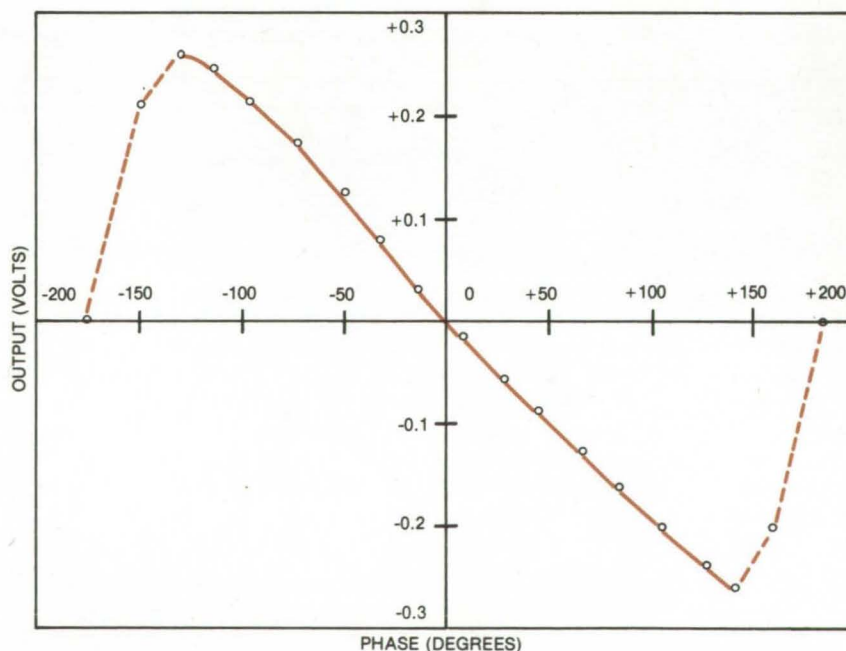


Figure 2. The Measured Output Voltage is linear over a 270° range of phase difference.

Digital Correlator With Fewer IC's

A novel configuration of adders reduces the circuitry needed to compare two 24-bit words.

Lyndon B. Johnson Space Center, Houston, Texas

A new digital correlator requires only a few integrated circuits to determine the synchronization of two 24-bit digital words. The modular circuit can be reduced or expanded easily to accommodate shorter or longer words. It uses a fully-parallel asynchronous structure for maximum speed without special clocks, counters, or accumulators, as would be needed for a serial correlator.

With little or no modification, the correlator can be utilized in industrial and commercial data processing and telecommunications. Digital filters, Hamming-distance calculators for error detection and correction algorithms, and threshold logic circuits are likely applications, in addition to digital correlators.

In the configuration shown in the figures, the correlator analyzes a received frame-synchronization pattern containing 24 bits and compares it bit by bit with the correct frame-sync pattern. If the Hamming distance (the number of disagreeing bits) between the received data and the ideal frame is less than 3, a "positive" correlation is discerned; and if the Hamming distance is greater than 21, a "negative" correlation is recognized.

The correlator functions in three stages. The first stage (Figure 1) generates 24 parallel check bits and stores them in shift registers SR₁, SR₂, and SR₃. A check bit is a "1" if a bit in the received frame-sync word differs the same bit in the ideal pattern.

The second stage (Figure 2) counts the "1's" in the 24-bit pattern to generate the Hamming distance. This stage consists of three rows of adders.

The first row uses four standard 4-bit full adders in a novel configuration that allows each adder to sum the number of logical "1's" in a 5-bit pattern. This row of adders uses the highest-order bit cell to add unit inputs. The double input gives access to the carry
(continued on next page)

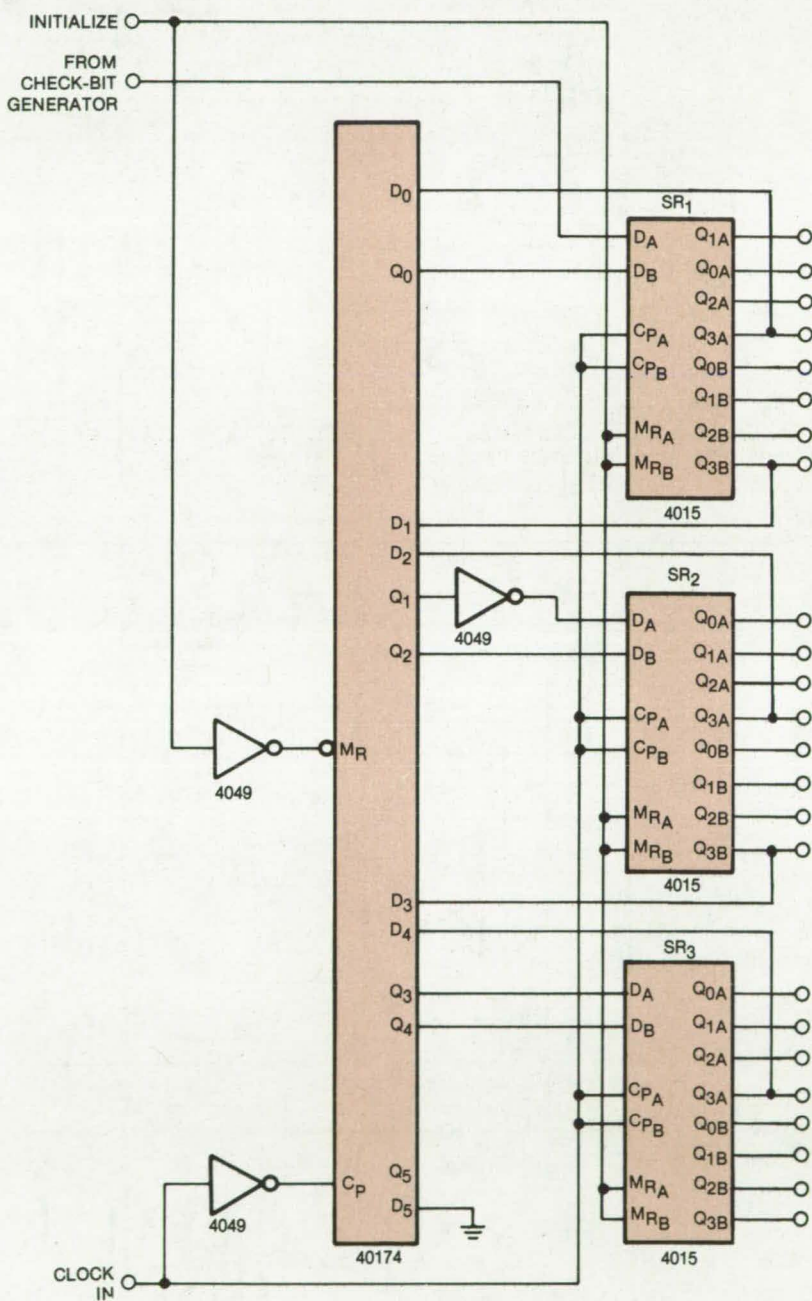


Figure 1. At the input to the **First Stage of A Digital Correlator**, a 24-bit frame-synchronization word has been compared with a reference word to create 24 "check" bits. The comparison is made serially, and the results are stored in shift registers SR₁, SR₂, and SR₃. A "zero" is stored if a bit in the incoming word is the same as the corresponding bit in the reference word; if the bits differ, a "one" is stored.

input of the highest cell. This double input in no way affects the output of the cell to which it is connected. Any carry from the second cell appears at the output of the third cell.

Thus the IC chip in each adder is, in effect, partitioned into two devices. The output and carry of the highest cell are additional inputs to the first and second cells, respectively. This

arrangement allows one chip to sum up to five 1-bit inputs.

The second row of adders sums the outputs of the first row in pairs, and the third row adds the outputs of the second row. (The carry inputs of the second and third rows are also used as unit inputs.) The second stage, as described so far, can sum up to 23 inputs. When a half adder is included, as shown in the figure, the circuit can sum 24 inputs. The output of the second stage is a 5-bit binary sum of the 24-unit inputs.

The third stage (Figure 3), consisting of combinatorial logic, examines this result and checks to see if it is less than 3 (positive correlation) or greater than 21 (negative correlation).

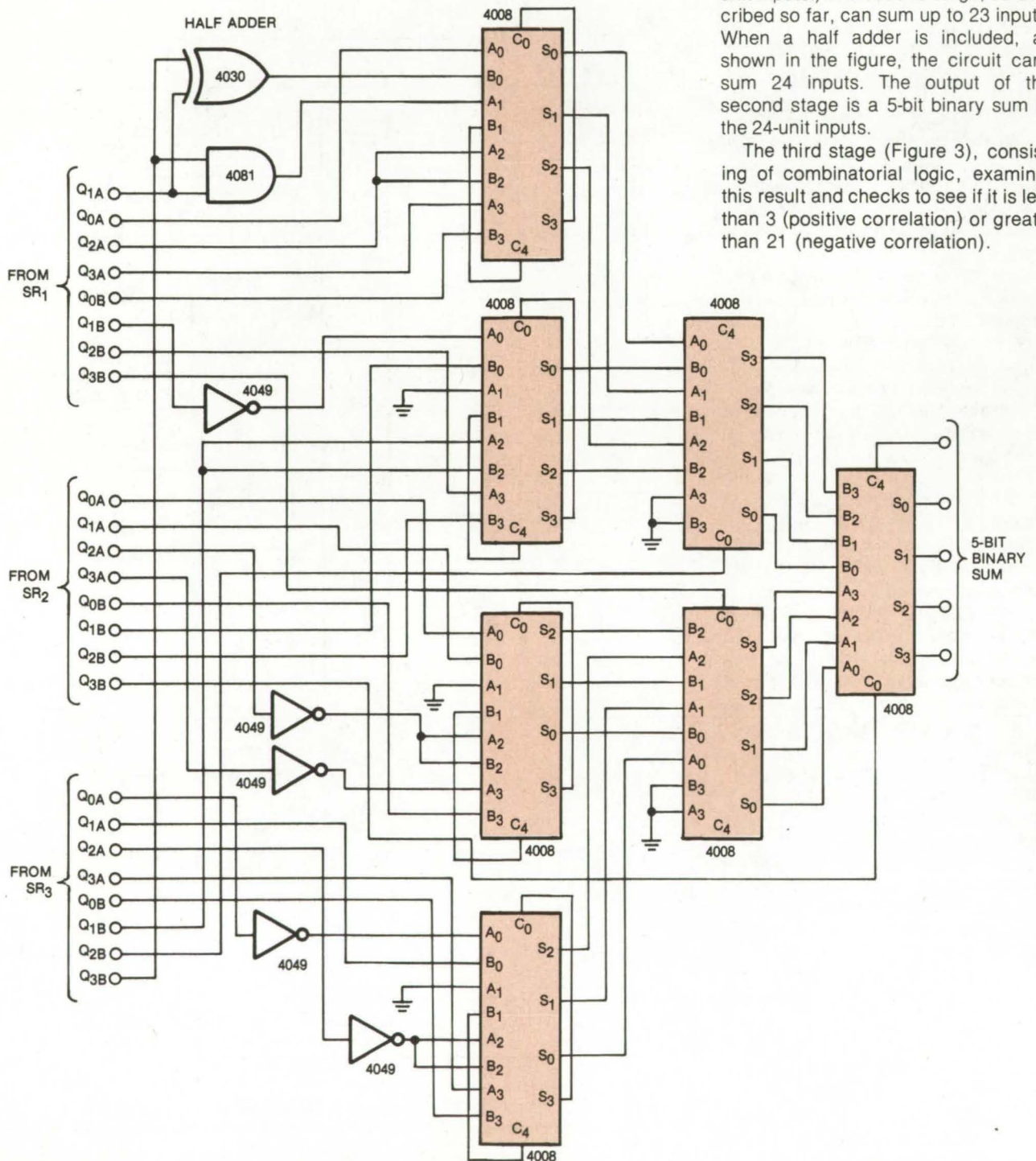


Figure 2. The digital-correlator **Second Stage** employs three rows of adder IC's to sum the "1's" in the output of stage one and determines the Hamming distance. Each element in the first row of 4-bit adders is configured to sum 5 bits.

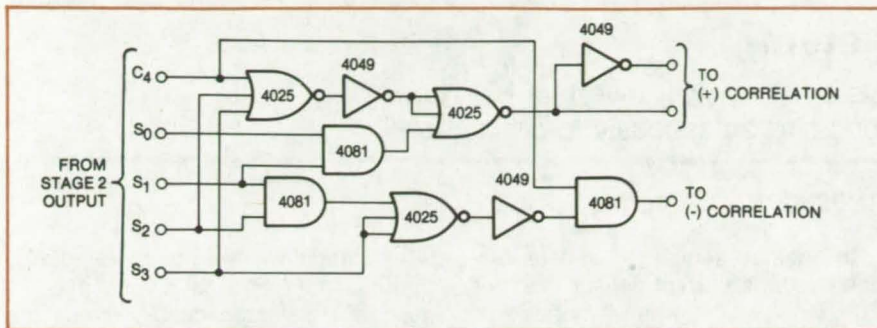


Figure 3. In the **Third Stage**, the 5-bit output word of stage two is checked for positive correlation (when the word value is less than 3) or negative correlation (when the value is greater than 21).

This work was done by Garrett G. Apple and Lawrence Rubin of TRW, Inc. for **Johnson Space Center**. No further documentation is available. MSC-16743

Pulse-Width-Modulated Attenuator for AGC

Automatic-gain-control circuit has high linearity and wide dynamic range.

NASA's Jet Propulsion Laboratory, Pasadena, California

An automatic-gain-control (AGC) circuit regulates the gain of intermediate-frequency and radio-frequency signals over a wide dynamic range with high linearity and very low phase shift. It has potential uses in radio and television receivers, in signal distribution systems, and in test and measurement instruments.

The circuit operates on a form of pulse modulation by switching the input signal on and off with a duty cycle that depends on the widths of a series of pulses. A duty cycle of 100 percent produces zero attenuation, and a zero-percent duty cycle gives complete attenuation. The attenuation varies linearly with pulse width between these extremes.

The input signal is turned on and off by an RF switch (see Figure 1). The essential requirement is that the switch have a high on/off ratio; the higher the ratio, the greater the attenuation that is possible before

phase shift starts to build up. (Theoretically, if the on/off ratio is infinite, there will be zero phase shift.) With PIN diodes, for example, 60 dB of attenuation are possible with only a 2° phase shift. Isolation amplifiers ensure that the widely changing impedances of the switches do not affect the source, load, or band-pass filter. Figure 2 shows the circuit waveforms for a 6-dB attenuator (50-percent duty cycle).

The band-pass filter eliminates sidebands. When a single-carrier-frequency signal is applied to the input switch, the ac output consists of the carrier and many sidebands spaced at the pulse frequency. The filter removes the sidebands so that the carrier output is essentially the same as the input except that the carrier amplitude is a function of the pulse width. The filter should be well matched so that the output phase does not drift with pulse-width

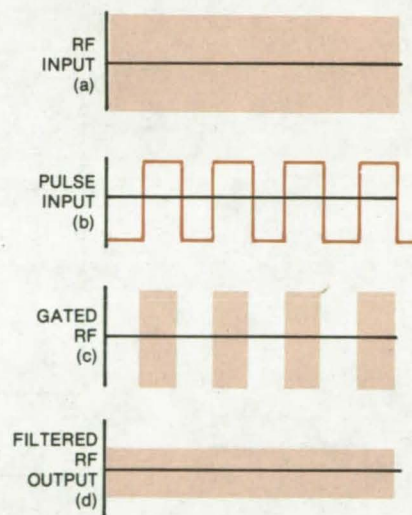


Figure 2. An **RF Input (a)** is **Attenuated** by switching it on and off with a pulsed gate input (b) to an RF switch. The gated RF (c) is filtered to produce an attenuated RF output (d). A 50 percent duty cycle (as shown) gives 6-dB attenuation.

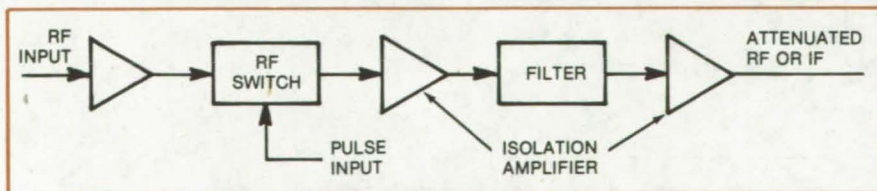


Figure 1. **Gain-Control Circuit** applies pulse-width modulation to the input signal through solid-state RF switching diodes and mixers. Thus the output attenuation is proportional to the pulse-width duty cycle. (Zero-percent duty cycle gives complete attenuation, 100-percent duty cycle gives no attenuation.)

changes; it should also be narrowband compared with the pulse repetition rate so that the sidebands are down by 60 dB or more.

This work was done by John W. MacConnell of Caltech for **NASA's Jet Propulsion Laboratory**. For further information, Circle 8 on the TSP Request Card. NPO-14127

Overload Protection System

A two-stage overload protection system for power inverters is inactive under normal conditions and responds instantaneously to an overload.

NASA's Jet Propulsion Laboratory, Pasadena, California

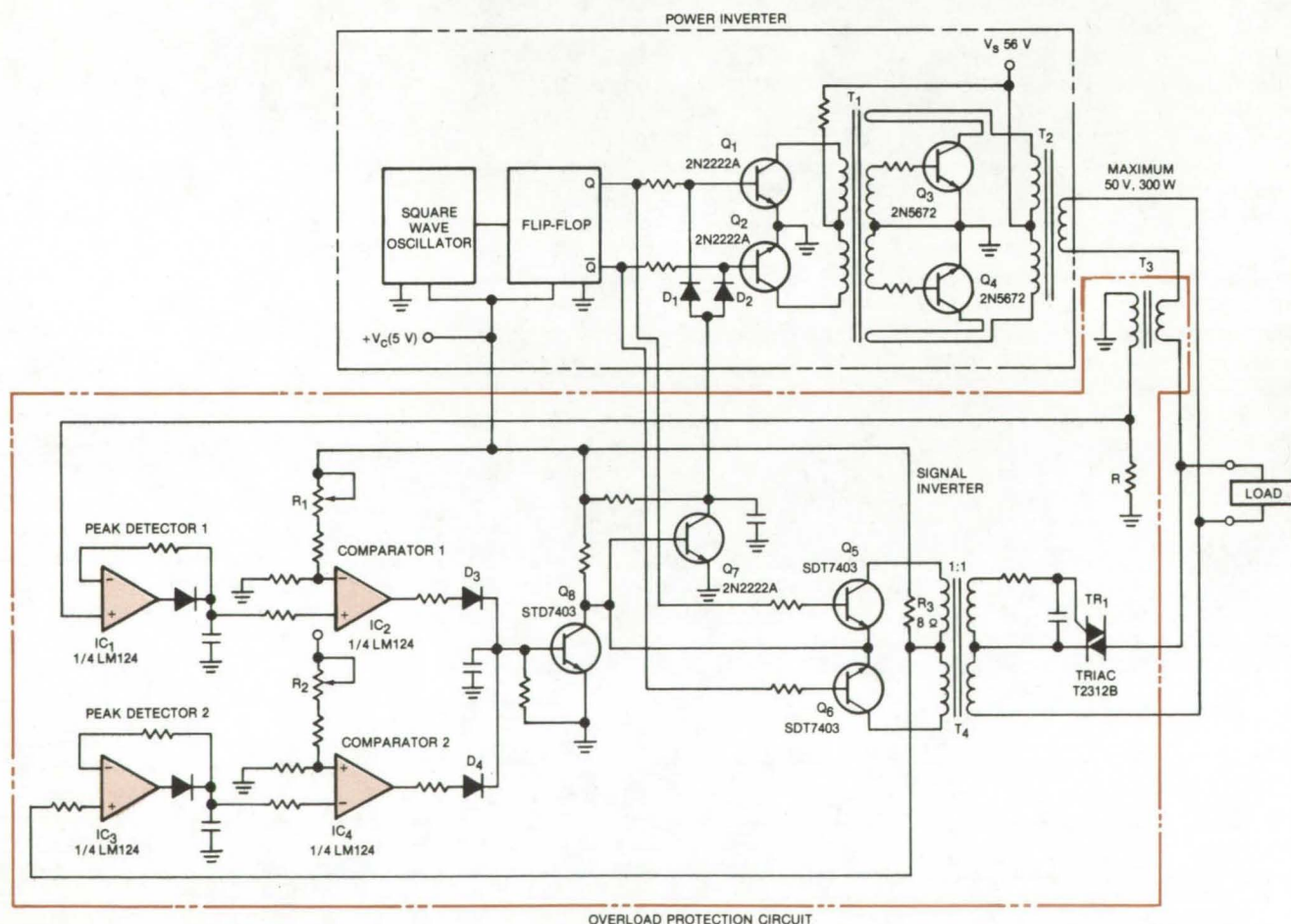
Power-inverter dc-to-ac converters require current limiting or overload protection to safeguard the supply against short circuits and other current overloads. A feedback loop that turns off a transistor in series with the dc supply and turns on a parallel high-resistance path is sometimes used for protection. However, this limiter dissipates power in the switching transistor even under nonoverload conditions. Also, under some overloads, there is insufficient back bias to cut off the transistor completely, subjecting it to high currents that can cause permanent damage.

In another frequently-used protection circuit, a current sensor in series with the load triggers a monostable multivibrator to inactivate the inverter clock generator; however, this circuit can be sluggish since it depends on the time constant of the monostable. It is also subject to oscillation and current spiking, which can occur when the monostable is cleared and then reset during a long overload period.

A new overload protection circuit utilizes one circuit for suspending inverter action when a load abnormality is detected and a second circuit to monitor clearance of the abnormality.

The circuit wastes no power during normal operating conditions and responds instantaneously when the abnormality is cleared.

The new circuit is shown connected to a power inverter in the figure. The inverter delivers ac power to a load through current transformer T_3 . The load current generates a voltage across resistor R that is peak-detected and is compared with a reference level set by potentiometer R_1 . When an abnormality occurs and the reference level is exceeded, transistor Q_8 is turned on and transistor Q_7 is turned off, allowing $+V_C$ to forward-bias



This **Overload Protection Circuit** dissipates no current under normal load conditions. If an overload occurs, the circuit shuts off the inverter by biasing on transistors Q_1 and Q_2 and applies a small monitoring signal to the load through Triac TR_1 . When the abnormality is cleared, inverter action is instantaneously resumed.

diodes D_1 and D_2 , turning on transistors Q_1 and Q_2 and shutting down the power inverter.

Simultaneously, conducting transistor Q_8 grounds the emitters of transistors Q_5 and Q_6 , allowing them to be alternately switched on and providing a small monitoring signal to the load through Triac TR_1 . This monitoring signal, sensed as a voltage across resistor R_3 , is peak-detected by amplifier IC_3 , for comparison with a reference level established by potentiometer R_2 .

The comparator outputs are connected to transistor Q_8 through buffer diodes D_3 and D_4 , so that once the transistor has been activated by an overload (shutting down the power inverter), it will be held on by current through diode D_6 as long as the monitoring signal level indicates that the overload conditions still exist. When normal current resumes, transistor Q_8 is turned off and transistor Q_7 turns the power inverter back on.

This work was done by Satoshi Nagano of Caltech for NASA's Jet

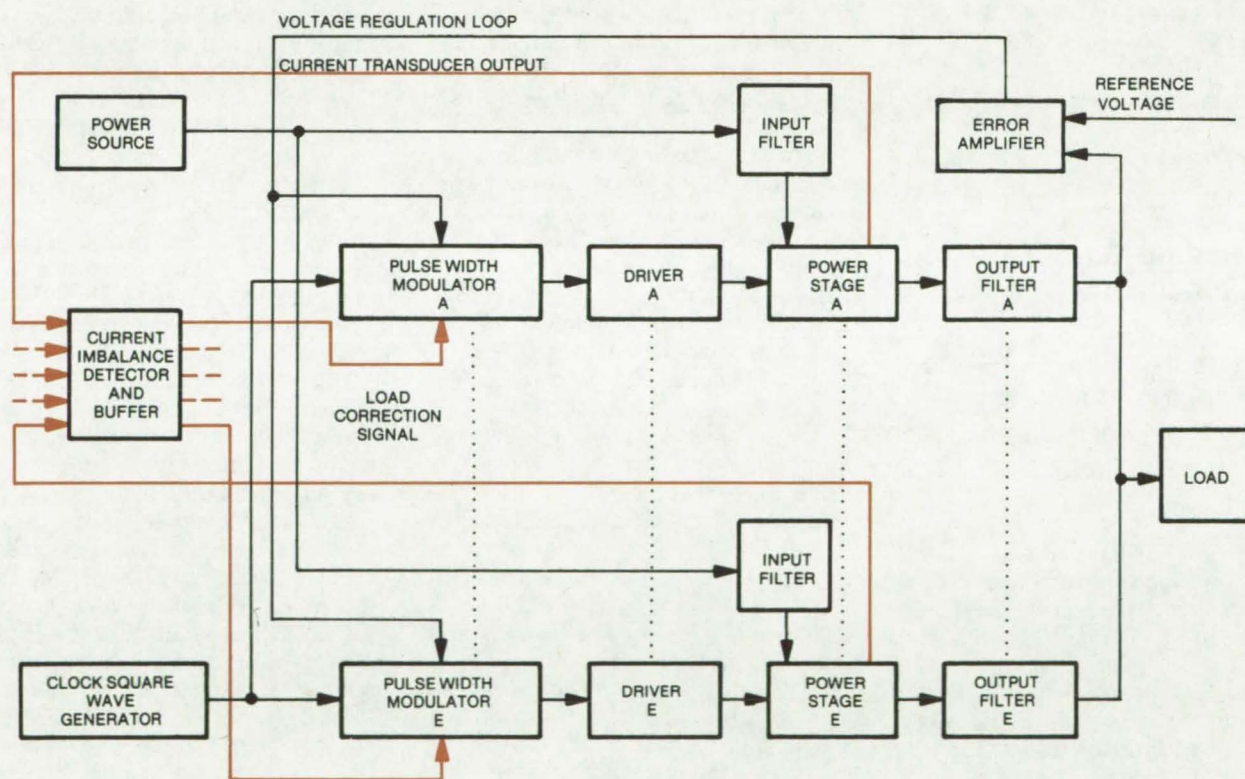
Propulsion Laboratory. For further information, Circle 9 on the TSP Request Card.

This invention has been patented by NASA [U.S. Patent No. 4,052,659]. Inquiries concerning nonexclusive or exclusive license for its commercial development should be addressed to the Patent Counsel, NASA Resident Legal Office-JPL [see page A8]. Refer to NPO-13872.

Load Balancing Multimodule Switching Power Converters

Regulating system individually adjusts duty cycles of modules so that all share the load equally.

NASA's Jet Propulsion Laboratory, Pasadena, California



Load-Balancing System of modular power converter senses the output of individual modules, compares it with average output, and adjusts individual output as necessary to bring it close to the average. The power system shown here is a five-module switching regulator with active redundancy.

A regulating system for parallel, modular power converters ensures that all the converters share the load equally. The regulating system thus protects individual modules and their components from overload and increases the reliability and life expect-

ancy of the power system.

Such multimodule power systems, consisting of many relatively low-power units, are a promising alternative to high-power, single-unit systems in applications where dependability is all-important — for example,

in offshore oil-drilling platforms, navigation buoys, remote weather-monitoring stations, and microwave relay stations. However, multimodule systems have been difficult to balance — small voltage differences among the

(continued on next page)

parallel units produce unequal loading on them.

The new regulating system assures equal load sharing by adjusting the duty cycle of each module according to the fraction of the total load current that it carries. The system senses the output current of each module and compares it with the average output for all modules. The system then adjusts the modules internally, increasing or decreasing their load to the average value.

A current transducer in the power output stage of each module monitors the current supplied by that module. (A module consists of a pulse-width modulator, a driver, a power output

stage, and a filter.) The outputs of the current transducers are delivered to a current imbalance detector (see figure).

The output voltage of each parallel module is controlled by its own pulse-width modulator, which contains a comparator with an output that is high or low depending on whether the error signal from the converter voltage-regulation loop is less than or greater than a triangular reference waveform. The pulse width of each modulator can be adjusted by changing the dc level of its triangular reference waveform.

Therefore a correction signal (the difference between the module output and the average output) is developed

by the current imbalance detector and applied to the pulse-width modulator of an out-of-balance module. This correction signal — a dc bias — automatically adjusts the pulse width to provide equal load sharing. The dc bias affects the pulse width in a modulator in the same way as the voltage-regulation error signal, but is in addition to the latter signal and does not affect the operation of the voltage-regulation loop.

This work was done by Colonel W. T. McLyman and Gene W. Wester of Caltech for NASA's Jet Propulsion Laboratory. For further information, Circle 10 on the TSP Request Card. NPO-13832

Books and Reports

These reports, studies, and handbooks are available from NASA as Technical Support Packages (TSP's) when a Request Card number is cited; otherwise they are available from one of NASA's Industrial Application Centers or the National Technical Information Service.

Eliminating Gold Migration in Microcircuits

The effects of moisture and other factors that cause bridging between conductors can be prevented.

The factors that affect dendrite growth in hybrid microcircuits are the subject of a new report. Gold dendrites, which bridge the insulating gaps between adjacent conducting paths, were discovered to be the cause of failure of between 1 and 2 percent of hybrids tested for use aboard the Space Shuttle. A common symptom of the failed circuits was excessive leakage currents caused by the internal shorts.

A detailed experimental study has found that moisture in the hybrid package is a major cause of the problems. Water vapor, an essential ingredient in the migration process, can come from a variety of sources. For example, water may not be completely baked out of the package

before it is sealed; or, the package may be inadequately sealed and allow moisture to penetrate. Another possibility is that water may be generated by chemical reactions inside the package.

The study found several factors that contribute to the moisture problems. These include:

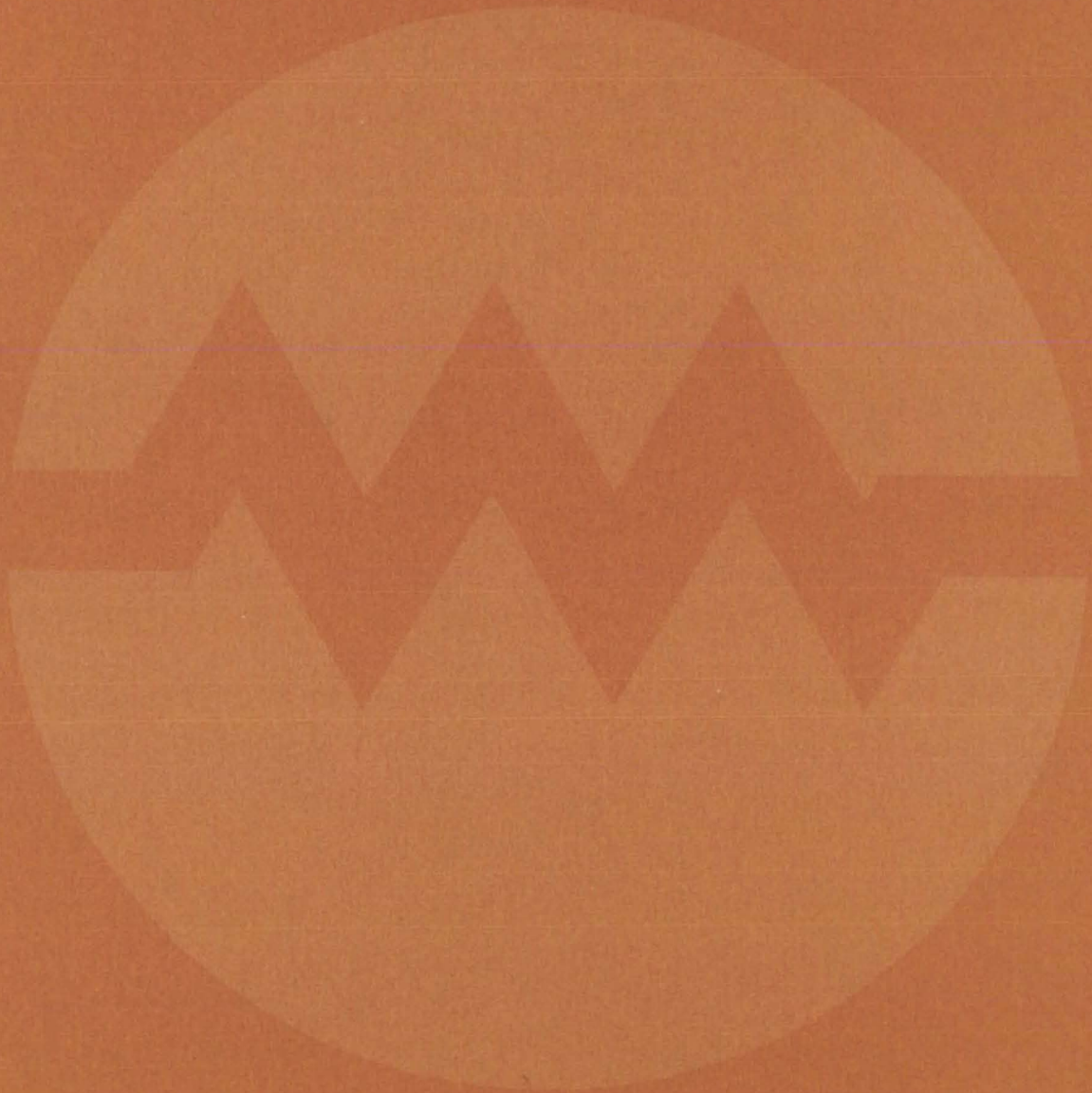
- **Contaminants.** Residues of the microcircuit manufacturing processes can start reactions that lead to migration. Sodium chloride is particularly problematical. It absorbs moisture in the package and corrodes the gold, forming gold chloride and gold sodium chloride, both of which absorb more moisture and accelerate the corrosion process.
- **Large Packages.** For a given relative humidity at sealing, large packages contain more moisture than small ones, and thus they have more moisture available to aid corrosion and dendrite growth.
- **High Voltage.** Voltages above 8 volts seem to increase the destructive effects of moisture.
- **Narrow Conductor Spacing.** The wider the space between conductors, the less likely it is that dendrites can bridge the gap. Below about 0.005 in. (0.13 mm), however, the moisture thresholds for migration are not affected by the spacing.
- **Temperature.** A high operating temperature, by preventing the condensation of moisture, may inhibit gold migration. On the other hand, if condensation does occur, high temper-

ature will accelerate the reactions that produce migration. Once the temperature drops below the dewpoint of the moisture in the package, irreversible processes may start that continue even after the temperature is raised. For example, condensed moisture may start a reaction that produces highly hygroscopic substances that cause gold migration even when the temperature is raised and the condensate evaporates.

It should be possible to prevent gold migration by observing strict precautions during the fabrication of hybrids. For example, a dry internal package environment should be ensured, and the package and substrate should be subjected to rigorous cleaning procedures. The cleaning processes should be selected to remove specific residues. Materials that might decompose during processing should be eliminated. Proper sealing techniques should be used and their effectiveness should be monitored by leak testing. Moisture sensors should be used to determine package dewpoints and to identify the processes that contribute to high moisture levels.

This work was done by Aaron DerMarderosian of Raytheon, Inc., and Charles R. Murphy of Rockwell International Corp. for Johnson Space Center. To obtain a copy of the report, Circle 11 on the TSP Request Card. MSC-18213

Electronic Systems



Hardware, Techniques, and Processes

- 489 Narrow-Bandwidth Receiver
- 490 Measuring Radio-Signal Power Accurately
- 491 Determining the Response of an FM Receiver
- 492 More Efficient Microwave-Power Transmission
- 493 Efficient Digital Encoding Scheme
- 494 Wideband Digital Spectrum Analyzer
- 495 Eliminating Ambiguity in Digital Signals
- 496 Data Reformatting With Less Hardware
- 497 Efficient Rectifying Antenna
- 499 Lightweight Conical Antenna Reflector
- 500 Compact Antenna Has Symmetrical Radiation Pattern
- 501 Multiplexed Battery-Bypass Control System
- 502 System for Monitoring Lightning Strikes

Computer Programs

- 504 Telecommunications Network Optimization

Narrow-Bandwidth Receiver

A synchronous switching circuit reduces the bandwidth and improves the sensitivity of a communications receiver.

Goddard Space Flight Center, Greenbelt, Maryland

The sensitivity and bandwidth of an 11.7-GHz radio receiver have been improved by using a phase-sensitive detector to demodulate the received signal. Previously, in a conventional superheterodyne receiver in which cascaded band-pass filters decreased the bandwidth, the minimum detectable signal was about -110 dBm with a -5 -dB signal-to-noise ratio (noise approximately twice the signal amplitude). With the modified receiver, a signal 35 dB below the noise level can be detected (noise 56 times the signal amplitude). The equivalent bandwidth of the circuit is only 0.159 Hz.

A reference signal that is phase-locked with the input signal operates a synchronous switch in the final stage of the new receiver. The input (and associated noise) is gated through the switch only during a portion of the reference cycle. Since the input is phase-related to the reference, it is passed by the switch with little attenuation. However, noise and signals that are not phase-related produce a time-averaged output of zero. The time constant of an integrating low-pass filter that follows the switch is chosen to give the desired bandwidth. The circuit can demodulate either amplitude-modulated (AM) or phase-modulated (PM) signals.

A block diagram of the improved receiver is shown in Figure 1. The incoming 11.7-GHz signal is received and first converted to a 1.05-GHz intermediate frequency that is applied to a phase-locked loop. A 10-MHz reference oscillator and a frequency synthesizer derive the control frequencies for the loop. The loop output, a 10.0000-MHz signal that has the amplitude- or phase-modulated information superimposed on it, is applied to a mixer that also receives a synchronous 10.0025-MHz signal from the synthesizer. The mixer output, a 2.5-kHz difference frequency is amplified and applied to the phase detector (in color) along with a reference 2.5-kHz signal.

(continued on next page)

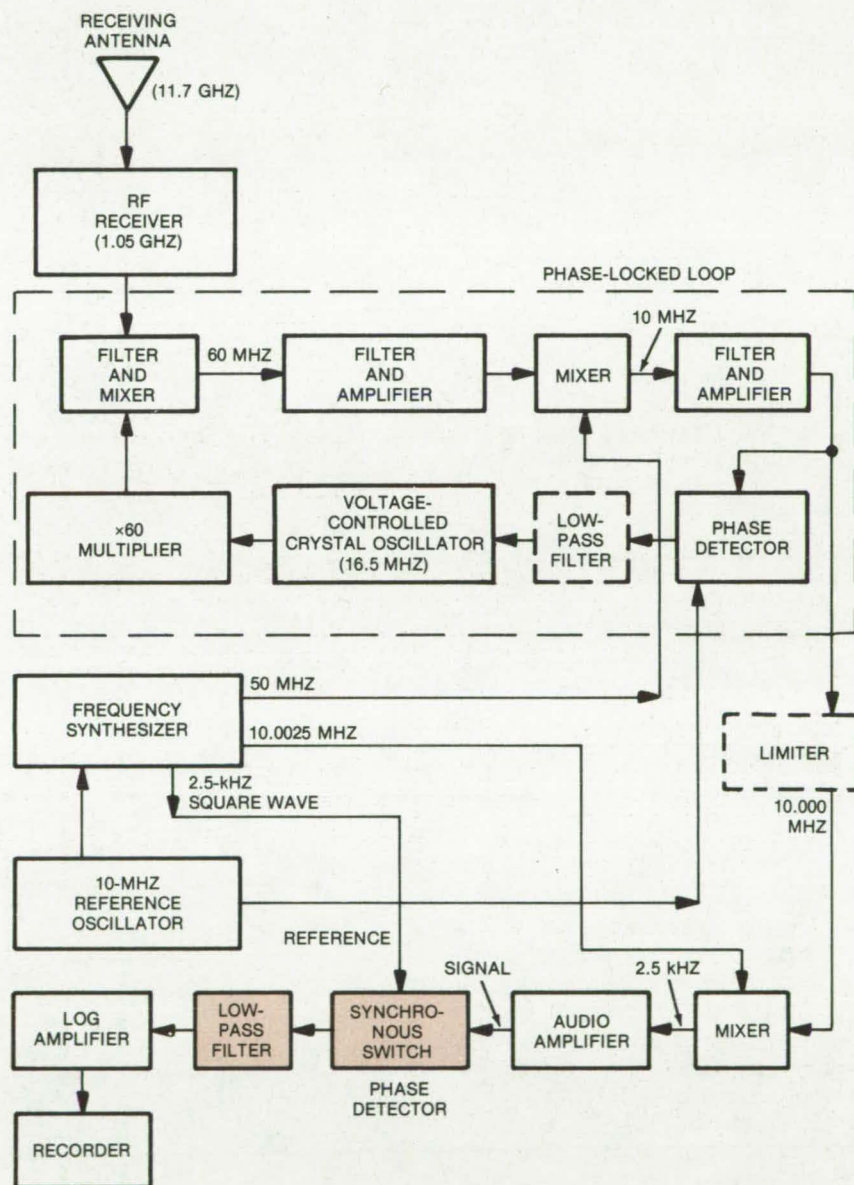


Figure 1. This **Narrow-Bandwidth Receiver** includes a synchronous switching circuit and low-pass filter in its final stage. Noise and other signals that are not phase-related to the 2.5-kHz square-wave reference produce an average zero output from the switch while the input signal passes with little attenuation. A limiter between the phase-locked loop and mixer is included for phase-modulated signals to reduce the effect of amplitude variations.

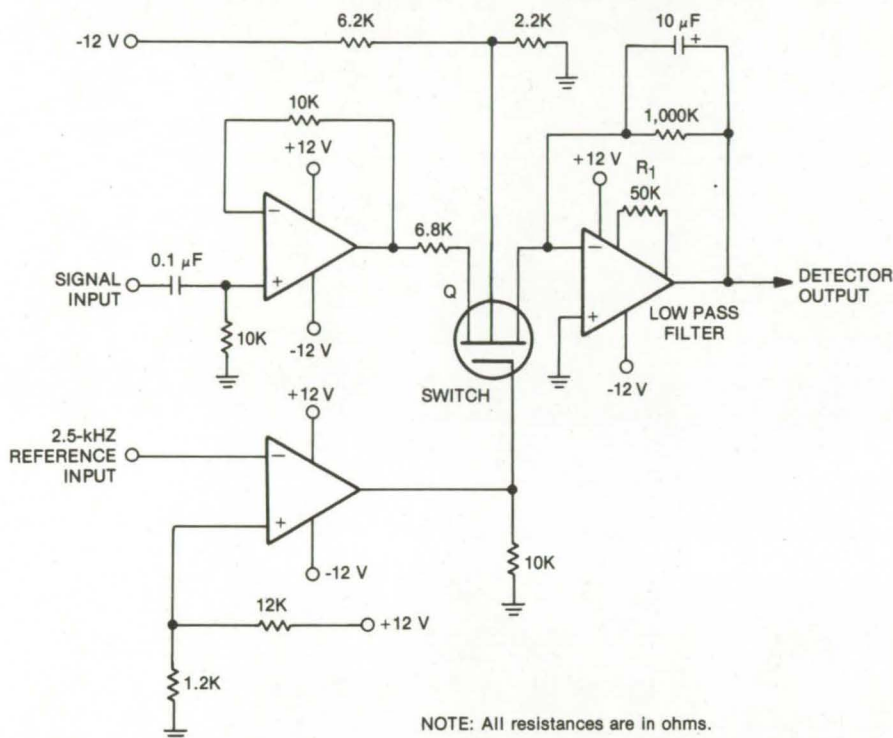


Figure 2. The **Switching Circuit and Low-Pass Filter** require only a few inexpensive components. To demodulate amplitude-modulated signals, the input and reference signals are in phase; for phase-modulated signals, they should be 180° out of phase.

A schematic of the phase detector and filter is shown in Figure 2. The signal input is amplified and applied to the drain of a field-effect transistor, Q, that is gated by the reference. A level-shifting amplifier in the reference leg generates the proper saturation and cutoff voltages for the FET from the reference square wave.

The low-pass filter includes an inverting operational amplifier with an RC network in the feedback path. The resistor and capacitor are chosen to give the desired bandwidth, which in this case is 0.159 Hz.

This work was done by Eugene A. Manus and Paris H. Wiley of Virginia Polytechnic Institute & State University for **Goddard Space Flight Center**. For further information, Circle 12 on the TSP Request Card.

This invention is owned by NASA, and a patent application has been filed. Inquiries concerning nonexclusive or exclusive license for its commercial development should be addressed to the Patent Counsel, Goddard Space Flight Center [see page A8]. Refer to GSC-12142.

Measuring Radio-Signal Power Accurately

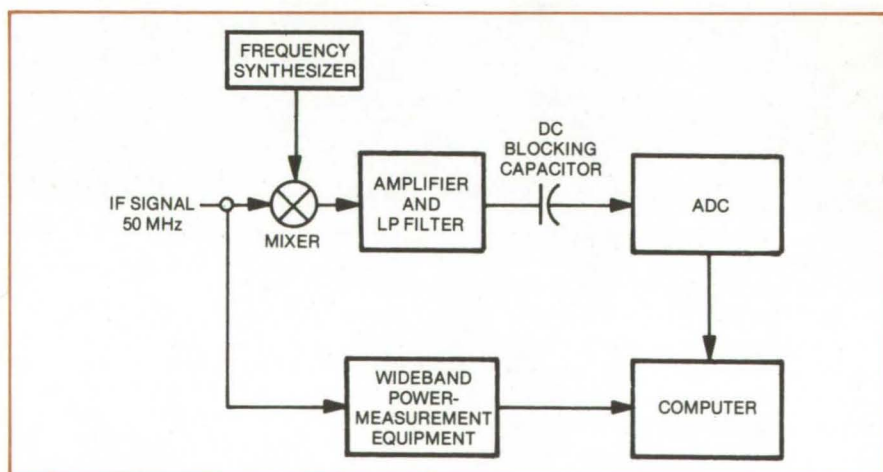
Computerized measurement is precise even at signal levels close to the sensitivity threshold of the receiver.

NASA's Jet Propulsion Laboratory, Pasadena, California

The absolute value of signal power in weak radio signals can be determined by computer-aided measurements. The equipment operates by averaging a received signal over a several-minute period and comparing the average value with the noise level of the receiver, which has been calibrated previously.

Power-spectrum information is important in space communication. It is necessary for selecting suitable telemetry rates for data transmission, and it is helpful in diagnosing trouble with equipment onboard a spacecraft.

A receiver automatic-gain-control (AGC) voltage has been used as an indicator of received signal-power level. However, although AGC indicates power accurately (within a few tenths of a decibel) at high signal levels, it becomes inaccurate when signal power drops close to the threshold of the receiver. Moreover,



Signal-Power Measurement System uses a computer to calculate signal power from data on narrow-band power spectra and wideband noise. The narrow-band data are accumulated over a period that becomes longer as the signal grows weaker.

the AGC voltage indicates only carrier power and cannot measure sideband power.

The new averaging method is accurate to 0.2 dB at signal strengths as low as -176 dBmW. The technique

consists of first measuring the power spectrum of the received signal in a bandwidth just wide enough for the background noise to be observed; second, processing the power-spectrum data to obtain the signal-to-noise power ratio; and third, obtaining an absolute value of signal power from the precalibration (or online measurement) of system noise temperature.

The input to the equipment is the 50-megahertz intermediate-frequency (IF) signal from a receiver channel not controlled by the AGC voltage (see figure). (Such a fixed-gain channel is used because measurement accuracy depends on receiver gain stability.) A mixer translates the IF signals

to baseband, near zero frequency. The frequency synthesizer permits the selection not only of the carrier frequency but of any desired sideband frequency as well.

A low-pass filter provides almost flat response and sharp cutoff — ripple is 0.1 dB and bandwidth is 22 hertz. An analog-to-digital converter samples the filter output at a 50-hertz rate, producing a derived spectrum width (half the sampling frequency) of 25 hertz.

The wideband power-measurement equipment measures the total power in the IF bandwidth, which extends over several megahertz. At this bandwidth, the contribution of the signal

power is negligible, and the total power measurement is proportional to the receiver-system noise temperature. (The receiver precalibration provides the proportionality constant.)

The computer accumulates the sampled signal data for a predetermined length of time (periods of 4, 8, and 16 minutes are used), then uses the value of noise temperature from the wideband power measurement to calculate the signal power.

This work was done by Richard M. Goldstein, John W. Newton, and Robin A. Winkelstein of Caltech for NASA's Jet Propulsion Laboratory. For further information, Circle 13 on the TSP Request Card.
NPO-13373

Determining the Response of an FM Receiver

A phase-modulation transmitter can be used to measure the postdetection frequency response of a frequency-modulation receiver.

Lyndon B. Johnson Space Center, Houston, Texas

The frequency response of a frequency-modulation (FM) receiver can be measured with the aid of a phase-modulation (PM) transmitter instead of an FM transmitter, by applying a simple correction to the output power level. As the modulating frequency is increased, the output level obtained in response to the PM input is monotonically reduced by 6 dB per octave.

This technique was developed on an occasion when the only FM transmitter available had a modulator bandwidth of merely 200 kHz and it was necessary to measure the response of a receiver with a bandwidth of about 8 MHz. A PM transmitter with modulator bandwidth of 13 MHz was available to supply test signals to the FM receiver; a network analyzer and a calculator programed the test frequencies and computed a graph of relative output power from the receiver as a function of frequency. A block diagram of the test arrangement is shown in Figure 1.

An FM transmitter has a modulation index given by $\Delta f/f_m$, where Δf is the frequency deviation (proportional to the modulation amplitude) and f_m is the modulation frequency. The rms output power that this signal produces from the FM detector is given by

$$[S_0(\text{dB})]_{\text{FM}} = 20 \log(\sqrt{2\pi}\Delta f)$$

Therefore if the modulating amplitude is held constant, the output power re-

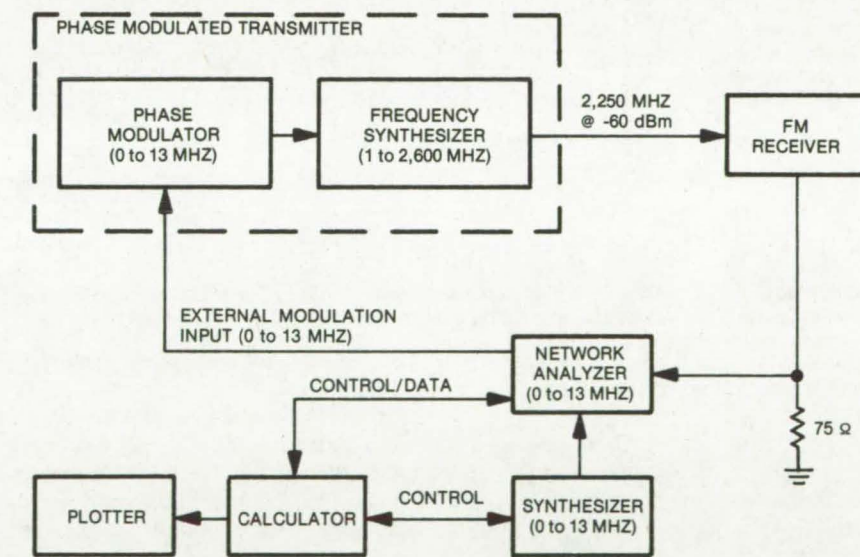


Figure 1. This Test Configuration was used to determine the postdetection bandwidth of the FM receiver by the use of a phase-modulated transmitter.

mains constant as shown in Figure 2(a).

A PM transmitter has a modulation index given by the peak phase deviation $\Delta\Phi$ (proportional to the peak amplitude of the modulating signal). The rms output power that the PM signal produces from the FM detector is

$$[S_0(\text{dB})]_{\text{PM}} = 20 \log(\sqrt{2\pi}\Delta\Phi) + 20 \log(f_m)$$

Therefore if the modulating power is held constant, the output power increases by 6 dB when the frequency doubles (i.e., 6 dB/octave), as shown in Figure 2(b).

Comparison of the two formulas shows that

$$[S_0(\text{dB})]_{\text{PM}} = [S_0(\text{dB})]_{\text{FM}} + 20 \log(f_m)$$

(continued on next page)

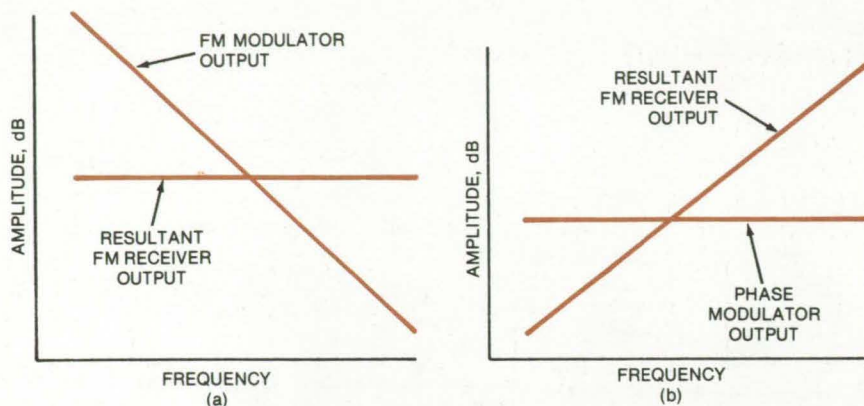


Figure 2. **Combining** phase-modulated and frequency-modulated systems produces these characteristics: (a) FM transmitter and receiver and (b) PM transmitter, FM receiver.

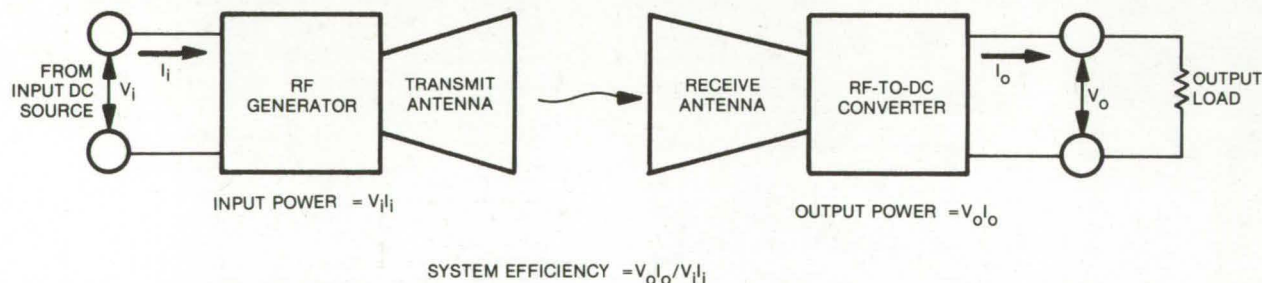
Therefore, when a phase-modulated input signal is used in measuring the postdetection response of an FM receiver, the calculator operating with the automatic network analyzer should be programed to subtract $20 \log (f_m)$ from the output power at each successive value of frequency. (Also, the phase angle should be comparable to the FM phase angle that would normally be used.)

This work was done by James C. Perry of Lockheed Electronics Co. for **Johnson Space Center**. For further information, Circle 14 on the TSP Request Card. MSC-16751

More Efficient Microwave-Power Transmission

Small improvements in components add to sizable improvement in microwave system efficiency.

NASA's Jet Propulsion Laboratory, Pasadena, California



Transmission System converts dc into microwave energy for transmission through air or vacuum to a receiving antenna. The receiver system converts the microwave energy back to dc.

An experimental microwave-power transmission system (see figure) has attained 54 percent overall efficiency — 9 percent higher than previous systems. The efficiency improvement was made possible by improvements in the magnetron, receiving diodes, radiating antenna, and circulator.

The system performs the following functions: (a) the conversion of input dc power into microwaves, (b) forming and radiating a microwave beam in the direction of the receiver, (c) collecting the radiated beam at the receiving sites, and (d) converting the received microwave energy into dc for delivery to a load.

The device that converts the dc source power into microwaves (or RF — radio frequency) is an air-cooled, directly-heated-cathode, permanent-magnet magnetron. Its dc-to-RF con-

version efficiency is approximately 72 percent.

In the magnetron output circuit are an impedance-matching device and a terminated circulator for load protection and for optimizing the magnetron-load impedance match. These devices account for a 4-percent loss in the magnetron output.

The radiating antenna is a 57-cm-diameter dual-mode horn. The I^2R loss, cross-polarization loss, and spillover loss add up to about 1 percent.

The receiving antenna is an array of 199 half-wave dipoles arranged in a triangular lattice above a reflecting plane. The array collection efficiency is 95 percent.

The RF-to-dc converter behind each receiving half-wave dipole consists of an RF low-pass filter, a

gallium arsenide half-wave diode rectifier, and a capacitor to match the diode impedance to that of the low-pass filter. The conversion efficiency is 85 percent.

For the future, the designers plan further improvements. A magnetron designed expressly for this would be more efficient. For example, the RF-to-dc converter diodes could be made more efficient with new materials and designs. The circulator could be removed and the power supply and the magnetron redesigned to tolerate low- or high-power levels.

This work was done by Richard M. Dickinson of Caltech for **NASA's Jet Propulsion Laboratory** and William Brown of Raytheon, Inc. For further information, Circle 15 on the TSP Request Card. NPO-13885

Efficient Digital Encoding Scheme

A modified NRZ code immunizes record and playback systems against dc drift and bit slippage.

Lyndon B. Johnson Space Center, Houston, Texas

Although the conventional non-return-to-zero (NRZ) code is the most efficient for recording digital data (if efficiency is measured by bits to unit length of tape ratio), it is subject to dc drift and bit slippage whenever long strings of "1's" or "0's" are encountered in the data. Codes that insert check bits in the data to break up long strings alleviate this problem, but only at the expense of recording efficiency.

Although some phase-modulated codes are almost as efficient as NRZ, there exist systems that need (for one reason or another) to maximize the bit packing density. For these cases, an improved code (called J-NRZ) gives 100 percent of NRZ efficiency yet also solves the dc drift problem. It does so by adding check bits in a specified format only when a long string is encountered. The rest of the data stream is encoded in standard NRZ format.

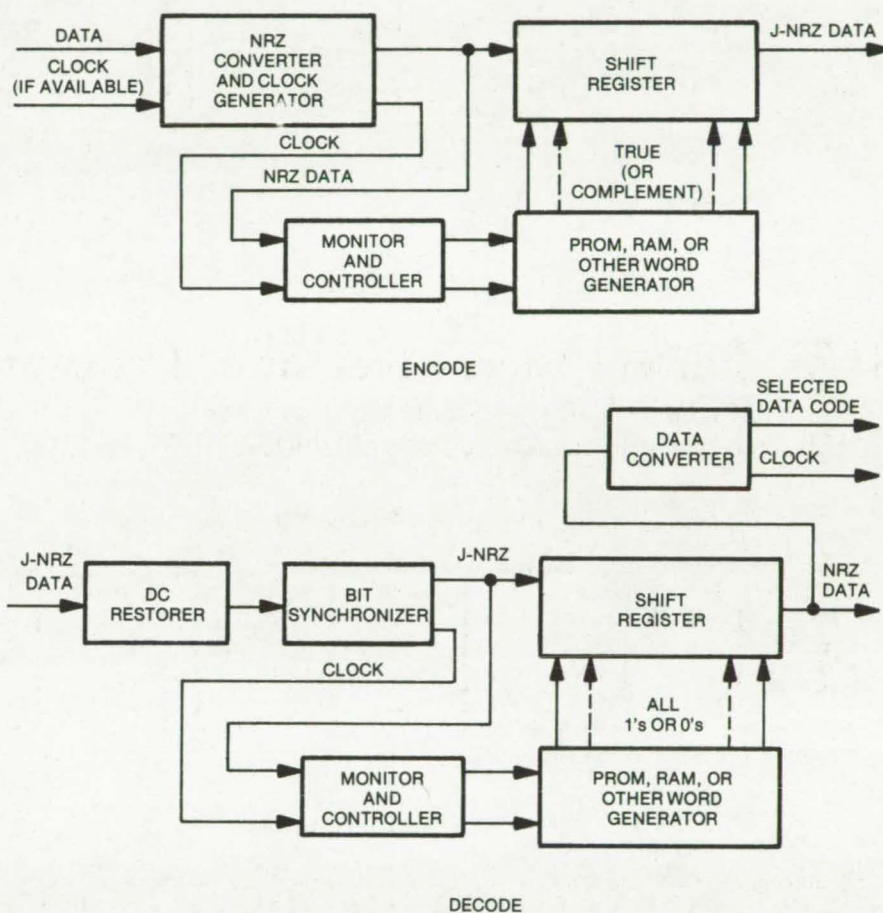
One such system, developed at Johnson Space Center, is programmed to search for 32 consecutive identical bits. The playback system is able to handle up to 64 identical bits without drift, ensuring a 2:1 error margin.

As shown in the figure, the system converts the input data into NRZ, and a clock is generated from the data. (If the input is already NRZ with a clock, it is routed to the next stage.)

A preselected 32-bit word is stored in either PROM or RAM (or other word generator). The word is symmetrical (i.e., the same when played back in the forward or the reverse direction), and it is balanced with an equal number of "1's" and "0's."

The circuit includes a counter that runs off the clock and resets each time there is a data transition. If the counter reaches a predetermined number (32 in this system), it triggers the controller to shift either the stored word (for a string of all "1's") or its complement (for all "0's") into the data stream.

A shift register accepts the NRZ



This **J-NRZ Digital Encoder and Decoder** replaces long strings of "1's" or "0's" in the NRZ stream with a preselected word (or its complement) stored in PROM or RAM. Since most of the data are unaffected, bit overhead is kept low. The selected word is symmetrical so that it can be played back in either forward or reverse, and it is balanced (with an equal number of "1's" and "0's"), which aids dc restoration on playback.

data bits in a serial train and holds them while the monitor, controller, and storage/transfer systems have time to function. If the predetermined number of "1's" or "0's" has been detected, the word is parallel-shifted out of storage and into the shift register to replace the long string. The register then resumes serial transfer of the data.

On playback, the coded data are routed to a dc restorer and bit synchronizer. The input J-NRZ is

processed by a monitor-and-controller stage that initiates a shift of all "1's" upon detection of the coded word or of all "0's" for the code-word complement. Upon command from the controller, the storage PROM or RAM shifts all "1's" or "0's" back into the shift register, restoring the data to their original form.

This work was done by David E. O'Brien III of Johnson Space Center. No further documentation is available. MSC-18267

Wideband Digital Spectrum Analyzer

A modular spectrum analyzer samples stochastic signals in 2^{20} channels.

NASA's Jet Propulsion Laboratory, Pasadena, California

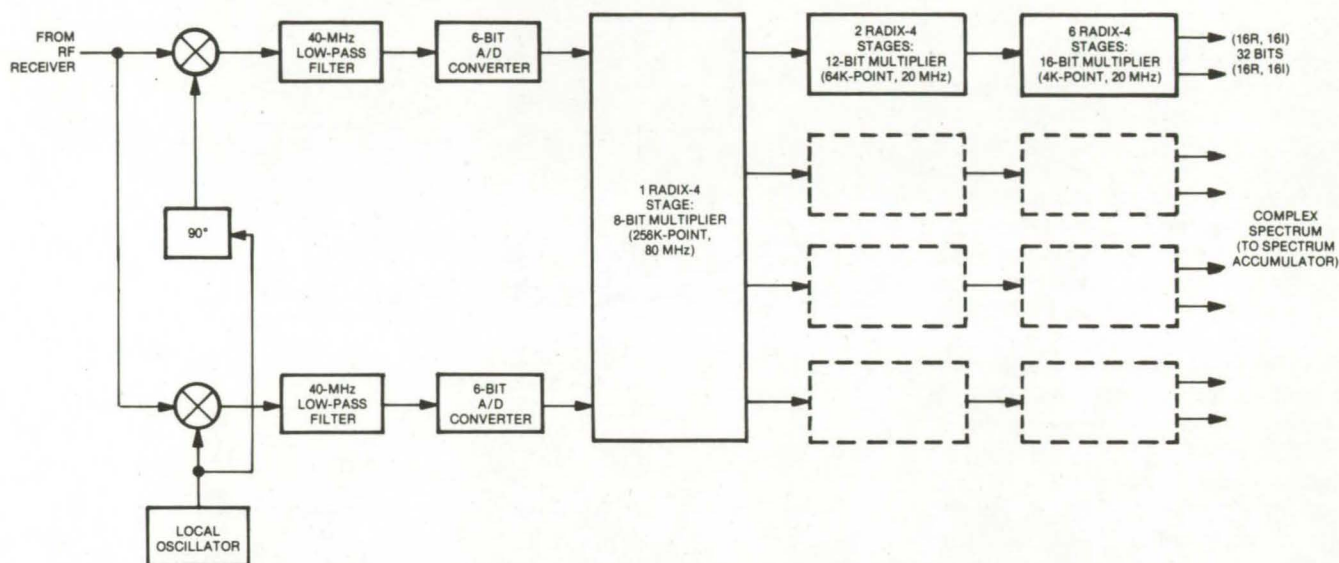


Figure 1. This **80-MHz Fast Fourier Transform Spectrum Analyzer** is one of four used in a wideband system. The four identical analyzers are collectively simpler (and less expensive) than one 320-MHz unit.

A 320-MHz-bandwidth digital spectrum analyzer, originally developed to assist in a search for extraterrestrial intelligence, is assembled from four spectrum analyzers and a data processor. The modular construction reduces the design and fabrication costs of the assembled unit. Each of the four 80-MHz-bandwidth, 2^{18} -point spectrum analyzers accepts 80-MHz-bandwidth stochastic signals; the combination yields a combined bandwidth of 320 MHz and 2^{20} (approximately 1 million) channels. The signals are analyzed by fast Fourier transform (FFT) techniques.

The complete system includes an RF receiver, followed by the FFT spectrum analyzer and the data processor. The analyzer accepts the incoming 320-MHz bandwidth and determines the complex voltage-versus-frequency spectrum for 2^{20} channels. The data processor records approximately 300 samples per second in each channel and decides if any interesting event has occurred. In this process, the first step is to average the spectrum over an approximately 1-minute interval to reduce

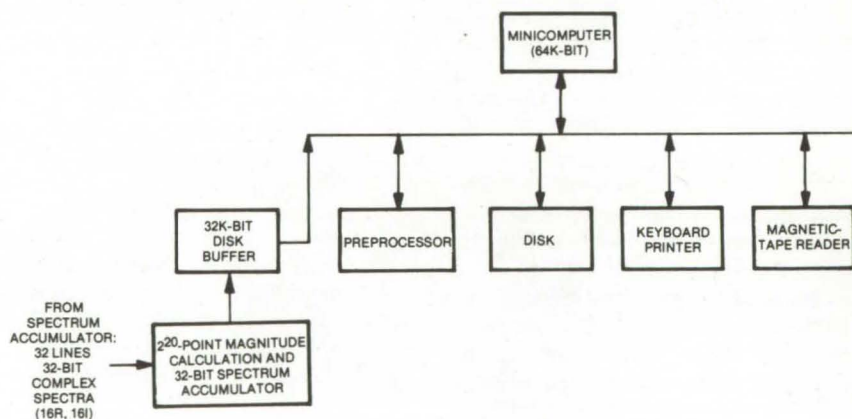


Figure 2. The **Data Processor** receives a complex voltage spectrum from the analyzer. It then calculates the spectrum magnitude and compares it with a model spectrum to search for nonrandom signals.

the data that must be searched by a factor of 18,000. The remaining 1 million points are examined once per minute to look for radio sources or other information-carrying signals. When nonrandom signals are detected, the raw data are recorded on magnetic tape and are preserved for later analysis.

A block diagram of one of the spectrum analyzers is shown in Figure 1. It includes a commercially-available analog/digital converter (ADC). The first stage of the analyzer uses emitter-coupled logic (ECL).

In the full system composed of four analyzers, there is redundancy that allows for easy maintenance and

several "fail-soft" modes. This arrangement also allows two analyzers to observe the same spectrum in different polarizations (e.g., for the calculation of Stokes' parameters) while still observing 240 MHz of total bandwidth.

The block diagram of the data processor is shown in Figure 2. The processor receives a complex voltage spectrum from the analyzer on 32 separate lines at a 10-MHz data rate. It then calculates the spectrum magnitude (rather than the power), using a hardware-efficient (and memory-efficient) algorithm.

The spectrum accumulator output is buffered onto the bus for storage on the computer system disk. Relatively large blocks are written onto the disk in normal frequency order. The accumulated spectrum is cleared after it is transferred to the disk. This technique of reading and clearing eliminates the need for a double-buffered memory when integrating adjacent frequency bins over similar time intervals. The spectrum integration time is under computer control, with the usual restrictions imposed by the disk transfer rate. Integrations longer than 30 s are permitted.

The data passing from the spec-

trum accumulator buffer to the disk are also read by a preprocessor that subtracts a model spectrum and examines the difference for information-carrying signals.

When an event is detected, the frequency and type are stored in an event table; it is subsequently passed to the computer for output to a magnetic tape and for the construction of an event summary log.

This work was done by George A. Morris, Jr., and Helmut C. Wilck of Caltech for NASA's Jet Propulsion Laboratory. For further information, Circle 16 on the TSP Request Card. NPO-14394

Eliminating Ambiguity in Digital Signals

Differential encoding helps receivers make distinctions in multi-amplitude and phase-shift-keyed transmissions.

NASA's Jet Propulsion Laboratory, Pasadena, California

A newly developed method of differential encoding overcomes the problem of ambiguity associated with advanced digital-transmission techniques. In multi-amplitude and phase-shift transmission systems designed to handle maximum data in minimum bandwidth, the receiver can recognize the pattern in the signal but cannot discern whether the elements in the pattern are "1's" or "0's."

The new differential-encoding method resolves this ambiguity and does so with little or no penalty in transmission rate, error rate, or system complexity. The method has been used in a 4-bit multi-amplitude minimum-shift-keying (MAMSK) transmission system.

In MAMSK, the increase in error probability was very small, as predicted by theoretical analysis (the "Gray coding penalty," was equal to 4/3). Moreover, the only additional circuits required were two Exclusive-OR circuits and an inverter at the transmitter and receiver. These are relatively minor penalties to pay for the elimination of ambiguity.

The method is no less applicable to quadrature-amplitude shift keying (QASK), independent amplitude and phase-shift keying (IAPSK), continuous-phase frequency-shift keying (CPFSK), and other symmetrical signal patterns. The principle of the method is that, if signal points are properly encoded and decoded, bits can be detected correctly regardless of rotational phase ambiguities. Most practical signal sets have a phase ambiguity, L , which is some power of 2. A method of differentially encoding a signal set of $M = 2^K$ bits, for which $L = 2^N$, is as follows:

- The signal space is divided into L equal pie-shaped sectors. Any signal point within one of these sectors is equivalent in terms of differential encoding.
- For each K bits of data, the first N bits are encoded as in N -ary PSK (phase-shift keying) but with the 2^N signal points replaced by 2^N sectors.
- The remaining $K - N$ bits determine the signal point within the sector. The 2^{K-N} points within the sector

must be Gray-coded to reduce the probability of bit error.

- The basic idea is that the first N bits define a change in sector while the remaining $K - N$ bits define the signal point within a new sector.

This scheme is consistent with the hypothesis that the best performance is obtained by differentially encoding as few bits as possible; this practice keeps error propagation to a minimum. The sectors should not be selected arbitrarily, but must be chosen so that the probability of sector error is minimized.

Because of the wide variety of possible signal sets, it is not possible to derive a general formula for differential encoding. Nevertheless, formulas have been developed for the more common signal designs and often can be extended by fairly simple analysis to special cases.

This work was done by William J. Weber III of Caltech for NASA's Jet Propulsion Laboratory. For further information, Circle 17 on the TSP Request Card. NPO-14289



Dual-function integrated circuits use one shift register array instead of two to feed video data to seven tape channels.

The twelve 4-bit shift registers are clocked at the 2,112-kHz data rate. The serial bits are rearranged at the 48th bit, so that when the 7 bits of a pixel transfer out of the shift register in parallel, bit 1 of the seven pixels in each group appears simultaneously at the seven output lines. Then bits 2 through 7 appear simultaneously — in that order. Pixel 1 always emerges on output line 1, pixel 2 on output line 2.

On the 48th clock, the reformatter performs a parallel load instead of a shift. This rearranges the first 48 bits of the block in the correct sequence for output. Since only 47 bits have entered the register at this time, bit 48 is parallel-loaded into the proper rearranging position. The 49th bit simply shifts along in proper sequence and is not needed in executing the rearrangement. Other blocks follow directly behind, with no break between blocks. The data flow is always continuous.

As noted, this reformatting concept may be used in other applications, such as decommutating and frequency division. In decommutating, the bits from any given source are always received at exactly the same spot within the serial incoming data stream. From this location, they are moved to different locations but always in a predictable pattern. The bits are always taken from the rearranged locations at the same time.

Frequency conversion is performed simply by changing from serial to parallel. For example, in the re-formatter, the incoming 2,112-kHz bit stream is divided by 7 to produce 301-5/7-kHz parallel outputs. By a similar rearrangement, other incoming rates may be divided into lower rates.

[illegible]

Figure 2. **Serial Data From a Vidicon**, consisting of consecutive 7-bit picture elements (pixels), are reformatted for recording on seven tracks of a magnetic tape recorder.

Engel and L. Richard Springer of Caltech for **NASA's Jet Propulsion Laboratory**. For further information, Circle 18 on the TSP Request Card.

This invention is owned by NASA, and a patent application has been

filed. Inquiries concerning nonexclusive or exclusive license for its commercial development should be addressed to the Patent Counsel, NASA Resident Legal Office-JPL [see page A8]. Refer to NPO-13676.

A rectifying antenna features reduced cost, high conversion efficiency, and high-power handling capability.

Recent improvements in rectifying-antenna (rectenna) elements of a microwave-power transmission system have resulted in a higher microwave-to-electrical-energy conversion efficiency and a better physical structure more suited for quantity production. Tests on the rectenna have demonstrated a new efficiency level of 82 percent in converting RF to dc, the dc exceeding a 30-kW power level.

The rectenna system comprises 17

subarrays positioned closely together to intercept the microwave beam. Each subarray has 270 rectenna elements to collect and rectify the incoming microwave power. Some key improvements in the element structure and in the subarray design have led to better overall system efficiency.

As shown in a simplified electrical schematic, each rectenna element consists of a half-wave dipole antenna, a two-section low-pass

microwave filter, a half-wave Schottky-barrier diode rectifier, an inductance section to resonate the rectifier circuit, a bypass capacitance and output filter serving as a microwave short, and a dc bus bar. The sliding microwave short, which incorporates a high value of capacitance, also serves as a smoothing filter to remove microwave components from the dc output. For improved reliability, the Schottky-barrier diode uses a plated heat-sink construction rather

(continued on next page)

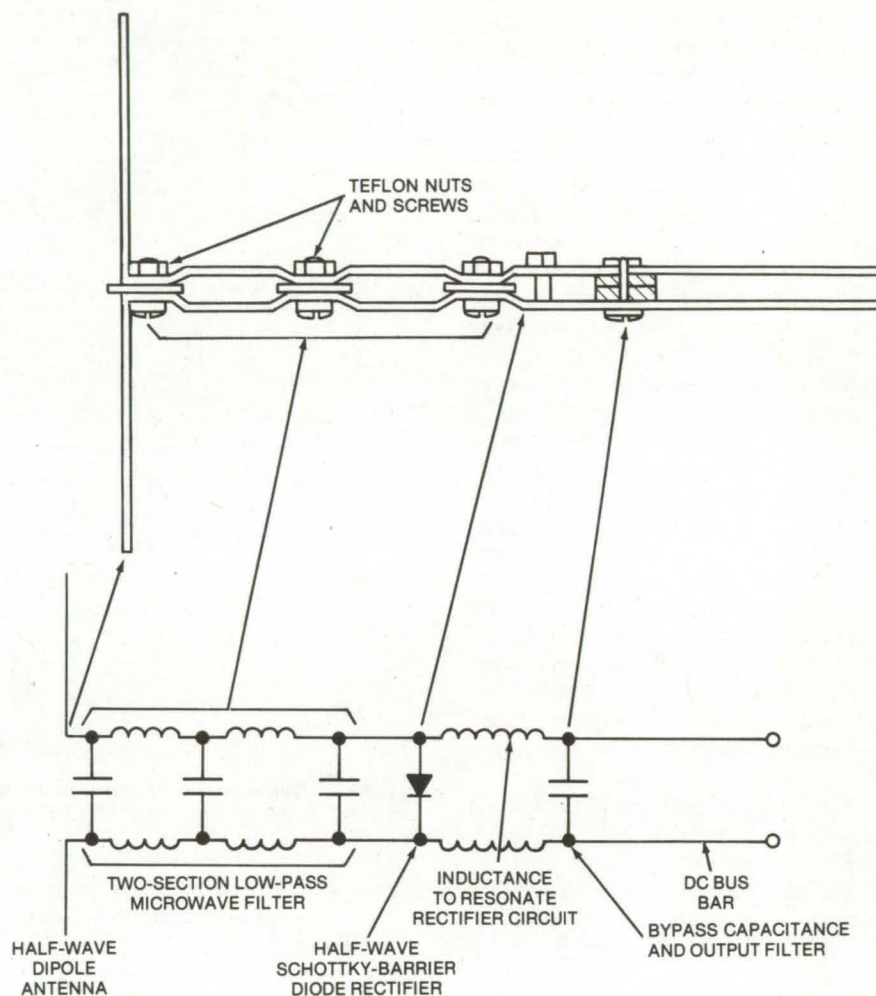
than the flip-chip construction.

The low-pass filter is a most essential part of the rectenna element. It serves to attenuate any harmonic power that propagates toward the half-wave dipole where it would be emitted as radio-frequency interference (RFI). Also, it stores energy during the nonconductive portion of the rectification cycle, acting as a buffer between the even flow of power into the half-wave dipole and the intermittent flow of power through the rectifier. The characteristic impedance of the filter is matched to the impedance of the half-wave dipole, both about 120 ohms.

The rectenna element utilizes Teflon machine screws, eliminating the previously-used nylon screws that developed mechanical problems due to temperature variations. In addition, each element is conformal coated to prevent corrosion between dissimilar metals. This coating also helps the elements to withstand extreme environmental conditions without the use of protective radomes. (Radomes add significantly to system cost and weight and make it more difficult to predict the rectenna performance.)

The elements are arranged in a subarray in 18 rows, 15 elements to the row. The placement of the elements is such that individual subarrays may be interchanged with one another without altering the interface symmetry. All of the rectenna elements in one row are connected in parallel to a common bus bar by a machine screw and nut with appropriate insulating washers.

Each subarray contains a number of protection and instrumentation features. These include crowbar protection for overvoltage, self-fusing of the diodes, temperature monitoring, and incident-power monitoring. The crowbar is a self-contained protective device that comes into play when the voltage across the output terminals of the subarray exceeds a value that can damage the rectifier diode. It is designed to place a short across the output terminals when a preset value of output voltage (200 V) is exceeded. The short is automatically removed when the incident microwave power is removed.



Rectenna Element is shown illustrating the mechanical construction and the electrical setup. This element is designed to withstand extreme environmental conditions without the use of expensive radomes.

The self-fusing protective feature of the individual diode immediately removes the diode from the circuit when it shorts. Gold wires 1 mil (0.03 mm) in diameter, which internally connect the diode chip to the package cover, provide this function.

The temperature is monitored in each subarray with a thermistor. Each subarray contains a thermistor mounted on one of the bus bars. This thermistor measures the temperature of the bus bar, which also serves as a heat sink for the rectenna elements. The thermistor is enclosed to prevent its heating from stray microwave radiation.

The incident-power is monitored with a separately-instrumented rectenna element in every subarray. This element, referred to as a subarray reference element, is used in connection with the computer and display to measure the incident-power density. This measurement is then used in the computation of the subarray efficiency.

This work was done by Richard M. Dickinson of Caltech for NASA's Jet Propulsion Laboratory and William C. Brown of Raytheon, Inc. For further information, Circle 19 on the TSP Request Card.
NPO-13884

Lightweight Conical Antenna Reflector

A conical antenna reflector,
using knitted metallic mesh

NASA's Jet Propulsion Laboratory, Pasadena, California

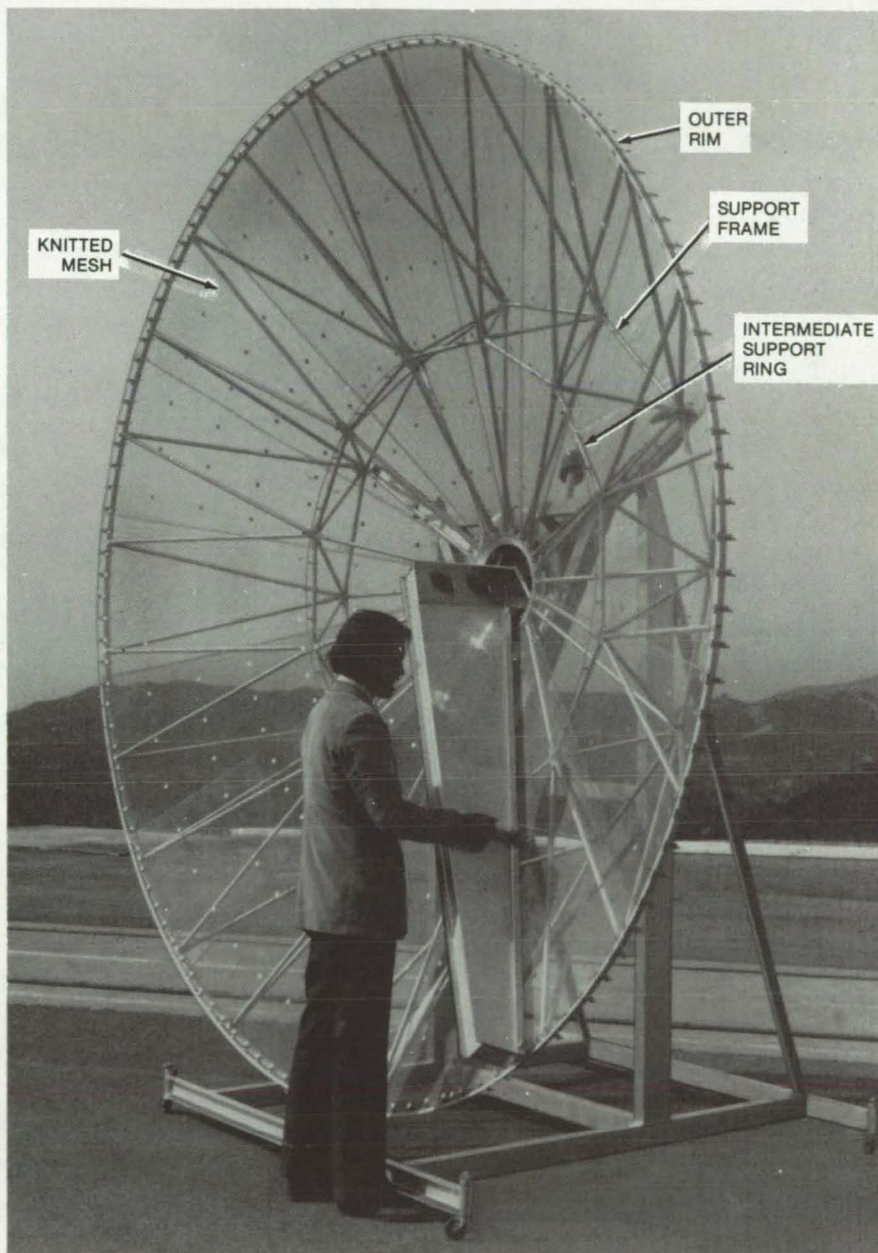
Conical main reflectors on conical-Gregorian and conical-quadreflex antenna configurations are usually constructed of aluminized Mylar, or equivalent, film. This lightweight surface reflects RF energy well. However, there are potential problem areas such as thermal distortion and long-term mechanical stability when the film is subjected to ultraviolet radiation.

These difficulties can be largely eliminated by substituting knitted-mesh materials for the aluminized film. These meshes can be produced from a wide selection of yarns to form the necessary mesh membrane. The material used for the reflector surface shown in the figure was a gold-and-silver-plated nickel chromium alloy knitted mesh. The entire surface is made up of 16 gores, this number being selected so that two gores could be obtained from standard-width material.

Before installation the mesh is stretched on a special table to pre-tension it to the desired circumferential and radial tensions. Next the gores are cut to the developed shape of the desired cone plus a seam allowance.

The reflector is assembled by sewing the seams of adjacent gores, using a TFE coated, fiberglass sewing thread 0.40 mm (0.016 in.) in diameter. Next, the outside edges of the mesh reflector are trimmed with a fiberglass tape 1/2 in. (1.3 cm) wide.

The mesh reflector is attached at its inner diameter to the hub of the support frame by screws installed through the fiberglass trim tape. Because there is no provision for adjustment at the inner hub, this establishes a fixed reference circle on the desired conical surface. The intermediate attachment ring must be adjusted to lie on the conical surface of the proper cone
(continued on next page)



The **Conical Antenna Reflector** uses a rigid aluminum frame supporting a knitted metallic-mesh surface. The surface material is pre-tensioned and supported by 120 cable spokes (not visible) to retain an accurate conical shape.

angle that passes through this reference circle. There are 120 equally-spaced attachment clips along the outside diameter of the reflector, which are used to attach the mesh and highly-tensioned Kevlar (or equivalent) spokes that resist the natural tendency of the tensioned mesh to bow toward the cone axis like a lampshade.

The reflector surface is finally adjusted at its outside diameter by moving the clips with respect to the support frame and tightening the screws that hold the clips to the frame.

The complete reflector measures 12 ft (3.66 m) in diameter and weighs 36.5 lb (16.6 kg). Tests show that its

rms (root-mean-square) surface deviation is 0.011 in. (0.028 cm).

This work was done by Donald M. Moore of Caltech for NASA's Jet Propulsion Laboratory. For further information, Circle 20 on the TSP Request Card.
NPO-13552

Compact Antenna Has Symmetrical Radiation Pattern

Helical filaments on a dielectric cylinder resist shock and vibration and give excellent radiation characteristics.

Ames Research Center, Moffett Field, California

A compact quadrifilar-helix antenna, originally developed for outer-planet spacecraft probes, has an exceptionally-uniform and axially-symmetric radiation pattern. Its mechanical stability and symmetric characteristics make it potentially useful for mobile citizens-band radios and other terrestrial communications systems.

A 550-MHz quadrifilar-helix receiver for a Jupiter probe was recently tested at one-quarter scale by using a 2.2-GHz model. The full-scale version would consist of four wires wound around a dielectric cylinder 6.1 to 7.6 cm in diameter and 38.6 cm long (Figure 1). As seen in Figure 2, the radiation patterns for the model are uniform to within 1 dB from zenith (along the axis of the helix) to about 10° above the equatorial plane, and they are symmetric to within 1.5 dB in planes perpendicular to the antenna axis.

The quadrifilar-helix design was chosen after it and three other types were evaluated. The other configurations and the reasons for rejecting them are as follows:

- *Lindenblad antenna*: This antenna has cantilevered elements that might not survive shock and vibration. In addition, its gain is well below that of the ideal antenna radiation pattern.
- *Conical spiral antenna*: This antenna is larger than the other antennas, and its radiation symmetry is no better than that of the others.

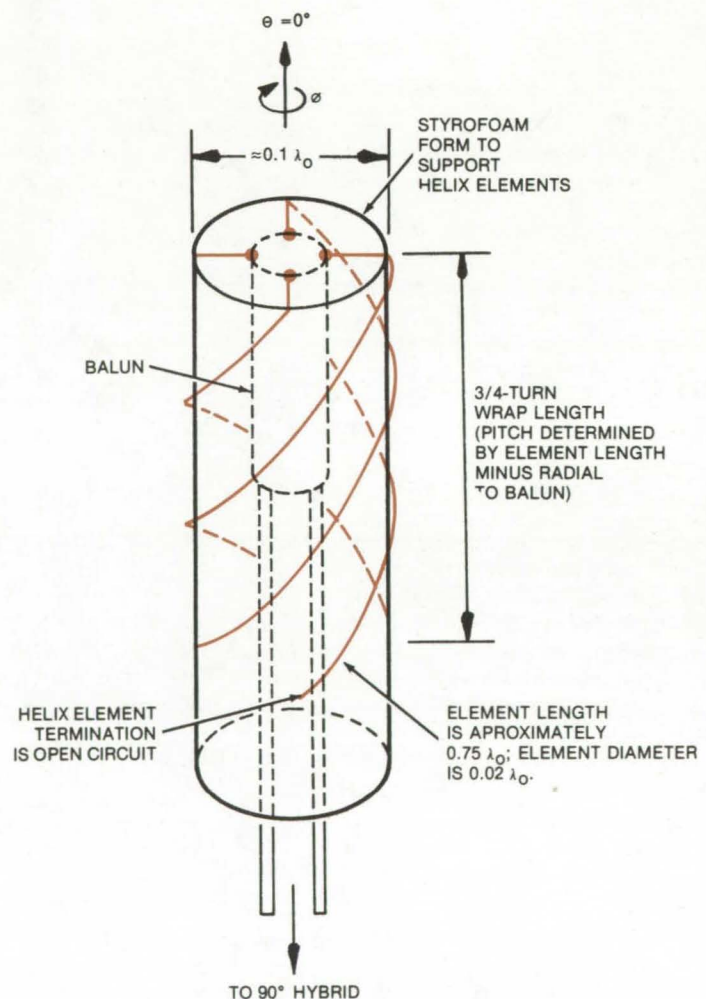


Figure 1. The element length of a Quadrifilar-Helix Antenna is approximately $0.75 \lambda_0$, where λ_0 is the wavelength of the center operating frequency. Improved radiation patterns and symmetry were recorded by locating the balun outside the helical elements, rather than inside, as shown in this drawing.

•**Loop-vee antenna:** The symmetry of this antenna is strongly influenced by its surroundings; and thus dielectric members required to stabilize its four vertical and loop-segment members may affect symmetry.

The elements of the 2.2-GHz quadrifilar helix are 1.19 mm in diameter, 10.82 cm long, and are wrapped around a Styrofoam core 1.52 cm in diameter with a wrap length of 9.47 cm. The elements are each 0.79 wavelength long and are wrapped around the core for more than three-quarters of a turn but less than one turn. They are fed by a pair of baluns from a 90° hybrid circuit so that each element is excited at the proper magnitude and phase. The performance of the antenna could be further improved by using special tooling in its fabrication to control the geometry of the quadrifilar-helix elements more precisely.

The peak circular gain of the antenna, when it is scaled up to its intended 550-megahertz operating frequency, is expected to be about 2.2 dB, on the basis of an expected efficiency of 71 percent (at the larger size). The voltage standing-wave ratio

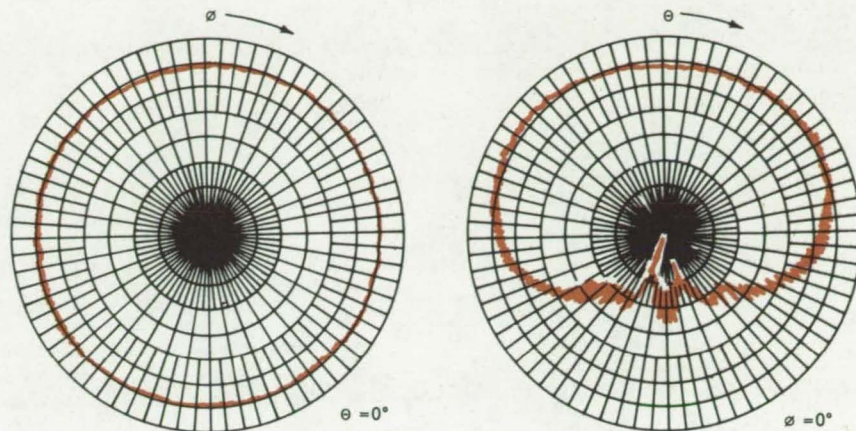


Figure 2. The **Radiation Patterns** of a quadrifilar-helix antenna show excellent uniformity and symmetry. The pattern at the left was taken in a plane perpendicular to the antenna axis ($\theta = 0^\circ$, ϕ variable); the pattern at the right was recorded in an azimuthal plane ($\phi = 0^\circ$, θ variable).

(VSWR) of the model is about 1.29:1 at 2.2 GHz and improves at higher and lower frequencies. There is a VSWR peak of 2.32:1 at 2.42 GHz, which was within the requirements of the Jupiter probe application.

This work was done by Ennis A. Kuhlman and Eddie D. McKee of McDonnell Douglas Corp. for **Ames**

Research Center. For further information, Circle 21 on the TSP Request Card.

Inquiries concerning rights for the commercial use of this invention should be addressed to the Patent Counsel, Ames Research Center [see page A8]. Refer to ARC-11189.



Multiplexed Battery-Bypass Control System

An automatic control circuit bypasses overcharged or discharged cells in a battery.

NASA's Jet Propulsion Laboratory, Pasadena, California

Circuit designers and users are frequently concerned when the capacity of one or more cells in a battery is lower than the capacities of the other cells. The lower capacity cells become fully charged or discharged earlier than the others during a charging or discharging cycle, liberating gas inside the battery and possibly rupturing the cell.

A new cell-bypass control system senses low-capacity cells before they overcharge or overdischarge. When a defective cell is detected, a relay automatically removes that cell from the battery circuit.

A version of the bypass control system (see figure) tested for batteries to be used on space probes consists of a multiplexing circuit, a single cell-

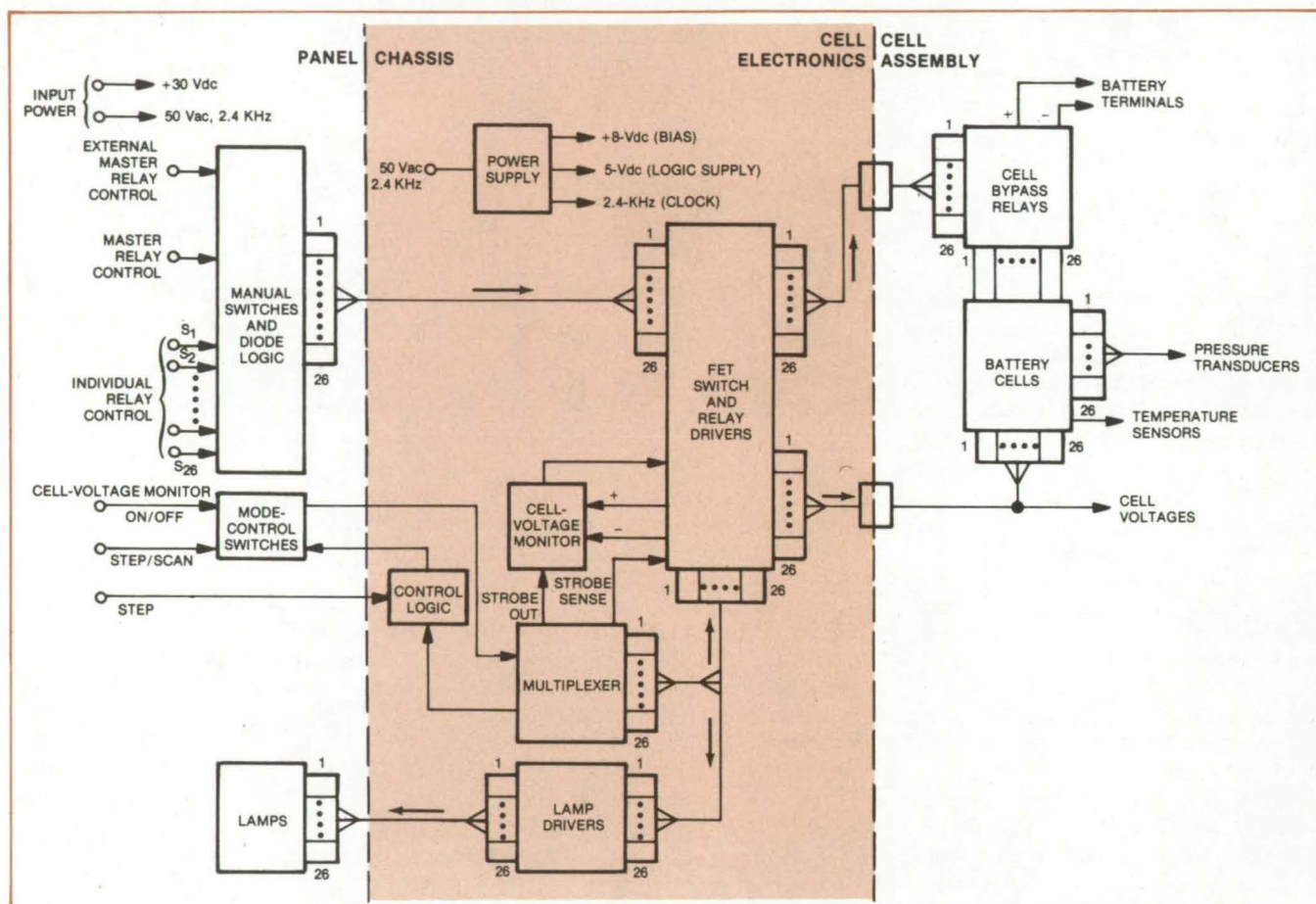
voltage monitor, and an electromagnetic relay for each cell. The multiplexer sequentially applies each cell voltage to the voltage monitor. If a particular cell voltage exceeds the preset upper limit (1.75 ± 0.05 volts for the Ni/Cd batteries being monitored) while charging, or if it falls below the minimum (0.90 ± 0.05 volt) while discharging, that cell is disconnected from the battery supply.

Illuminated lamps indicate which cell is being monitored. In addition, each cell may be set or reset by manual switches to override the bypass control circuit. The unit spends ~ 53 ms monitoring each cell and ~ 7 ms switching from cell to cell; the 26 cells are scanned in approximately 1.7 s.

Although this unit was originally designed for negative-limited Ni/Cd batteries that exhibit a sharp voltage rise at the point of 100 percent charge, it could easily be modified to detect the 100-percent charge point in most other rechargeable batteries. It also could be adapted to insert spare cells in place of those that are removed.

The circuit was tested and found to function well in controlling the 26-cell battery during months of simulated space flights. The final flight version of the system is projected to have a total parts count of 150 and to weight only 1.6 kg. It also shows promise for improving the life and reliability of batteries in computer standby power systems, electric vehicles, remote

(continued on next page)



This **Battery Charge Control System** monitors the voltages of 26 Ni/Cd cells during their charge and discharge cycles and automatically bypasses overcharged or overdischarged cells. The STEP/SCAN control selects either automatic scanning or manual scanning to check each cell individually; the latter is done by sequencing the STEP input.

weather stations, energy storage systems, and other applications.

This work was done by John C. Bennett, Harvey A. Frank, Jack LePisto, and Albert P. Wagner of

Caltech for **NASA's Jet Propulsion Laboratory**. Further information may be found in NASA CR-155271 [N78-12317], "Development of a Multiplexed Bypass Control System for

Aerospace Batteries" [\$5.25]. A copy may be purchased [prepayment required] from the National Technical Information Service, Springfield, Virginia 22151. NPO-14414

System for Monitoring Lightning Strikes

An optical link transmits data for remote processing, and data compaction minimizes storage requirements.

John F. Kennedy Space Center, Florida

A system for monitoring lightning strikes utilizes an optical data link between the lightning sensor and recording instruments. The data link is thus immune to electrical interference that could be induced in a wire by the huge burst of energy in a lightning strike. The nonconductive link also protects people and equipment at the data-receiving end from electrical shock.

The receiver also includes a data

"compactor" that continuously samples the received signal but records only significant changes in its level. No data are stored between lightning hits, and portions of a strike in which the lightning current remains constant over several samples are stored only once (after the first such sample) along with a time signature. Thus, the requirements for memory space, printout paper, and magnetic

tape are greatly reduced.

The lightning sensor is a coil encircling a long cable (see figure). When lightning strikes the cable, it induces a voltage in the coil. This voltage excites a light-emitting diode (LED) through a scaling resistor and full-wave bridge. The LED output is carried by an optical-fiber cable to the receiver, where it is detected by a photodiode. A voltage that measures the lightning current is developed by the photodiode.



This invention has been patented by NASA [U.S. Patent No. 4,100,487]. Inquiries concerning nonexclusive or exclusive license for its commercial development should be addressed to the Patent Counsel, Kennedy Space Center [see page A8]. Refer to KSC-11018.

Computer Programs

These programs may be obtained at very reasonable cost from COSMIC, a facility sponsored by NASA to make new programs available to the public. For information on program price, size, and availability, circle the reference letter on the COSMIC Request Card in this issue.

Telecommunications Network Optimization

Analysis to reduce operating costs

The STACOM (State Criminal Justice Communication) network-topology program helps to design and evaluate digital telecommunications networks. A digital telecommunications network is viewed as a set of terminations connected by a set of links. Each termination consists of one or more terminals or computers in the same area or city, called the terminal city. The main purposes of the network are assumed to be the

rapid exchange of information with the data-base system and fast intracity communications.

Because the operating cost of a given communication network depends on its layout, an initial configuration analysis can often produce significant cost reductions. By using STACOM, one can employ a modified Easu-Williams technique to search for those direct links between system terminations and a Regional Switching Center (RSC) that may be eliminated without impairing system performance.

Inputs to STACOM include traffic data, terminal locations, and functional requirements. During a program run, the network may be divided into any number of regions. Each Regional Switching Center can act as both a switching and a data-base center for terminals in its region. STACOM first defines regions with nearly equal traffic. Next, an RSC is selected to produce the minimal traffic-distance product sum. Before optimizing a regional network, STACOM constructs an initial "star" network in

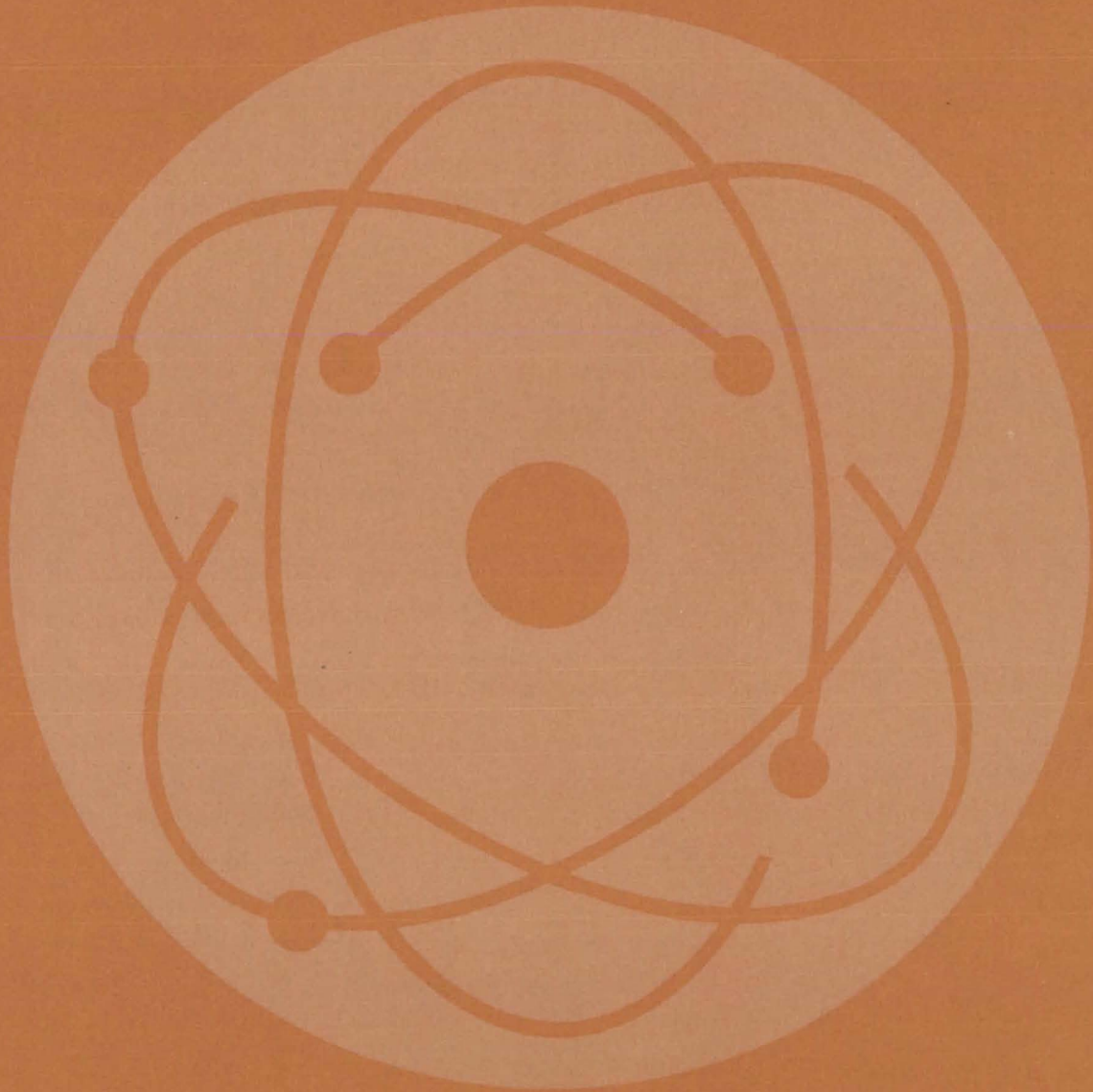
which each termination is directly connected to the RSC. The regional network is optimized by forming a multidrop network in which some lines have more than one termination. Interregional networks are formed and optimized similarly.

Printed output includes initial regional network and optimized network costs and assignments of system terminations. If requested, the geographical connections of the optimized network are plotted to detail multidrop line connections to all of the system terminations.

STACOM is written in FORTRAN V for execution in the batch or demand mode and has been implemented on a UNIVAC 1108 under control of EXEC 8. The code requires that the system support subroutine reentrancy. For plotted output, a CALCOMP plotting system is required.

This program was written by Jun-Ji Lee of Caltech for NASA's Jet Propulsion Laboratory. For further information, Circle A on the COSMIC Request Card.
NPO-14486

Physical Sciences



Hardware, Techniques, and Processes

- 507 Solar Simulator Test Facility
- 508 Voltage Regulator for Solar Panels
- 509 More Efficient GaAs Solar Cells
- 510 Infrared Scanners Detect Thermal Gradients in Building Walls
- 511 Solar-Powered Hot-Air System
- 512 Ocean Thermal Plant
- 513 Wind/Water Energy Converter
- 514 Thermoelectrically-Cooled Variable-Temperature Probe
- 515 Improved Fourier Interference Spectrometer
- 515 Low-Power Tuner for Lasers
- 516 Diffractoid X-Ray Focusing
- 517 Improved Servo for a Michaelson Interferometer
- 518 Instrument Measures Many Optical Properties in Visible and IR
- 519 Hydrogen-Maser Frequency Standard
- 520 Ultrathin Films as Photomechanical Transducer

Books and Reports

- 521 Solar-Heating System — Design Data Brochure
- 522 Solar-Heating System — Performance Tests
- 522 Solar-Heating System
- 522 Solar Hot-Water System
- 523 Residential Solar-Heating System — Design Package
- 523 Development and Testing of a Hot-Air Solar Collector
- 523 Design and Installation of a Flat-Plate Solar Collector
- 524 Liquid Solar Collector — Performance Tests
- 524 Concentrating Solar Collector — Installation Package
- 525 Corrosion Inhibitors for Solar-Heating and Cooling Systems
- 525 Chemical-Vapor Deposition of Silicon From Silane

Computer Programs

- 526 Multidimensional Histograms

Solar Simulator Test Facility

Facility duplicates Sunlight, wind, and solar-energy system characteristics for testing flat-plate collectors.

Marshall Space Flight Center, Alabama

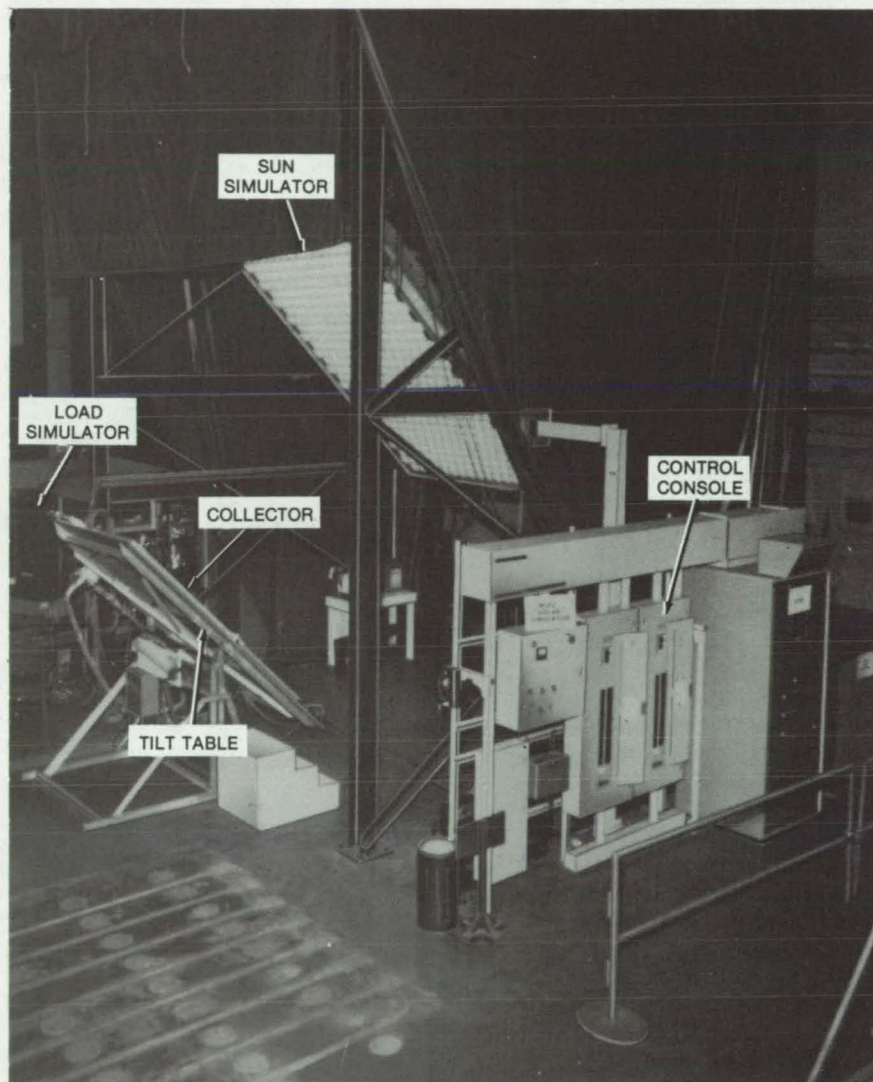
A facility has been constructed at Marshall Space Flight Center to evaluate the performance of solar-energy collectors under simulated outdoor operating conditions. Most flat-plate collectors utilizing either air or liquid transport media can be tested by the system.

The facility simulates Sunfall properties, such as radiation intensity, spectrum, collimation, uniformity, and direction. Wind conditions of varying velocity and direction are also reproduced. It is also capable of duplicating the characteristics of the solar-energy system to which the collector is attached, including the transport medium and flow rate, the fluid inlet temperature, and geometric factors such as collector tilt and azimuth angles.

As seen in the figure, "Sunlight" is generated by 405 tungsten/quartz/halogen lamps that duplicate the solar spectrum very closely. The lamps are rated at 300 W (at 120 V), and the tungsten filament has an equivalent source temperature of 3,350° F (1,843° C). Each bulb is attached to a dichroic-coated glass reflector that, in addition to directing the light, also limits infrared emission. The lamps are mounted in a 27- by 15-lamp array that irradiates a 4- by 8-ft (1.2- by 2.4-m) planar surface area.

Directly in front of the lamp array is a lens housing that holds a Fresnel focusing-lens array (there is one lens in front of each lamp). The entire lens/lamp array is cooled by room air that is transported across the bases of the lamps. The heated air is collected in a tapered plenum and drawn off through a 25-in. (63.5-cm) exhaust duct.

The radiation intensity is varied by a voltage control located on the console adjacent to the simulator. Cooling flow rate is also controlled from this console. The lamp-array power and output are varied by chopping the sinusoidally varying voltage to provide



This **Solar Simulator Test Facility** for flat-plate solar collectors uses an array of tungsten/quartz/halogen lamps to simulate solar radiation. A tilt table beneath the lamp array holds the collector under test. The facility can simulate collector orientation, fluid/thermal loads, and wind, among other factors.

a lower, or higher, rms-average voltage to the lamps.

The lamps are connected to three voltage phases (from a 3-phase, 208-volt line) in zones, so that different zones of the simulator are on different voltage phases. This arrangement smooths nonuniformities in radi-

ation intensity that might result from voltage disparities between the phases.

A tilt table underneath the Sun simulator holds the flat-plate solar collector. A photocell detector can be moved over the table surface to map the radiation flux. Sun orientation is

(continued on next page)

simulated by tilting the table to different angles, from horizontal (0°) to 72° . Azimuth adjustments can be made by rotating the table from 0° to 60° .

The fluid/thermal loop simulation includes both an air loop and a liquid loop. These are distinct systems capable of controlling fluid flow rates of their respective media. For example, the air loop can control airflow rate to within ± 2 percent from zero to 160 stdft³/min (zero to 4.5 stdm³/min). The collector inlet temperature

can be varied from near ambient to 200°F (93°C) and can be controlled to within $\pm 1^\circ\text{F}$ ($\pm 0.6^\circ\text{C}$).

The liquid loop utilizes a 50/50 water/ethylene glycol mixture. Liquid flow rates may be controlled from 6 to 67 gal/h (0.02 to $0.25\text{ m}^3/\text{h}$) within ± 2 percent. The inlet temperature can be adjusted from 10°F (6°C) above ambient to a maximum of 220°F (104°C).

Wind simulation is created by two floor fans blowing against the collector surface. Wind velocities of from 3 to

13 mi/h (1.3 to 5.8 m/s) are simulated by moving the fans farther away from, or closer to, the collector.

This work was done by William R. Humphries of **Marshall Space Flight Center**. Further information may be found in DOE/NASA TM-78165, "Use of The Marshall Space Flight Center Solar Simulator in Collector Performance Evaluation," a copy of which may be obtained at cost from the New England Research Application Center [see page A7].
MFS-23972

Voltage Regulator for Solar Panels

A shunt regulator for solar panels

NASA's Jet Propulsion Laboratory, Pasadena, California

A shunt voltage regulator for solar panels uses the internal resistance of the panel (which varies nonlinearly with illumination) to control its output voltage. Since the regulator has parallel output transistors, it can be scaled up for high-current solar panels simply by adding more transistors.

The voltage regulator, shown in Figure 1, is connected in parallel with the solar panel. This example shows a 12-Vdc regulated supply. The 12-V reference voltage is set by Zener diode D_1 and diodes D_2 through D_5 . A resistor R_1 in series with the diode string controls the base/emitter bias on transistors Q_1 and Q_2 . When the solar-panel voltage exceeds the 12-V output, the voltage across R_1 forward-biases transistors Q_1 and Q_2 . This causes them to conduct through resistors R_2 and R_3 . Figure 2, which shows typical I-V characteristics for a solar array, indicates how the load voltage can be held at 12 V by controlling the current through the shunt. When the Sunlight diminishes to where the load current drops the panel voltage to 12 V, the regulator acts like an open circuit, drawing no current from the panel.

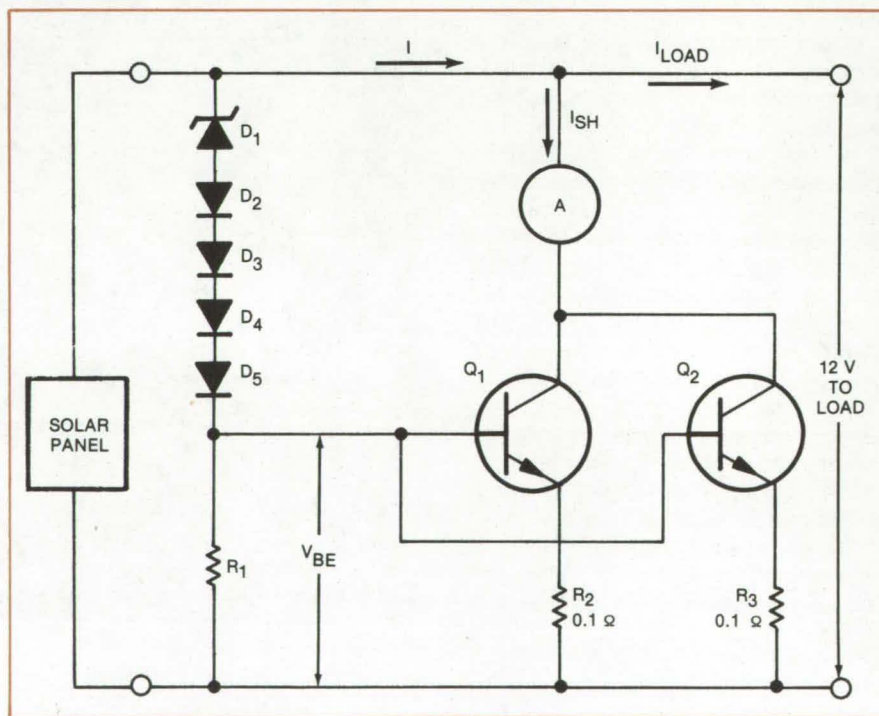


Figure 1. This **Voltage Regulator** is connected in parallel with the solar panel. When the panel output exceeds 12 Vdc, a forward base/emitter voltage (V_{BE}) develops across R_1 . This causes Q_1 and Q_2 to conduct current I_{SH} through R_2 and R_3 to maintain the 12-Vdc supply to the load. When the panel voltage drops below 12 volts, the regulator is equivalent to an open circuit.

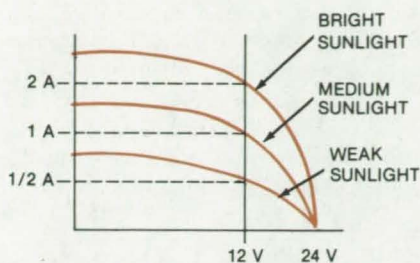


Figure 2. **Typical Solar-Array I-V Characteristics** show how the panel output voltage can be held constant by controlling the output current. Excess current not drawn by the load is shunted through the regulator.

The regulator should be applicable to solar-powered electric motors or battery chargers. In these instances, voltage regulation is needed to prevent motor speed variation or battery overcharging.

This work was done by Theodore A. Casad of Caltech for NASA's Jet Propulsion Laboratory. For further information, Circle 23 on the TSP Request Card.
NPO-13895

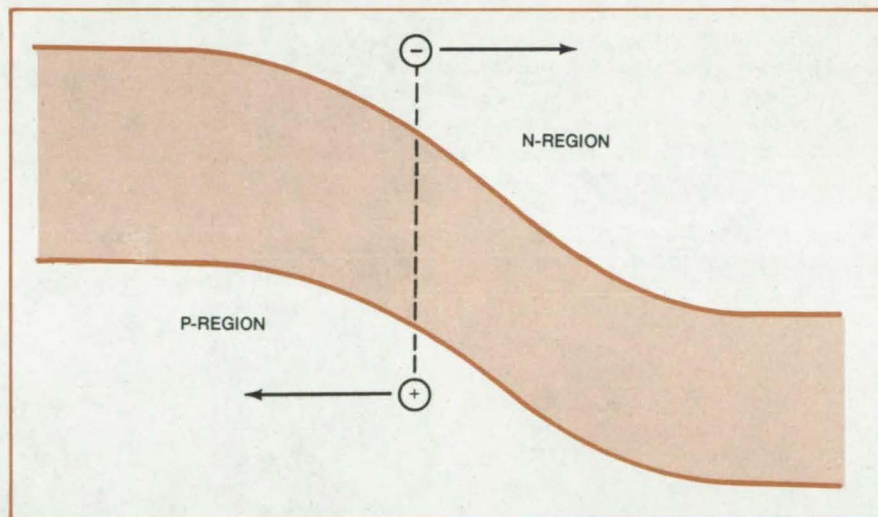
More Efficient GaAs Solar Cells

Electron-hole pair production in space charge layer converts nearly 100 percent of photogenerated carriers to useful current.

Langley Research Center, Hampton, Virginia

When a solar cell with a pn junction near the surface is illuminated, the photons create electron-hole pairs on both sides of the junction. The extent of the junction space-charge region is negligible compared with the absorption length in most solar-cell materials. The minority carriers created must survive all capturing or annihilating mechanisms to traverse the junction and join the majority carriers in order to contribute to the useful current. Doping levels in the p and n regions are high to minimize internal cell resistance. Theory and experimental results agree well for silicon solar cells.

GaAs, with a band gap of 1.4 eV as compared to 1.1 eV for silicon, is potentially more efficient in solar-cell applications. However, the direct transition of electron-hole pairs means a very short absorption length and very short minority-carrier lifetimes. It is desirable either to increase the minority-carrier lifetimes or to avoid generating the carriers in the regions where the conduction mechanism is by diffusion. If the carriers could be generated in the electric field region, the problem would be eliminated. GaAs solar-cell construction based on conventional theory fails to yield high efficiency. In order to achieve higher efficiency, modifications such as the use of AIAs as a front layer have been tried in the past.



Electron-Hole Pairs generated in the space-charge region do not tend to recombine. Separation and collection of these electrons and holes occur with virtually unity probability.

A promising new approach is to generate electron-hole pairs primarily in the space-charge region of the junction. The electrons and holes will immediately travel out of the junction in opposite directions, as shown in the illustration, and become useful majority carriers. In this manner the short-life problem is eliminated, and the conversion of photogenerated carriers to useful current is nearly 100 percent efficient.

With a typical n-type GaAs material, a space-charge region can be obtained at the surface by applying a very thin film of a metal such as Pt so that a metal/GaAs barrier height of 1 eV exists at the surface. The space-charge layer would extend 1 micron inward if the doping level were 10^{15} cm^{-3} . By adjusting the doping level, the space-charge layer can be extended to about five times the average absorption length of the absorbed photons in GaAs. The

(continued on next page)

extension of the space-charge layer to five times the photon absorption length results in less than 1 percent of absorbable light passing through. Electroding and antireflection coating procedures presently used would be directly applicable with this solar cell.

The methodology, therefore, for producing highly-efficient solar cells includes:

- Placing the junction at the surface, in the form of a Schottky barrier or a thin p^+ layer on the n material;

- Extending the barrier on the n side to five times the absorption length;
- Increasing the doping level so that at $x > L$, n would increase rapidly to the highest available level, or

$$n \rightarrow 10^{18} \text{ for } x > L$$

$$n \approx 10^{14} \rightarrow 10^{15} \text{ for } 0 < x < L$$

where

L is the depth of the space-charge layer,
 n is the doping level, and
 x is the distance from the surface.

This work was done by Wirojana Tantraporn of General Electric Co. for Langley Research Center. For further information, Circle 24 on the TSP Request Card.
 LAR-12216

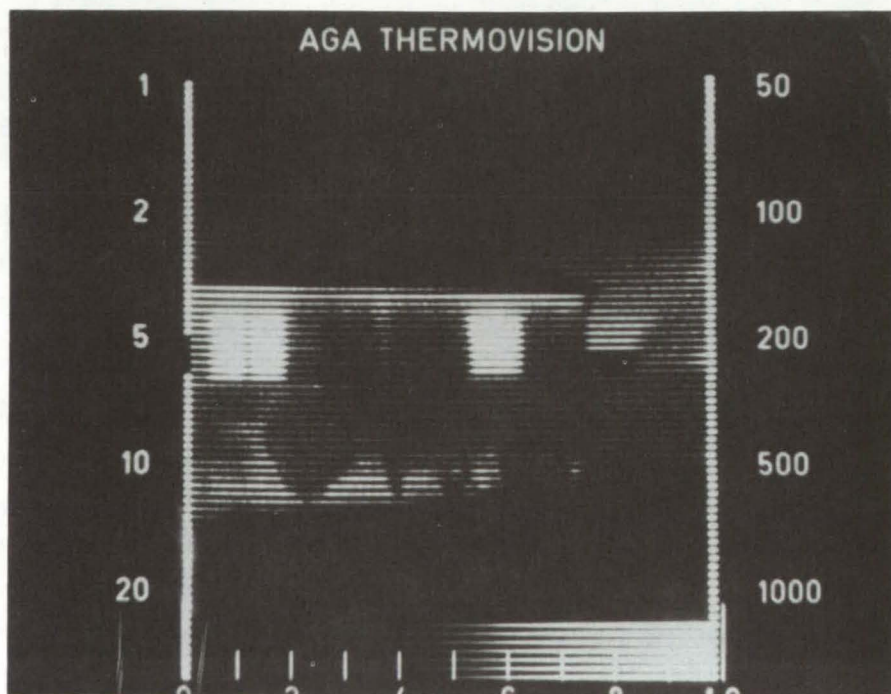
Infrared Scanners Detect Thermal Gradients in Building Walls

IR study of outside walls can be used to help minimize energy loss.

Langley Research Center, Hampton, Virginia

An infrared scanner has been used to detect thermal gradients in outside walls of two typical homes in Virginia Beach, Virginia, under a joint effort by Langley Research Center, the Virginia Energy Office, and the city of Virginia Beach in the Virginia Beach Energy-Conservation Pilot Project. The electro-optical scanner operates in the near infrared, at 2 to $5.6\mu\text{m}$, and receives radiation emitted by the wall surface. The radiation is converted to an electrical signal by an infrared detector (InSb). The signal is fed into an oscilloscope where it is displayed as a televisionlike picture from which photographs are made. The instrument is sensitive to radiation from surfaces with temperatures that vary from -20° to 800°C . Resolution in the temperature span anticipated from a home outside wall is better than 0.3°C .

Where insulation is lacking or where the insulation thermal properties are not uniform, more heat will pass through the wall, resulting in a "hot point" on the outside wall. By mapping the infrared pattern on the wall with the infrared scanner system, the areas that are hotter or colder can be identified and further investigated. Displays



Thermal Gradient Display of the outside wall of a residence shows areas of varying heat loss.

of this thermal pattern can be shown either in black and white with varying contrast to depict the thermal gradient (see figure) or in color with color bands representing a temperature interval.

This work was done by Andronikos G. Kantsios of Langley Research Center. For further information, Circle 25 on the TSP Request Card.
 LAR-12157

Solar-Powered Hot-Air System

Modular collectors furnish hot air for residential and commercial buildings.

Marshall Space Flight Center, Alabama

A solar-powered air heater can supply part or all of the space-heating requirements of residential or commercial buildings. It can also be interfaced with an air-to-water heat exchanger to heat domestic hot water.

The system, shown in one possible configuration in Figure 1, consists of modular flat-plate solar collectors, ducting that leads into and out of the collectors, and a fan for forced-air convection. A rock bed for thermal storage may also be added to supply nighttime heating requirements.

As shown in Figure 2, each collector module has three bottom pans made of 22-gage galvanized steel. The pans are covered by 26-gage steel sheets painted with heat-resistant black paint, and the structure is covered by a transparent plastic film, 4 mils (0.1 mm) in thickness. Forced air passes over and under the absorber plate and through plenums at the top and bottom of the collector array. The panels are waterproof and can be installed as a structural part of the roof in new buildings, or they can be added to the roof of an existing building. Each panel module is 3 feet (0.91 m) wide and can be manufactured in lengths up to 40 feet (12.2 m); the modules may be joined to form a collector of any width (in multiples of 3 feet).

In addition to its use in heating buildings, the system has potential applications (after appropriate modifications) for drying agricultural products, including cotton, lumber, corn, grains, and peanuts.

This work was done by the Solar Engineering and Equipment Co. for Marshall Space Flight Center. For further information, Circle 26 on the TSP Request Card.
MFS-23976

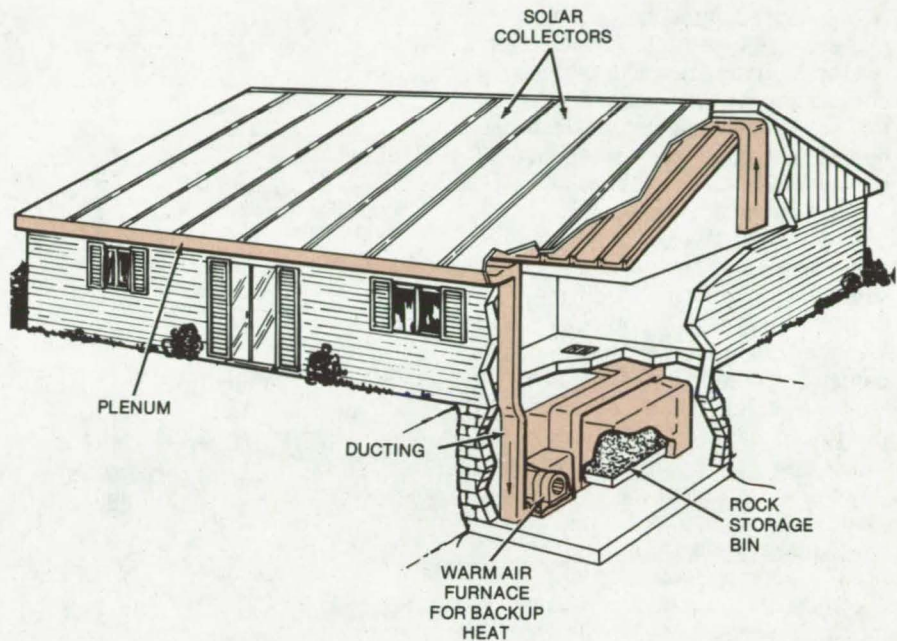


Figure 1. This **Solar-Powered Hot-Air System** delivers space heat and may be used with an air-to-water heat exchanger to heat domestic hot water. The collector panels can be made an integral part of the roof structure.

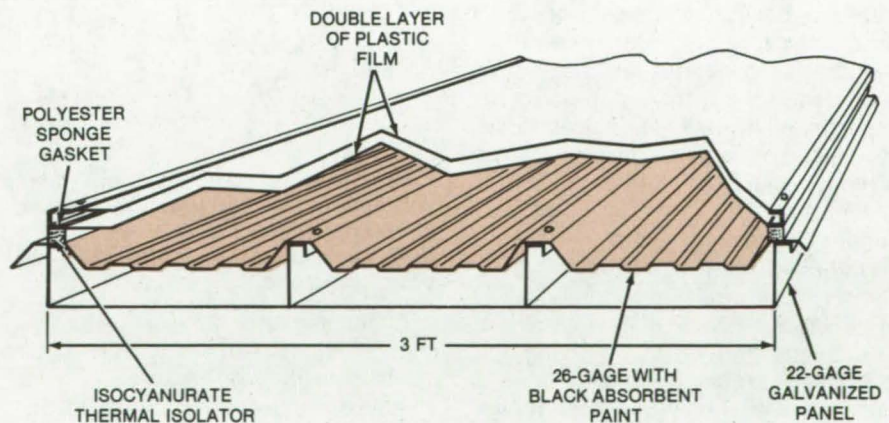


Figure 2. This **Collector Panel Module** is covered with two layers of transparent plastic film. It can be joined to adjacent modules to form a solar panel of any width (in increments of 3 feet).

Ocean Thermal Plant

Modular construction would allow in situ testing of experimental components.

John F. Kennedy Space Center, Florida

A proposed, modular, ocean thermal-energy-conversion (OTEC) plant (shown in Figure 1) would permit vital component research and testing. At the same time, it could serve as an operational generator for about 100 megawatts of electric power.

The modular construction will permit newly developed evaporators and condensers to be tested in the same environment in which they will be used. Such testing could result in a standardization on the design specifications for the most efficient plant facilities in the future. A number of removable modules can be attached to a single control structure or core. When the modules have been removed, the openings in the central structure are sealed off from the ocean waters by foldable door panels. The modules would contain evaporators and condensers constructed of different materials and configurations for comparing cost effectiveness and performance.

The "conventional" OTEC plant concept utilizes the temperature differences between warm surface water and colder layers near the ocean bottom to generate electric power (Figure 2). The electric power can be transmitted by undersea cables to the mainland. A working fluid, such as Freon, ammonia, or propane, is pumped as a liquid into an evaporator where it is converted to high-pressure vapor by surface seawater at a temperature of about 80° F (27° C). The vapor is then used to drive a turbine generator for producing the electricity. After the vapor passes through the turbine, it is routed through a condenser and reconverted to a low-pressure liquid by the cold seawater (approximately 40° F or 4° C), which is pumped from a depth of about 1,500 ft (457 m).

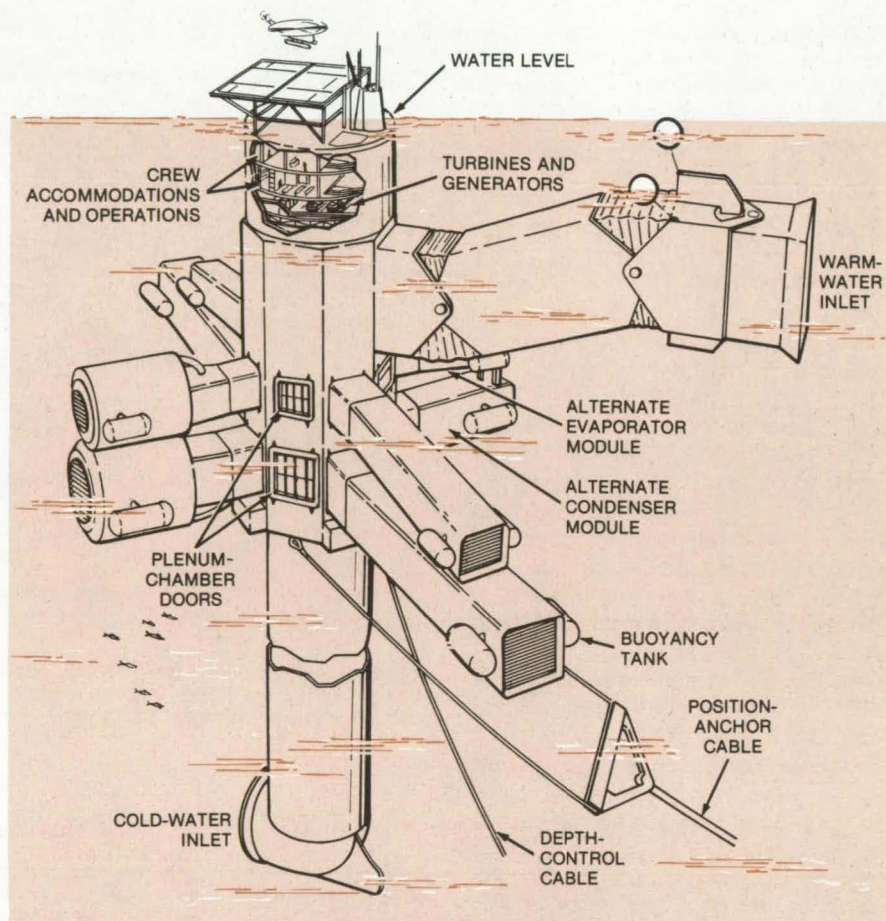


Figure 1. This proposed **Ocean Thermoelectric Powerplant**, designed as a modular test bed, has a central core containing crew facilities, turbine generators, and a cold-water entrance duct; warm water enters from the inlet near the top. A working fluid that is cyclically vaporized and condensed in the plant drives a turbine electric-power generator.

Other important design improvements include warm- and cold-water inlets having swivel sections with directional water vanes to take advantage of the water currents such as those in the Gulf Stream. These features help to reduce the requirement for large pumps to move the water into and out of the plant. The

evaporators and condensers are also equipped with a biofouling preventive device that sprays fluid under pressure on the rows of heat-exchange surfaces to retard marine growth.

The central structure of the plant includes crew quarters, repair and maintenance facilities, control room, turbines, pumps, and generators.

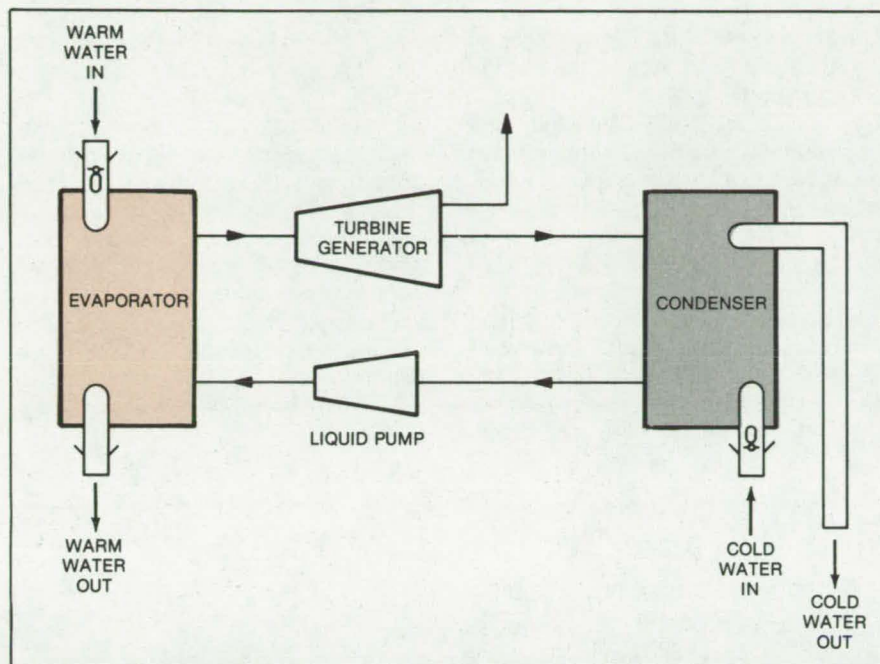


Figure 2. In this **Flow Schematic** of the ocean powerplant, warm seawater evaporates the working fluid, which drives the turbine generator. Cold seawater condenses the fluid so that it can be recycled.

A dock and a helicopter landing pad are also provided atop this central structure. A double-anchoring system prevents excessive movement of the plant due to currents and ocean waves. The anchoring system consists of a positioning harness and a depth-control cable that can also be used to pull the plant underneath the water surface in the event of a hurricane or tropical storm.

This work was done by Lester J. Owens of **Kennedy Space Center**. For further information, Circle 27 on the TSP Request Card.

This invention has been patented by NASA [U.S. Patent No. 4,087,975]. Inquiries concerning nonexclusive or exclusive license for its commercial development should be addressed to the Patent Counsel, Kennedy Space Center [see page A8]. Refer to KSC-11034.

Wind/Water Energy Converter

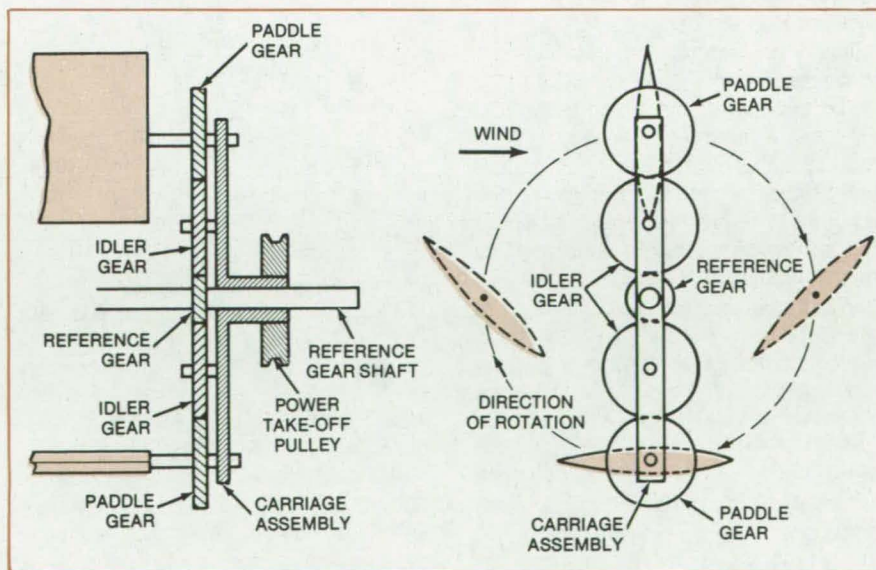
A proposed device that could be driven by wind or water currents would generate electricity or operate pumps.

Goddard Space Flight Center, Greenbelt, Maryland

A proposed machine would convert wind, water, tidal, or wave energy into electrical or mechanical energy. Windmill-like paddles, or blades, are synchronously geared to orient themselves to the wind direction for optimum energy extraction.

In the simplified illustration of the machine shown in the figure, just two paddles are shown for clarity. The complete machine would have four or more paddles. Several such machines could be installed along the axis of a single shaft to increase the energy output. The paddles are oriented by a set of gears with predetermined ratios. Each paddle is connected to a paddle gear, and each paddle gear meshes with an idler gear. The two idler gears, in turn, mesh with a stationary reference gear. The idler and the paddle gears are supported by a carriage assembly that rotates around the reference

(continued on next page)



A **Proposed Wind/Water Energy Converter** incorporates a system of gears to turn paddles that capture wind or water current forces. The converter could operate from wind, from ocean surf and tides, or from river currents. The energy can be utilized to run electrical generators or mechanical machinery.

shaft. Rotational energy is tapped from a power takeoff pulley, a gear, or other device rotating with the carriage assembly. The machine can be operated either vertically, as illustrated, or horizontally. The system is bidirectional and will rotate either clockwise or counterclockwise depending on the direction of the driving wind or water current.

To harness wind power, the machine would be mounted in an open windy area and connected to drive an electrical generator or a mechanical pump. Alternately the machine can operate in a river or stream partially or

fully submerged and driven by water currents. Another possibility would be installation in ocean surf where the machine can be driven by tidal forces. Depending on the installation, the gear ratios would be selected so that the driving paddles receive a maximum force, while those paddles on the opposite side would present a minimum area of resistance so as not to interfere with the motion.

A number of system modifications are possible. One includes the use of three paddles and a chain-sprocket drive to eliminate idler gears. Another involves an automatic directional

control on a horizontally mounted machine using a supplementary paddle rigidly mounted to the reference shaft. The paddle would rotate the reference gear so that the driving paddles would always present their maximum area to the wind direction. A vertically installed machine, on the other hand, can be mounted on a rotary platform equipped with deflectors to turn it into the wind.

This work was done by John Paulkovich of Goddard Space Flight Center. For further information, Circle 28 on the TSP Request Card. GSC-12361

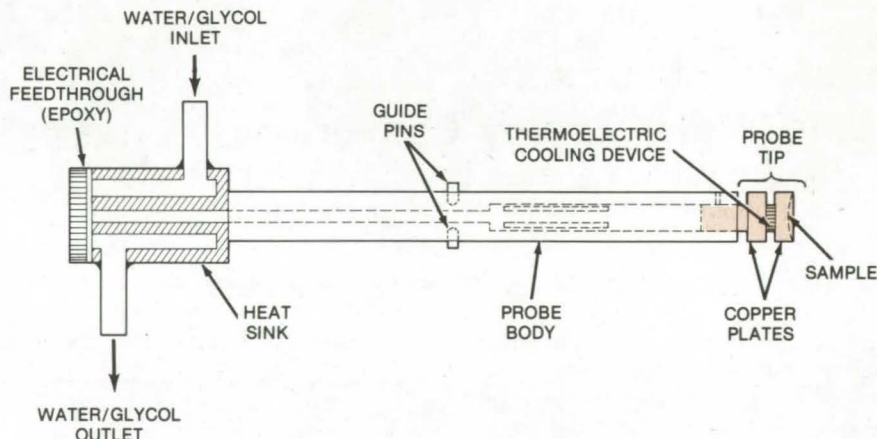
Thermoelectrically-Cooled Variable-Temperature Probe

A variable-temperature probe for electron spectroscopy requires no cryogenic liquids or resistance heating elements.

Lyndon B. Johnson Space Center, Houston, Texas

A new variable-temperature probe uses a thermoelectric cooling device and a water/glycol-cooled heat sink to lower the temperature of a sample and thereby to limit outgassing in a high-vacuum chamber. Originally developed for use in electron spectroscopy, the probe is considerably simpler than conventional cryogenic probes since it requires no refrigerant liquids or supporting equipment such as insulated storage tanks and transfer lines.

The new device, shown in the figure, consists of a probe tip (on which the sample is placed), a heat sink, and a nickel-plated copper body that resists oxidation and transfers heat efficiently between the tip and the heat sink. The probe tip includes upper and lower copper plates separated by the small thermoelectric device. The device absorbs heat when a current flows through it and thus transfers heat from the sample into the copper body. A water/glycol solution flows through the heat sink in the lower portion of the probe to improve the heat-transfer capability. The sample temperature is monitored by a thermocouple installed in the upper probe tip.



This **Variable-Temperature Probe** includes a thermoelectric cooling device that is powered by a 0- to 8-volt supply. The probe measures 0.5 in. (1.27 cm) in diameter by 8.5 in. (21.6 cm) in length.

In tests, the probe was successfully operated over a temperature range of -51° to 121° C at a pressure of 10^{-7} torr. The low-temperature limit was reached (starting at room temperature) in about 7 minutes.

Although originally developed to cool samples for ESCA (electron spectroscopy for chemical analysis) experiments, the probe could be

easily adapted to other spectroscopies, such as Auger, scanning electron microscopy, and optical spectroscopy.

This work was done by Robert M. Kelso and Robert G. Richmond of Johnson Space Center. For further information, Circle 29 on the TSP Request Card. MSC-18192.

Improved Fourier Interference Spectrometer

Proposed system would correct for scan-velocity variations.

NASA's Jet Propulsion Laboratory, Pasadena, California

In a conventional scanning Fourier interference spectrometer, the detector output is sampled at constant time intervals, integrated, and converted to a digital signal that is analyzed to obtain the wavelength distribution of the source. The use of a constant sampling interval presumes that the scanning velocity of the interferometer remains constant. In any real system, however, there will be velocity fluctuations that can lead to errors.

One conventional way to overcome this problem is to put a feedback loop into the system. In this approach, a reference monochromatic laser of known wavelength is scanned at the

same time as the unknown light source. Since the reference wavelength is known, the time between successive intensity maximums or minimums at a set velocity is also known. Any shift in this timing provides the error signal for the loop. However, since this approach is not totally effective, a new proposal has been devised to eliminate residual fluctuations.

The new concept would compensate for velocity changes by multiplying the detector output by a signal proportional to the scan velocity. A velocity-sensing circuit detects the scan velocity by monitoring the signal

from the reference laser. Any increase in the velocity, which would lower the integrated signal strength, is compensated for by an increased signal from the velocity circuit. Conversely, a decrease in velocity would raise the integrated output signal and would be offset by a smaller signal from the velocity-sensing circuit. In this way the output signal is made nearly velocity independent.

This work was done by Rudolf A. Schindler of Caltech for NASA's Jet Propulsion Laboratory. For further information, Circle 30 on the TSP Request Card.
NPO-14025

Low-Power Tuner for Lasers

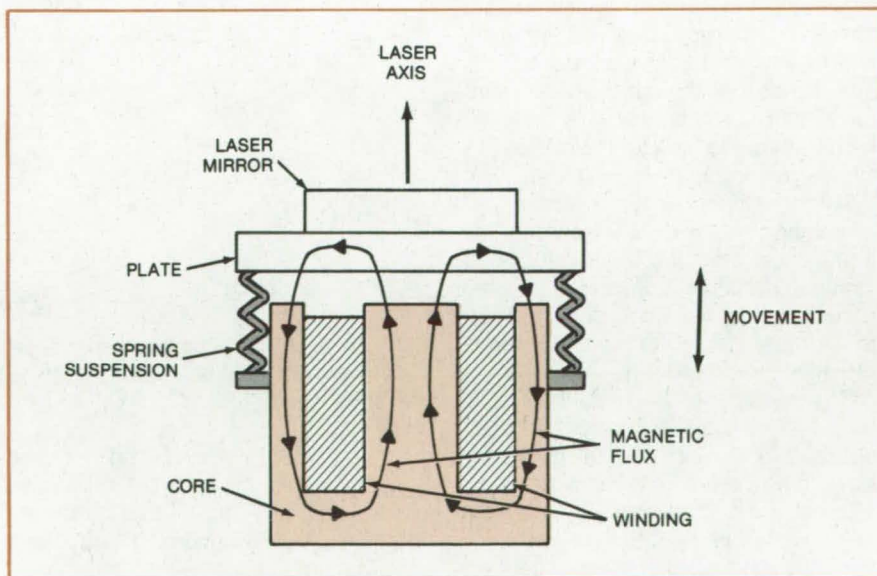
An electromagnetic device that operates at 5 volts accurately controls the length of a laser cavity.

Marshall Space Flight Center, Alabama

A magnetic transducer tunes a laser by making small, precise adjustments in the length of the laser resonant cavity. The transducer adjusts the laser output wavelength by moving a mirror over a range of 5.3 microns, which corresponds to a half-wavelength change in the length of a 10.6-micron carbon dioxide laser cavity.

Previously, eight piezoelectric transducers were stacked to accumulate the total dimensional change of 5.3 microns. This arrangement, however, had several disadvantages. It tended to resonate mechanically at 2,700 hertz, making the feedback control system unstable at that frequency; and the cantileverlike transducer stack could be damaged by the resonance vibration. Moreover, up to 800 volts were required to drive the piezoelectric transducers. This high voltage created a standby power drain

(continued on next page)



This **Magnetic Transducer Laser-Tuning Device** pulls on a spring-mounted plate with a force proportional to the current through the transducer windings. The device moves a mirror to change the length of the laser cavity.

of as much as 6.4 watts per transducer in the driver amplifiers.

The new magnetic transducer, in contrast, operates at a voltage of only 5 to 7 volts, and it is a simple, stable structure. It consists of an electromagnet that pulls on a spring-supported magnetic plate (see figure). The current through the magnet coil is varied to control the position of the plate and of the mirror mounted on it.

In preliminary models of the magnetic transducer, synthetic rubber was used as the spring material. However, this design had excessive mechanical hysteresis, making the deflection-versus-current characteristic dependent on whether the current setting was approached from above or below. In

addition, there was a dead zone of about ± 5 percent around each current setting, corresponding to a displacement error of as much as 0.0025 mm ($1/4$ wavelength) at 10.6 microns. These problems were solved by substituting steel springs for the rubber ones and by redesigning the moving element to minimize friction.

Magnetic hysteresis affects the performance of the transducer less than mechanical hysteresis because much of the magnetic flux is located in the airgap. Magnetic hysteresis was not noticeable with ferrite cores, but was significant with steel cores made of cold-rolled stock. With cores made of transformer steel, the effect is negligible.

In one magnetic transducer, the airgap is 0.010 in. (0.025 cm), and a coil of 750 turns of No. 36 wire is wound around a ferrite core. The core pulled with a force of about 200 grams at 100 milliamperes of excitation current. The driver is a 1-watt transistor in a 5-volt emitter-follower circuit.

This work was done by Samuel Levinson of United Aircraft Corp. for **Marshall Space Flight Center**. For further information, Circle 31 on the TSP Request Card.

Inquiries concerning rights for the commercial use of this invention should be addressed to the Patent Counsel, Marshall Space Flight Center [see page A8]. Refer to MFS-23863.

Diffractoid X-Ray Focusing

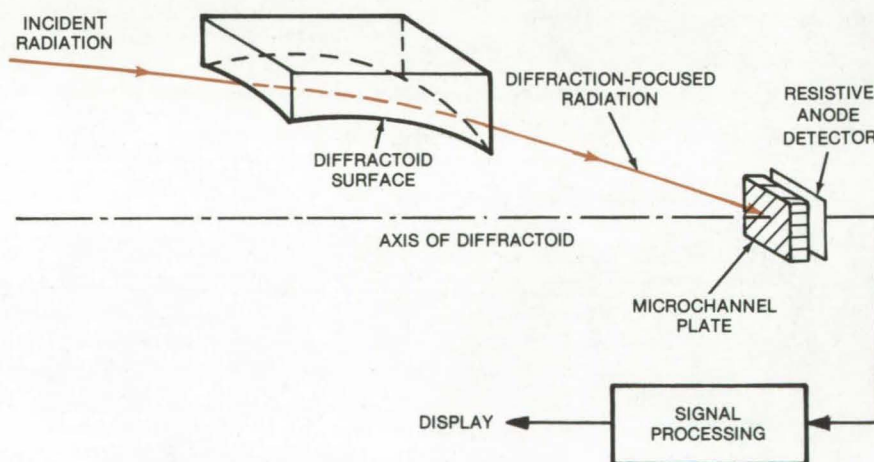
New aspheric grating surface sharply focuses a given EUV radiation wavelength.

Goddard Space Flight Center, Greenbelt, Maryland

Focusing ultra-short-wavelength radiation, such as ultraviolet light and soft X-rays, is a difficult task, and is usually done by "bouncing" the radiation from a concave metallic grating at extremely low grazing angles. However, the formed image is not sharply focused, due to inherent aberrations of a spherical surface.

A newly-developed aspheric concave diffraction surface is able to focus sharply a single wavelength of X-rays or ultraviolet radiation. The incident rays may originate from either a nearby or a far-distant source. The figure illustrates the device focusing incident radiation from a far source; reflection from two successive diffractoid gratings can be used to focus radiation from nearby.

The surface of the new device is called "diffractoid" because it does not have a constant radius of curvature, but instead has a surface of revolution that is defined by a differential equation specified in terms of the diffraction condition dependent on wavelength and the ruling spacing. The grating lines of the diffractoid can be machined on a solid aluminum support block or on a glass block that can later be coated with a reflective gold coating.



The **Diffractoid Focusing Element** can accept incident radiation at reasonably low grazing angles and focuses it more sharply on the detector plate than can a spherical grating.

A possible focusing and imaging system could consist of an appropriately-placed diffractoid element that focuses the oncoming rays into a microchannel plate. A resistive anode detector or ranicon converts the image to electrical signals, which can then be processed and displayed as desired.

This work was done by Sidney O. Kastner of **Goddard Space Flight**

Center. For further information, Circle 32 on the TSP Request Card.

This invention is owned by NASA, and a patent application has been filed. Inquiries concerning nonexclusive or exclusive license for its commercial development should be addressed to the Patent Counsel, Goddard Space Flight Center [see page A8]. Refer to GSC-12357.

Improved Servo for a Michaelson Interferometer

A simplified constant-velocity servosystem for a continuous-scan interferometer

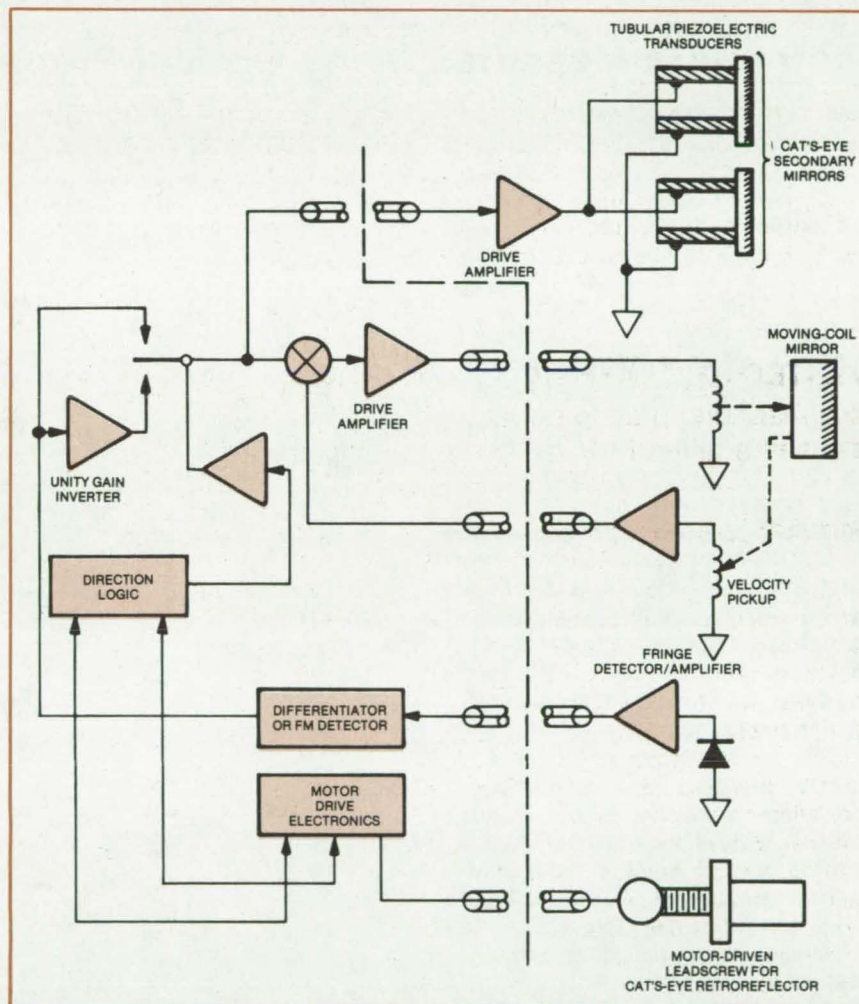
NASA's Jet Propulsion Laboratory, Pasadena, California

An improved velocity servo for driving a continuous-scan interferometer replaces a more complex earlier system. The earlier version, designed for atmospheric sampling experiments, used a standard full feedback loop to control the speed of the lead-screw actuator in one arm of the interferometer. In the new system, the lead screw is run open loop by a synchronous motor that has its speed accurately controlled by a crystal oscillator. Short-time-period velocity variations are sensed by detecting the fringes from a reference laser beam that has gone through the interferometer. These variations are compensated for by moving-coil and piezoelectric actuators and their servos. With these changes the overall system design can be simplified with no degradation in performance.

As shown in the illustration, the primary scanning is provided by a lead-screw-driven cat's-eye retroreflector. In this system, the lead screw is driven by a synchronous motor or a stepping motor. To accelerate the motor and lead screw at the start of the scan, the drive frequency is gradually brought up to the required scan velocity. Thereafter, the motor is driven by an accurate, crystal-controlled frequency source, which, along with a precision-ground ball-screw and ball-nut assembly with antibacklash compensation, ensures high velocity stability at low frequencies.

To correct for the inevitable velocity variations at frequencies above approximately 5 to 10 Hz, two additional path-difference error-correcting actuators are used. A moving-coil actuator drives a bending mirror in one of the interferometer arms to correct for variations in the frequency range from 5 to 500 Hz, and piezoelectrically-driven secondary mirrors in the cat's-eyes correct for variations above 500 Hz.

The velocity variation is sensed by detecting the fringes from a reference



In this **Velocity-Scan Servosystem**, the lead screw is driven open loop from a frequency-stable current source. Any variation in speed is sensed as a variation in the rate of reference laser fringes. If any compensation is necessary, it can be handled by moving-coil and piezoelectric actuators and their servo elements.

laser beam that has gone through the interferometer. The signal from the fringes varies sinusoidally at a constant frequency if the scan velocity is constant. The fringe signal is differentiated and full-wave rectified to produce a dc signal proportional to velocity. An FM detector or phase-lock loop can also be used. This signal is low-pass filtered to remove ripple and then

is ac coupled to the moving-coil and piezoelectric actuators. The cross-over frequency of the ac coupling for the moving-coil actuator is less than 10 Hz and is about 250 Hz for the piezoelectric actuator.

In operation, if the lead screw turns at a constant rate, no change in the fringe-velocity signal will occur, and the moving-coil and piezoelectric

(continued on next page)

actuators receive no signal. The actuators will respond only when there is a change in velocity.

Because the interferometer scanning is done in both directions, the dc velocity signal is inverted for the reverse scanning direction. This is

done by direction logic operating off of the scan and by a unity-gain inverter.

This work was done by Rudolf A. Schindler of Caltech for **NASA's Jet Propulsion Laboratory**. For further information, Circle 33 on the TSP Request Card.

This invention is owned by NASA, and a patent application has been filed. Inquiries concerning nonexclusive or exclusive license for its commercial development should be addressed to the Patent Counsel, NASA Resident Legal Office-JPL [see page A8]. Refer to NPO-14093.

Instrument Measures Many Optical Properties in Visible and IR

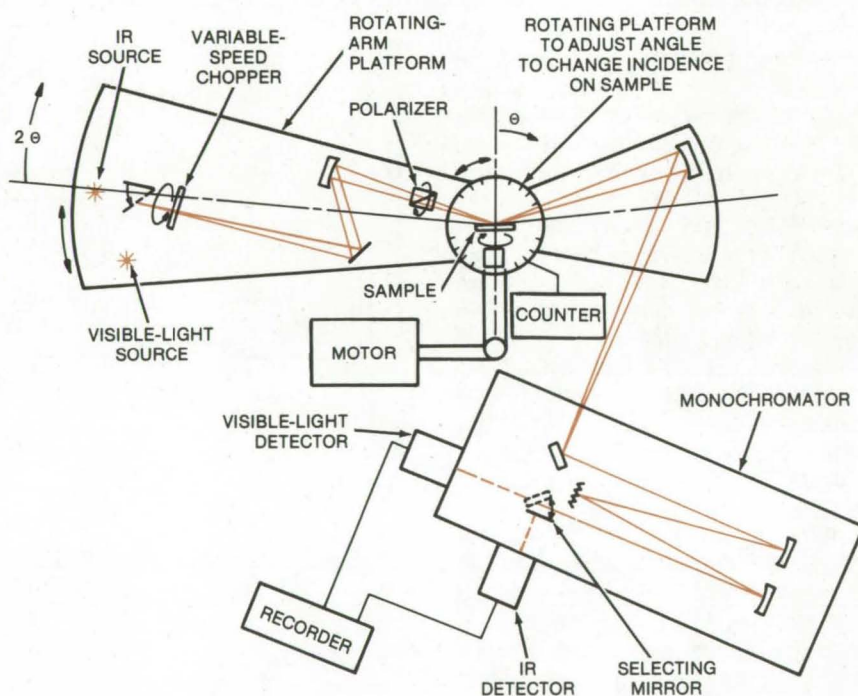
Electro-optical system measures visible and infrared reflectance ratios and combines capabilities of ellipsometer, reflectometer, and spectrophotometer.

Langley Research Center, Hampton, Virginia

An electro-optical system developed at Langley Research Center is capable of determining the optical properties of solids or liquids, such as metals, semiconductor materials, thin films, and solutions. In both the visible and infrared (IR) spectral regions, it measures reflectance, reflectance ratio, transmission, absorption, refractive index, and absorption coefficient. Unlike most prior systems, the instrument can operate in both the visible and IR spectral regions and features continuous angle-of-incidence rotation from 12° to 90° , continuous polarizer rotation, and sample-to-reference automatic ratioing.

The system consists of several component parts. The visible/IR horizontal goniometer is shown in the diagram along with the 1-meter double monochromator, which features automatic wavelength selection from 0.3μ to 12μ or greater. Separate visible and IR detectors cover the required spectral range. These detectors are fixed, but their positions in the light path are interchanged by a selector mirror in the monochromator. A lock-in amplifier coupled to a variable-speed chopper synchronously rectifies signals to minimize the effect of spurious signals and allows ratioing of sample and reference signals. The addition of a ratiometer could automatically determine the ratio of the parallel and perpendicular components of the light reflected from the sample.

In operation, the radiation from either a visible or IR source is directed by a selector mirror through the variable-speed chopper onto a flat mirror. The light is collimated, passed



Visible/Infrared Horizontal Goniometer combines the capabilities of an ellipsometer, reflectometer, and spectrophotometer. Operating over a wide spectral range, this system is expected to find applications in environmental and material-composition testing.

through a polarizer that polarizes the light into either parallel or perpendicular components, and is reflected onto the sample surface at the desired angle of incidence (selected by rotating the arm platform). Then the light beam is reflected into the monochromator and to the visible or IR detector.

The light is reflected from the sample with a change in polarization phase, causing a proportional change

in light intensity, which can be measured with the electronic accessories. The polarization phase change is a function of the angle of incidence of the light on the sample surface and of the optical constants of the sample material.

This work was done by Carmen E. Batten of **Langley Research Center**. For further information, Circle 34 on the TSP Request Card. LAR-12285

Hydrogen-Maser Frequency Standard

A proposed variable-volume maser would have a frequency stability of 1 part in 10^{14} .

Goddard Space Flight Center, Greenbelt, Maryland

In theory, the 1.420-GHz hydrogen-maser line could serve as a primary frequency standard with an accuracy of about 1 part in 10^{14} . As is the case more often than not, however, certain practical difficulties have to be overcome before theory can be reduced to practice. In building a frequency standard, a problem that must be faced is the so-called "wall shift" in frequency caused by collisions between the hydrogen atoms and the walls of the container.

Variable-volume hydrogen masers have been suggested as a way of correcting for the wall shift. In these devices, the frequency is measured at two or more volumes to determine the dependence of the shift on mean free path (λ). This dependence is then extrapolated to $\lambda = \infty$ to find the unshifted frequency. In most previous masers, however, the expansion and contraction of the variable volume may introduce stresses in the wall that affect the wall shift in a way that cannot easily be accounted for when determining the frequency correction. Another problem is the introduction of instabilities in the maser frequency that make 1 part in 10^{14} measurements difficult if not impossible.

In a proposed new variable-volume maser, the wall shift could be accurately determined, and a frequency standard with an accuracy of 1 part in 10^{14} would be possible. As shown in Figure 1, the new maser has a fixed-volume section inside a microwave resonant cavity. The variable volume, outside the cavity, is enclosed by a flexible sheet of Teflon in the shape of a truncated cone. A metal baffle separates the fixed and variable volumes and contains the microwave field within the cavity. Apertures in the baffle allow hydrogen atoms to move freely between the volumes. A feedback-loop temperature controller holds the temperature of the cavity and bulb stable to within $5 \times 10^{-5}^\circ \text{C}$ of a preset value.

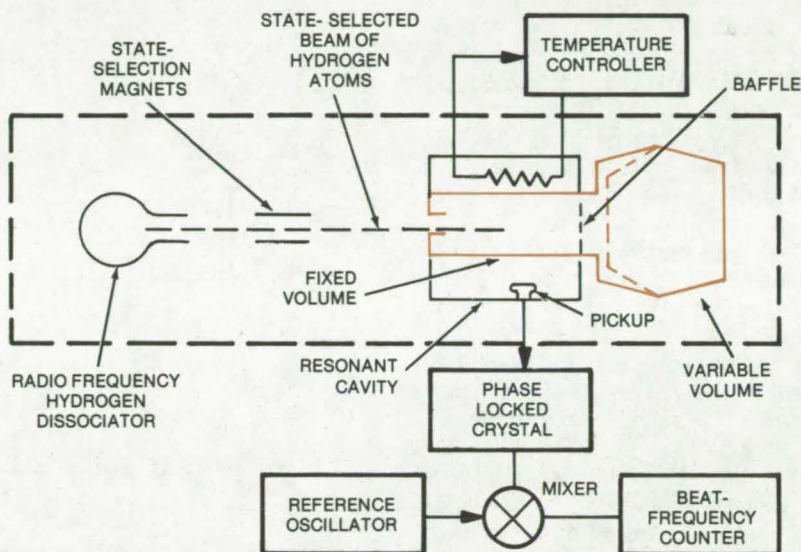


Figure 1. This **Variable-Volume Maser** has a fixed-volume section inside a microwave cavity that resonates in the TE 011 mode. The variable-volume section external to the cavity is made of thin, flexible Teflon shaped in the form of a truncated cone. For best stability and accuracy, the length-to-diameter ratio of the microwave cavity should be at least 2 to 1.

As shown, the variable volume has two stable positions: one with the cone "folded" inward and the other with the cone folded outward. With this design, stresses on the walls are essentially the same for either configuration (except for a negligible area near the folded-over edges), and thus they do not affect the wall shift. Also, the design allows a large change in volume between the two states, which improves the accuracy when correcting for the wall shift. Since the variable volume is external to the cavity, changes in the maser volume do not destabilize the cavity resonance.

To use the maser as a frequency standard, the wall shift is measured at two temperatures and at the two volumes (see Figure 2). These frequencies are plotted against the reciprocal of the mean free path of the hydrogen atoms. The curves are extrapolated back to $\lambda^{-1} = 0$ to determine the unshifted frequency.

This work was done by Victor Reinhardt of **Goddard Space Flight**

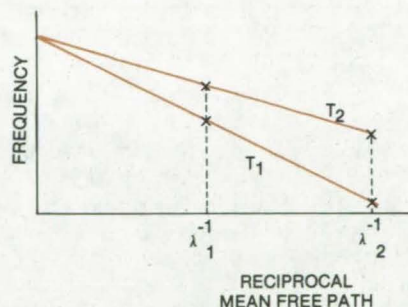


Figure 2. The **Maser Frequency Shift** is plotted against reciprocal wavelength (λ^{-1}) and is extrapolated to $\lambda^{-1} = 0$ to determine the unshifted frequency.

Center and Peter Cervenka of Phoenix Corp. For further information, Circle 35 on the TSP Request Card.

This invention is owned by NASA, and a patent application has been filed. Inquiries concerning nonexclusive or exclusive license for its commercial development should be addressed to the Patent Counsel, Goddard Space Flight Center [see page A8]. Refer to GSC-12334.

Ultrathin Films as Photomechanical Transducer

The stress in an ultrathin film varies with the intensity of light shining upon it.

NASA's Jet Propulsion Laboratory, Pasadena, California

A stretched ultrathin film can be used to detect the presence of light and to measure total light exposure over a period of time. This new photomechanical transducer that responds to light energy shows promise as a low-cost, nonelectrical substitute for photocells.

The transducer converts time-varying light into a time-varying mechanical stress that can easily be monitored by strain gages. The effect was discovered during the course of experimental studies of the physical properties of very thin film materials for the Solar Sail program. A 0.1-mil (2.5- μm) film of polyimide (Kapton, or equivalent), metalized on one side with aluminum and on the other with chromium and stretched in a test fixture, was illuminated with a flashlight to make calibration marks on the film more visible. Immediately, strain-gage instrumentation attached to the film showed a sharp decrease in stress in the film. When the flashlight was turned off, the original stress returned.

This photomechanical effect is believed to be caused by reversible and rapid heating of the film, induced by absorption of the incident radiation. The stress change, $\Delta\sigma$, produced by an incident energy density Q , is given by

$$\Delta\sigma = -E\alpha kQ/C_p$$

where E is Young's modulus for the film, α is its coefficient of linear expansion, k is its absorption coefficient, and C_p is its heat capacity. Thus a thin film (low heat capacity) with high absorption exhibits the effect strongly. In tests of various film materials with various reflecting and absorbing coatings (or no coatings at all), the response has varied from -1.5 to -16 g/cm²-W.

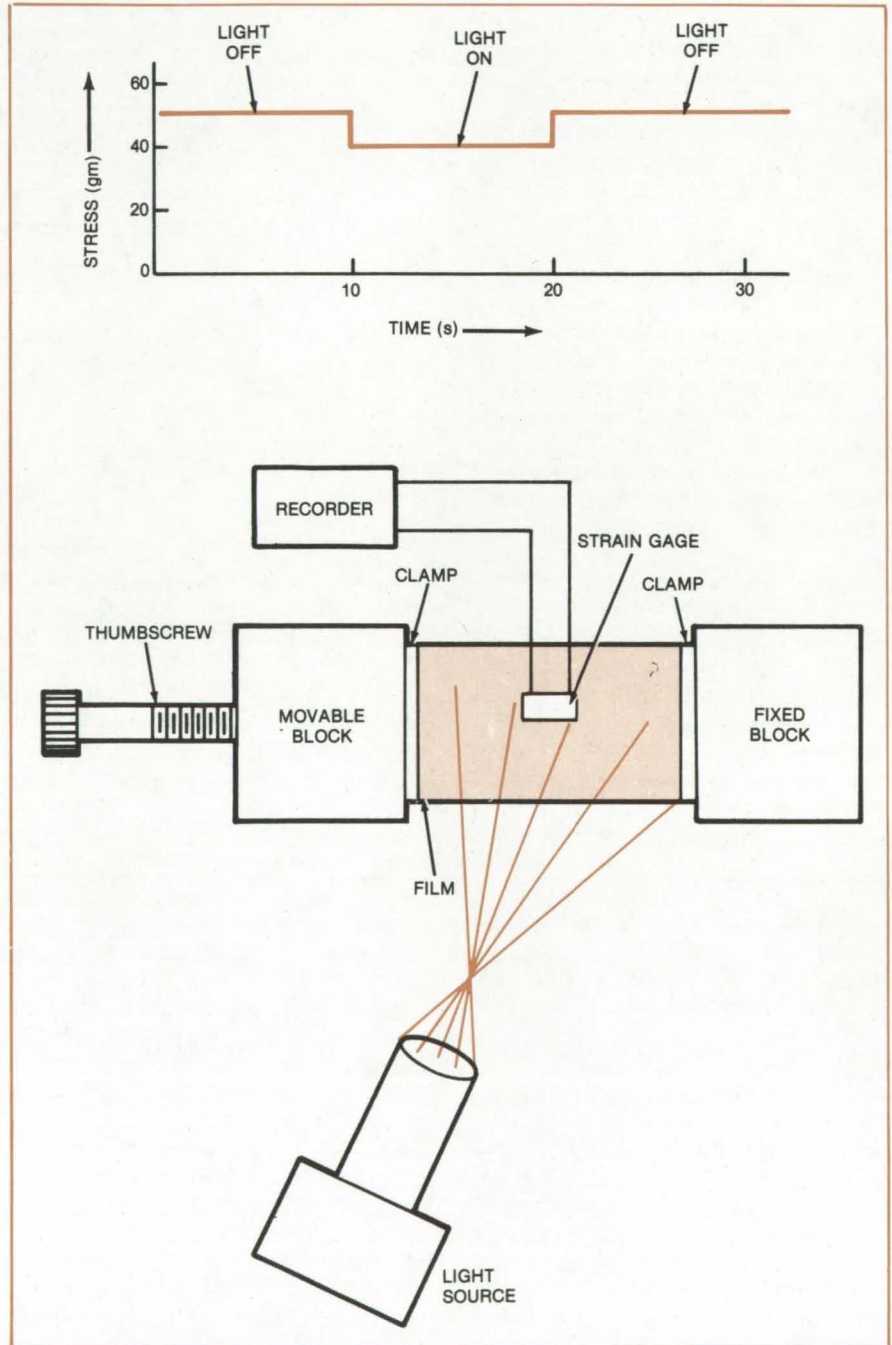


Figure 1. Film is Prestressed by stretching in a clamp fixture. Light falling on the film alters the prestress, and the change is recorded. The film stress drops by 10 to 20 percent when the film is illuminated. The chart trace shown here is the response to light switched on and off. Light that is changed more gradually produces a similarly gradual response.

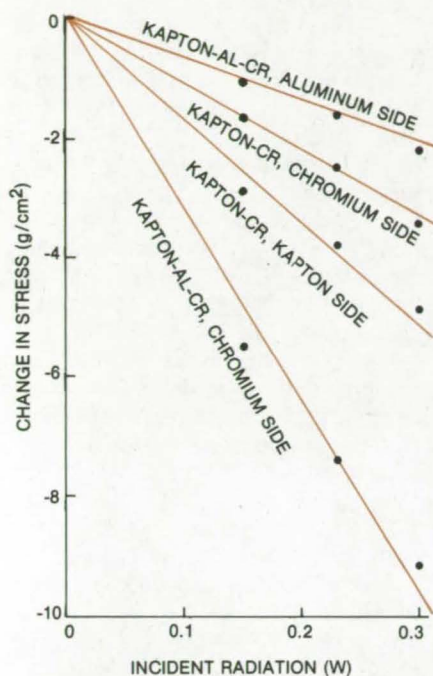


Figure 2. The Linearity and Accuracy of the photomechanical effect in thin plastic films are shown here.

A practical transducer exploiting this effect consists of a 3- by 8-cm metalized film held by clamps on two support blocks, one of which is movable and the other fixed (Figure 1). Tension in the film is adjusted to about 50 g by a thumbscrew on the movable block. The film contains an integral strain gage, which is attached to an amplifier and strip-chart recorder to indicate light-induced changes in the film stress.

The stress in the film decreases by 10 to 20 percent, depending on the brightness of the light and the nature of the film. A 100-watt light bulb produces a more pronounced effect than a flashlight, for example (see Figure 2). If the light intensity is varied sinusoidally instead of just

turned on and off, the stress in the film follows a similar sinusoidal variation. The total light exposure can be determined by graphical integration of the area under the response curve on the strip-chart recorder.

This work was done by Robert F. Fedors and Mohammad N. Sarbolouki of Caltech for **NASA's Jet Propulsion Laboratory**. For further information, Circle 36 on the TSP Request Card.

This invention is owned by NASA, and a patent application has been filed. Inquiries concerning nonexclusive or exclusive license for its commercial development should be addressed to the Patent Counsel, NASA Resident Legal Office-JPL [see page A8]. Refer to NPO-14363.

Books and Reports

These reports, studies, and handbooks are available from NASA as Technical Support Packages (TSP's) when a Request Card number is cited; otherwise they are available from one of NASA's Industrial Application Centers or the National Technical Information Service.

Solar-Heating System — Design Data Brochure

Design and performance specifications for a complete system that is assembled from commercially available components

A recently released report describes a complete system for space and hot-water heating that is assembled from commercially available components. The system can meet the needs of a single family dwelling

having approximately 1,200 ft² (110.4 m²) of floor area, and it can be scaled to the requirements of larger or smaller installations. The design, performance, and hardware specifications will be helpful to architects and engineers in planning and operating an equivalent solar system.

The major hardware components comprising the closed-volume system are:

- the flat-plate, liquid solar collectors;
- a 1,000-gal (3.7-m³) hot-water tank for storing thermal energy;
- a 65-gal (0.24-m³) storage tank for domestic hot water;
- water/air and water/water heat exchangers;
- three variable-head circulator pumps; and
- a solid-state system controller.

Manufacturer's literature describing the hardware is included in the report.

For each installation, the performance (measured as percent solar contribution to the total heat load) is a function of the load and system size. It

is possible to determine a building "load coefficient" (BLC) from the expression

$$BLC = \frac{U(\text{Floor Area})}{24}$$

where U is the building load in Btu/day/°F per ft² of floor area. The BLC is used in calculating the size of the water/air heat exchanger.

Graphs for determining the collector size from the load requirement and available roof area are also contained in the report, as are guidelines for the selection of pumps and the liquid/liquid heat exchanger. The last two sections of the report are devoted to information on system installation, operation, and maintenance.

This work was done by the Federal Systems Division of IBM Corp. for **Marshall Space Flight Center**. To obtain a copy of the report "Design Data Brochure SIMS Prototype System 3," Circle 37 on the TSP Request Card.

MFS-23977

Solar-Heating System — Performance Tests

To determine its suitability for field installation

Results of performance tests on the solar-heating system described in the previous article are contained in a recently released report. Tests were carried out in two phases, using the Marshall Space Flight Center solar-heating and cooling test facility. In phase 1, temperature inputs and loads on the thermal-storage and domestic hot-water subsystems were varied to test the energy-transfer function of the system. Normal, "as-installed," operation was simulated in phase 2.

The major test objectives were to verify that the individual commercially-available hardware subcomponents performed to their design requirements and to insure that the system performed to specification. The tests also were intended to generate a performance data base for comparison with future tests on a field-installed system. The percent solar contribution to the overall building heat load was used as a primary performance indicator.

The tests gave the following significant findings:

- The system will supply 53 percent of a 75.5×10^6 -Btu/yr (79.6×10^9 -J/yr) total heating load (assuming weather data appropriate for Huntsville, Alabama).
- The electrical energy required to drive the solar portion of the system is approximately 2.5 percent of the collected energy.
- The flow distribution manifolds produce thermal stratification in solar storage. This stratification improves the collector efficiency if space heat is not energized. If space heat is energized, space heating is enhanced usually at the expense of collection efficiency.
- A single-tank solar domestic water heater is a viable design option.
- The system was judged suitable for field installation.

This work was done by the Federal Systems Division of IBM Corp. for Marshall Space Flight Center. To obtain a copy of the report "SIMS

Prototype System 3 — Engineering Analysis," Circle 38 on the TSP Request Card.

MFS-25021

Solar-Heating System

System can be used in buildings for which roof-mounted collectors are not feasible.

A solar domestic-hot-water and space-heating system that uses air in the collector loop is described in a new report. The modular system consists of the collectors, a rock-storage bin, blowers, dampers, ducting, an air-to-water heat exchanger, a domestic-hot-water preheat tank, piping, and system controls. Included in the 82-page report are design, performance, and hardware specifications in sufficient detail to assemble the system and to allow architectural engineers and contractors to procure, install, operate, and maintain it.

This system is intended for use in a small, single-family dwelling where a roof-mounted collector is not feasible (because of lack of space or other restrictions). A prototype unit has 203 square feet (18.7 m^2) of effective collector surface and 113 cubic feet (3.1 m^3) of rock storage. Expansion or reduction of the collector array and the storage bed is possible in 68-ft^2 (6.2-m^2) and 37-ft^3 (1.0-m^3) increments, respectively.

Three modes of operation are possible, to maintain three different air-circulation loops: (1) collector-to-storage, (2) collector-to-load, and (3) storage-to-load. Airflow is controlled by two blowers and two dampers. Solar energy is collected in modes 1 and 2; space heating is generated in modes 2 and 3.

Water is siphoned in the domestic-hot-water preheat loop between the air-to-water heat exchanger and the preheat tank. The domestic hot water is heated, primarily in mode 1, when air temperatures in the heat exchanger are hottest; however, when the air temperature into the heat exchanger is higher than the preheat-tank water temperature, the water may also be heated in modes 2 and 3.

At a projected demonstration site for the prototype in Clinton, Mississippi, the system is expected to supply 48 percent of the total building-heat requirements (35 percent of space heat and 68 percent of heat for domestic hot water). For this system, the hot-water demand is 130 gal/d (492 l/d), the domestic-hot-water temperature is 140°F (60°C), and the peak heating load is projected at 30,604 Btu ($32.3 \times 10^6 \text{ J}$). Although these figures can serve as guidelines in planning other systems, the actual system performance is sensitive to various site-dependent and building-dependent factors.

This work was done by the Federal Systems Division of IBM Corp. for Marshall Space Flight Center. To obtain a copy of the report "SIMS Prototype System 4 — Design Data Brochure," Circle 39 on the TSP Request Card.

MFS-25022

Solar Hot-Water System

Design data brochure describes domestic hot-water system for single-family residences.

A solar water heater that meets the needs of a family of four is described in a brochure that can be obtained on request. The direct-feed system is designed to produce 80 gallons (300 liters) of 140°F (60°C) hot water per day.

Heating is accomplished by the circulation of potable water from the bottom of the storage tank up through the solar collectors and back down to the top of the storage tank. An electronic controller regulates the flow of water in response to the solar energy absorbed by the collectors. The electronic controller also operates the freeze protection system. This direct-feed solar water heater eliminates the need for heat exchangers and antifreeze solutions by providing freeze protection with "circulating tank water" for geographic areas below 31° latitude or "collector draindown" for geographic areas above 31° latitude.

The four basic components of the system are:

- Collectors,
- Storage tank,
- Flow controls, and
- Transport lines.

The brochure describes the function, operation, and installation of each component. It also reviews the annual movements of the Sun relative to Earth and explains the geographical considerations in collector orientation and sizing. Practical examples using brand-named hardware are included.

This work was done by Solar Engineering and Manufacturing Co. for **Marshall Space Flight Center**. To obtain a copy of the brochure "Design Data Brochure: Solar Hot Water System," Circle 40 on the TSP Request Card.
MFS-25043

Residential Solar-Heating System — Design Package

Includes performance specifications, design data, and installation guidelines

A design package for the residential solar-heating system introduced on page 202 of *NASA Tech Briefs*, Vol. 3, No. 2, has been made available. Included in the 65-page package are performance specifications, design data, installation guidelines, and other information that should be valuable to those interested in evaluating the system (or similar systems) for projected installations.

The modular system has air-heating solar collectors. An air-to-water heat exchanger transfers heat to a domestic-hot-water storage tank and to water in an energy-storage tank. When installed in an insulated "energy-saver" home, the system can supply a large percentage of the total energy needs of the building.

Drawings, graphs, and data in tabular form complement the text material of the design package. Information on system electrical wiring and a parts list are also included.

This work was done by Solafern, Ltd., for **Marshall Space Flight Center**. To obtain a copy of the

design package, "Design Package for a Complete Residential Solar Space Heating and Hot Water System," Circle 41 on the TSP Request Card.
MFS-25071

Development and Testing of a Hot-Air Solar Collector

Includes design details, materials recommendations, and performance specifications

A new report summarizes the development of the solar collector described in two articles in a previous issue of *NASA Tech Briefs*. [See "Prototype Air Flat-Plate Solar Collector" (MFS-23893) and "Flat-Plate Solar Collector — Installation Package (MFS-23921) on page 214 of *NASA Tech Briefs*, Vol. 3, No. 2.] The collector is an array of three or more flat panels, each measuring 4 by 8 feet (1.2 by 2.4 m). Air flows over a flat solar-heat-absorbing surface under a glass plate. In flowing through three panels, the air is heated to at least 172° F (78° C). During tests on a clear December day in Colorado, a three-panel array produced 14,400 Btu/h (4,200 J/s), enough to meet much of the space- and water-heating requirements of a small building such as a home or shop.

The report discusses structural details of the panel, including the aluminum frame, the seal between the glass plate and the frame, and the stretched plastic film that protects the glass from damage. Reasons for the choices of materials are explained. Development work is described — in particular, the selection of a solar-absorbent coating and of the proper spacing for airflow between this coating and the glass plate. The report gives a complete performance specification and an extensive certification test report.

[Also see related article "Subsystem Design Package for Solar II Collector" (MFS-23941) on page 355 of *NASA Tech Briefs* Vol. 3, No. 3.]

This work was done by John M. Caudle of **Marshall Space Flight Center**. To obtain a copy of the report, "Development, Testing, and

Certification of Life Sciences Engineering Solar Collector — Final Report," Circle 42 on the TSP Request Card.
MFS-23997

Design and Installation of a Flat-Plate Solar Collector

Includes information on collector sizing

Performance and installation information for a flat-plate, liquid solar-energy collector is presented in a new report. The single-glazed collector consists of 30 closely-spaced elastomeric twin tubes cemented to an insulating base and covered by flexible plastic. The panel area is selected to meet the requirements of the building in which it is installed; it can be assembled in sizes up to 4 by 25 ft (1.2 by 7.6 m). Several panels can be ganged to make larger sizes.

The collector is designed to meet Housing and Urban Development (HUD) Department standards for home use. Its performance is summarized by the criterion that it collect at least 500 Btu/day/ft² (0.00157 cal/s/cm²) at an inlet fluid temperature of at least 130° F (54.4° C) under the following conditions:

- Tilt angle = 50° with respect to the horizontal.
- Azimuth is due south.
- Ambient temperature = 40° F (4.4° C), average.
- Wind velocity = 600 ft/min (3.05 m/s), average.
- Noon solar flux = 290 Btu/h/ft² (0.0219 cal/s/cm²) normal to the collector surface.
- The date is November 21.
- Latitude = 74°.
- Longitude = 41°.

A plot of minimum efficiency for different operating conditions is included in the report.

In addition to descriptions of the performance specifications, the installation, operation and maintenance procedures, and detailed drawings, the 61-page report describes methods for determining the optimum collector size. Collector sizing is an economic decision as well as a technical one. In

(continued on next page)



contrast to conventional heating or air-conditioning systems that are sized to handle peak loads (since they do not generally operate in cooperation with backup systems), the solar system is sized to handle only a portion of the peak-load demand. The balance of the load is absorbed by a backup system.

The sizing calculation is thus carried out in two steps: (1) The total energy requirements for domestic hot water and space heating are ascertained, and (2) the collector is sized to meet a portion of these requirements. A table of the average hot-water requirements for various single-family dwellings is included in the report for use in the first calculation. In making the second part of the calculation, the collector tilt angle is determined and is used in determining the amount of insolation received per unit area of collector surface. Finally the area required to meet roughly 50 to 60 percent of the domestic hot-water requirement and 40 to 50 percent of the space-heating requirement is calculated. Comprehensive tables of collector tilt factors and average daily degree-day factors for many locations are given. [See the following article "Liquid Solar Collector — Performance Tests" (MFS-25082)].

This work was done by the Calmac Manufacturing Co. for Marshall Space Flight Center. To obtain a copy of the report "Design and Installation Package for the Sunmat Flat Plate Solar Collector," Circle 43 on the TSP Request Card. MFS-25010

Liquid Solar Collector — Performance Tests

To verify compliance with HUD standards

A 156-page report describes comprehensive performance tests on a commercially-available, flat-plate, liquid solar collector. The tests were initiated to verify that the collector meets U.S. Housing and Urban Development (HUD) Department Standards for "thermal stability." The test program consists of three parts: (1) initial thermal performance; (2)

30-day stagnation; and (3) final thermal performance.

The test item is a modular non-metallic single-glazed liquid solar collector that is designed for field assembly. It consists of 30 closely-spaced elastomeric twin tubes cemented to an insulating base and covered with flexible plastic. The panel is 4 ft (1.2 m) wide by up to 25 ft (7.6 m) long. The length can be selected to meet the requirements of the building in which the system is installed.

The initial thermal performance test consists of four parts:

- **Preconditioning.** The collector is filled with water, and the inlet is sealed. Then the panel is held in a nonoperational stagnation mode in which the water is allowed to evaporate. The stagnant collector is exposed for 3 days to cumulative solar radiation of at least 1,500 Btu/ft²/day (4.73×10^{-3} cal/cm²/s).
- **Time Constant.** The transient response of the collector to a step change in insolation is measured.
- **Instantaneous Efficiency.** The collector efficiency is determined as a function of solar radiation flux, ambient temperature, and fluid inlet temperature.
- **Incident-Angle Modifier.** The efficiency is measured for solar radiation incident at 30°, 45°, and 60° with respect to the normal to the collector.

Possible materials or construction problems are identified during the 30-day stagnation exposure tests that follow the initial thermal performance tests. During this period, the stagnant water-filled collector is exposed to 1,500 Btu/ft²/day solar flux. A 4-hour exposure to 300 Btu/ft²/h (0.0227 cal/cm²/s), after boilout of the water, is made at least once. The physical appearance of the collector is monitored, and data on ambient temperature, wind, and precipitation are recorded.

The final thermal performance test differs from the initial test in that there is no preconditioning, no time-constant measurement, and no incident-angle modifier measurement. The efficiency measurements are made at 12 test points instead of the minimum of 16 points in the initial sequence.

A special test of the instantaneous efficiency at four points, with the

collector glazing removed, was carried out. This was done to determine indirectly the losses through the cover. [Also see preceding article "Design and Installation of a Flat-Plate Solar Collector (MFS-25010).]

This work was done by Calmac Manufacturing Co. for Marshall Space Flight Center. To obtain a copy of the report, "Certification and Verification for Calmac Flat Plate Solar Collector," Circle 44 on the TSP Request Card. MFS-25082

Concentrating Solar Collector — Installation Package

Drawings and guidelines to assist in field assembly

Information on the installation and maintenance of a concentrating solar collector and tracking system has been made available in a 51-page report. The collector area is 301 square feet (27.6 m²) in seven panels. Each panel is fitted with a modified Fresnel prismatic lens that gives a concentration ratio of 10 to 1. The system includes supporting framework, fluid manifolding, and a tracking drive, all of which are supplied by the manufacturer in kit form and are intended for assembly in the field.

The report contains a general description of the system and a comprehensive set of drawings that illustrate the assembly procedure. Also included is information on receiving, unpacking, storage, and handling of the subcomponents, along with separate discussions of installation procedures for each. Information on system testing, startup, and maintenance is also included, as is a materials list.

This work was done by Northrup, Inc., for Marshall Space Flight Center. To obtain a copy of the report "Installation Packages for Concentrating Solar Collector Panels," Circle 45 on the TSP Request Card.

Inquiries concerning rights for the commercial use of this invention should be addressed to the Patent Counsel, Marshall Space Flight Center [see page A8]. Refer to MFS-25068.

Corrosion Inhibitors for Solar-Heating and Cooling Systems

Twelve formulations were tested in the laboratory.

Twelve candidate corrosion inhibitors for solar-heating and cooling systems were tested under laboratory conditions at Marshall Space Flight Center. The test results are described in a new report. Four of the inhibitors are proprietary products available from commercial vendors; most are based on sodium salts, including nitrates, borates, silicates, and phosphates. The 12 were evaluated for their abilities to protect aluminum, steel, copper, and stainless steel at temperatures typical of those encountered in a solar-heating system.

Test specimens were cleaned and immersed in solutions of the inhibitors in a corrosive aqueous solvent (containing sodium chloride, sodium sulfate, and sodium bicarbonate). The test assemblies were made by drilling a small hole in one end of each specimen. Aluminum, steel, copper, and stainless-steel specimens were placed on a screw, with a stainless-steel nut between adjacent specimens to act as a separator and to insure electrical contact. The assemblies were immersed in 450 ml of the test solutions (contained in Erlenmeyer flasks) and the flasks were placed in hot-water baths (at 80° C).

The assemblies were removed from the solutions and placed in empty covered flasks each working day for 8 hours (to simulate a system drained at night during the winter to prevent freezing). Each specimen was visually inspected each day, and the solution level was maintained by the addition of distilled water to insure constant solution concentration. After 1 year of exposure, the assemblies were removed, disassembled, cleaned, and weighed.

Evaluation of the corrosion inhibitors was based on the corrosion protection they afforded aluminum and mild steel because neither copper nor stainless steel was significantly corroded in any of the solutions or in uninhibited water. The inhibitors are rated in three categories according to

protection afforded aluminum, protection afforded mild steel, and protection afforded a combination of the two.

Two inhibitors were found to be very effective for aluminum and steel under the conditions of this test and are recommended for consideration in multimetallic solar-heating and cooling systems. Their evaluation under simulated or actual service conditions is recommended. Two others show promise, but neither protected aluminum, and additional testing is required before they can be recommended.

For systems where aluminum components are not corrosion-critical, two of the inhibitors may give adequate protection, and another may be considered for systems having no corrosion-critical steel parts. An all-stainless-steel, copper, or combination system is probably the most corrosion-resistant, but the cost may be prohibitive.

This work was done by T. S. Humphries of Marshall Space Flight Center. To obtain a copy of the report, "Corrosion Inhibitors for Solar Heating and Cooling Systems," Circle 46 on the TSP Request Card. MFS-25023

Chemical-Vapor Deposition of Silicon From Silane

A theoretical study may help reduce the cost of silicon for solar arrays and other applications.

A recent investigation of chemical-vapor deposition (CVD) of silicon by silane pyrolysis is described in a new report.

The study began by considering the heat of the reaction and the free-energy change to determine the feasibility of the reaction for producing silicon, along with the extent of conversion, and the energy requirements for the process. The results are presented in a table that lists the standard free-energy change, the equilibrium constant, and the heat of the reaction, all calculated for a temperature range of 100 to 1,600 K. An analysis of these data indicates that silicon CVD is an irreversible and exothermic reaction over a wide

temperature range. It is promising for development as an economical commercial process.

The chemical-vapor deposition consists of several physical and chemical steps; however, the exact mechanisms are not completely understood. In the study, rate expressions were derived for every conceivable elementary step. The elementary steps were conveniently grouped into six categories: (1) mass transport of silane and hydrogen, (2) homogeneous pyrolysis of silane, (3) homogeneous nucleation of silicon, (4) heterogeneous pyrolysis of silane, (5) heterogeneous nucleation of silicon, and (6) silicon crystal growth.

The actual mechanism of silicon CVD is thought to consist of three or more of these six categories. The controlling step depends on the reaction temperature and on the silane concentration. The experimental evidence leads to some general conclusions about silane pyrolysis: The reaction is predominantly homogeneous at temperatures between 300° and 500° C and is predominantly heterogeneous at higher temperatures between 500° and 1,200° C; the heterogeneous reaction is a diffusion-limited process above 1,000° C; and the crystal structure of the deposited silicon depends strongly on the substrate temperature. All of these factors are taken into consideration in developing rate expressions for the CVD process.

Two basic elements needed to use the rate expressions to formulate the global state of silicon CVD from the elementary steps are the exact mechanism of silicon CVD and numerical values for the various constants in the rate expressions. Numerical values of the coefficients and constants are reported in the literature, or they can be estimated. If one of the steps is particularly slow, it can be designated as the rate-limiting step, and the remaining steps can be assumed to occur at equilibrium conditions. The rate of the limiting step will then be the global rate.

This work was done by George C. Hsu, Ralph Lutwack, and Ananda K. Praturi of Caltech for NASA's Jet Propulsion Laboratory. Further information may be found in NASA CR-155044 [N77-32265], "Chemical

(continued on next page)



Vapor Deposition of Silicon From Silane Pyrolysis" [\$4.50]. A copy may be purchased [prepayment required]

from the National Technical Information Service, Springfield, Virginia 22151.
NPO-14403

Computer Programs

These programs may be obtained at very reasonable cost from COSMIC, a facility sponsored by NASA to make new programs available to the public. For information on program price, size, and availability, circle the reference letter on the COSMIC Request Card in this issue.

Multidimensional Histograms

Fast-routine for statistical analysis of Landsat images

The multidimensional histogram program was developed to examine the multidimensional statistics of multispectral image data. In one Landsat image there are 7,581,600 picture elements (pels). Each pel corresponds to a particular location of approximately 80 meters resolution in the ground scene and is represented by a four-dimensional vector. The four components of this vector correspond to the reflected light intensity of the ground location in each of four different spectral bands. This program identifies and counts the number of unique multispectral vectors that occur in a Landsat image. It also counts the number of times that the unique vectors are repeated in the image. Thus the program computes a four-dimensional histogram of the

Landsat multispectral image data. This histogram is a measure of the complexity of the image data and can be used to predict the most cost-effective and accurate procedures for registering, compressing, and classifying the image data.

Multispectral image handling and processing can be enhanced by expressing the image data in histogram format. The histogram format is obtained by extracting all of the unique vectors and their number of occurrences from a Landsat image. The image is described at each picture-element location by one number, which identifies the unique four-dimensional vector that belongs there.

Important cost reductions for most types of processing can be realized by processing each unique vector once and applying the results to the picture-element locations with a table lookup procedure. In the histogram format, one obvious way to reduce processing cost significantly is to reduce the number of unique vectors in an image and approximate an image with a reduced vector representation. Statistical results indicate that 30 to 50 percent of the unique vectors only occur once in an entire image, 12 to 16 percent occur twice, and 7 to 10 percent occur three times. By appropriately combining the vectors that occur a relatively few times with their nearest spectral neighbors, significant cost reductions can be achieved.

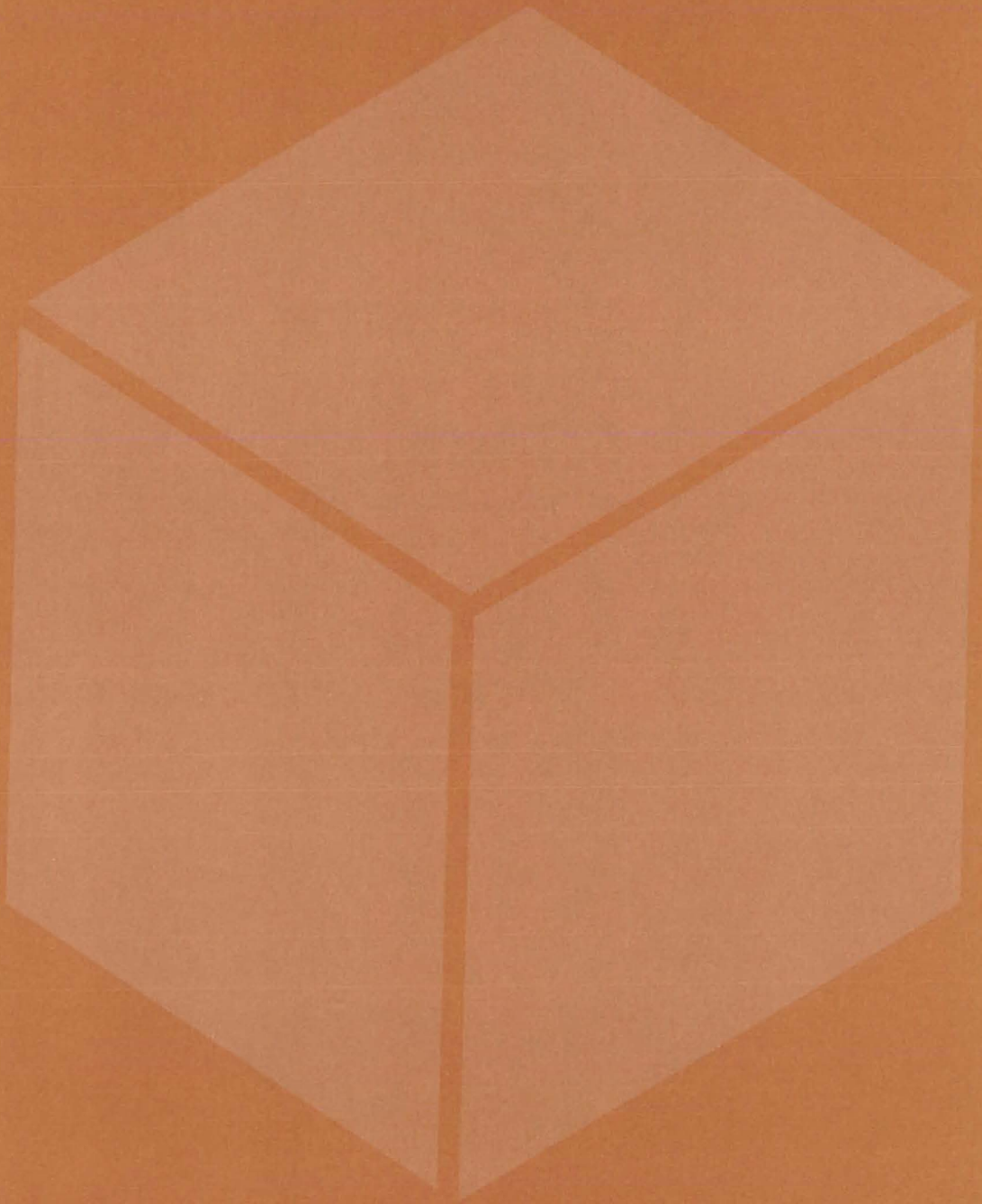
As a means for ordering the different vectors, it would be convenient if each different four-dimensional vector could be represented by a unique number for a table lookup procedure in a way that would not waste computer memory. It would be even more convenient if these single numbers could be consecutive integers starting with "1" and ending with a maximum number that can be determined from the amount of memory available.

It is not possible to assign a unique number to all of the possible unique vectors since it is not possible to count all the vectors with most computer systems. It is possible, however, to count a considerable number of different vectors if each different vector is assigned an identifier number that is "approximately unique." This "approximately-unique" identifier number is derived by means of a divisor, base, and multiplier technique. The program can handle up to 40,000 unique vectors in this manner.

This program is written in FORTRAN IV for the IBM FORTRAN H compiler and has been implemented on an IBM 360 with a central memory requirement of approximately 350K of 8-bit bytes.

This program was written by Robert R. Jayroe, Jr., of Marshall Space Flight Center. For further information, Circle B on the COSMIC Request Card.
MFS-23855

Materials



Hardware, Techniques, and Processes

- 529 Ultrafine PBI Fibers and Yarns
- 530 Measurement of Subcoat Thickness by Characteristic X-Rays
- 530 Ion-Beam-Textured Graphite
- 532 Absorptive Coating for Aluminum Solar Panels
- 532 Fire-Resistant Wood Composites
- 534 Antistatic Coating for Acrylics
- 535 Coated-Felt Thermal Insulation
- 535 Low-Temperature Refining of Coal
- 536 Accelerated Purification of Colloidal Silica Sols
- 537 Forming "Dynamic" Membranes on Stainless Steel
- 538 Deaerating High-Viscosity Silicon Rubber
- 538 High-Pressure Liquid Chromatography of Aromatic Amines
- 540 Automated Electrophoresis Apparatus
- 541 Improved Imide Polymerization Catalyst
- 542 Porous Bead Packings for Gas Chromatography
- 543 Scratch-Resistant Plastic Lenses

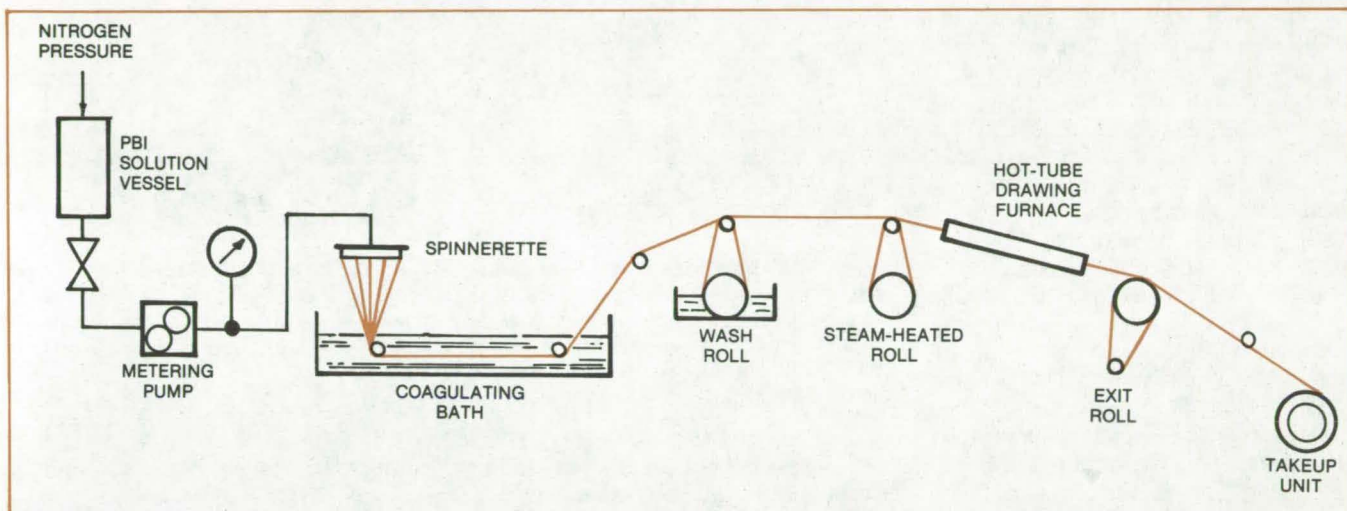
Books and Reports

- 544 Model of Silicon Production in a Fluidized-Bed Reactor

Ultrafine PBI Fibers and Yarns

A gentle, precisely controlled process draws polybenzimidazole fibers to denier as low as 0.17 per fiber.

Ames Research Center, Moffett Field, California



PBI Extrusion From a Spinnerette is coagulated, washed, dried, and drawn to form a yarn of ultra-low-denier fibers. Careful filtering is among the many precautions taken to ensure a high-quality, extremely fine product. To remove any traces of particulate matter, the PBI solution passes through a heated-candle filter and, just before it enters the spinnerette, a stainless-steel sintered-disk filter.

PBI, or polybenzimidazole, is a synthetic fiber that is nonflammable, strong, and exceptionally stable. Now, PBI fabrics also can be made extremely light in weight by a new process that produces ultra-low-denier PBI fibers. Filaments having deniers as low as 0.17 (that is, weighing 0.17 gram per 9,000 meters) can be made in five-filament yarns of 0.80 denier. In contrast, conventional PBI fibers are at least 1.5 deniers, and yarns often range from 75 to 15,000 deniers. Despite a roughly order-of-magnitude reduction in denier, the normalized physical properties of the fibers are essentially unchanged.

The new process was developed to make ultralight fabric for a solar "sail" that propels a spacecraft by the force of reflected Sunlight. It should be useful in other applications in which a lightweight textile must withstand high heat, corrosion, or radiation. For example, the solar sail must resist radiation in space and high temperatures (up to 370° C), and its area density must be low (3 grams per square meter).

The ultra-low-denier fibers are

made by the dry-jet/wet-spinning process in which they are spun and drawn on a continuous, in-line system. As shown in the figure, the PBI solution from a pressurized vessel is fed by a metering pump to a spinnerette and is extruded through five holes, each 40 nanometers in diameter. The five streams of PBI solution fall into a water bath, where they coagulate into fibers.

The spinnerette is positioned over the coagulating bath so that the extruded filaments fall a short distance and create minimum turbulence as they enter the bath. (Turbulence in conventional wet spinning, in which the filaments enter the bath horizontally, could break the ultrafine fibers.) Leaving the bath, the fibers pass over wash rollers that remove any residual solvent and over steam-heated rollers that dry the fibers.

The five-fiber yarn passes through a drawing furnace at a temperature of from 400° to 500° C, where the combination of heat and tension on the yarn elongates the fibers. In this stage, the polymer structure becomes better organized, and the physical

properties of the yarn are developed. The drawn yarn is taken up on a winder, the speed of which can be regulated to minimize takeup tension. This permits longer periods of continuous operation without breaking the ultrafine fibers.

The most critical element in the process is the drawing ratio in the hot drawing furnace. The relative speeds of the entrance and exit rollers are precisely controlled to ensure that the fibers are drawn to the proper thinness and yet do not lose their strength.

This work was done by Joseph R. Leal and Marshall Tan of Celanese Research Corp. for Ames Research Center. Further information may be found in NASA CR-152057 [N78-16189], "Ultralow Denier Polybenzimidazole [PBI] Yarns," a copy of which may be obtained at cost from the Western Research Application Center [see page A7].

Title to this invention has been waived under the provisions of the National Aeronautics and Space Act [42 U.S.C. 2457 (f)], to the Celanese Research Corp., P. O. Box 1000, Summit, NJ 07901. ARC-11221

Measurement of Subcoat Thickness by Characteristic X-Rays

X-ray scanning system depicts layer structure on video screen within seconds.

Lyndon B. Johnson Space Center, Houston, Texas

The identification of topcoat and subcoat boundaries has been a source of difficulty in inspection of the NASA Space Shuttle heat shield: Once the double-coated ceramic material of the shield is sintered, the final thickness of the layers is no longer measurable by conventional scanning electron microscopy or photomacrography.

A recent technique for determining the thickness of each coat should also be useful for quality control of other ceramics. The ceramic layers are measured by analyzing X-rays emitted upon electron bombardment. The difference in components of the two layers results in a difference in the wavelength of the emitted X-rays.

The equipment utilized in the system includes a microprobe analyzer that identifies a ceramic layer from the wavelengths of the X-rays it emits when excited by a thin beam of electrons. X-rays are detected by a spectrometer having a crystal of known wavelength and a mechanism for moving both the crystal and a

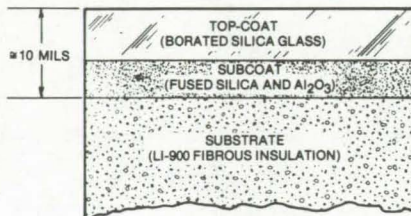


Figure 1. The **Cross Section of Material** in the NASA heat shield shows the relative thicknesses of the layers. Note that the subcoat contains aluminum in the form of Al_2O_3 , which can be scanned by the X-ray analysis system.

phototube over a range of Bragg angles. The sample is scanned in a raster pattern, and within seconds the image appears on a cathode-ray tube for viewing or photographing.

Figure 1 shows the cross section of the silica-based coating applied to tiles on the Space Shuttle. Both the topcoat and the subcoat are primarily SiO_2 , but the subcoat also contains 2.5 percent Al_2O_3 . Therefore the



Figure 2. This **CRT Display** photograph shows the subcoat thickness. Relatively small quantities of the aluminum can be detected and analyzed with this system.

detection system was adjusted to search for the aluminum. A typical photograph demonstrating the subcoat/substrate boundary is shown in Figure 2.

This work was done by W. J. Harris and R. A. Quinn of Lockheed Missiles & Space Co., Inc. for Johnson Space Center. No further documentation is available.
MSC-16718

Ion-Beam-Textured Graphite

A low secondary-electron emitting surface for depressed collectors in microwave amplifiers

Lewis Research Center, Cleveland, Ohio

Seven different materials (copper, tantalum, titanium carbide, beryllium, soot, smooth pyrolytic graphite, and ion-beam-textured graphite) were evaluated to determine which material had the lowest secondary-electron emission

The attainment of highest possible efficiencies from multistage depressed collectors for microwave amplifiers requires the use of electrodes with low secondary-electron yield surfaces. Coating copper electrodes with (low-yield) soot improves the collector efficiency by 2 to 4 percentage points. Since soot is not a practical solution to this problem

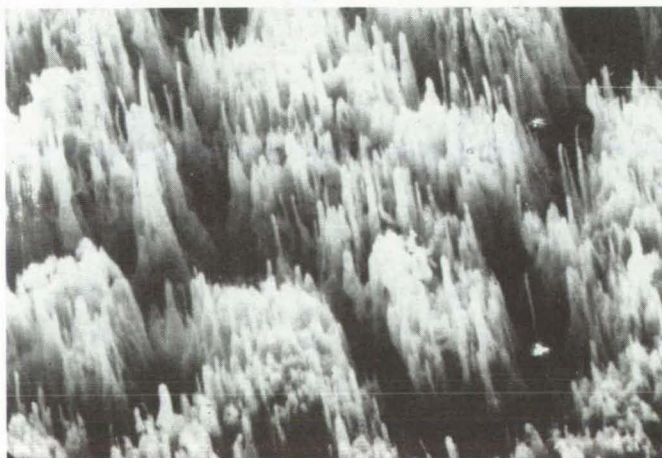


Figure 1. **Ion-Beam-Textured Pyrolytic Graphite**, shown magnified 1,000 times, has a needlelike, or spired, surface texture.

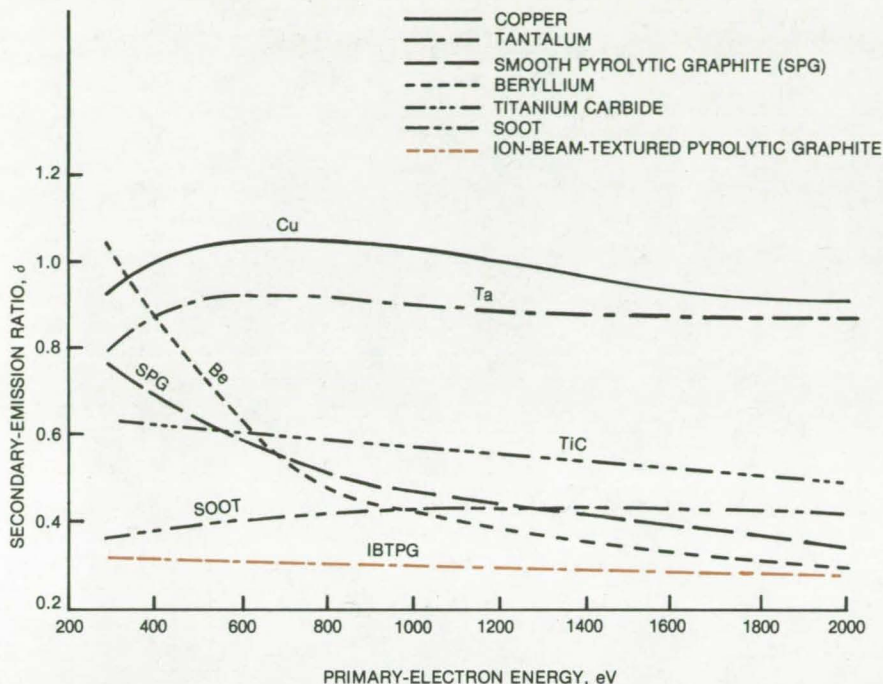


Figure 2. **Secondary-Emission Ratio** is shown as a function of primary-electron energy for beryllium, copper, pyrolytic graphite, soot, titanium carbide, and tantalum surfaces in range 300 to 2,000 eV.

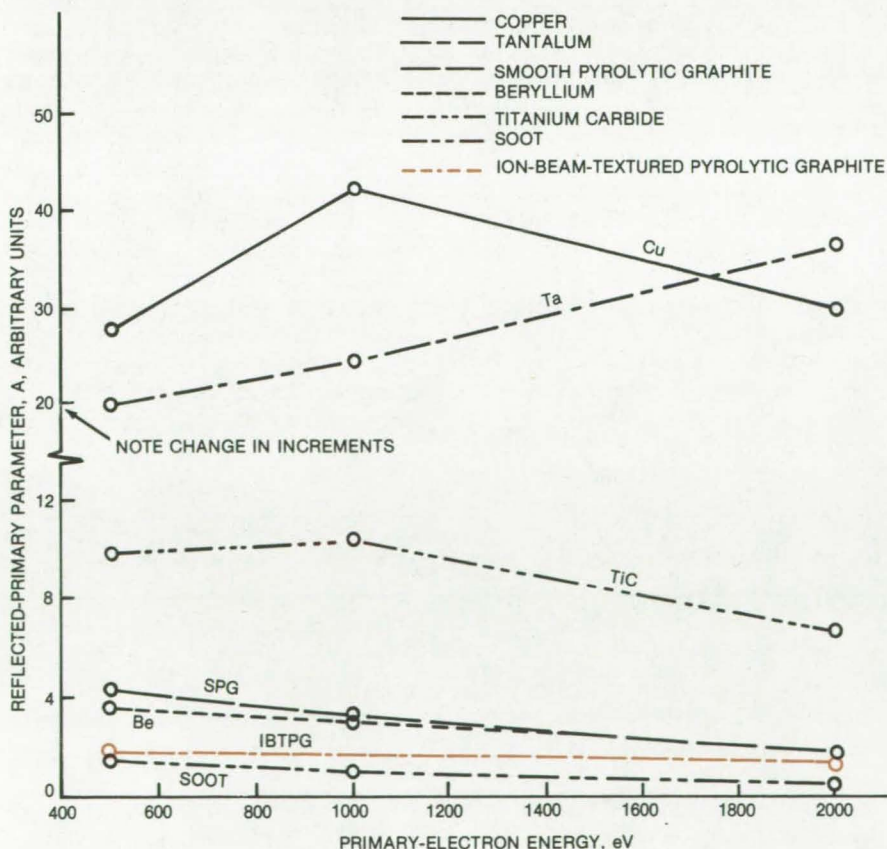


Figure 3. **Reflected-Primary Parameter A** is shown as a function of primary-electron energy for beryllium, copper, pyrolytic graphite, soot, titanium carbide, and tantalum surfaces in range 500 to 2,000 eV.

because of its poor adhesion properties, alternate electron collector materials were evaluated to ascertain secondary-electron ratios as well as reflected-primary-electron characteristics.

It is well known that carbon exhibits a very low secondary-electron yield. Further, electrode roughness also inhibits secondary-electron emissions. An electrode with these desirable qualities may be processed by ion-beam-texturing pyrolytic graphite, which also exhibits exceptional strength and is easily machined. The textured surface was obtained by exposing the pyrolytic graphite to a 1-keV argon ion beam. Suitable surface structure may be obtained with ion doses ranging from 0.004 to 0.03 A-h/cm². Figure 1 shows the resulting needle or spire surface structure.

Of all the materials evaluated, ion-beam-textured pyrolytic graphite has the lowest secondary emission ratio as well as an extremely-low reflected-primary-electron yield when compared to copper, tantalum, titanium carbide, beryllium, and smooth pyrolytic graphite (Figures 2 and 3). The data for beryllium, graphite, copper, and tantalum were obtained from degassed, ion-cleaned surfaces. The secondary-electron yield for pyrolytic graphite, however, is relatively insensitive to surface impurity effects. This is not the case with materials such as copper or beryllium.

The results indicate that ion-beam-textured pyrolytic graphite shows the greatest potential for use as a depressed collector for high-efficiency microwave amplifiers.

This work was done by Arthur N. Curren, Ralph Forman, and James S. Sovey of **Lewis Research Center** and Wayne R. Hudson of NASA Headquarters. Further information may be found in NASA TP 1097 [N78-11230], "Secondary-Electron-Emission Properties of Conducting Surfaces with Application to Multistage Depressed Collectors for Microwave Amplifiers," a copy of which may be obtained at cost from the New England Research Application Center [see page A7]. LEW-12724

Absorptive Coating for Aluminum Solar Panels

A layer of copper oxide, formed by etching high-copper aluminum in a strong base, is an inexpensive surface for collecting heat from the Sun.

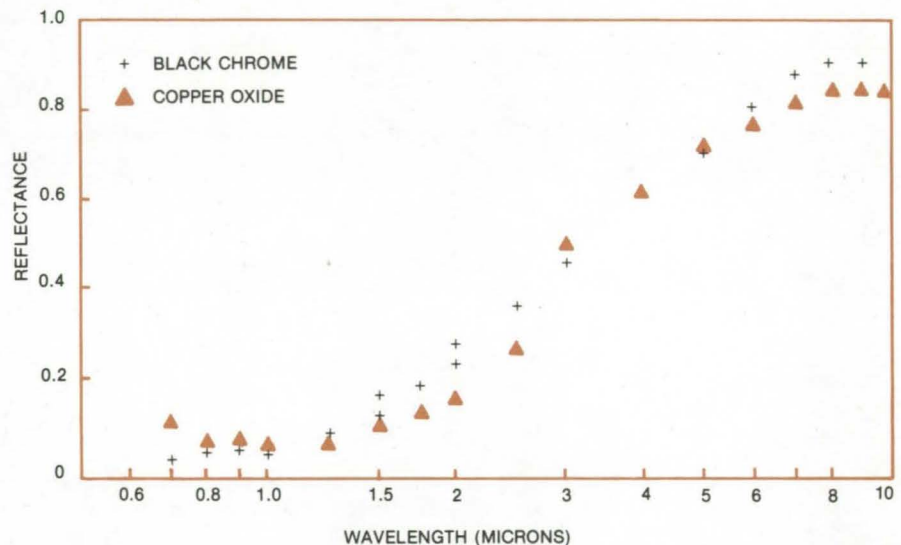
Marshall Space Flight Center, Alabama

In most ways, aluminum is an ideal choice as the material for solar-heat collector panels: The metal is widely available, inexpensive, easily formed, strong, and durable. Because it is highly reflective, however, aluminum needs a coating of a light-absorbing material to function effectively in such applications as space heating and water heating.

Now, a method has been developed for forming an absorptive coating from the copper component of an aluminum/copper alloy. The coating consists of copper oxide and has solar absorption characteristics similar to those of the best previously available coating, black chrome (see figure). The copper oxide coating, however, is much simpler and less costly to produce.

Sheet aluminum alloy with high copper content (6 percent or more) is used as the starting material. One surface of the sheet is etched in sodium hydroxide solution, and a matrix of small copper oxide granules forms on the surface. If the aluminum sheet has been previously tempered (2219-T87 aluminum alloy, for example), the copper oxide forms as a coherent (i.e., continuous, nongrainy) layer. Whether grainy or coherent, the layer adheres strongly to its aluminum substrate.

The copper oxide layer selectively absorbs the solar wavelengths with the



A Copper Oxide Layer on aluminum reflects little (and absorbs much) of the Sun's energy at wavelengths between 0.5 and 2 microns — wavelengths that have most of the heat content. Black chrome has similar absorption characteristics, but cannot be formed directly on aluminum; a layer of copper must first be applied to the aluminum.

greatest heat content (visible and infrared wavelengths) and therefore collects heat efficiently. The copper oxide is unaffected by high heat and humidity and hence is well suited to outdoor use.

The oxide coating is actually a form of "smut" — a hard-to-remove oxide of the constituents of an alloy that remains after the alloy has been chemically etched. Smut has long

been a nuisance in alloy processing operations, but in the case of aluminum solar collectors is turned to good advantage.

This work was done by Donald De Smet, Andrew Jason, and Albert Parr of the University of Alabama for Marshall Space Flight Center. For further information, Circle 47 on the TSP Request Card.
MFS-25033

Fire-Resistant Wood Composites

A modified resin binder makes wood composite more fire-resistant.

Ames Research Center, Moffett Field, California

Modified novolak resins, which are used in binding wood flour, sawdust, chips, and fibers, improve fire resistance of pressed wood products. These wood compositions are common in the building industry. The resin selected is mixed with the wood

particles, which are then shaped and cured by applying heat and pressure. Wood panels made with the modified resin have a burnthrough time of 450 s as compared to 280 s for products using conventional novolak resin. By incorporating an inorganic filler, such

as ammonium phosphate or its mixture with ammonium oxalate, into the resin, the flame spread index of panels is reduced from more than 200 to 60 or 70.

The modified resins are novolak-type polymers prepared by the reac-

tion of an aralkyl ether of the general formula $R'[-(CH_2OR)]_a$ and/or an aralkyl halide of the general formula $R''[-(CH_2X)]_a$ with an excess of a phenolic compound or a phenolic compound and a compound containing aromatic nuclei. Radical R' is a divalent or trivalent aromatic hydrocarbon or hydrocarboxy radical; R'' is a divalent or trivalent aromatic hydrocarbon radical. Both R' and R'' can contain inert substituents in the aromatic nucleus. Radical R is an alkyl radical containing less than six carbon atoms; X is chlorine, bromine, or iodine; and a has a value of 2 or 3.

As phenolic compound, any compound or mixture of compounds derived from benzene and containing preferably one or two, hydroxyl radicals attached to the aromatic nucleus may be used. Not more than three substituents may be attached to carbon atoms in the benzene nucleus. Specific compounds fitting these descriptions are p-xylylene dichloride, p-xylyleneglycoldimethylether, phenol, p-cresol, resorcinol, cathecol, and the like.

The reaction between the aralkyl compound and the phenol to form a prepolymer is carried out in the presence of a Friedel-Crafts-type catalyst, stannic chloride being most preferred. The prepolymer is then cured by heating to a temperature between 100° and 200° C or higher, using a hardening agent such as hexamethylene tetramine.

Prior to application, the resin and inorganic filler selected are dissolved and suspended in a carrier liquid at a viscosity that can be sprayed onto the wood particles. In the fabrication of, for example, oriented-strand boards, the dried strands are sprayed. Then they are air-filtered and alined in successive 90° layers to form a mat. A mat with several layers is prepressed and then formed into a panel of desired thickness or density on a

Panels and Properties			
Materials ^a	Thickness (mm)	Burnthrough Time (s)	Flame Spread Index
1 625 g Wood Strands ^b 150 g Phenolic Resin ^c 50 g Water	9.72	287	>200
2 700 g Wood Strands 145 g Xylok Resin ^d 50 g Isopropanol	9.72	422	--
3 As in Example 2 Plus 29 g NH ₄ Oxalate ^e	9.72	464	>200
4 As in Example 2 Plus 30 g NH ₄ Phosphate ^e	9.72	--	70
5 175 g Wood Strands 109 g Xylok Resin 38 g Isopropanol Plus (added to one surface layer) 36 g Xylok Resin, 40 g Isopropanol, 42 g NH ₄ Oxalate, and 42 g NH ₄ Phosphate ^f	10.06	588	60

a Mixtures of materials spread in three layers of oriented strands and formed into 337- by 337-mm panels

b Douglas fir strands

c Standard commercial novolak resin having 50 percent solids

d Propolymer of p-cresol with 1,4-dimethoxymethylbenzene, mixed with hexamethylene tetramine, as in example 1 of patent 3,576,788

e Ammonium salt present throughout panel

f Ammonium salts in top surface layer only

Fire Resistance of Differently-Treated Wood Products

hot press, with simultaneous heat-curing of the adhesive. The finished panel is removed to an air cooler and then to a trimming station, followed by a finishing station for sounding, painting, and the like.

While they are being sprayed, the strands are also fluffed continuously in a blender. The quantities of the binder and inorganic filler applied may vary in different layers of strands. However, when inorganic fillers are used, they are usually placed in layers at the surface of the panel. The quantity of the resins used constitutes 10 to 20 percent of the total weight of composite panels.

The accompanying table illustrates changes in burnthrough time and in flame spread index for five examples.

The contrast is quite evident between the examples using the earlier novolak resin formulation and the modified one. All of the panels except in example 1 had been hot-pressed for 75 min at 174° C. In example 1 this time is 10 min at a temperature of 165° C.

This work was done by Paul M. Sawko of Ames Research Center. For further information, Circle 48 on the TSP Request Card.

This invention is owned by NASA, and a patent application has been filed. Inquiries concerning nonexclusive or exclusive license for its commercial development should be addressed to the Patent Counsel, Ames Research Center [see page A8]. Refer to ARC-11174.

Antistatic Coating for Acrylics

Treatment with selected low-molecular-weight solvents helps dissipate electric charge on clear plastics.

NASA's Jet Propulsion Laboratory, Pasadena, California

Clear acrylic plastics, such as polymethyl methacrylate (PMM), can be made antistatic without degrading their optical properties. After immersion in a solvent such as acetonitrile, the acrylics dissipate 50 to 70 percent of an induced electric charge within 1 minute, yet they retain their optical clarity. The antistatic properties remain even after the treated plastic has been washed, rubbed, and exposed to vacuum.

The treatment solves persistent problems associated with charge buildup on PMM plastics used in commercial applications. In aircraft, for example, prolonged and repeated charge accumulations have caused windows made of PMM to fracture; and in hospitals, electronic equipment cases and covers made of PMM have been a fire hazard, especially when the equipment is used near oxygen supply lines.

Various solvents were studied as possible antistatic agents for PMM (see table). Only acetonitrile and nitromethane, however, were found to dissipate static charge without destroying the optical clarity of the plastic. It is conjectured that the low molecular weight of these solvents allows them to penetrate the acrylic ester matrix, so that they cannot be removed easily from the plastic. The electrochemical properties of the absorbed solvent (high electron affinity, large dipole moment, and polarizability) probably help to screen intermolecular potential barriers between PMM molecules, allowing

Solvent	Dissipation of Static Charge	Optical Clarity
acetonitrile	yes	good
nitromethane	yes	good
propanol	no	good
dimethyl sulfoxide	yes	bad
benzene	no	bad
ethyl acetate	no	bad
ethylene glycol	no	fair
acrylonitrile	no	bad

Comparison of Measured Antistatic Optical Properties of treated polymethacrylate, using various solvents, as described in the text

charge to flow more readily.

The solvent can be applied by dipping, brushing, spraying, or immersion. Immersion gives the clearest finished product. The solvent should be at a temperature in the range of 10° to 30° C. After immersion for a period of between 5 and 30 minutes, the plastic absorbs about 0.1 percent by weight of the solvent.

Alternatively, the solvent can be applied in a viscous mixture of monomeric methyl methacrylate and PMM as a 3- to 5-mil layer on a PMM sheet. When the layer has been polymerized by exposure to mercury-arc light, it forms a clear, antistatic coating.

The antistatic properties of the various solvents listed in the table were determined by measuring static charge dissipation in an environment with known humidity, using a high-

impedance electrometer. Static charge was induced by rubbing the surface with fresh wool. Ultraviolet, visible, and infrared spectra were measured to find the effect of the solvents on the optical properties. The amounts of solvent absorbed were found by spectrometry and vapor pressure measurements.

This work was done by Vaclav Hadek, Alan Rembaum, and Robert B. Somoano of Caltech for NASA's Jet Propulsion Laboratory. For further information, Circle 49 on the TSP Request Card.

This invention has been patented by NASA [U.S. Patent No. 4,061,834]. Inquiries concerning nonexclusive or exclusive license for its commercial development should be addressed to the Patent Counsel, NASA Resident Legal Office-JPL [see page A8]. Refer to NPO-13867.

Coated-Felt Thermal Insulation

Thin, flexible, lightweight insulation
tile for temperatures below 700° F

Lyndon B. Johnson Space Center, Houston, Texas

A thin coated-felt insulation tile has been shown to be a lighter and easier-to-install replacement for silica tiles. During the design of NASA's Space Shuttle Orbiter, the felt insulation was developed as a potential replacement for low-temperature reusable surface insulation (LRSI) made of silica.

At temperatures under 700° F (370° C), silica tiles of the minimum durable thickness (about 0.5 cm) would overprotect the Orbiter, thereby adding unnecessary weight. The felt tiles could not only be made thinner and lighter but could be applied in larger sheets (1 by 2 meters) to save time, and they are flexible to accommodate buckling and conform to curved surfaces.

The felt is a commercially-available modified nylon-fiber material. For use

as insulation, it is pretreated and coated. The pretreatment is exposure to 750° F (400° C) to prevent adverse shrinkage during service. The felt is heated in five incremental steps to drive off volatiles that might otherwise burn in the presence of oxygen.

For application as a reusable insulation tile, the felt must be coated to prevent charring, to waterproof it, and to give it the needed optical (thermal) properties. An elastomeric silicone, pigmented with TiO₂, meets these requirements, giving the tile a solar absorptance-to-emittance ratio less than 0.4, and also imparts a relatively-smooth aerodynamic surface. The coating is applied and allowed to cure at room temperature (with a 15-minute postcure at 650° F/345° C).

The felt thickness can be from 0.16 to 0.4 in. (0.4 to 1 cm) as dictated by the local structural heat sink, the expected maximum heat load, and other considerations. It can be applied to the surface to be insulated with a room-temperature-vulcanizing adhesive.

This work was done by Robert L. Dotts, Robert J. Maraia, James A. Smith, Ivan K. Spiker, and George Strouhal of Johnson Space Center. For further information, Circle 50 on the TSP Request Card.

This invention is owned by NASA, and a patent application has been filed. Inquiries concerning nonexclusive or exclusive license for its commercial development should be addressed to the Patent Counsel, Johnson Space Center [see page A8]. Refer to MSC-12737.

Low-Temperature Refining of Coal

Laboratory-tested process promises
economical removal of sulfur and ash.

NASA's Jet Propulsion Laboratory, Pasadena, California

Recent laboratory experiments have demonstrated the technical feasibility of a new low-temperature chemical pretreatment of raw coal that yields a purified product with low sulfur, oxygen, and inorganic ash content. The purified coal would be the desirable starting material for gasification or liquefaction processes. It is estimated that any increases in processing time or costs as a result of the pretreatment would be more than offset by the improved efficiency of the subsequent conversion.

The new process is an extension of the one reported on page 199 of *NASA Tech Briefs*, Vol. 2, No. 2, "Low-Temperature Coal Desulfurization" (NPO-13937), in which coal powder is

oxidized by chlorinolysis, leached with water, and then recovered in a dechlorination step. In the new process, a solvent-refining step is added following an initial mild oxidation treatment (such as chlorination), with the result that the end product has a low ash content. No effective treatment for removing ash had been demonstrated in the earlier process.

The process, as outlined in the illustration, is initiated as the coal structure is loosened up through low-temperature oxidation. This step — penetration of solvent into the coal matrix — also modifies the coal solubility parameter so that it can be dissolved by proper solvents at a relatively low temperature and at

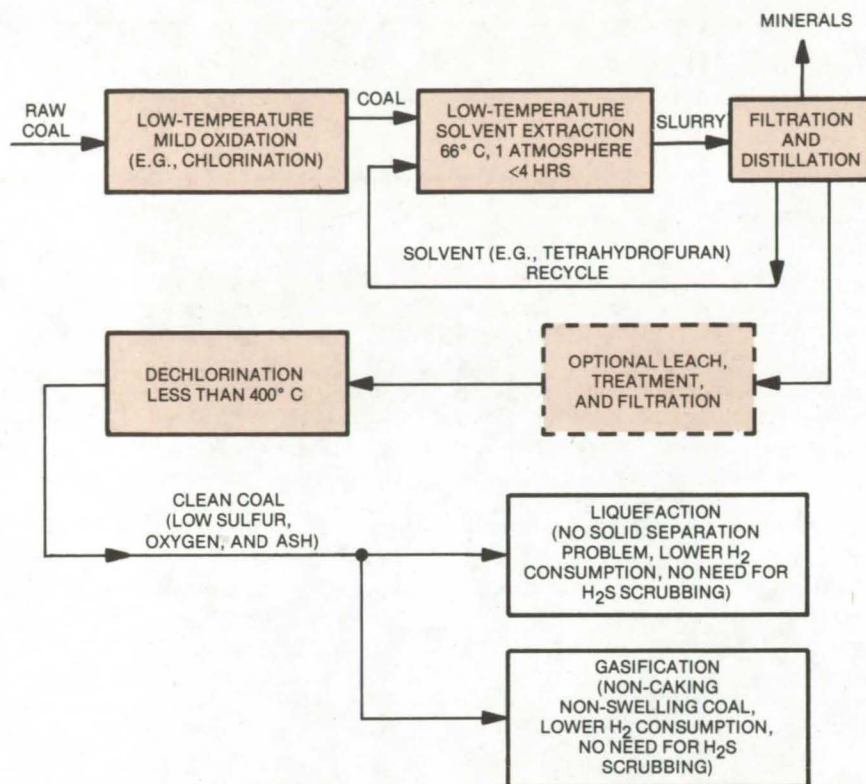
atmospheric pressure.

The chemically treated coal is extracted with a common solvent such as tetrahydrofuran (THF) at 66° C and atmospheric pressure for less than 4 hours. The THF is an effective solvent at these low temperatures and is easily removed and recovered. Other organic solvents may also be suitable.

The resulting slurry is filtered to remove undissolved mineral matter and is then distilled to recover the THF solvent for recycling. The solid, after extraction, filtration, and distillation (or evaporation), contains most of the organic matter and 20 percent of the original mineral content. It is

(continued on next page)





An **Efficient Coal-Refining Pretreatment** yields coal with low sulfur, oxygen, and ash content. The process features energy-saving low-temperature steps and recyclable solvent. Pretreated coal reduces hydrogen consumption in subsequent liquefaction or gasification and eliminates costly H₂S scrubbing in gasification and liquefaction. It also alleviates the need for flue-gas desulfurization when burning the coal.

leached with water at 60° C and is then dechlorinated by heating up to around 400° to 500° C for about an hour. The final product retains only a small amount of residual chlorine (less than 0.3 percent), contains very little sulfur with essentially no inorganic sulfur, and is expected to be noncaking and nonswelling.

The economical features of the process are its use of relatively low temperatures and recyclable solvent. Further cost savings are realized in subsequent coal gasification or liquefaction. In both processes there is reduced hydrogen consumption due to the cleaner coal. An earlier problem of solid separation during coal liquefaction is eliminated due to the low ash content of the pretreated coal. Finally, a costly step of scrubbing in coal gasification and liquefaction to remove H₂S is also avoided.

This work was done by Partha S. Ganguli and George C. Hsu of Caltech for **NASA's Jet Propulsion Laboratory**. For further information, Circle 51 on the TSP Request Card. NPO-14210

Accelerated Purification of Colloidal Silica Sols

A heat/deionization scheme sharply reduces the time required to purify silica sols.

Lyndon B. Johnson Space Center, Houston, Texas

In an accelerated purification process for colloidal silica sols, the waiting time between deionization cycles is reduced from several months to a few days. The process produces the same high-purity silica sol as the previous, more time-consuming method. The key to the new technique is the use of elevated temperatures to accelerate the removal of Na⁺ ions following the first deionization.

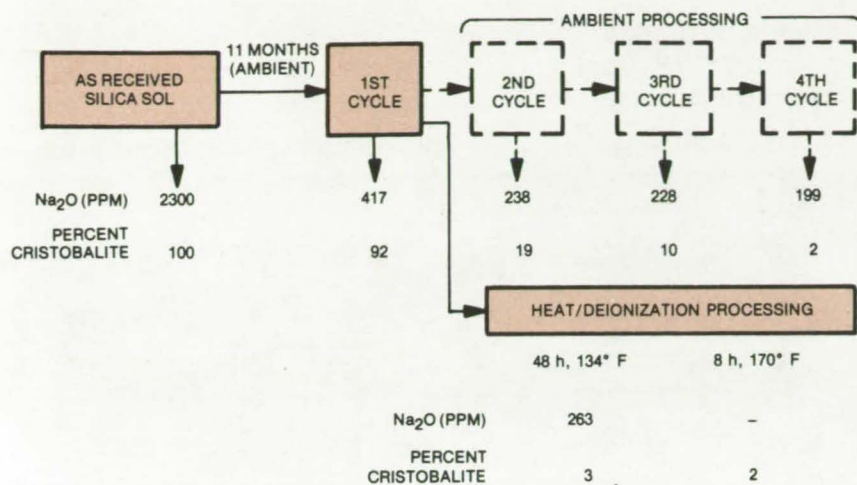
High-purity silica sol is a binder for pure silica fibers in reusable surface insulation. The sol must retain its amorphous structure if the insulation is to be stable at high temperatures. A major contaminant and destabilizing factor is sodium, which is used in the

processing of colloidal sols. It is derived either from sodium silicate or from high-pressure/high-temperature processing in which NaOH prevents gelation. At high temperatures, the sodium devitrifies the structure into crystalline phases, such as cristobalite, degrading the cohesiveness of the binder.

The objective of the purification process is to reduce the Na₂O content from around 2,300 ppm to a purified level of less than 300 ppm. In the conventional approach, a quantity of sol is treated by column deionization to remove Na⁺ by ion exchange. This is followed by a 30-day storage at ambient temperatures to allow resid-

ual Na⁺ to migrate to the surface of the silica particles. The process is repeated in three additional ionization cycles requiring 30-day intervals between each.

The new process was developed after a series of experiments. The first approach — heating the product prior to the first deionization — showed no improvements. Significant improvement, however, did occur when heat was applied following the first deionization cycle, and the particle diameters were about 15 μm. The purified sol was obtained after about 48 hours at 134° F (57° C) and in 8 hours at 170° F (77° C). Moreover, ion-exchange resin deionization with the



A Comparison of Conventional and New Purification Processes for Colloidal Silica Sols is shown here. The particle diameter of silica is about 15 μm . The Na_2O -ppm content is based on ignited weight, and the percent of cristobalite formed after 4 hours at 2,300° F (1,260° C) indicates the stability of the product at elevated temperatures.

sol at elevated temperatures further reduced purification times to 3 hours at 170° F. The new process and results are compared with the previous method in the figure.

Other alternatives have also been examined. One, for example, involves growing the colloidal particles from parent silica acid stabilized with an amine rather than the NaOH . This process, however, is limited to particle sizes of only about 4 μm . Another ion-exchange process, using a recycling, pressurized heating system to build up sols with 15- to 150- μm particle sizes, does not meet the high-purity standard but is of interest in particle-growing systems evolving colloidal silica solutions.

This work was done by E. Bahnsen, S. Garofalini, and A. Pechman of Lockheed Missiles & Space Co., Inc., for **Johnson Space Center**. No further documentation is available. MSC-16793

Forming "Dynamic" Membranes on Stainless Steel

Nitrate chemistry is used in the formation of quality zirconium oxide-polyacrylic acid membranes.

Lyndon B. Johnson Space Center, Houston, Texas

"Dynamic" membranes of zirconium-polyacrylic acid (PAA) on the surfaces of porous substrates can remove contaminating chemicals from solutions by reverse osmosis. Reverse osmosis membranes have been used for filtration and desalination equipment, and they have potential applications in the textile industry for separating dyes from their aqueous solvents.

Methods for depositing the dual layer dynamic membranes on porous ceramic supports, using chloride chemistry, are well established, but until now, it has not been possible to form them on stainless steel without severely corroding the steel in the process. Nonetheless, stainless steel is attractive as a substrate because of its durability.

Recently, quality zirconium oxide-PAA membranes have been made directly on stainless-steel substrates, using a dilute aqueous solution of sodium nitrate and zirconium nitrate. The solution is circulated through a porous stainless-steel tube.

A water solution of 0.01 to 0.05 molar sodium nitrate and about 0.04 g/l of zirconium nitrate (at a pH of about 4) is circulated through a porous stainless-steel tube having pore ratings (based on absolute particle retention) of 0.2 to 10 microns. An inert "filter aid", such as powdered carbon, may be included in the process.

After a period of time ranging from a few seconds to several hours, depending on the pressure, flow through the tube pores diminishes to an average rate of from 10^{-4} to 5×10^{-3} m/s at an applied pressure of 4×10^6 to 7×10^6 N/m², and the electrical conductivity of the throughflow becomes 4 to 40 percent lower than the feed-flow conductivity. These changes indicate that the zirconium oxide membrane has been formed.

Nitric acid then is added to the solution to reduce the pH to 2. Also, 50 ppm of polyacrylic acid are added. The pH is then slowly raised to neutral by adding sodium hydroxide, at which time the procedure is complete.

The electrical conductivity of the throughflow (filtrate) is typically 5 to 10 percent of the conductivity of the feed solution. The throughflow velocity normally ranges from 3×10^{-5} to 5×10^{-5} m/s.

It is important that sintered-powder technology be used in fabricating the stainless-steel tubes. Stainless-steel powder is compacted and sintered into a strong, porous tubular substrate. Tube porosity is controlled by the powder size, initial compaction, and sintering conditions. Substrate configurations other than tubes can also be used.

This work was done by C. A. Brandon and J. L. Gaddis of Clemson University for **Johnson Space Center**. No further documentation is available.

Inquiries concerning rights for the commercial use of this invention should be addressed to the Patent Counsel, Johnson Space Center [see page A8]. Refer to MSC-18172.

Deaerating High-Viscosity Silicone Rubber

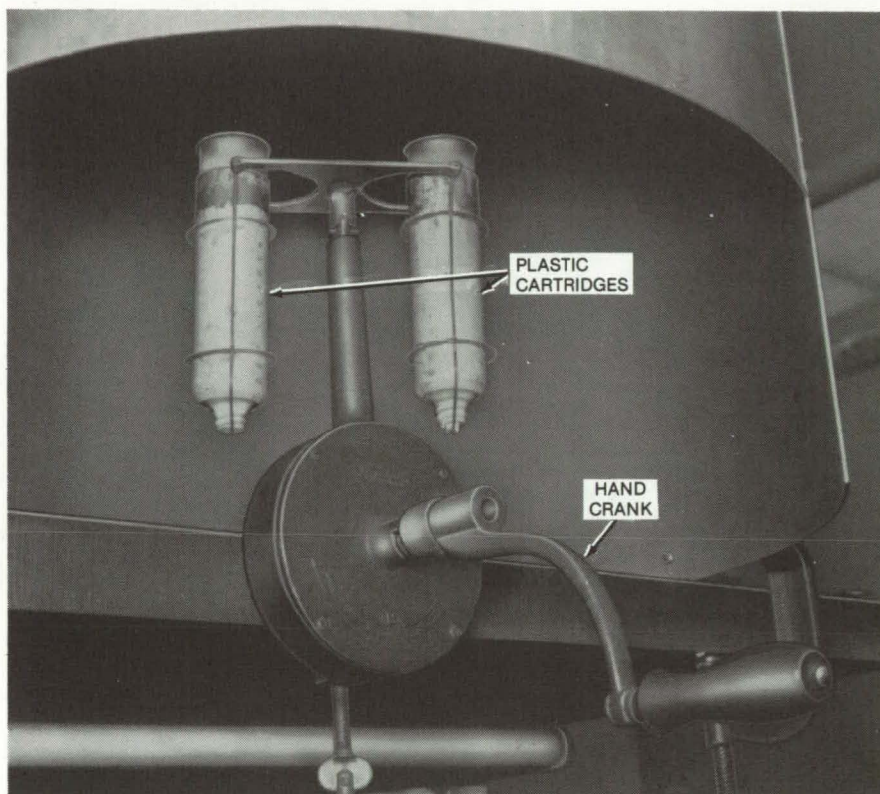
Low-cost method produces void-free silicone-rubber seals.

Lyndon B. Johnson Space Center, Houston, Texas

Conventional methods of producing seals and other molded silicone-rubber parts often include a vacuum deaeration step to remove air from the rubber before molding. Air is trapped when the rubber is measured, catalyzed, mixed, and transferred to plastic cartridges for injection into molds. Unfortunately, vacuum deaeration does not always adequately deaerate the high-viscosity silicone, and molded parts must often be rejected due to residual air inside the rubber.

This problem is eliminated by centrifuging the rubber after vacuum deaeration. An inexpensive hand-operated centrifuge can be modified to accept the plastic cartridges (see figure). A mixed, high-viscosity (6,000-poise) silicone rubber is pushed into the cartridges and vacuum-degassed for several minutes. Then the cartridges are placed in the centrifuge holders and are centrifuged to eliminate any remaining air.

Centrifuging draws most of the silicone rubber to the bottom of the cartridge with only a thin layer of silicone on the inner cartridge wall. A quick check of the centrifuged rubber shows that it does not have the bubbly surface that it normally has after vacuum deaeration. The cartridges are then inserted into a pressure gun that applies positive air pressure to



A Modified Hand-Operated Centrifuge aids in deaerating high-viscosity silicone rubber. The rubber is contained in plastic cartridges that will later be used in injection molding.

inject the rubber into molds.

This work was done by Richard W. Gabriel of Rockwell International

Corp. for Johnson Space Center. No further documentation is available. MSC-16694

High-Pressure Liquid Chromatography of Aromatic Amines

Techniques developed for analysis of mono-, di-, and tri-amines

Langley Research Center, Hampton, Virginia

The high-pressure liquid chromatographic conditions for the separation of approximately 50 aromatic amines have been demonstrated. The types of amines studied ranged from simple aniline derivatives to complex multiring

di- and tri-amines. These analyses were made on a commercially-available liquid chromatograph equipped with a valve-loop injector, a 6,000-psi pump, and a 254-nm ultraviolet detector. Chromatographic amine sepa-

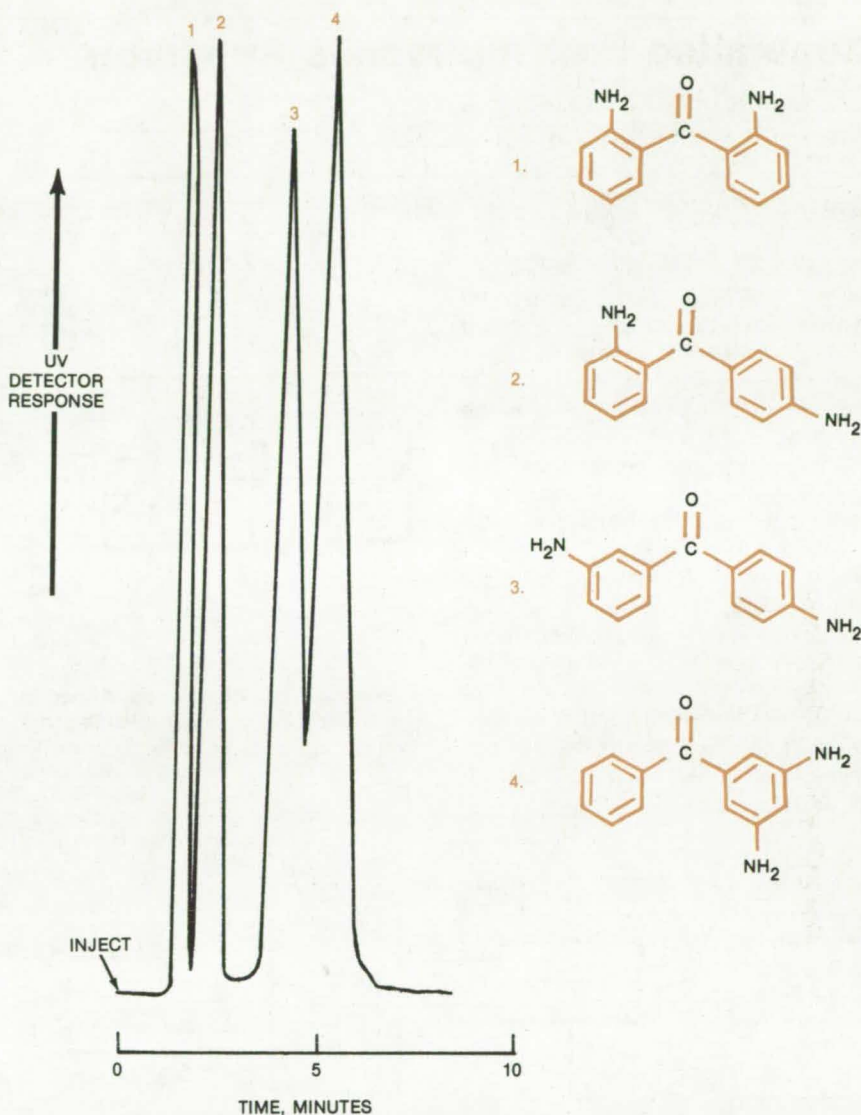
rations were previously limited to primarily thin-layer, ion-exchange, or gas-chromatographic analyses of aliphatic amines. HPLC has been used in only a few cases to separate aromatic amines. This technique offers speed, the poten-

tial for sample scaleup, and a stable environment for analysis of these reactive species.

Many of the chemicals controlled by the second emergency standard issued by the Occupational Safety and Health Administration are aromatic amines. Classically important in the dye industry, the physiological activity of these compounds makes them of interest to the biomedical field. Furthermore, in the field of polymer chemistry, isomeric aromatic diamines have become increasingly important in studying the effects of chemical structure on the properties of polyimides, polyamides, epoxies, and urethanes. They are valuable chemicals in many areas of industry and research. As interest in this class of compounds expands, their separation and analysis become more important.

The figure shows the HPLC chromatogram obtained at room temperature for a synthetic mixture of four isomeric aromatic amines. It demonstrates the special ability of this technique to separate complex amine mixtures. Impurities as low as 0.1 percent were easily detected. Satisfactory separations were obtained using various silica gel adsorbents with chloroform and/or cyclohexane mobile phases. The chromatographic conditions that led to a satisfactory separation in a reasonable time were determined by changing the polarity of the mobile phase for one of the adsorbents and then, when necessary, repeating the process using an adsorbent of higher or lower surface area as appropriate. Thus, both mobile-phase polarity and adsorbent surface area as well as adsorbent type were considered in optimizing a separation.

The primary separation mechanism for these compounds was found to depend upon an interaction between the basic amino group and the slightly-acidic silica adsorbent. In most cases, this interaction was related to the base strength of the amine. A linear correla-



Chromatogram of Aromatic Diamine Isomer Mixture was obtained using a column of Corasil II, a mobile phase of chloroform, and a flow rate of 1.5 ml/min at a pressure of 625 psi. The sample size was 3 μ l (1 μ g/ μ l), the temperature was 25° C, and the detector wavelength was 254 nm.

tion between amine basicity and chromatographic behavior was established for several series of similar amines. The general conditions developed in this study should apply to the separation of a wide variety of aromatic amines as long as the amino

group plays a major role in the adsorption process.

This work was done by Philip R. Young of **Langley Research Center**. For further information, Circle 52 on the TSP Request Card. LAR-12163

Automated Electrophoresis Apparatus

Greatly-increased sampling rate
improves analysis of particle motion.

Marshall Space Flight Center, Alabama

Manual electrophoresis techniques used to measure the velocity of charged particles such as blood cells have long faced limitations in speed and accuracy. In addition, manual measurements could not follow the individual motions of particles.

A new computer-controlled electro-optical system tracks particles in essentially real-time, analyzes data, and presents video and hard-copy results. The computer controls particle-image recognition, image acquisition and tracking, optical-focus chamber voltage, and water-bath temperature.

The two major interactive components of the system are the electrophoresis chamber and microscope

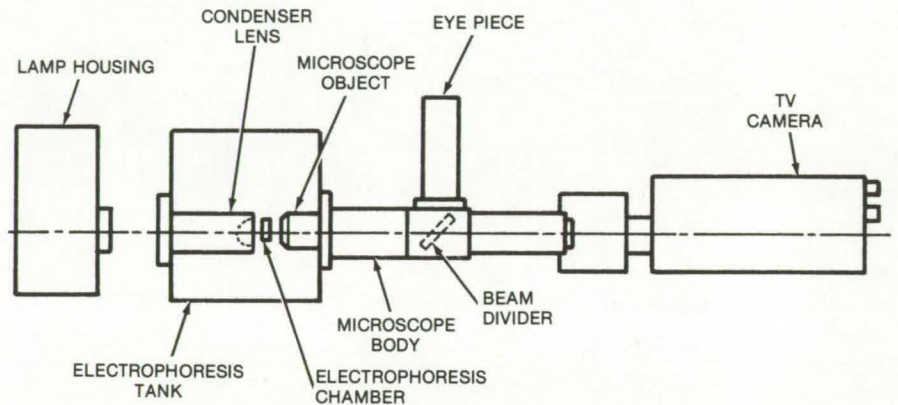


Figure 1. The **Microscope Aimed at the Electrophoresis Chamber** provides a continuous image of particle motion to the TV camera. The high scanning rate of the camera improves system accuracy in analyzing the particles.

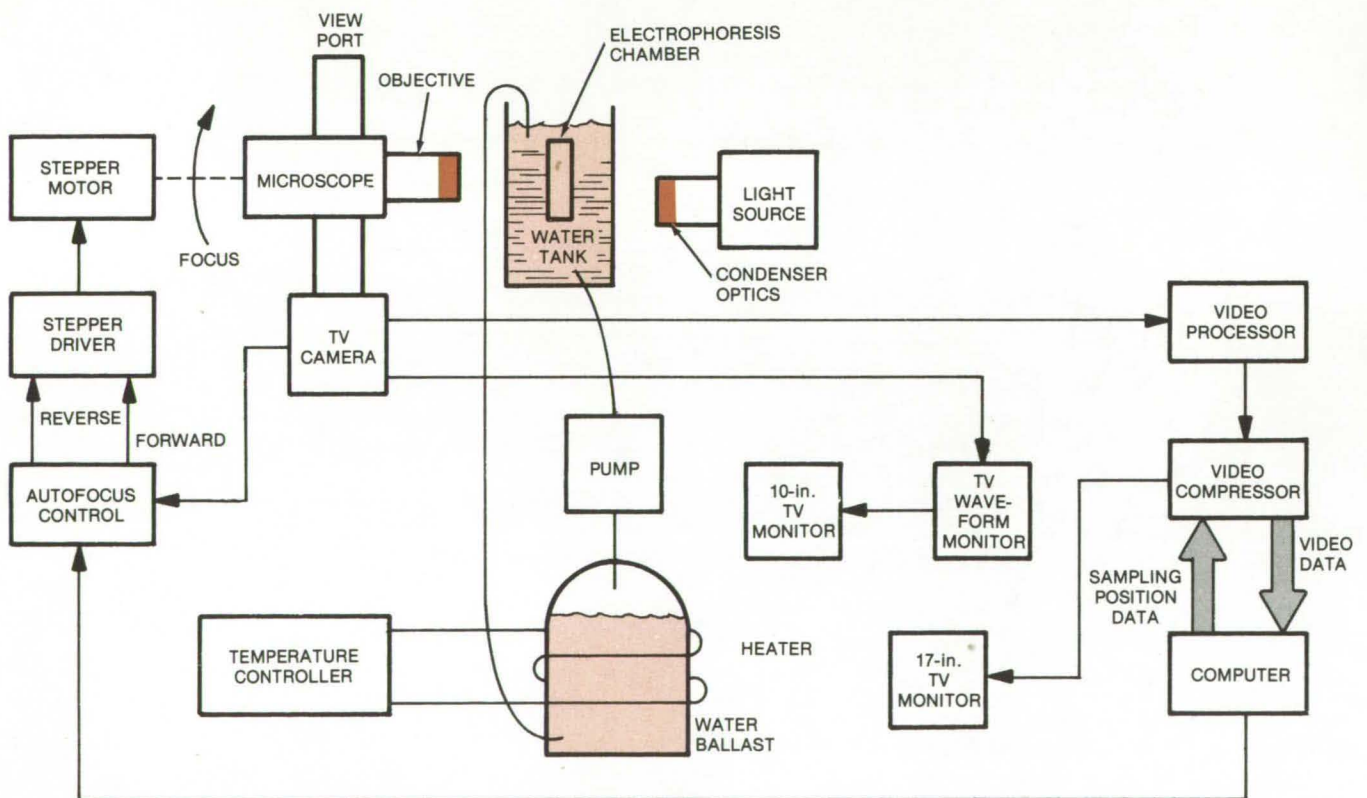


Figure 2. The **Automated Electrophoresis System** uses computer control to gather and process data. A printer may be added to the output of the computer to produce a hard-copy output.

and the computer. Figure 1 illustrates the main components and, Figure 2 outlines how the data entering the TV camera are processed in the system and how the electrophoresis chamber conditions are controlled by the computer.

Particles are tracked electro-optically. A light source illuminates the electrophoresis chamber, and the magnified image of the particle is picked up by the TV camera through the microscope optics. A beam divider splits the light from the objective into two paths so that visual or video camera ports can be used either alternatively or simultaneously. In the visual port, an eyepiece is used; in the TV camera port, a projection eyepiece or optical zoom projective is used. These optical elements magnify the intermediate image produced by the microscope objective.

The video signal from the TV camera goes to the processor, which adjusts and enhances the video contrast. From the video processor,

the signal is fed to the video compressor. The video compressor samples the video under program control at a rate compatible with the computer data rate and thus functions as a scan converter. Each pixel (picture element) is digitally encoded to a word that represents its intensity. The digital word is transmitted to the computer. The computer commands the video compressor where to sample data via the digital signal.

The TV camera also feeds video to the autofocus electronics and to the TV signal-quality monitoring equipment; i.e., the TV waveform monitor and the 10-in. (25.4-cm) picture monitor. The autofocus analyzes the TV signal for image detail and derives a signal proportional to the degree of focus. It is used to drive a stepper motor. Logic in the autofocus electronics determines whether the focus is getting better or worse and forms the proper logic signals to drive the motor to maintain optimum focus. The autofocus electronics also contain

circuitry to form a "window" in the TV raster where the video analysis takes place, and to assist the operator, this window is superimposed over the microscope image on the TV monitor.

The temperature controller has a sensor in the tank mounted close to the electrophoresis chamber to regulate the water-tank temperature by heating the water ballast and pumping the heated water into the tank. This constant circulation maintains the temperature of the electrophoresis chamber to the tolerances required for accurate electrophoresis work.

This work was done by L. Ralph Baker, Peter H. Bartels, Charles Blenman, Jr., Cai-wah Chan, and John M. Holcomb of the University of Arizona for Marshall Space Flight Center. For further information, Circle 53 on the TSP Request Card.

Inquiries concerning rights for the commercial use of this invention should be addressed to the Patent Counsel, Marshall Space Flight Center [see page A8]. Refer to MFS-23983.

Improved Imide Polymerization Catalyst

Flame-resistant foams can be produced in a single step.

Ames Research Center, Moffett Field, California

A more efficient catalyzation of imide polymers is made possible by using the metallic salts of 2-ethyl hexanoic acid. The improved catalyst allows the reaction to be carried out in one step without the formation of undesirable heat-sensitive byproducts.

Previously, polymers containing polyimide linkages have been synthesized from tetracarboxylic acid dianhydrides and polyisocyanates. The catalysts used promoted the formation of urea, urethane, cyanurate linkages, and carbodiimides as byproducts. The byproducts were found to be unstable at elevated temperatures.

The imide polymer reaction works best with either stannous, ferric, or aluminum octoates. The reaction can be carried out in either of two ways.

Method I calls for the formation of a prepolymer by causing a polyisocyanate to react with the anhydride at temperatures in the range from 187°

to 197° C with constant agitation in the presence of a catalyst such as stannous octoate. This reaction is allowed to proceed until the loss of carbon dioxide equals about 5 to 7 percent of the weight of the dianhydride-polyisocyanate mixture, a loss which corresponds to the reaction of one dianhydride group with one isocyanate group. The prepolymer thus obtained is placed in a mold preheated at about 275° to 300° C and is allowed to expand freely at those temperatures for a period of 20 minutes.

In method II, on the other hand, the foam is formed directly by adding the octoate catalyst to a slurry of finely-divided (about 325 mesh) solid dianhydride to an approximately stoichiometric quantity of aromatic diisocyanate containing about 3 percent by weight of a suitable surfactant based on total weight. The resulting slurry

mixture is then poured into a mold that has been heated at 200° C, and the mold is placed in a preheated oven at 200° C for a period of 30 minutes.

The flame-retardant and mechanical properties of the polymer foam can be enhanced by the incorporation of reinforcing fibers. Silicon dioxide, carbon, graphite, and certain organic fibers can be added to make up about 1 to 20 percent of the foam weight.

This work was done by Carlos A. Estrella, Salvatore R. Riccitiello, and Paul M. Sawko of Ames Research Center. For further information, Circle 54 on the TSP Request Card.

This invention is owned by NASA, and a patent application has been filed. Inquiries concerning nonexclusive or exclusive license for its commercial development should be addressed to the Patent Counsel, Ames Research Center [see page A8]. Refer to ARC-11107.



Porous Bead Packings for Gas Chromatography

New polymer beads are mechanically strong and easy to produce.

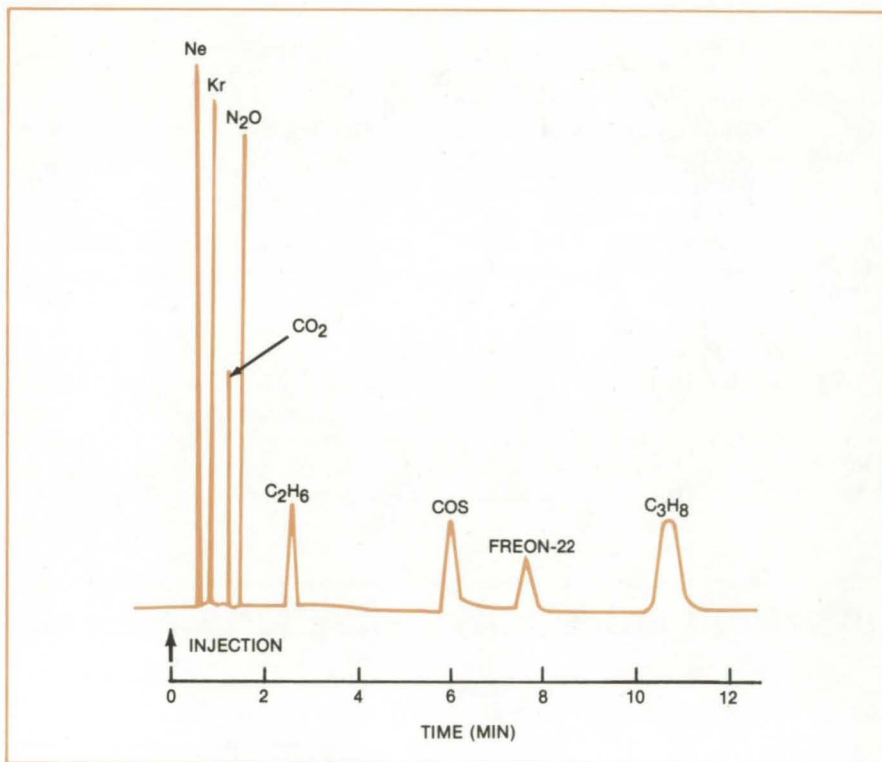
Ames Research Center, Moffett Field, California

Porous polymer beads can be synthesized for use as packing in gas chromatographs. The polyaromatic packings have low polarity, high efficiency, and short retention time; the beads range in size from 50 to 150 micrometers (100 to 270 mesh).

Various materials can be used for the beads, depending on the elements and compounds to be identified. The figure shows the performance of polymerized divinylbenzene (DVB), with peaks for neon, nitrous oxide, and Freon 22 among others. The use of pDVB derivatized with 3,3'-imino-bispropylamine (IBPA) allows the resolution of air, NH_3 , H_2O , and low-molecular-weight amines, such as CH_3NH_2 , $\text{C}_2\text{H}_5\text{NH}_2$, and $(\text{CH}_3)_2\text{NH}$. Polyethyleneimine (PEI) is used for higher-molecular-weight amines. Originally created to detect amines in extraterrestrial atmospheres, the divinylbenzene polymer beads can find many uses in terrestrial applications because they are easy to manufacture and to customize for special needs.

The polymer manufacture involves the purification of the divinylbenzene monomer and polymerization by a suspension process in a two-phase mixture of monomer, organic diluents, surfactant, and dilute aqueous ammonia. A second-stage polymerization can also be carried out, to give the beads desirable properties for chromatography of low-molecular weight gases. The derivatization process modifies the bead properties even further for use in amine analysis.

Monomer purification is carried out in small quantities by H_2SO_4 extraction and water washing. A second



Chromatograph Performance of two-stage pDVB — column: 1 mm I.D. by 240 cm; bead size: 63 to 88 μm (170 to 230 mesh); temperature: 71° C; helium carrier input: 245 psig ($1.7 \times 10^6 \text{ N/m}^2$); flow rate: 45 stdcm³/min; and sample gas: 0.2 μM total

extraction is carried out with NH_4OH .

Thermal polymerization is carried out in sealed ampoules mechanically rotated inside a small drying oven. The ampoules are heated to $108^\circ \pm 1^\circ \text{C}$ for 20 hours and then cooled to 50° C. Breaking open the seals at this point yields polymer beads, which are then washed in methanol.

At this stage, the beads can be cured, used for the second-stage

preparation, or derivatized with amines. The second-stage polymerization is carried out with the beads suspended in a toluene-divinylbenzene mixture.

This work was done by Glenn E. Pollock and Fritz H. Woeller of Ames Research Center. For further information, Circle 55 on the TSP Request Card.

ARC-11222

Scratch-Resistant Plastic Lenses

Three-step plasma deposition produces a tenacious antiabrasion film on optical plastics.

Ames Research Center, Moffett Field, California

A new process deposits a durable, strongly-adhering, antiabrasion coating on optical plastics. Such plastics offer several advantages over glass as lenses in cameras, projectors, telescopes, and other optical instruments: Plastic materials are inexpensive and lightweight, they can be injection-molded, and they require no further finishing when released from the mold. The new process eliminates a major disadvantage of plastic lenses: the tendency to become scratched under routine cleaning.

In the new process, a plastic lens (for example, one composed of polymethyl methacrylate) is subjected to three consecutive steps:

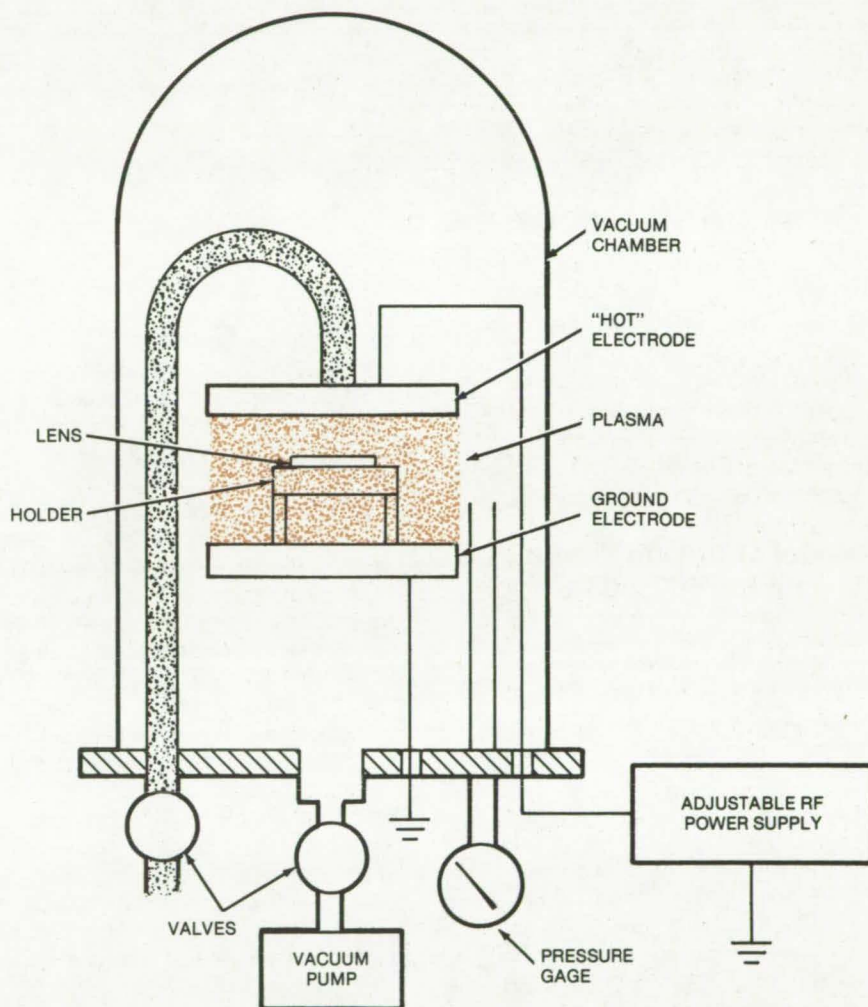
1. Exposure to a water-vapor plasma, which forms hydroxyl groups on the lens surface;
2. Exposure to a plasma of silicon-based monomers; and
3. Exposure to an argon plasma.

The first step ensures good adherence of the coating to the lens. The second step deposits the coating, and the third step cross-links the coating into a strong, scratchproof polymer.

All steps are carried out in the same vacuum chamber (see figure). So that both sides of the lens are coated, the lens is positioned about midway in the 2-inch (5-cm) space between the chamber electrodes. The upper ("hot") electrode is connected to an adjustable radio-frequency (RF) power supply. The lower electrode is connected to ground.

The chamber is evacuated, and distilled-water vapor is supplied through an inlet tube while valves maintain chamber pressure at 15 to 25 newtons per square meter. The RF field ionizes the water vapor between the electrodes into a plasma that deposits hydroxyl groups on the lens. The deposition period lasts for 100 to 1,000 seconds.

Following this step, the chamber is again evacuated; the monomers are introduced through the inlet tube (for example, a mixture of vinylidimethyl-



The three steps of the **Plasma Deposition** process for depositing antiabrasion coatings on polymethyl methacrylate lenses are carried out in a single chamber. The same process can also deposit antireflection coatings on lenses of higher-index material.

ethoxysilane and hexamethyldisilazane in equal portions). Pressure is regulated to about 7 to 13 newtons per square meter. The electrodes ionize the monomer mixture, and it deposits on the hydroxyl-coated lens at a rate 0.1 to 0.25 nanometer per second. A monomer layer up to 3,000 nanometers thick can be deposited; above that value, internal stresses become

large enough to pull the layer away from the lens surface.

The chamber is evacuated a final time, and argon is introduced at a pressure of about 20 newtons per square meter. The ionized argon generates ultraviolet light, heat, and electrons that both cross-link and stress-relieve the monomer film over a period of 200 to 1,000 seconds.

(continued on next page)

Films formed in this manner pass the standard military-specification test for adhesion. Films formed without the initial hydroxyl-coating step, on the other hand, did not pass this test.

When films made by the three-step process were rubbed many times with an eraser — rough treatment even for a hard glass lens, the only scratch marks visible under a 40-power microscope were those made by bits

of pumice in the rubber eraser. (The plastic substrate "gives way" under the coating due to the much higher force loading per unit area caused by the pumice particle.) The films withstood attack by water, Freon, and standard lens-cleaning solutions. There was no delamination, discoloration, or cracking in films stored at 170° F (77° C) for long periods.

This work was done by Ronald M. Kubacki of Bell & Howell Co. for Ames

Research Center. For further information, Circle 56 on the TSP Request Card.

This invention is owned by NASA, and a patent application has been filed. Inquiries concerning nonexclusive or exclusive license for its commercial development should be addressed to the Patent Counsel, Ames Research Center [see page A8]. Refer to ARC-11039.

Books and Reports

These reports, studies, and handbooks are available from NASA as Technical Support Packages (TSP's) when a Request Card number is cited; otherwise they are available from one of NASA's Industrial Application Centers or the National Technical Information Service.

Model of Silicon Production in a Fluidized-Bed Reactor

Model aids in evaluating fluidized-bed production of semiconductor-grade silicon.

A mathematical model of fluidized-bed process for making high-purity silicon can help to evaluate the potential performance and economics of such processes. The model uses input parameters such as the initial bed height, the composition of the gas stream, the particle size, and the production rate. From these, one determines the gross behavior of the bed including information on its operating height, the pressure drop across the bed, the superficial fluid velocity, and the type of fluidization (either particulate or bubbling).

Although the model is a simplified description, and will require additional

experimental input and further refinement, it represents a good beginning toward understanding the fluidized-bed process. With it, researchers can begin to predict the deposition rate of silicon for a given set of operating conditions. They can also determine the best gas and particle flow rates and the power requirements.

The fluidized-bed process is under consideration as a means of producing inexpensive silicon for solar cells. In the process, silicon particles are fed into a stream of silane and hydrogen so that the particles form a fluidlike bed. The silane pyrolyzes in the bed, depositing additional silicon on the particles. The particles grow, and the larger ones are continuously extracted from the reactor. The process is continuous, and since it has a very large reaction area (the particle surfaces), it is a potential source of pure silicon on a much larger scale than conventional chemical-vapor deposition.

Several assumptions and limiting conditions were used to make the problem tractable, including:

- At temperatures above 1,000° C, the primary reaction is the heterogeneous pyrolysis of silane on the surface of the silicon particles.
- The rates of adsorption and reaction are faster than the transport of

silane; thus the particle-growth rate is diffusion limited.

- The fluidization of particles smaller than 50 microns in diameter, which would cause abnormal fluidization, is not considered; the bed is assumed to be either bubbling or particulate fluidized.

If the bed is particulate fluidized — that is, if the particles are uniformly distributed through the gas, the particle growth rate can be obtained relatively simply. If the bed is bubbling — that is, if bubbles of gas coexist with a particle-and-gas emulsion, the bubble and the emulsion characteristics must be studied separately in experiments that examine the interaction between the two phases. When the growth rate is obtained, the mass balance of silicon particles in the feed, product, and entrainment streams and in the bed is calculated.

This work was done by George C. Hsu, Ki-Bong Kim, Ralph Lutwack, and Ananda K. Praturi of Caltech for NASA's Jet Propulsion Laboratory. Further information may be found in NASA CR-154120 [N77-28581], "Modeling of Fluidized Bed Silicon Deposition Process" [\$4.50]. A copy may be purchased [prepayment required] from the National Technical Information Service, Springfield, Virginia 22151. NPO-14404

Life Sciences



**Hardware,
Techniques, and
Processes**

- 547 Separating Biological Cells
- 548 Flow-Compensating Pressure Regulator
- 549 Intraocular Pressure Reduction and Regulation
- 551 Hand-Held Vital-Signs Monitor
- 553 Hybrid Temperature-Monitoring Circuit
- 554 Hybrid ECG Signal Conditioner
- 556 Hybrid Respiration-Signal Conditioner
- 557 Hybrid Heart/Breath-Rate Processor
- 559 Hybrid LCD Driver
- 560 Hybrid Clock Generator
- 562 Improved Probe for Rectal-Cancer Detection
- 563 Self-Propelling, Self-Locating Colonoscope
- 564 Noncontacting Electrokinetography System

Separating Biological Cells

An electric field makes cell separation possible in zero gravity and aids separation in normal gravity.

Marshall Space Flight Center, Alabama

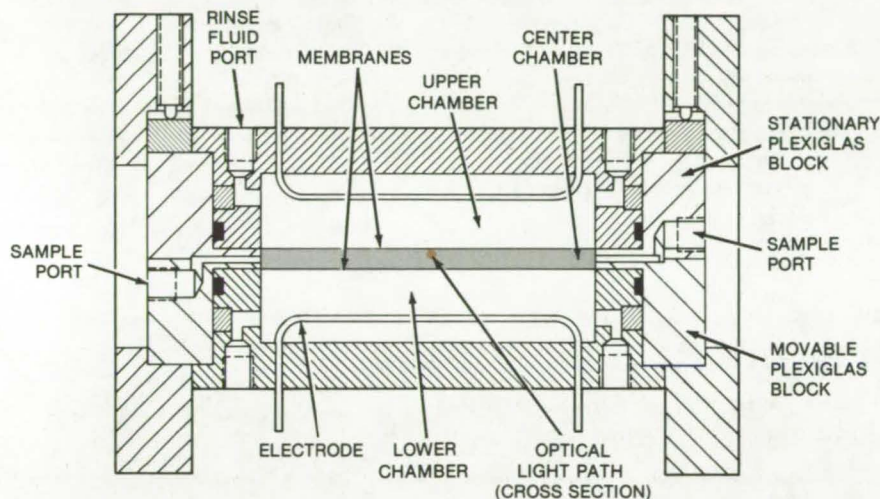


Figure 1. **Biological Cell Separation** occurs in the center chamber (5 by 0.5 by 0.2 centimeters), which is enclosed by membranes; progress is monitored by transmission of a light beam. The apparatus, including electrode chambers, is constructed of polymethyl methacrylate and is designed so that its upper and lower halves can be opened.

Biological cells can be separated from a suspending medium by an electric field. The concept was developed for biological experiments in space or diving aircraft, where the absence of gravity effects makes conventional cell-separation methods ineffective. However, it also greatly speeds up separation in normal gravity, reduces sedimentation, and improves separation efficiency.

The new technique represents an extension of a biological-cell separation method that utilizes a two-phase aqueous polymer system as the cell-suspending medium. Cell separations can take place in such systems because, if a mixed cell population is shaken up in the polymer solution and the phases are allowed to separate by settling, cells with certain surface properties are found to be associated with only the top phase, while the remainder of the cells is adsorbed at the interface between the phases.

Extension of this method to separate the phases with an electric field has been demonstrated with polymer emulsions that are not suitable for

biological cells. However, polymers that are suitable are already under development.

The prototype apparatus for field-driven phase separation consists of two electrode chambers separated from a central "phase" chamber by membranes (see Figure 1). The center chamber is filled with an emulsion of two polymers (two phases). An electric field is applied between the two platinum electrodes (on the order of 10 volts per centimeter) as rinse solution circulates through the upper and lower chambers to remove unwanted electrochemical reaction products from the electrodes.

Under the influence of the electric field, the droplets in the emulsion separate. The droplets of one of the polymer components move to and coalesce in the upper half of the center chamber, while the components of the other polymer do the same in the bottom half.

In practice, a different kind of biological cell would associate with each polymer, so that after migration of the droplets, the upper half of the center

chamber contains mostly cells of one type and the bottom half contains mostly cells of the other. Thus cell separation is effected.

For effective separation, the two polymers must have high droplet electrophoretic mobilities of opposite polarity. In the demonstration, the two components were sodium dextran (continued on next page)

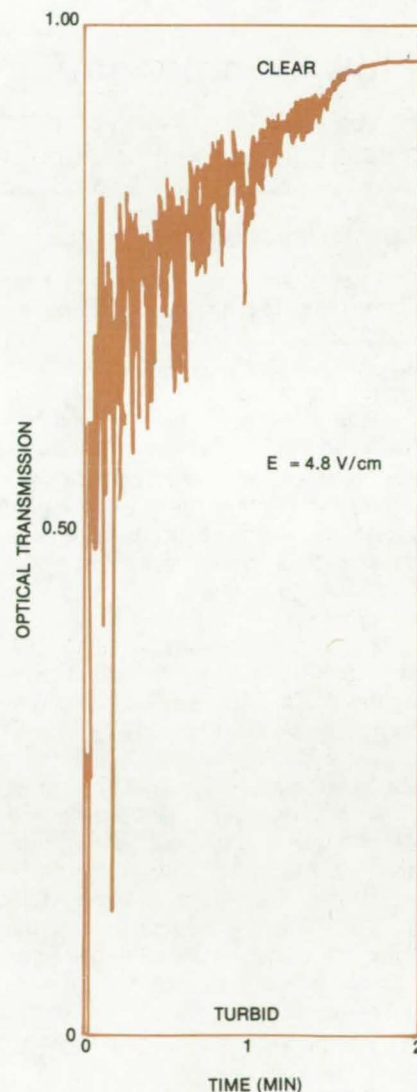


Figure 2. **Strip-Chart Record** of optical sensor output shows progression from a turbid emulsion to clear, fully separated phases.

sulfate (NaDS, molecular weight about 500,000) and a copolymer of polyethylene glycol and polypropylene glycol, molecular weight 5,400 (Pluronic P-104). A small amount of potassium citrate is added as the supporting electrolyte. In a by-weight mixture of 8 percent NaDS, 8 percent P-104, and 0.2 percent potassium citrate in water, the 6.5-micron droplets have mobilities of $+17.6 \times 10^{-4}$ and $-15.3 \times 10^{-4} \text{ cm}^2\text{-s}^{-1}\text{-V}^{-1}$ (NaDS and P-104, respectively).

Under gravity, the heavier NaDS droplets tend to move to the bottom half of the chamber. Thus, to assist gravity, the bottom electrode is made the cathode to attract the positive-mobility NaDS droplets. The separation

is complete in about a minute — one-tenth the time required with gravity alone.

As an aid in measuring the progress of the separation process, an optical system measures the turbidity of the emulsion. A ruby laser beam passes into and out of the center chamber through 0.03-centimeter-diameter apertures. Mixed-phase droplets scatter the laser beam, but separated-phase, coalesced droplets are clear and allow the beam to pass directly out of the exit port. The outgoing beam intensity is sensed by a solid-state detector and amplifier and is displayed on a strip-chart recorder (Figure 2).

Because biological cells themselves have electrophoretic mobility, it is

conceivable that the electric field might pull cells out of their proper polymer medium and into the wrong one, thus negating the separation process. This occurrence, however, in all probability will be prevented by tension at the interface of the two separated phases.

This work was done by Donald E. Brooks of the University of Oregon for Marshall Space Flight Center. For further information, Circle 57 on the TSP Request Card.

Inquiries concerning rights for the commercial use of this invention should be addressed to the Patent Counsel, Marshall Space Flight Center [see page A8]. Refer to MFS-23883.

Flow-Compensating Pressure Regulator

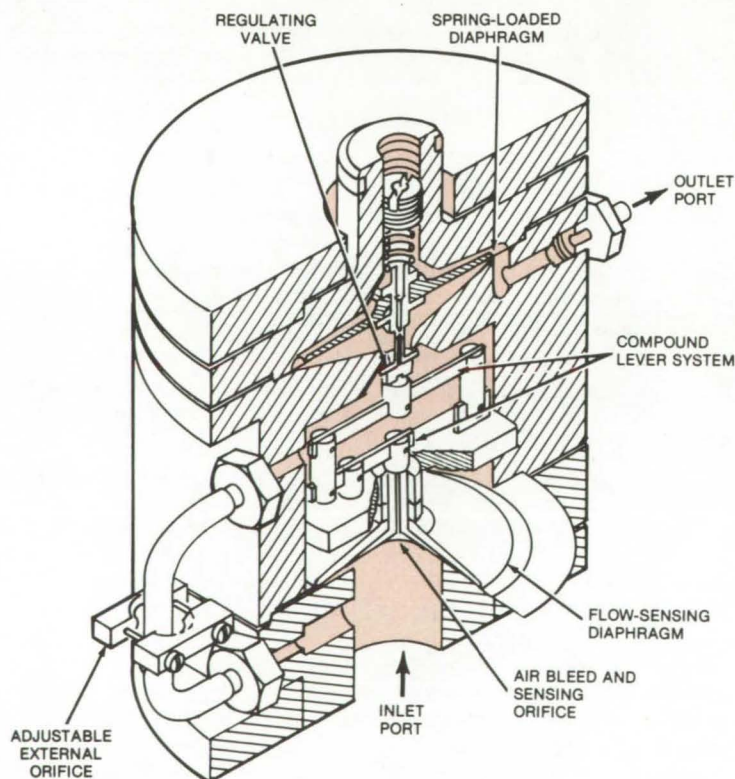
Regulator maintains a constant pressure at the working end of a surgical instrument, despite variations in infusion-fluid flow rate.

Lewis Research Center, Cleveland, Ohio

A flow-compensating pressure regulator (see diagram) has been developed for use with a surgical instrument for the removal of cataracts. [This instrument is described in "Intraocular Pressure Reduction and Regulation" (LEW-12723), page 549 of this issue.] The pressure regulator controls the intraocular pressure during substantial variations in the flow rates of the infusion fluid. The regulator may be applicable to a variety of eye-surgery instruments.

The regulator uses a standard-arrangement spring-loaded diaphragm as the basic pressure-regulating element (see figure). The no-flow output pressure of the regulator is set by a spring force pushing against the outlet pressure-sensing diaphragm. A second diaphragm is located a small distance below the first on the same centerline. This diaphragm responds to the pressure drop across an adjustable external orifice and a small internal orifice in parallel with it.

The external orifice, a length of silicone tubing with an adjustable pinch section, provides a means to calibrate the unit to match the pressure-drop characteristics of different instruments. This orifice is adjusted so that the pressure at the



The **Flow-Compensating Pressure Regulator** could be used with a cataract-surgery instrument to keep intraocular pressure constant, despite variations in infusion flow rate. As fluid enters the inlet port, there is a pressure drop across the flow-sensing diaphragm; this force is amplified and reversed by a compound lever to open the valve. With any change in pressure at the outlet, the two diaphragms will cause a compensating flow-rate (and thus pressure-drop) change to keep the outlet pressure constant.

outlet of the surgical instrument with flow is the same as the no-flow output pressure of the regulator. The small internal orifice, located on the centerline of the conical flow-sensing diaphragm, also acts as an air bleed to assure that the regulator is completely liquid filled with no trapped air volume.

As infusion fluid flows through the regulator, the pressure drop across the two orifices generates a force on the flow-sensing diaphragm. An interconnected compound-lever system transmits this force to the regulating valve. The lever system multiplies the diaphragm force by a factor of 5 and reverses its direction so as to pull the valve open.

The force on the flow-sensing diaphragm combines with the spring force to maintain a constant pressure at the instrument outlet. Any tendency of the pressure at the instrument outlet to increase or decrease will cause the two diaphragms to decrease or increase the flow from the regulator enough to restore that pressure. The actions of the flow-sensing diaphragm, the lever system, and spring-loaded

diaphragm exactly compensate for the pressure drop in the surgical instrument that controls the flow rate. Thus the regulator can maintain a constant pressure at the working end of a surgical instrument, even with variations in flow rate of infusion fluid through the instrument.

The regulating valve is the machined end of a cylinder with a small radius edge that presses against a flat silicone seat for positive shutoff during no-flow (standby) conditions. The flat valve surface provides rapid increases in flow capability for very small axial valve motions.

The infusion fluid, a sterile salt solution, must not be contaminated as it passes through the regulator. Those components that come in contact with this fluid are made either from clear, high-temperature-resistant plastic or Monel. The regulator is designed to have a small fluid volume. A vertical flow path through the regulator easily eliminates trapped air.

The gain of the regulator, the ratio of outlet pressure increase relative to sensed pressure drop in the flow-

sensing orifice, can be altered by changing the multiplication factor in the lever system or by using diaphragms of unequal area. The present unit uses diaphragms with equal effective area of 1 in.² (6.5 cm²).

The pressure regulator has had substantial evaluation in experimental laboratory use including extensive animal surgery. The functional performance appears to be consistent and satisfactory. Manufacturing engineering has not been done and is not planned.

This work was done by Edward F. Baehr of Lewis Research Center. Preliminary drawings can be reproduced and made available at cost if requested.

This invention has been patented by NASA [U.S. Patent No. 4,084,612]. A copy of the patent may be obtained from the U.S. Patent and Trademark Office, Washington, DC 20231. Inquiries concerning nonexclusive or exclusive license for its commercial development should be addressed to the Patent Counsel, NASA Lewis Research Center [see page A8]. Refer to LEW-12718.

Intraocular Pressure Reduction and Regulation

Pressure within the eye can be controlled relatively accurately and without drugs.

Lewis Research Center, Cleveland, Ohio

A recently-developed pressure reduction and regulation system appears to have a number of potential uses in ophthalmology. The system is designed to reduce intraocular pressure — pressure inside the eye — hydraulically to any level desired by the physician over a set time and in a controlled manner. It may be most immediately useful in dealing with cases where intraocular pressure remains markedly elevated in spite of medical treatment immediately prior to glaucoma surgery.

Glaucoma is a widespread group of eye diseases characterized by elevated intraocular pressure. Such increased pressure if not reduced can cause impaired visual function and eventual blindness. Medical treatment to reduce and control the pressure is not always successful; in such

cases, surgery may be used to relieve the pressure.

Prior to the ophthalmic surgery, medication is used to reduce intraocular pressure temporarily. Such procedure requires some time to obtain the desired reduction in pressure. In addition, drugs may have undesirable side effects on some people and may be insufficiently effective on others.

As a supplement to drugs and perhaps eventually as an alternative, the new system can be used safely to reduce abnormally high intraocular pressure hydraulically during a predetermined time interval. Once intraocular pressure has been reduced to the level desired by the surgeon, a pressure regulator will maintain this set minimum pressure within a reasonable range during intraocular surgery.

As shown in the figure, a fluid supply at a pressure matched to the existing intraocular pressure is connected to the anterior chamber of the eye through a small cannula inserted near the edge of the cornea. Pressure of the fluid supply is reduced and controlled so that the intraocular pressure is reduced by the same amount and at the same rate.

If only very small liquid flows are expected during the surgery and after surgical penetration of the eye, intraocular pressure can be established and maintained by adjusting pressure (i.e., height) of the fluid supply alone, and the pressure regulator need not be part of the system. However, for larger and variable flows, the pressure regulator is desirable.

The system shown in the figure
(continued on next page)

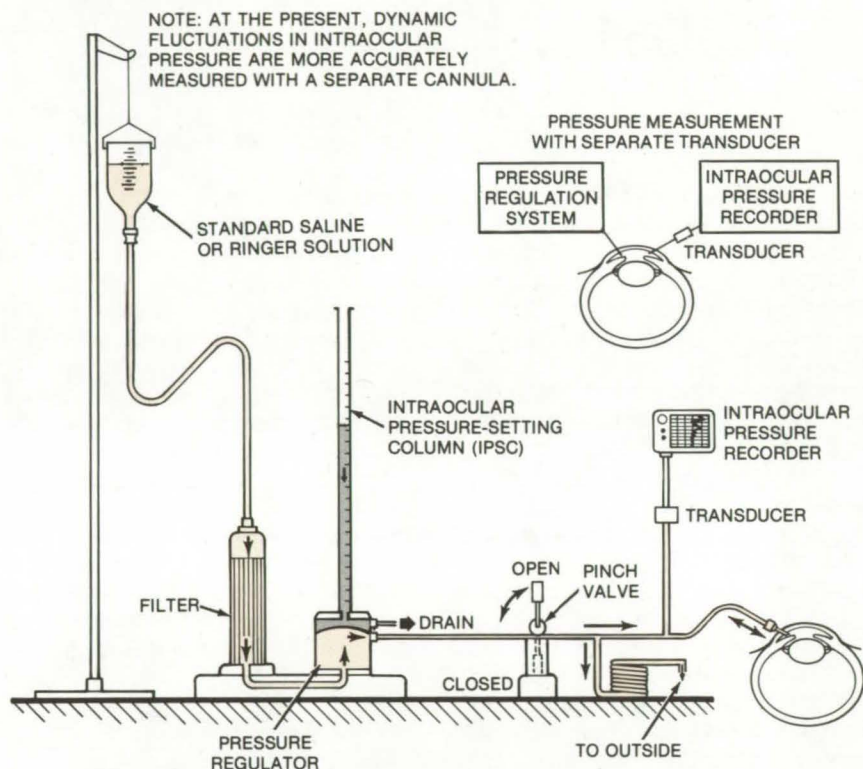


makes use of a flow-compensating pressure regulator [see "Flow-Compensating Pressure Regulator" (LEW-12718) on page 548 of this issue] that adjusts automatically to maintain the set minimum intraocular pressure after the eye has been opened by surgical penetration during the glaucoma surgical procedure. The regulator has a spring-biased diaphragm that is initially adjusted so the regulator will produce the desired minimum intraocular pressure. A vertical tube or standpipe connected to the top of the regulator contains a column of liquid that provides an additional regular bias. The level of the column of liquid is selected so that the total output pressure of the regulator equals the measured intraocular pressure.

After the cannula has been inserted, liquid is bled out of the standpipe at a predetermined rate, reducing the bias on the regulator diaphragm and, consequently, causing a gradual reduction in regulator output pressure. The system is entirely liquid filled, and the pressure regulator permits only forward, not reverse, flow. Also, the eye is essentially an elastic chamber where pressure reduction is accompanied by the movement of a very small amount of fluid out of the eye. Accordingly, a pressure-relief tube between the regulator output and cannula is provided to furnish a flow path to the outside for treatment fluid; this pressure-relief tube permits the eye pressure to decrease at the same rate as the liquid head in the standpipe decreases.

When the standpipe is completely drained, intraocular pressure will be the same as the regulator output pressure initially set by the spring adjustment. During surgery the regulator will maintain this minimum pressure through the cannula connected to the anterior chamber. A measuring system records intraocular pressure continuously.

Investigations with the system



Intraocular Pressure Regulator can be used by a physician to reduce pressure inside the eye hydraulically. Fluid pressure within the eye stays at the same pressure as the fluid system to which the eye is connected by a cannula. The pressure in the system is set by a pressure regulator and setting column. The special pressure regulator replaces fluid loss by the eye (during surgery for instance) without changing the pressure.

have shown that intraocular pressure excursion peaks resulting from external loads such as surgical manipulations are reduced if the intraocular resting pressure is first lowered. This result was expected. Use of this new system reduces such intraocular pressure excursion peaks even further, however, because the penetrating cannula and the external fluid system provide a pressure-relief mechanism.

Based on its demonstrated capability, the new intraocular pressure reduction and regulation system may be useful as a tool to permit controlled studies of several post-eye-surgery complications (e.g., cataract forma-

tion, choroidal detachment, flat anterior chamber, macular edema, and malignant glaucoma), which may be due at least in part to marked intraocular pressure fluctuations and/or hypotony during surgery.

This work was done by Edward F. Baehr of **Lewis Research Center** and William J. McGannon. For further information, Circle 58 on the TSP Request Card.

This invention is owned by NASA, and a patent application has been filed. Inquiries concerning nonexclusive or exclusive license for its commercial development should be addressed to the Patent Counsel, Lewis Research Center [see page A8]. Refer to LEW-12723.

Hand-Held Vital-Signs Monitor

Body temperature, heart rate, and breath rate are monitored and displayed by a miniature battery-powered instrument.

Lyndon B. Johnson Space Center, Houston, Texas

A complete physiological vital-signs monitor has been miniaturized by hybrid integrated-circuit technology. The compact, low-power circuit displays body temperature, heart rate, and breath rate, and it has provision to display blood-pressure data fed from external circuitry.

Six new hybrid circuits form the basis of the unit. Only a display, a battery, a case, and miscellaneous hardware would be needed to package a completely-self-contained hand-held instrument (see Figure 1). As part of a modern physician's "black bag," the monitor could be used by doctors on house calls and by others in medical emergencies in remote areas or confined spaces. This article gives an overview of the vital-signs monitor. Details of the six hybrid circuits are contained in the articles that follow.

Figure 2 is a functional block diagram of the vital-signs monitor. Its essential elements are a liquid-crystal display, a four-channel two-input digital switch, and the six hybrid circuits, including:

- A Temperature Monitor
- An ECG Amplifier and Cardiometer Signal Conditioner
- An Impedance-Pneumograph and Respiration-Rate Signal Conditioner
- A Heart/Breath-Rate Processor
- A Liquid-Crystal Display Driver
- A Clock Circuit

Each of the hybrids evolved from existing conventional-scale circuits that drew too much power and required too many interconnections to be easily hybridized. Thus, the circuits were redesigned to conform to the special requirements imposed by hybridization. Large capacitors and potentiometers were eliminated, circuit configurations were changed, and the number of calibration adjustments was reduced. Flexibility in display modes was also increased. Each of the circuits can also be used independently for other applications.

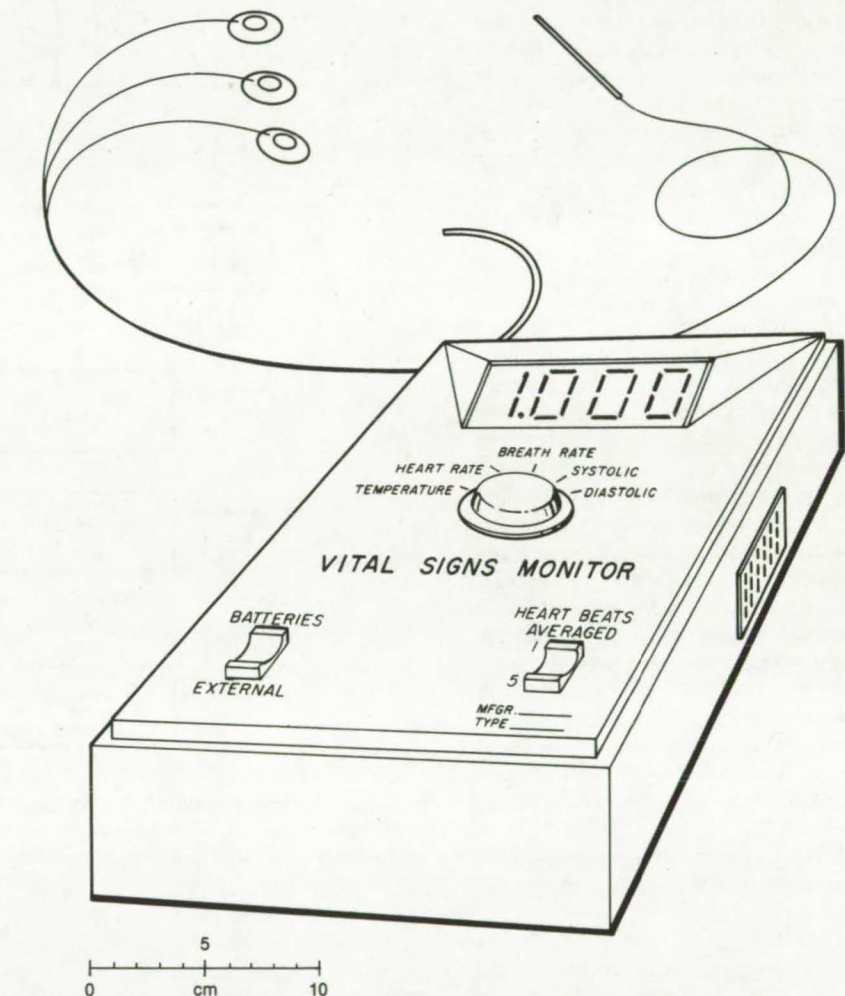


Figure 1. **Hand-Held Vital-Signs Monitor**, shown in this artist's concept, would process and display body temperature, heart rate, and breath rate. Systolic and diastolic blood pressure (processed by external circuits) could also be displayed. The hybrids have been designed, built, and tested, as has a prototype of the complete circuit. Standard packaging techniques could be used to make the hand-held version.

Referring to Figure 2, the input to the circuit is derived from three chest electrodes and one temperature-monitoring thermistor. In addition, digital blood-pressure data can be accepted from external circuitry.

The chest electrode signals are fed to both the ECG and the respiration sig-

nal conditioners. In the ECG circuit, the signal is amplified, filtered, and used to generate standardized output pulses synchronized with the ECG pulses.

The respiration-rate circuit measures the change in impedance (at 50 kHz) of the chest as it expands and contracts during the breathing cycle. A

(continued on next page)

Since the data latches have three-state outputs, all internal data signals can be decoupled from the display.

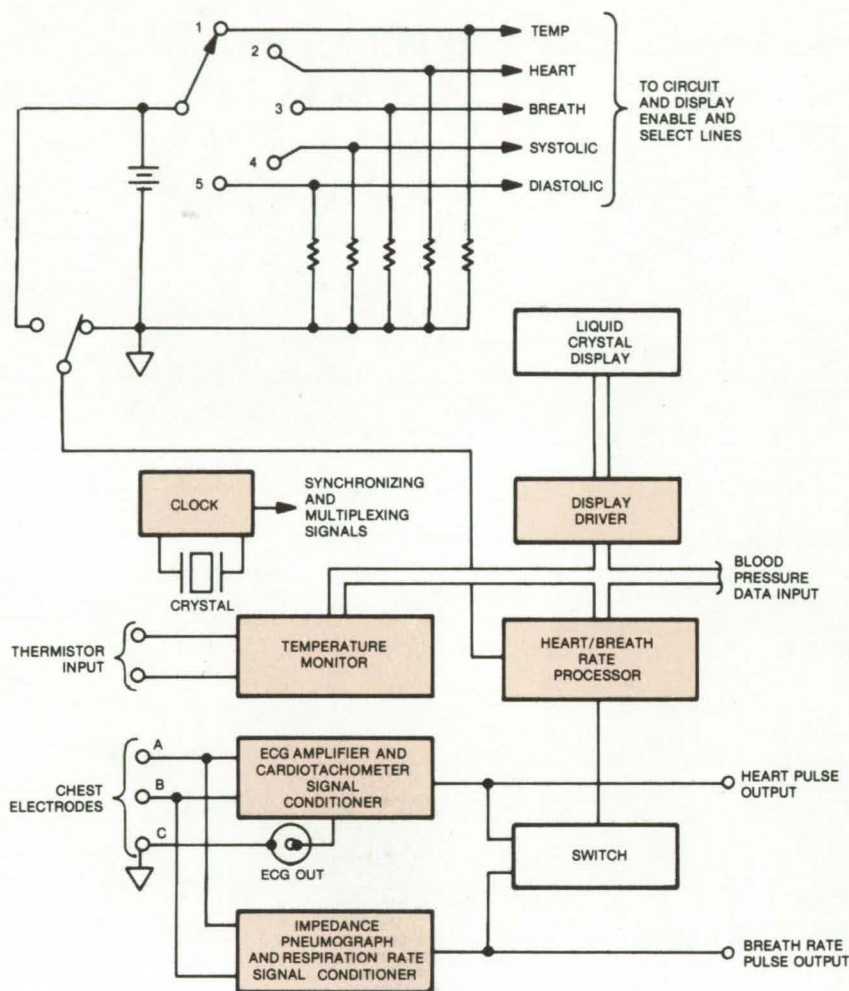


Figure 2. This **Schematic Diagram** shows the elements and interconnections of the vital-signs monitor. In addition to the display, ECG and respiration signals are available as outputs and can be displayed on a chart recorder or an oscilloscope.

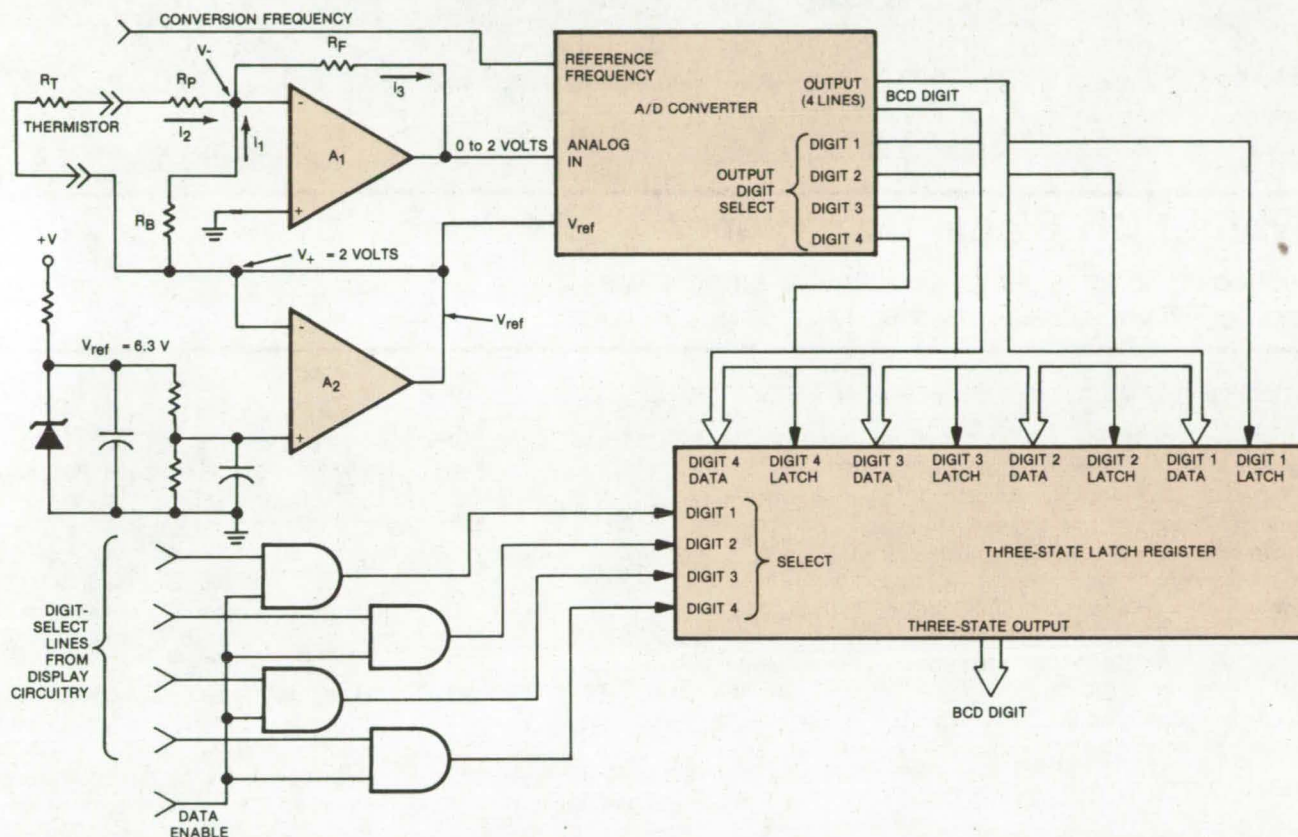
The six circuits are packaged in platform hybrid cases that allow them to be plugged into sockets on a printed-circuit board and replaced easily. Since the hybrids eliminate many electrical connections and solder joints that would be needed for a conventional circuit, the monitor is more reliable.

*This work was done by George A. Rinard, Dale A. Steffen, and Ronald E. Sturm of the Denver Research Institute for **Johnson Space Center**. Title to this invention has been waived under the provisions of the National Aeronautics and Space Act [42 U.S.C. 2457(f)], to the Denver Research Institute, Denver, Colorado 80208.*
MSC-18232

Hybrid Temperature-Monitoring Circuit

Device converts the resistance of a thermistor to a 3-1/2-digit temperature readout.

Lyndon B. Johnson Space Center, Houston, Texas



Hybrid Temperature-Monitoring Circuit converts the resistance of a thermistor to a digital temperature reading. In tests, the temperature could be measured to within 0.1 percent of a calibration point [e.g., 98.6° F (37° C)] by selecting a resistor with 1 percent tolerance for R_F . The linearity of the monitor was 1 percent.

The hybrid temperature-monitoring circuit developed for a hand-held vital-signs monitor (see preceding article) produces a 3½-digit BCD (binary-coded-decimal) output that corresponds to the temperature of a thermistor probe. The output is multiplexed, one digit at a time, onto a 4-bit output port.

As with the other elements of the vital-signs monitor, the temperature circuit can be used with or without the other hybrid circuits. If used independently, it can form a "stand-alone" temperature monitor or can transmit temperature data via telemetry to data-acquisition systems. The hybrid

includes an internal clock that requires only a single outboard capacitor to set its frequency for these applications.

Referring to the accompanying block diagram, it is seen that the resistance of the thermistor, R_T , determines the output voltage of amplifier A_1 . This voltage is converted to digital form by an analog-to-digital converter and then is stored in a three-state latch register. The three-state latch is in a high impedance state until one of the digit-select lines is enabled. The enabled digit then appears at the latch output.

The circuit around amplifiers A_1 and

A_2 compensates for the inherent non-linearity of the thermistor. The output of A_1 is given by

$$V_{out} = \left(\frac{R_F}{R_T + R_p} + \frac{R_F}{R_B} \right) V_{ref} \quad (1)$$

and the thermistor response can be represented by

$$R_T = \frac{a}{T-b} - p \quad (2)$$

where T is the temperature and a , b , and p are empirically determined constants.

(continued on next page)

If the resistors R_F , R_P , and R_B are chosen according to the following scheme

$$R_F = \frac{a}{KV_{ref}} \quad (3)$$

where $K = 100 \text{ } ^\circ\text{F/volt}$

$$R_B = a/b \quad (4)$$

$$R_P = p \quad (5)$$

then the voltage V_{out} becomes simply

$$V_{out} = T/K \quad (6)$$

Thus, the output of A_1 is linearized and is independent of V_{ref} . With the scaling factor K chosen as in (3), the circuit output will read directly in degrees Fahrenheit.

If the circuit is always used with the same model thermistor, it is possible to fix R_B and R_P within the hybrid package and use R_F as an "outboard" component that adjusts the circuit for the particular unit selected.

This work was done by George A. Rinard, Dale A. Steffen, and Ronald

Sturm of the Denver Research Institute for Johnson Space Center. Title to this invention has been waived under the provisions of the National Aeronautics and Space Act [42 U.S.C. 2457(f)], to the Denver Research Institute, Denver, Colorado 80208. MSC-18231

Hybrid ECG Signal Conditioner

Electrocardiogram signals from chest electrodes are amplified, filtered, and converted to standardized pulses.

Lyndon B. Johnson Space Center, Houston, Texas

High common-mode rejection and the ability to accept electrocardiogram (ECG) signals of varying amplitude, shape, and polarity are some of the features of the hybrid ECG amplifier and cardiometer of the vital-signs monitor. [See "Hand-Held Vital-Signs Monitor" (MSC-18232) on page of this issue.] Besides filtering and amplifying the analog ECG, the low-power circuit develops standardized pulses that can be counted and averaged by the heart/breath-rate processor.

The circuit receives the heart signal from three electrodes, one of which is a common or reference electrode. The signal is amplified by a balanced differential amplifier with very high input impedance and large common mode rejection and is fed to a band-pass filter to suppress noise and interference. The filtered signal is then sent to a normalizing circuit that standardizes the amplitude of the heart pulses regardless of their polarity. A bipolar threshold circuit detects the pulses, and the threshold output is then standardized in width and amplitude.

As shown in the figure, the input amplifier consists of three operational amplifiers. The gain of the input differential amplifier is +40 dB. An additional 50-dB common-mode rejection ratio is added by the final amplifier in this group of three.

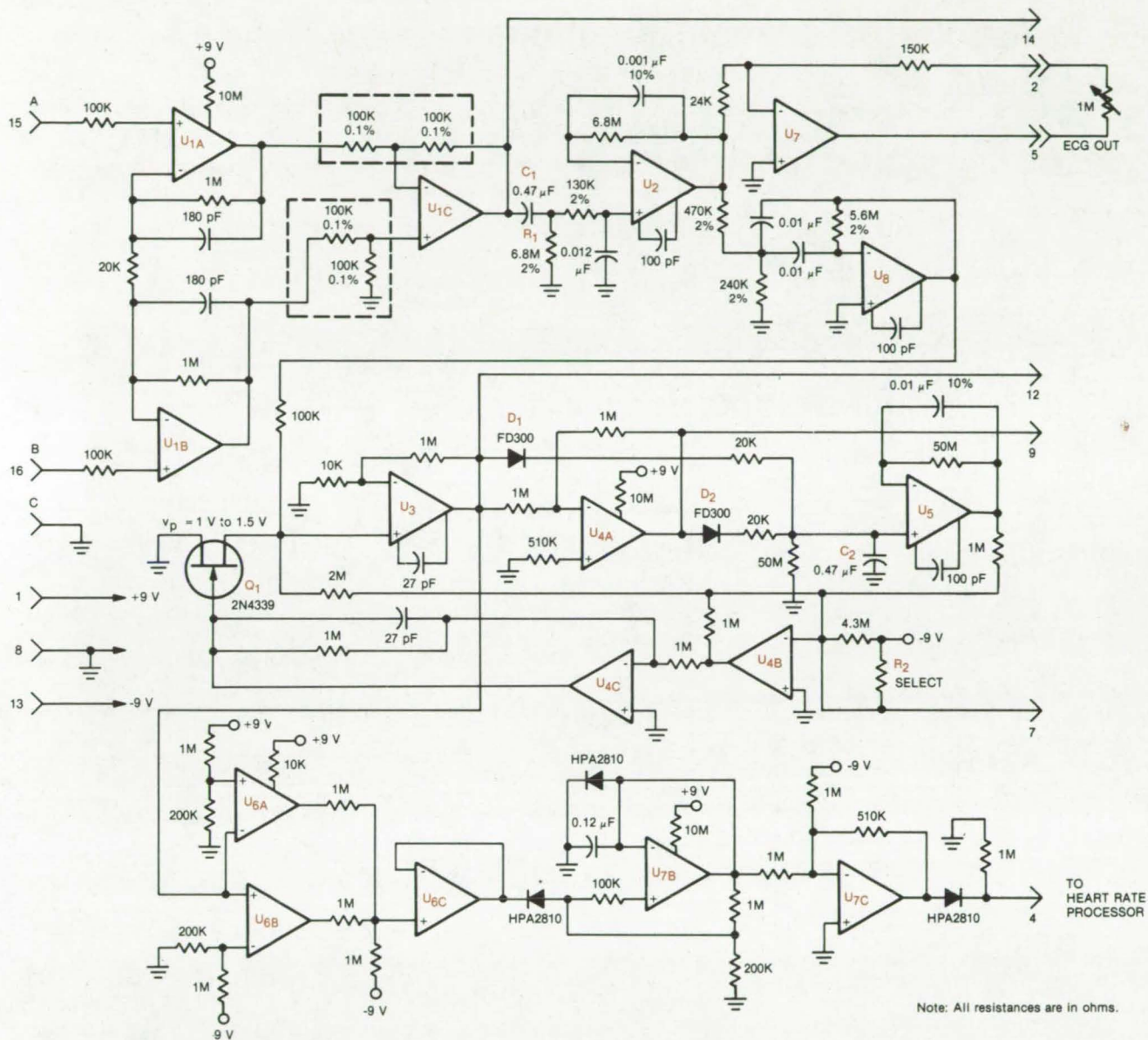
Capacitor C_1 and resistor R_1 determine the low-frequency cutoff at 0.05 Hz for the heart signal. R_1 is a very high resistance to ensure that C_1 is small enough to fit in the hybrid package. The gain of U_7 , the ECG output amplifier, is adjustable from 6.25 to 48. At maximum gain, the dc offset at the ECG output does not exceed 0.125 volt.

U_8 and associated circuitry constitute a high-impedance active band-pass filter with low output impedance. The filter, with a center frequency of 17 hertz and a Q-factor of 3, prevents cardiometer triggering on an abnormally large T-wave. U_3 is a high-gain amplifier for which field-effect transistor (FET) Q_1 is a variable shunt attenuator that controls the overall gain. The output of U_3 and inverter U_{4A} are full-

wave peak detected by D_1 , D_2 , and C_2 . Thus, the maximum peak amplitude (regardless of polarity) is stored on C_2 and is transferred to the output of voltage follower U_5 . The summing amplifier U_{4B} combines the peak-detector output with a portion of the original filtered ECG signal to linearize the FET voltage characteristic.

R_2 is selected to set the dc operating voltage at the FET gate, calibrating the normalized output of U_3 at 2 volts peak. Therefore, the largest peak of the filtered ECG signal will be 2 volts, regardless of the input amplitude, over the specified range. The bipolar threshold circuit (consisting of U_{6A} , U_{6B} , and U_{6C}), biased at plus and minus 1.5 volts, reacts whenever the absolute value of the normalized signal exceeds this value. U_{7B} and surrounding components set the width of the output pulses.

This work was done by George A. Rinard, Dale A. Steffen, and Ronald E. Sturm of the Denver Research Institute for Johnson Space Center. Title to this invention has been waived



The **Automatic Gain Control** of amplifier U_3 allows the ECG signal conditioner to process a wide range of signal characteristics from many different electrode configurations. The circuit also accepts signals of either polarity.

under the provisions of the National Aeronautics and Space Act [42 U.S.C. 2457(f)], to the Denver Research Institute, Denver, Colorado 80208.

MSC-18230

Circuit monitors changes in the impedance of the chest during the breathing cycle and develops a standardized signal for further processing.

The hybrid impedance-pneumograph and respiration-rate signal-conditioner element of the vital-signs monitor [see "Hand-Held Vital-Signs Monitor" (MSC-18232) on page 551 of this issue] measures changes in the impedance of the chest during the

The circuit (see figure) requires two active chest electrodes that are driven

with balanced 50-kHz current. A reference (common) electrode is also provided. These can be the same electrodes that monitor the ECG heart signal in the vital-signs monitor. The voltage developed across the chest impedance is amplified, rectified, and filtered

to monitor the amplitude envelope of the 50-kHz signal as it is modulated by the subject's breathing. After additional gain and filtering, the respiration signal is converted to a standardized square wave.

Capacitors C_1 and C_2 balance the output current with respect to the common electrode. Since the chest impedance is very nearly resistive, the excitation circuit acts like a differentiator. Thus, to obtain a square-wave excitation, a triangular-wave generator (U_1) is used. (The triangular wave becomes a square wave when differentiated.) U_2 is an inverter that produces a waveform of opposite polarity and equal amplitude. The excitation-generator output is very nearly 18 volts peak-to-peak, which is the total supply voltage.

The 50-kHz voltage drop across the chest impedance is amplified by the balanced differential amplifier U_3 and U_4 , and it is rectified at the input to U_5 . The slowly varying voltage that follows the breathing cycle is then coupled into voltage follower U_6 by capacitor C_3 and resistor R_1 , which set the pass-band lower 3-dB frequency limit at 0.1 Hz. U_7 furnishes a gain of 200 and sets the upper 3-dB frequency limit at 10 Hz. The output of U_7 is available as the impedance pneumograph signal.

To discriminate against spurious signals that can arise when the subject moves, a second-order low-pass filter (U_8 and surrounding components) with a cutoff at 1 Hz is added to reduce the active bandwidth. Also, U_9 and associated components form a bipolar dc

restorer that shortens the recovery time after a large extraneous signal. U_{10} is a threshold circuit, with some hysteresis, that converts the respiration signal to a square wave; and U_{11} translates the squarewave voltage limits to zero and +9 volts, as required by the rate processor circuit.

This work was done by George A. Rinard, Dale A. Steffen, and Ronald E. Sturm of the Denver Research Institute for Johnson Space Center. Title to this invention has been waived under the provisions of the National Aeronautics and Space Act [42 U.S.C. 2457(f)], to the Denver Research Institute, Denver, Colorado 80208.

MSC-18226

Hybrid Heart/Breath-Rate Processor

Hybrid circuit processes the signal-conditioner outputs to determine the heart rate and the respiration rate.

Lyndon B. Johnson Space Center, Houston, Texas

A single hybrid circuit converts the time between pulses from the ECG signal conditioner or the breath-rate signal conditioner (see preceding articles) to determine the heart-rate or respiration-rate output of the vital-signs monitor. [See "Hand-Held Vital-Signs Monitor" (MSC-18232) on page of this issue.] The desired operating mode (heart or breath) is selected by routing control frequencies from the clock circuit to the heart/breath-rate processor.

The circuit determines the heart rate from either a beat-to-beat time or from the time of five consecutive beats. No analog techniques are required for the conversion. Because only digital processing is used, no calibration is required, and no components external to the hybrid package are needed. The computed value of heart rate or breath rate is stored in a three-state latch for transfer to the display driver discussed in the next article.

The processor calculates heart rate (from 40 to 200 beats per minute) with an accuracy of 1 beat per minute; it calculates breath rate (from 6 to 24 breaths per minute) with an accuracy

of 1 breath per minute. The calculations are made by dividing a constant factor by the period between beats (or breaths), such that the quotient is equal to the rate in beats or breaths per minute.

Edge-triggered counter 1 (see figure) is clocked by the heart/breath pulses. The one-count or five-count output of counter 1 is selected and transferred (through switch 1) to counter 2. Concurrently, switch 2 routes the correct frequency to the rest of the circuit for the one-beat or five-beat computation mode. Because the time between breaths is relatively long, the respiration rate is computed only on a breath-to-breath basis.

The output of counter 2 initializes the rest of the circuitry for the processing of a heart or breath rate based on a total count, N , accumulated in counter 3 between two successive pulses at counter 2. The count N equals the period between heart or breath pulses multiplied by frequency f_0 (counted by counter 3 during this period).

The count N is latched into register 1, which is used as the preset input for

counter 4, a presettable down counter. Counter 4 is preset at the beginning of the cycle and also whenever it has counted down to zero during the processing. The carry output of counter 4 pulses at a frequency, f_4 , given by

$$f_4 = \frac{f_3}{N} = \frac{f_3}{f_0 T}$$

where T is the heart/breath period, in seconds.

Binary-coded-decimal (BCD) counter 5 counts the frequency f_4 for a period of time, t , generated by shift register 1. At the end of t , a second output of shift register 1 latches the count accumulated by counter 5 in three-state latch register 2. This three-state output allows all three digits to be wired together to form one 4-line BCD output. The digit output-enable lines are controlled through AND gates.

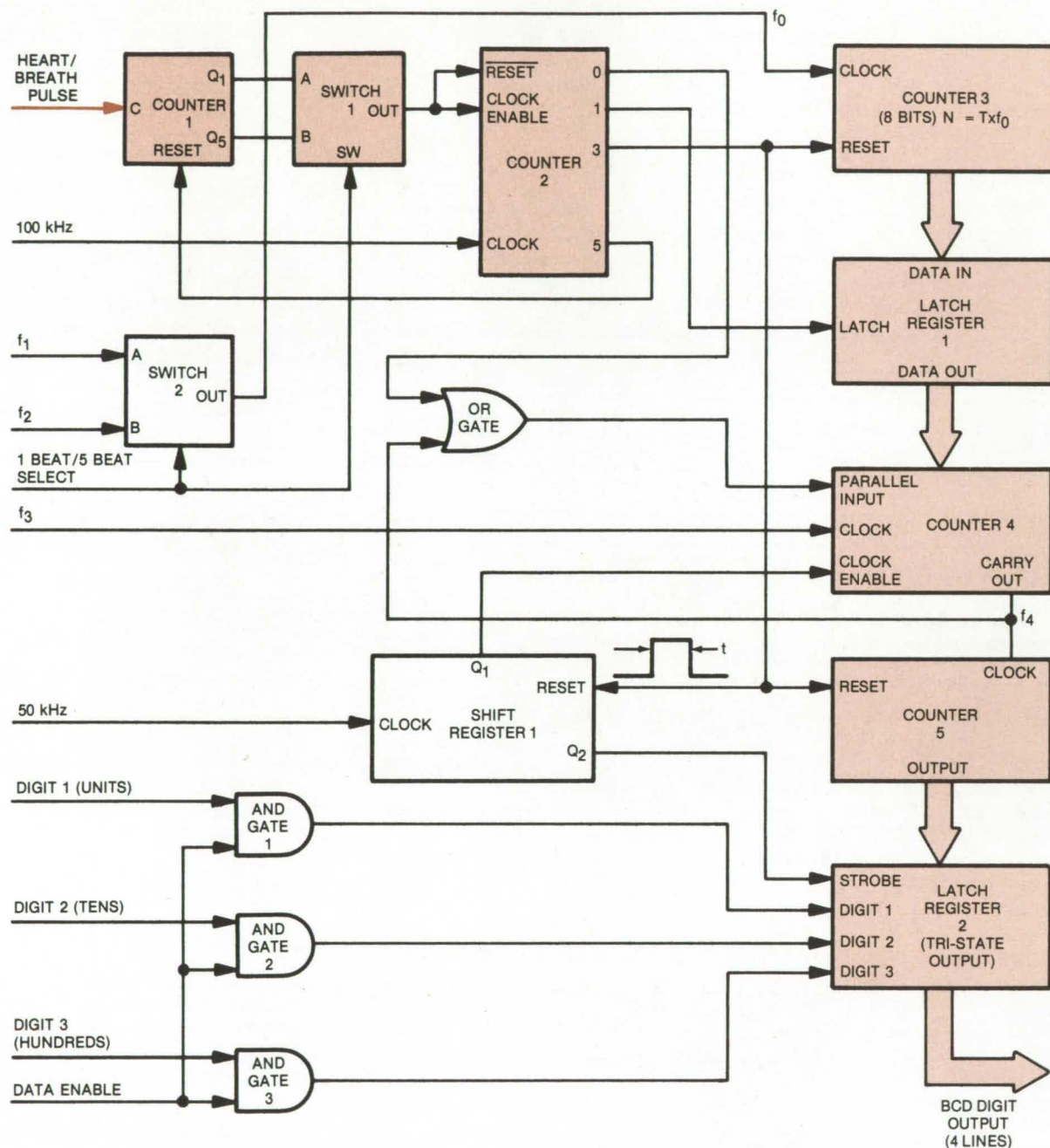
The displayed output is equal to

$$\text{Output} = f_4 t = \frac{f_3 t}{f_0 T}$$

The quantities f_0 , f_3 , and t are selected so that the output reads directly in

(continued on next page)





This **Signal Processor** determines the period between heartbeats or breaths and converts it to a digital heart rate or respiration rate.

beats or breaths per minute. For example, for the heart-rate determination, $f_0 = 166.6$ Hz, $f_3 = 50$ kHz, and $t = 0.2$ s. For these values, the output is $60/T$ breaths per second, as required.

This work was done by George A. Rinard, Dale A. Steffen, and Ronald E. Sturm of the Denver Research Institute for Johnson Space Center. Title to this invention has been waived under the provisions of the National

Aeronautics and Space Act [42 U.S.C. 2457(f)], to the Denver Research Institute, Denver, Colorado 80208. MSC-18227

Hybrid LCD Driver

Display driver can operate either 4-digit or 16-digit liquid-crystal displays.

Lyndon B. Johnson Space Center, Houston, Texas

The display driver for the vital-signs monitor [see "Hand-Held Vital-Signs Monitor" (MSC-18232) on page 551 of this issue] can be configured to operate either a 4-digit liquid-crystal display (LCD) or, by paralleling four drivers, to operate a 16-digit display. Multiplex and control circuitry included in the hybrid can synchronize four drivers to route the binary-coded-decimal (BCD) data from the vital-signs processors to the proper digits on the display.

Figure 1 is a schematic of the driver circuit. It includes four BCD-to-LCD decoders and two one-of-four decoders that work with a divide-by-16 counter to generate the digit- and display-select signals. The vital-signs data are held in three-state output latches in the processors and are multiplexed one digit at a time along the four incoming BCD lines to the display driver. The digit-select output of the driver multiplexing logic sequences the display decoders to route each incoming BCD digit to the correct part of the display. In this 3½-digit mode, a switch on the front panel would select the vital function to be viewed by the operator.

The circuit shown in Figure 2 controls a 16-digit readout that would simultaneously display all the vital signs. In this mode, each incoming BCD digit is OR-wired to the inputs of all four drivers, and the display-select lines from driver No. 1 would turn on the correct driver output to route the digit to its proper position on the display.

(continued on next page)

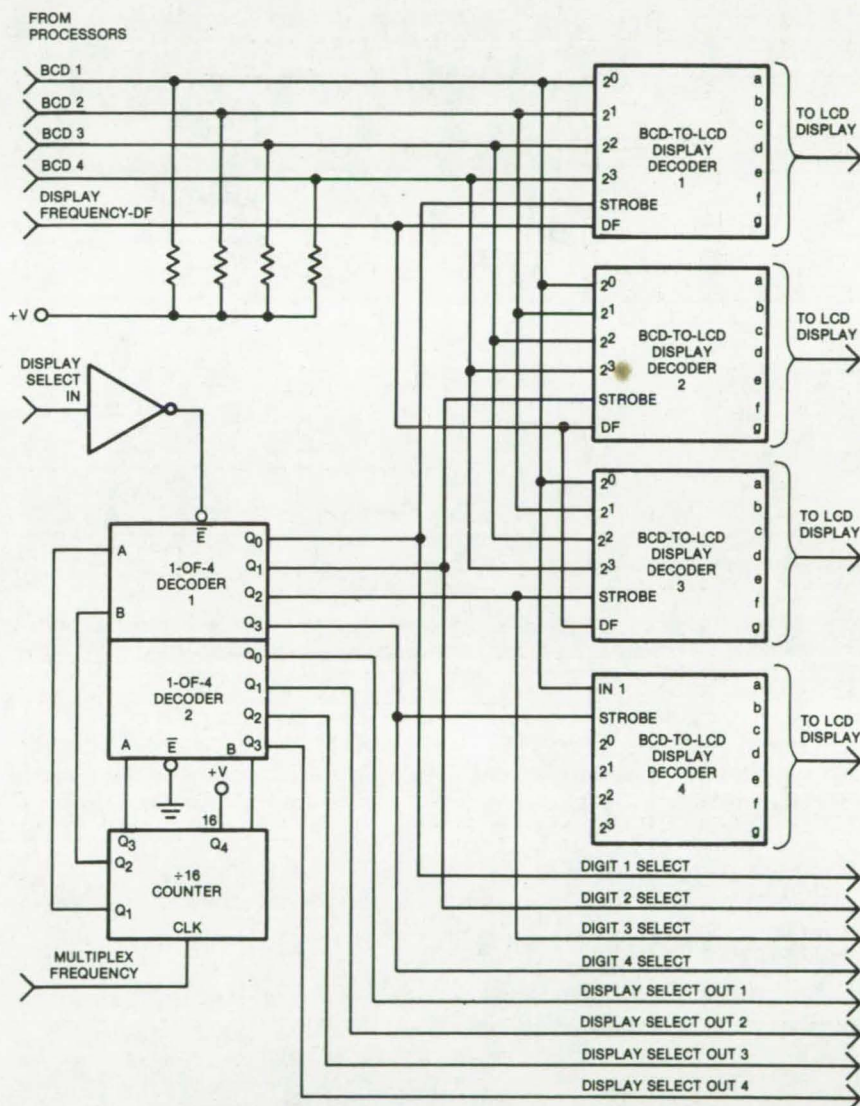


Figure 1. This **Liquid-Crystal-Display Driver** is housed in a single hybrid package. It generates digit- and display-select signals to operate a 16-digit display (as in Figure 2); or it can be used to operate a 3½-digit display for a hand-held unit.

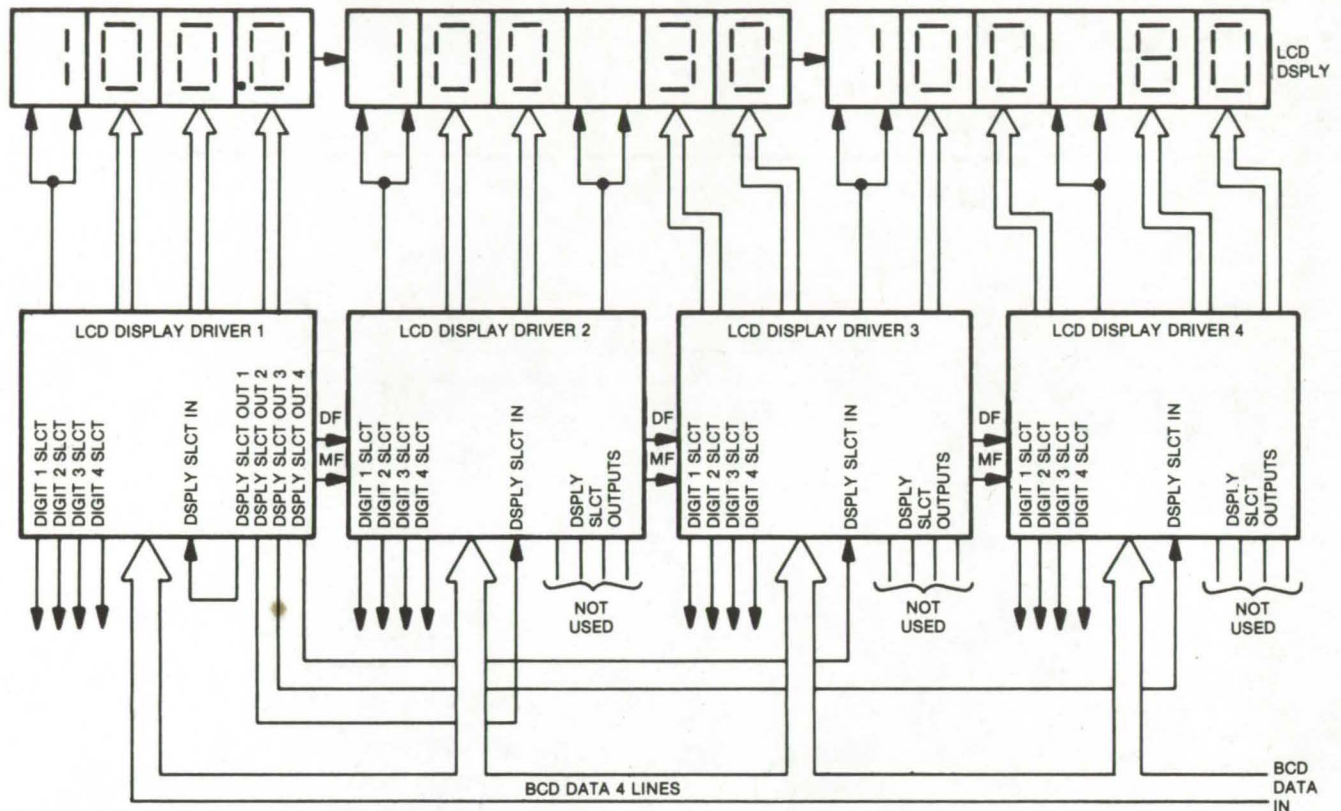


Figure 2. A 16-Digit Vital-Signs System would use four display drivers of the kind shown in Figure 1. Driver No. 1 provides the display-select signals that synchronize the "on" times of all four drivers with the incoming data.

This work was done by George A. Rinard, Dale A. Steffen, and Ronald E. Sturm of the Denver Research Institute for **Johnson Space Center**. Title to this invention has been waived

under the provisions of the National Aeronautics and Space Act [42 U.S.C. 2457(f)], to the Denver Research Institute, Denver, Colorado 80208. MSC-18229

Hybrid Clock Generator

Nine discrete frequencies are produced by a low-power hybrid circuit.

Lyndon B. Johnson Space Center, Houston, Texas

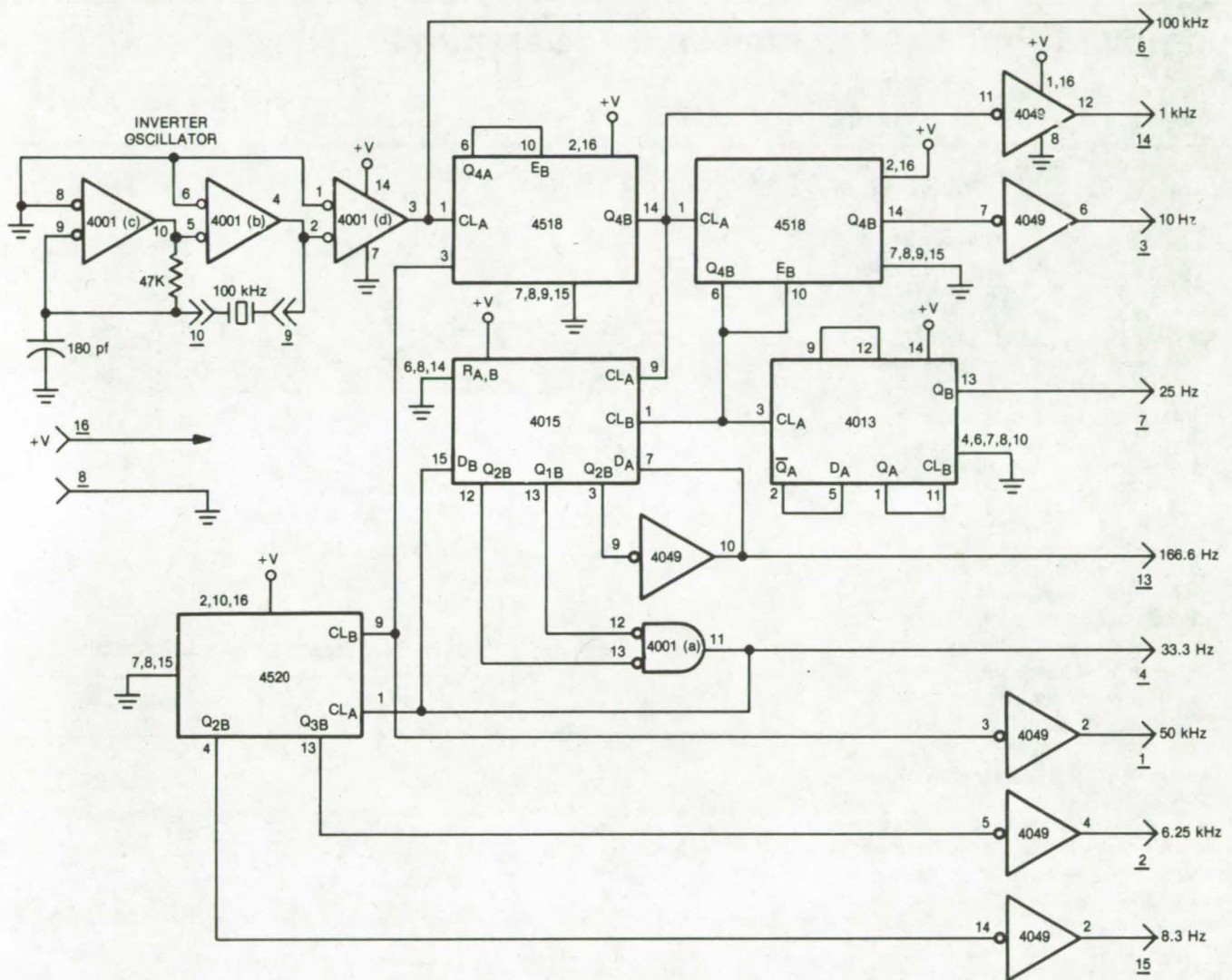
The clock driver hybrid for the vital-signs monitor [see "Hand-Held Vital-Signs Monitor" (MSC-18232) on page 551 of this issue] generates all the frequencies required for operation of the vital-signs system in a compact low-power configuration.

As shown in the figure, the primary clock frequency (100 kHz) is developed

by a crystal-controlled inverter oscillator. The oscillator is followed by several divider stages that produce a range of selected frequencies between 6.25 Hz and 50 kHz.

All of the circuitry uses standard 4000-series CMOS logic. Included among the IC chips that go into the hybrid are:

- A dual binary-coded-decimal (BCD) counter that is wired as a divide-by-2 stage followed by a divide-by-50 stage (4518);
- another dual BCD counter, wired as two divide-by-10 stages (4518);
- a dual D flip-flop, wired as a divide-by-4 stage (4013);



This **Hybrid Clock Generator** provides the nine frequencies required for the vital-signs monitor.

- a dual 4-bit shift register, wired as one divide-by-6 stage and one divide-by-3 stage (4015);
- a dual binary counter, wired as a divide-by-6 stage and a divide-by-4 stage (4520);
- a 4 hex buffer and (4049);

- a quad NOR gate (4001). The 100-kHz quartz crystal is connected between terminals 9 and 10 of the 16-pin hybrid package.

This work was done by George A. Rinard, Dale A. Steffen, and Ronald E. Sturm of the Denver Research Insti-

tute for **Johnson Space Center**. Title to this invention has been waived under the provisions of the National Aeronautics and Space Act [42 U.S.C. 2457(f)], to the Denver Research Institute, Denver, Colorado 80208. MSC-18228

Improved Probe for Rectal-Cancer Detection

Modified proctosigmoidoscope permits forward and lateral vision of the colon wall.

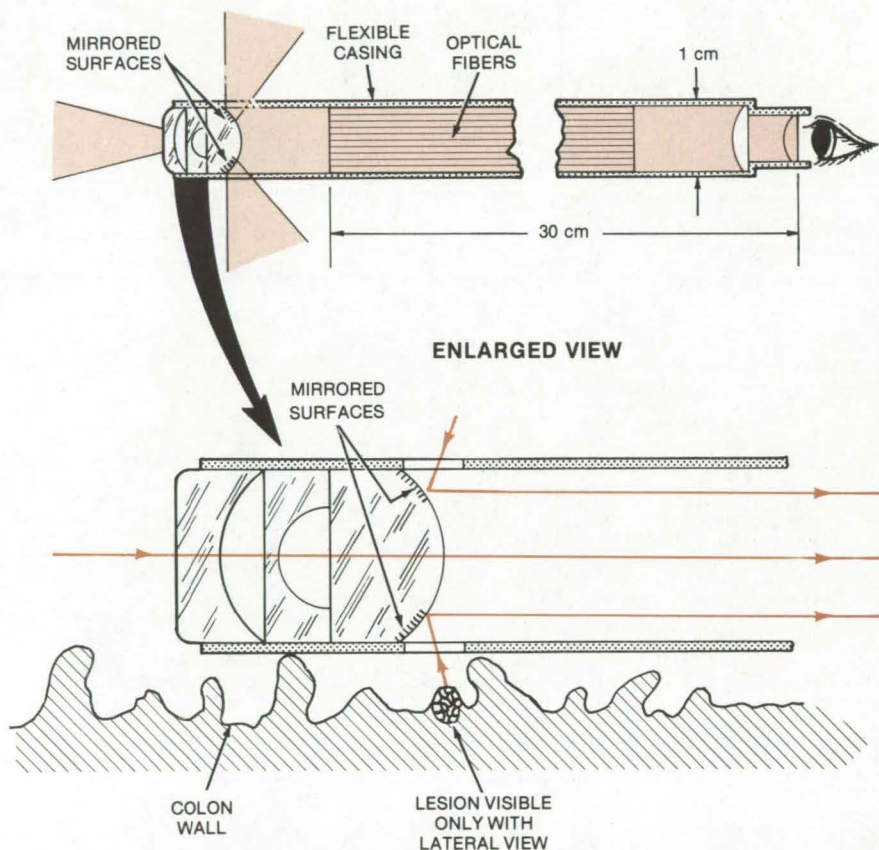
NASA's Jet Propulsion Laboratory, Pasadena, California

The thorough examination of patients for malignant and premalignant lesions of the colon and rectum ideally requires an instrument that gives both forward and lateral visibility. As the examiner guides the instrument through the large intestine, it is important that he sees ahead to avoid perforating the wall of the intestine and also that he sees to the side to view around intestinal folds.

Currently-available optical devices for this purpose include the colonoscope, a thin flexible probe, usually administered by a skilled clinician, that carefully examines the entire large intestine, and the proctosigmoidoscope, a larger probe for the rectum and colon. The proctosigmoidoscope is a less-expensive and more easily administered device. Both instruments have restricted lateral vision.

The modified proctosigmoidoscope shown in the figure is able simultaneously to "see" in the forward direction and laterally. It differs from the conventional two-lens designs by the addition of a third lens which is partially mirrored. The central circle of the lens is not mirrored and is one element of the refracting system that forms an image of the frontal view. The mirrored convex surface around the perimeter of the lens reflects the lateral image of the colon wall.

The operator sees a double image when using the instrument; he sees a central image of the forward direction and an outer concentric ring that shows what is directly to the side or slightly behind the viewing port.



This **Modified Proctosigmoidoscope** is given an expanded field-of-view by the addition of a partially mirrored lens. The examiner sees both frontal and lateral views. The light source is outside the body and is piped into the colon through a sheath that surrounds the outer casing.

This work was done by Robert E. Frazer of Caltech for **NASA's Jet Propulsion Laboratory**. For further information, Circle 59 on the TSP Request Card.

This invention is owned by NASA, and a patent application has been filed. Inquiries concerning nonexclusive or exclusive license for its commercial development should be addressed to the Patent Counsel, NASA Resident Legal Office-JPL [see page A8]. Refer to NPO-14247.

Self-Propelling, Self-Locating Colonoscope

Proposed articulated instrument would move by air-actuated bladders, defining its position by ultrasonic or RF signals.

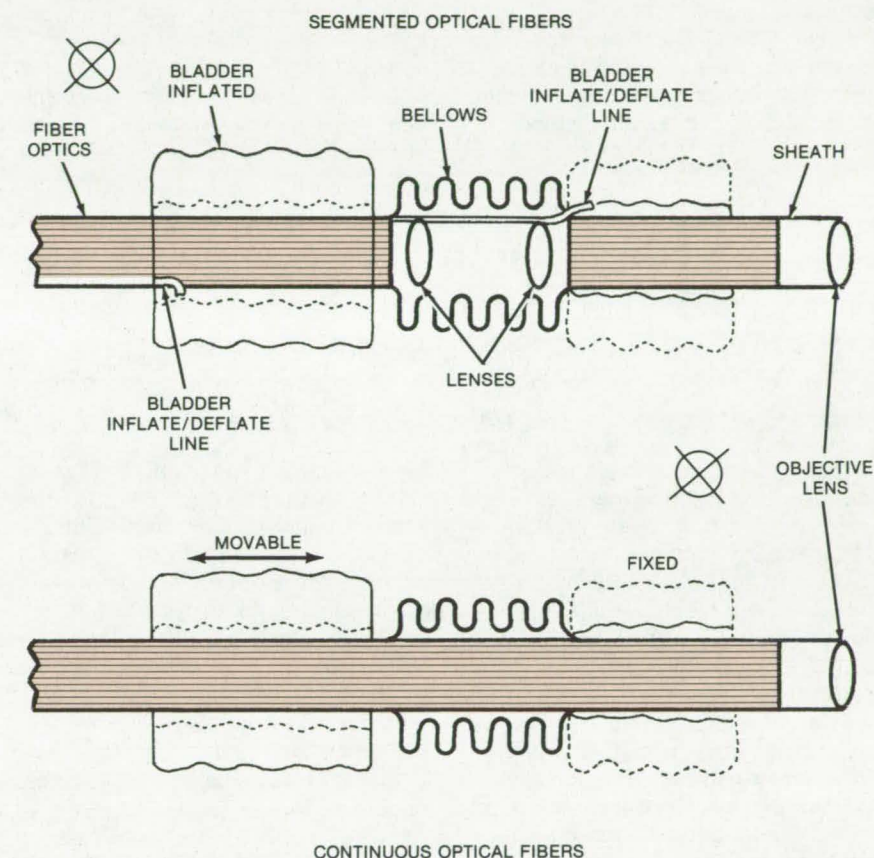
NASA's Jet Propulsion Laboratory, Pasadena, California

New concepts in the design of a colonoscope would facilitate its movement through the colon and make it easier to pinpoint its location. The design would allow optical inspection of the large bowel, from the cecum to the rectum, with minimal discomfort or risk to the patient and no exposure to harmful radiation of the patient or the diagnostician.

The colonoscope would be simple to operate and could be administered by relatively unskilled clinicians. It is expected to make gastrointestinal examinations, which are now performed only by experienced colonoscopists, more widely available for early diagnosis of inflammation, polyps, colonic tumors, intestinal parasites, and other ailments.

The new design (see figure) has an articulated end that flexes its way through the colon. Within the end are optical fibers, some of which illuminate the wall of the colon and others of which receive an image of the wall. The light is transferred through the articulating bellows by a lens, linked by optical fibers to an external light source and a screen. The diagnostician views a continuous display of small areas of the colon as the instrument moves through it. Inflatable bladders fore and aft of the bellows are sequentially inflated and exhausted as the bellows is expanded and contracted so that the articulated end moves through the colon.

Several tracking methods have been proposed, using ultrasonic or radio-frequency (RF) signals. In using ultrasonics, a single transmitter (e.g., a piezoelectric crystal) on the tip of the colonoscope could be sensed by an array of two or more receivers on the anterior or lateral surfaces of the abdomen. The arrival times of a pulse signal from each transmitter could be used to generate an X,Y-coordinate display of the path on a cathode-ray tube. The transmitter crystal must lie at the intersection of two circles, the centers of which are located at the detectors and



Two **Possible Self-Propelling Colonoscopes** are shown. In the version illustrated in the upper figure, the bladders inflate and deflate, but they do not move laterally along the probe; lenses relay the image between the sections of optical fibers. In the lower figure, the bladder on the right is fixed laterally, and the bladder on the left moves along the probe body. In this version, a continuous fiber-optic bundle is used.

the radii of which are proportional to the elapsed time between the transmitted and received pulses.

For each pulse transmitted by the piezoelectric crystal at the tip of the colonoscope, a point would be defined and displayed on the CRT. Since the crystal can be pulsed in rapid succession, the position of the moving tip can be displayed as a series of points. With ultrasonics, acoustic coupling between the transducer and the body is essential since an airpath offers too much impedance; a liquid or gel layer could be provided for this purpose.

Other methods for tracking the colonoscope can be simpler than ultrasonics but may compromise the opportunity for real-time display of its location. Possible methods include mounting a magnet on the distal end of the colonoscope and detecting and tracking its position and direction with a small magnetometer on the abdomen; and incorporating a tuned circuit at several points along the length of the colonoscope. In this approach, external RF generators, tuned to resonate with the internal circuits, would exhibit
(continued on next page)

characteristic changes in load when directed toward the colonoscope resonator. A similar concept has a set of external opposing Helmholtz coils arranged to buck each other and create a moving nulled-out zone in the region of the colonoscope. Two pairs of coils would create a null zone in X and Y coordinates covering the area of the abdomen. When this zone traverses the position of the resonant circuits, the load could undergo a transient that would be displayed on a CRT or an X-Y recorder.

In addition to the bladder/bellows system, other methods of locomotion are also being studied. One proposal calls for small compliant paddles arranged in a helix around the articulated end. If the end is rotated, the paddles would pull themselves along like a propeller.

Another possibility replaces the bellows by a tube of plastic that softens and hardens over a narrow temperature range. Under external control, this tube could be heated so that it bends around the flexures of the colon; it

would be cooled for passage through the straight regions.

This work was done by Robert E. Frazer of Caltech for NASA's Jet Propulsion Laboratory. For further information, Circle 60 on the TSP Request Card.

Inquiries concerning rights for the commercial use of this invention should be addressed to the Patent Counsel, NASA Resident Legal Office-JPL [see page A8]. Refer to NPO-14092.

Noncontacting Electrokinetography System

Remote ultrasonic probe measures the motion of the chest wall to aid in the diagnosis of heart condition.

Lyndon B. Johnson Space Center, Houston, Texas

A noncontact acoustic technique for recording the motion of the chest wall during the cardiac cycle can give information on changes in the size, shape, and compliance of the heart ventricles. The technique utilizes air-coupled ultrasonic transducers that operate only slightly above audible frequencies. The transducers are arranged in a phasemeter configuration for measuring absolute changes in the distance between the transducer assembly and the chest wall. Because the skin surface reflects very-low-frequency ultrasound, only chest-wall motion is sensed by this technique.

In a prototype of the new probe, known as an acoustic kinetocardiometer, the transducers are housed in plastic cones that direct the ultrasound, and the assembly is mounted on an adjustable rotating arm. When

the probe is in position, the transmitting and receiving crystals are about 10 inches (25 cm) from the chest wall. The transducer cones are focused on the chest in a pattern corresponding to the standard "V" positions used to identify electrocardiogram (EKG) leads. All the necessary electronics and data recorders are located on a table near the patient's bedside.

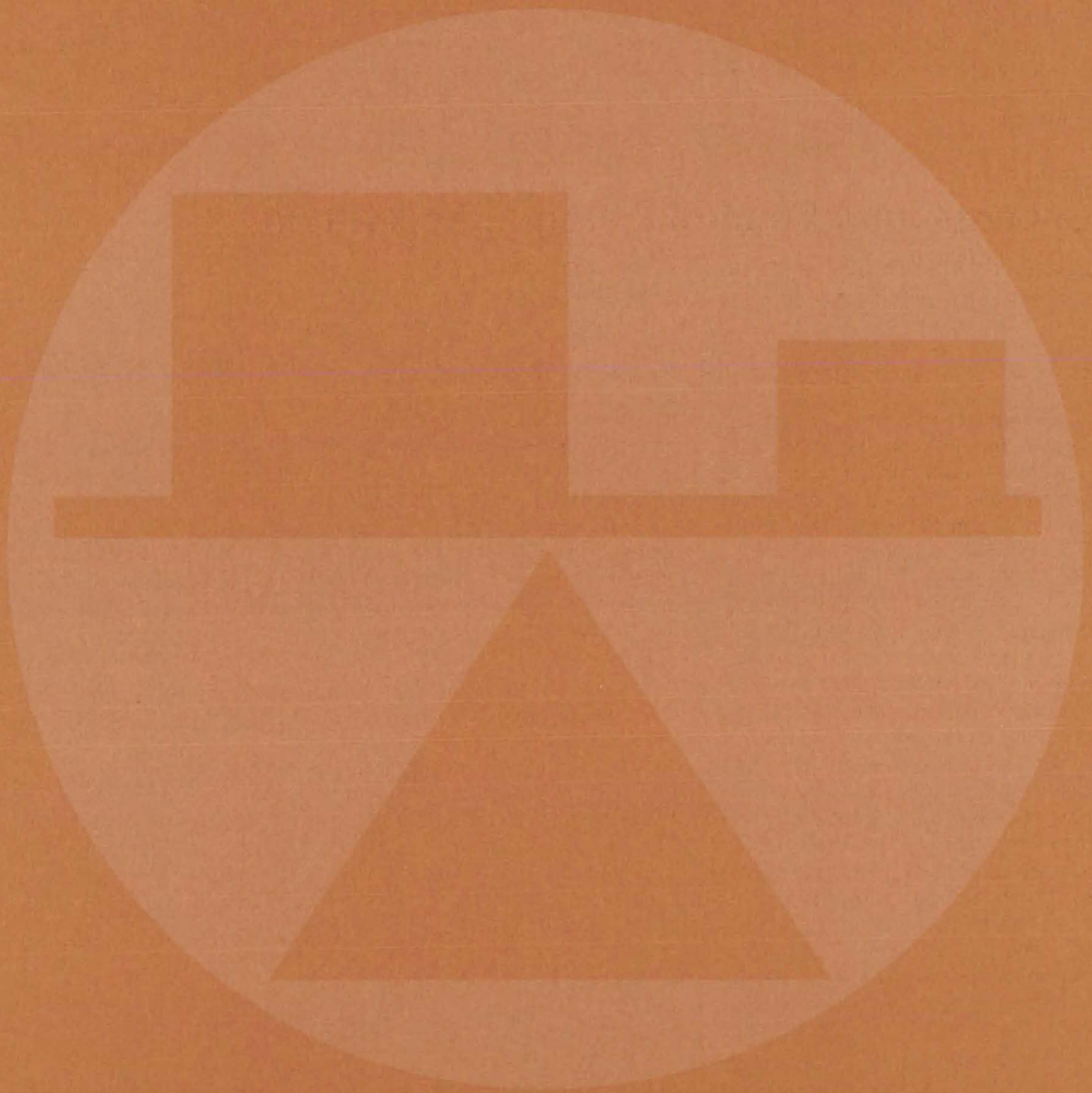
Clinical studies using the probe are underway for the early diagnosis of right ventricular hypertrophy associated with obstructive respiratory disease. For this purpose, it has been found that the acoustic kinetocardiometer is an effective adjunctive diagnostic tool that complements radiological evaluation. It provides data that cannot be obtained by other noninvasive methods. Because of its

simplicity, it would probably require only a fraction of the investment required for an echocardiographic apparatus (which uses high-frequency ultrasound to image the heart). Also the output of the probe could be digitized and fed to a microprocessor for rapid storage and analysis.

This work was done by Jerry G. Davis and David M. Hickman of the Lovelace-Bataan Medical Center for Johnson Space Center. Further information may be found in NASA CR-151626 [N78-17664], "Specialized Physiological Studies in Support of Manned Space Flight." A copy may be obtained for \$6.50 [prepayment required] from the National Technical Information Service, Springfield, Virginia 22151.

MSC-18162

Mechanics



Hardware, Techniques, and Processes

- 567 Real-Time Instrument Averages 100 Data Sets
- 568 Miniature Thermocouple Disconnect
- 569 High-Sampling-Rate Pressure Transducer Has In Situ Calibration
- 570 Shock-Swallowing Air Sensor
- 571 Measuring Projectile Speed
- 572 Miniature Velocimeter
- 573 Multiple-Sample Holder for IC Testing
- 574 SEM Probe of IC Radiation Sensitivity
- 575 Topping Pressures for Gas-Storage Cylinders
- 576 Dynamic Measurement of Bulk Modulus
- 577 Elastic Deformation of Ball Bearings, Gears, and Cams
- 578 Compact Turbidity Meter
- 579 Automated Inspection of Wire-Frame Assemblies
- 580 Detecting Surface Deformations Photographically
- 581 Compression Testing of Flammable Liquids
- 582 Acousto-optical Imaging Without Immersion
- 583 Detecting Moisture in Composite Honeycomb Panels
- 583 Refrigerant Leak Detector
- 585 "Gentle" Holder for Brittle Ceramics

Computer Programs

- 586 Potential Flows in Propulsion System Inlets
- 586 Orbital Heat Rate Package
- 587 Tumbling-Vehicle Entry Heating
- 588 Flow in Axisymmetric Ducts With Struts

Real-Time Instrument Averages 100 Data Sets

Averager curves for automobile-engine parameters are obtained instantly.

Lewis Research Center, Cleveland, Ohio

An instrument has been designed and built that can generate the average curve of 100 consecutive cycles of any function that occurs as a time-varying electrical signal. This instrument has been successfully used to average parameters on a 1975 Chevrolet V-8 engine and on a Continental 6-cylinder aircraft engine. The curve is generated in real time and is available immediately after the conclusion of the 100th cycle.

The curve-averaging instrument can be considered in four sections as shown in the block diagram of Figure 1: the curve-averaging and storage section, which adds the 100 curves and divides the output by 100; the 100-sample logic, which detects when 100 samples have been averaged and stored; the input and output multiplying circuits, which allow multiple traces to be averaged and stored; and the timing logic, which initiates the analog-to-digital conversion pulse.

The instrument, shown in Figure 2, was developed to measure the important parameters associated with the operation of an internal-combustion engine, such as mass-fraction burn rate, ignition energy, and the indicated mean effective pressure. A major characteristic of internal-combustion engines is the cycle-to-cycle variation of these parameters.

These variations are particularly prominent at lean mixture ratios, which are currently of great interest for investigating emission reduction and economy gain.

Because of the cycle-to-cycle variation, a single cycle curve cannot be used to characterize engine operation at any given time. The curve-averaging instrument was designed to generate an average curve over 100 cycles of engine operation. Each individual curve is sampled at 2,048
(continued on next page)

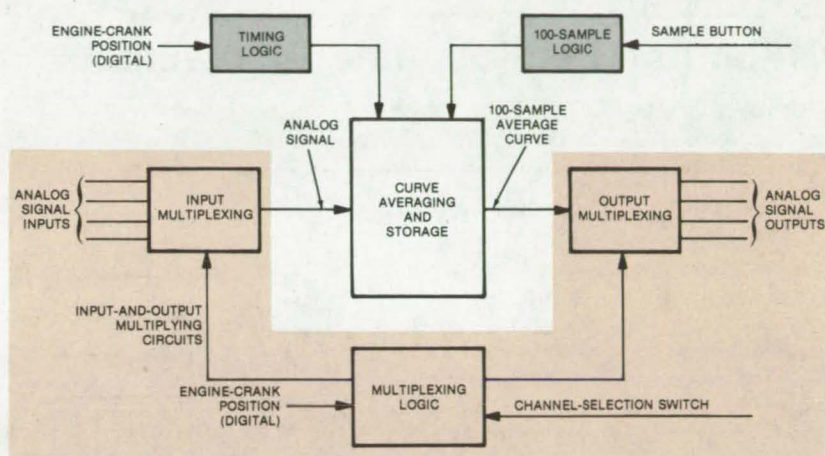


Figure 1. **Curve Averager** receives 100 input curves (data sets) and produces an average curve in real time.

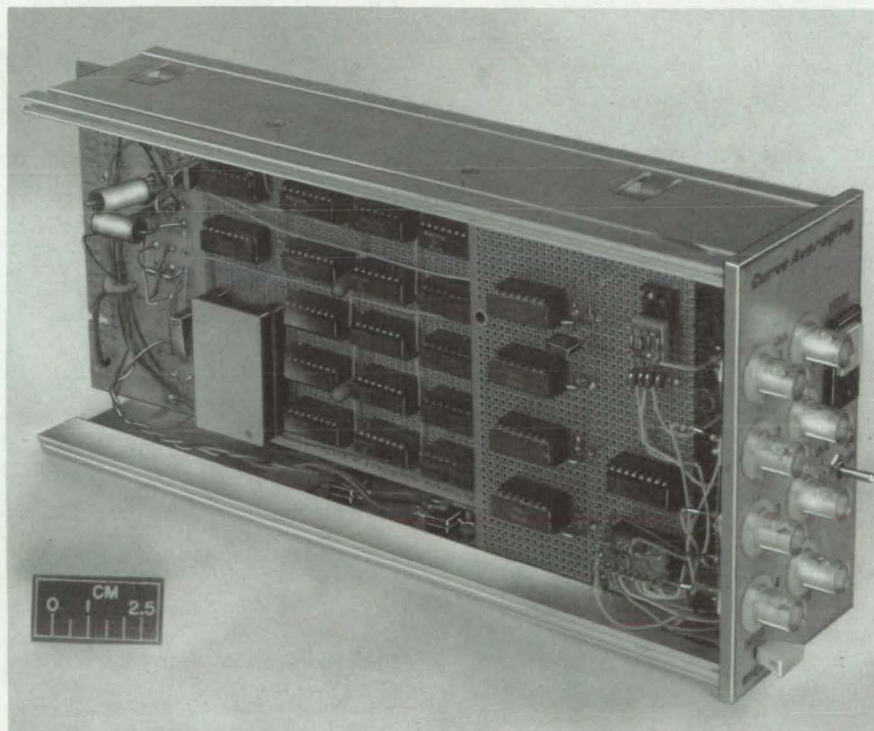


Figure 2. **Modular Construction** and compact size make the curve-averager potential compatible with other diagnostic equipment.

discrete points. Inputs can be any parameter that is expressed as a ± 10 -volt signal. The value of each curve at these points is added to the corresponding values for each of the 100 consecutive curves and is then divided by 100 to yield the average

curve. As many as four parameters can be averaged simultaneously with some decrease in resolution.

This work was done by Arthur G. Birchenough, William J. Rice, and George B. Tuma of **Lewis Research Center**. Further information may be

found in NASA TP-1055 [N78-11301], "Instrument to Average 100 Data Sets," a copy of which may be obtained at cost from the New England Research Application Center [see page A7].
LEW-13093

Miniature Thermocouple Disconnect

Small, reliable disconnect designed for wind-tunnel model instrumentation

Langley Research Center, Hampton, Virginia

A commercially-available subminiature connector has been modified for use with both flexible and small-diameter metal-sheathed thermocouples. The result is a reliable thermocouple for instrumentation on wind-tunnel models that is smaller than the commercial disconnect normally used.

The standard connector is modified with a combination sheath connector (Figure 1) and termination support. Figure 2 illustrates the connector assembly for a flexible-wire thermocouple. It is made by stripping and properly tinning the leads, which are then electrically insulated and soldered into the connector cups. Heat-shrinkable sleeving is put on to insulate the terminals and to help support the thermocouple wire.

The connector assembly for the metal-sheathed thermocouple is also shown in Figure 2. In this case, the metal sheath is first removed from the termination area, and the exposed leads are then properly tinned and formed. The sheath termination/connector support is positioned and attached to the sheath, and the following steps are carried out in sequence:

1. Trim leads to proper length.
2. Attach connector body to the support.
3. Solder leads into solder cup.
4. Clean the assembly.

The contact metal of the connector is not a thermocouple material. Therefore, one must insure a uniform temperature over the connector contacts. This can be done by properly positioning the termination and covering it entirely with thermal insulation.

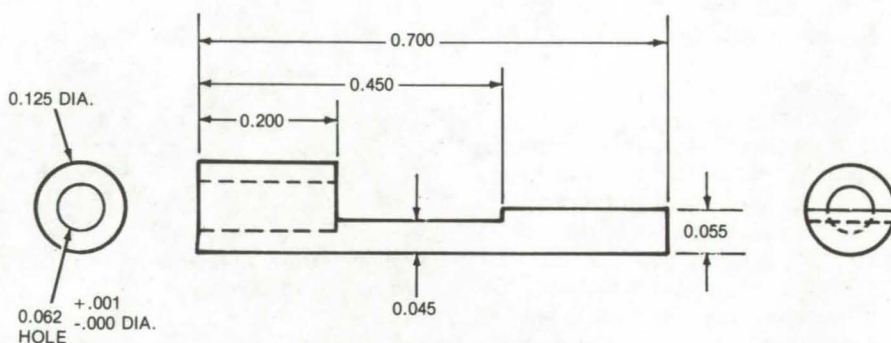


Figure 1. **Sheathed-Cable-to-Connector Support** is machined from a 1/8 in. O. D. stainless steel.

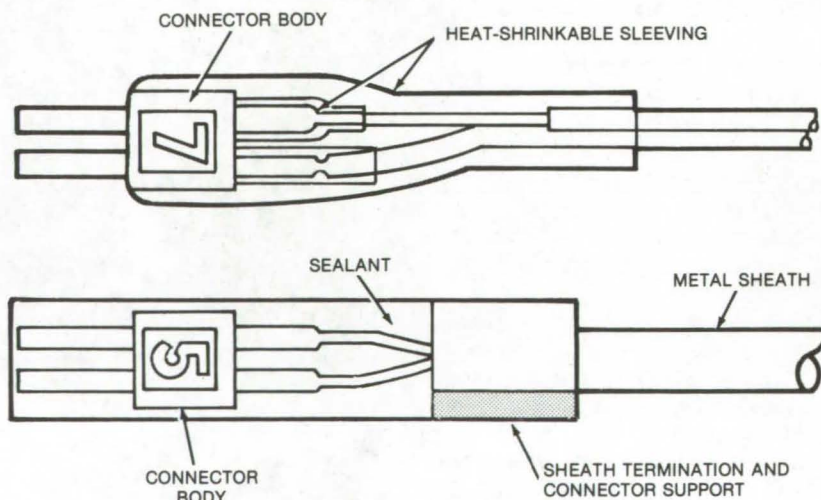


Figure 2. **Thermocouple Disconnects** are shown for flexible-wire and rigid thermocouples. The flexible-wire disconnect is made by soldering the leads into the cups of subminiature connector and covering with heat-shrinkable tubing. The rigid-thermocouple disconnect for a metal-sheathed thermocouple is made with a subminiature connector and a special combination sheath termination and connector support (see Figure 1).

This work was done by Kenneth L. Quinn of **Langley Research Center**. No further documentation is available.
LAR-12013

High-Sampling-Rate Pressure Transducer Has In Situ Calibration

Electrically-multiplexed pressure sensor is designed for tests requiring rapid sampling rates.

Langley Research Center, Hampton, Virginia

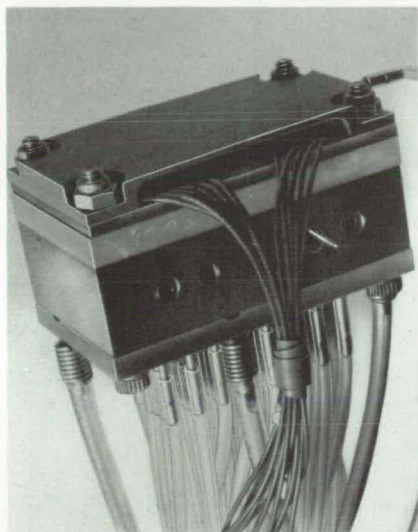


Figure 1. **48-Channel Pressure Sensor** can take pressure measurements at a rate of 1,000 reading/s. With the 48 pressure ports, it measures 4.3 by 2.5 by 2.4 cm with a volume of 25.7 cm³. A disassembled view is shown in Figure 2.

A new high-data-rate pressure-sensor module can be calibrated after it is attached to an experimental setup. It was developed for use with wind tunnels and other applications requiring accurate measurement of many pressures in a short period of time.

Conventional methods of measuring pressures on wind-tunnel models involve many pressure ports and are characterized by either low data rates, large size, low accuracy, or high cost. For instance, electromechanically-scanned pressure-sampling switches allow accurate measurements of many ports, but at a maximum data rate of 10 measurements per second. The use of individual pressure transducers to achieve a high data rate is often impractical because of size requirements and cost. Some prog-

ress in the development of pressure-sensing concepts with potentially high data rates has been made recently. However, such systems either lack in situ calibration capability or are too large to be mounted in most wind-tunnel models.

The newly-developed 48-channel module largely overcomes the drawbacks of size, accuracy, and cost of previous systems. The module uses miniature silicon-diaphragm pressure sensors, miniature electronic multiplexers, and a miniature, multiport, pneumatically-operated pressure-selector switch. It is small, has a high data rate, and can be kept accurate by in situ calibration.

The 48-channel pressure-sensor module is shown in Figure 1. The module substrate contains 16 solid-state pressure-sensor chips and signal (continued on next page)

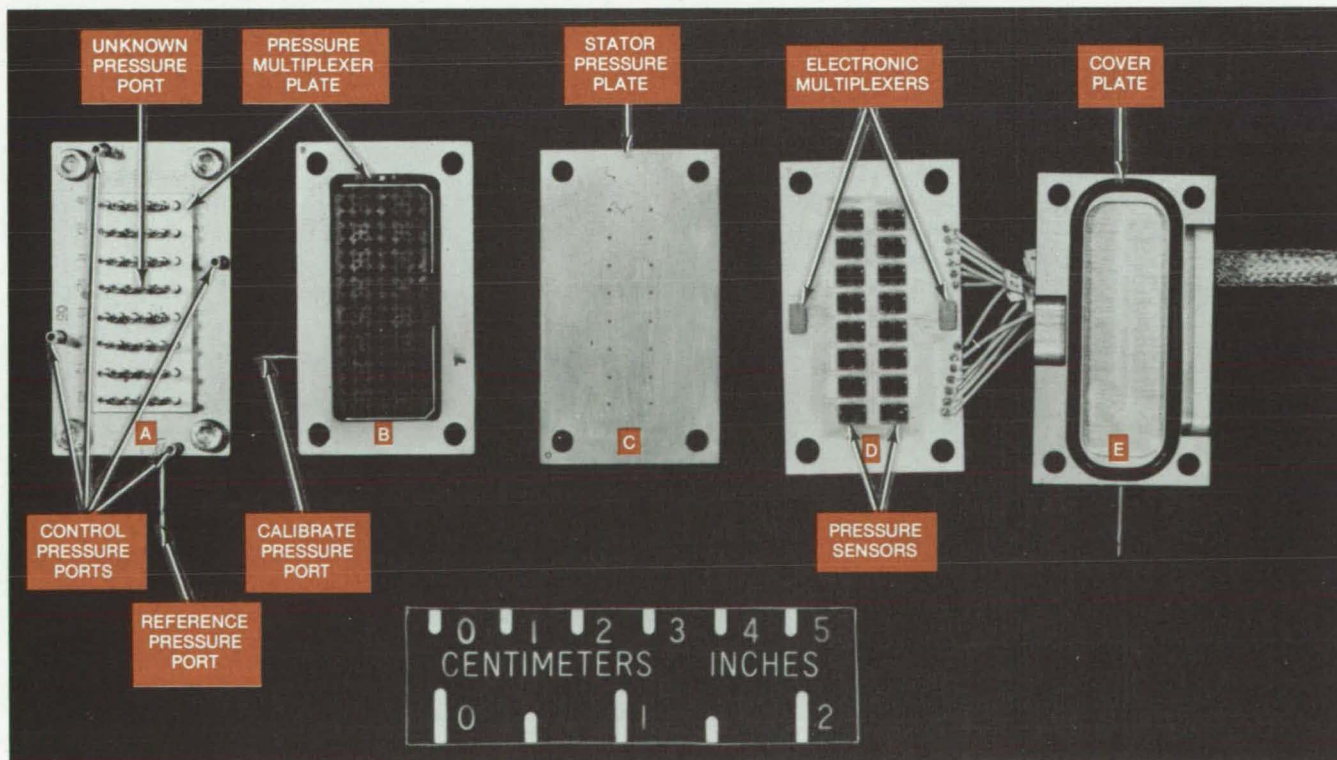


Figure 2. **Disassembled View** of the 48-channel pressure module shows major components. The use of miniature solid-state pressure-sensor chips helps reduce cost and size of the instrument.

multiplexing electronics connected to a four-position pressure-selector switch. One of the four positions allows in situ calibration of the pressure-sensor chips; the other three are for measuring 48 unknown pressures (three sets of 16).

The pressure-sensor substrate board (see Figure 2) contains 16 epoxy-bonded pressure-sensor chips and two 8-channel signal multiplexers with etched metal interconnections. Pressures to be measured are introduced via holes beneath each chip. Each silicon-diaphragm pressure-

sensing chip contains four junction-isolated piezoresistance strain-sensing elements in a Wheatstone-bridge configuration. Pressure is measured by the change in the bridge output caused by varying stresses. The analog outputs from the pressure sensors are fed into the two 8-dual-channel signal multiplexer chips. The multiplexer chips have a channel-on resistance of approximately $2\ \Omega$ with maximum access time of 1 microsecond. The 16-sensor array may be scanned at high data rates by

addressing each sensor with a specific digital code.

This work was done by Chris Gross of Langley Research Center. For further information, Circle 61 on the TSP Request Card.

This invention is owned by NASA, and a patent application has been filed. Inquiries concerning nonexclusive or exclusive license for its commercial development should be addressed to the Patent Counsel, Langley Research Center [see page A8]. Refer to LAR-12330.

Shock-Swallowing Air Sensor

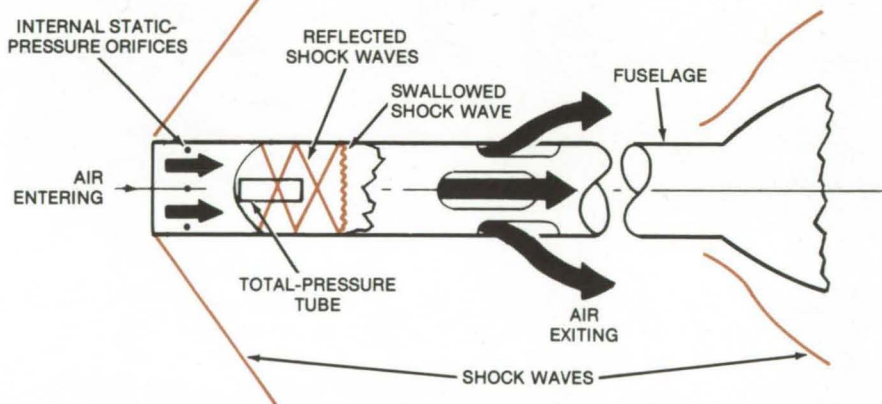
Probe measures mach number more accurately by removing shock wave.

Dryden Flight Research Center, Edwards, California

A new "shock-swallowing" probe measures air data over a wide range of speeds, from supersonic to hypersonic, with high accuracy. The probe eliminates the error created by shock waves in conventional probes — error that varies with airspeed and must be corrected by calculations.

The new probe allows air to flow through it (see figure), thereby "swallowing" the bow shock wave and removing it from measurement orifices. The probe is open at its forward end so that it can ingest air and has slots at its aft end so that the air can leave. Internal static-pressure orifices are located near the forward end, and a total-pressure tube is positioned along the probe axis. (Instruments determine the mach number from the total internal pressure and the static-pressure measurements.) The shock wave, instead of forming at the tip of the probe as it does in conventional sensors, forms inside the probe toward the rear, well behind the measurement orifices where it would distort the measured values.

Shock-swallowing probes have previously been used in wind tunnels and arc jets to measure mass flux and other free-stream flow parameters. The new probe is intended for measuring mach number in high-performance aircraft over widely varying altitudes and speeds. Like conventional probes, it can be mounted on an airplane nose boom.



Air-Data Probe allows air to flow through it so that the inevitable supersonic shock wave forms behind pressure-measuring orifices and tube instead of directly on them. Measured pressures therefore are close to those in free-flowing air and are used to determine mach numbers of flying aircraft.

In wind-tunnel tests, the probe demonstrated a number error comparable to existing probes. It was tested at various angles of attack and angles of sideslip. The exit slot area was found to be critical. With small slot openings, the shock wave is not swallowed; measurements are erratic, and error is unacceptably large. Once the slot area is increased beyond a certain size, however, the shock wave enters the probe, and measurement error drops to a uniformly low level.

The tests also explored the effects of altering the positions of the internal static-pressure orifices and the total-pressure tube. The measurement error

was smallest, the tests showed, when the orifices were near the probe entrance, where they are least likely to be influenced by reflected shock waves. For the same reason, the total-pressure tube should be placed near the probe entrance. The probe data were also used to determine flow direction.

This work was done by Jack Nugent, Glenn M. Sakamoto, and Lannie D. Webb of Dryden Flight Research Center and Lana M. Couch of Langley Research Center. For further information, Circle 62 on the TSP Request Card.

FRC-10107

Measuring Projectile Speed

The time-of-flight of a projectile down a barrel is measured by an optoelectronic detector.

Langley Research Center, Hampton, Virginia

The apparatus shown in Figure 1 measures the speed of a small projectile by noting the times at which it passes two stations that are spaced a known distance apart. The instrument was developed for an aircraft structural-research program, in which the impact resistance of a composite material is determined by propelling an aluminum sphere down a steel barrel and against the surface of the composite. To analyze the impact damage, it is necessary to know the momentum of the sphere.

The two stations are mounted about 15 cm apart on an aluminum housing that is bored and threaded to screw onto the muzzle end of an air gun. The station closest to the muzzle generates a start signal to a time-interval meter, and the second station supplies the stop signal. The meter readout is in microseconds.

(continued on next page)

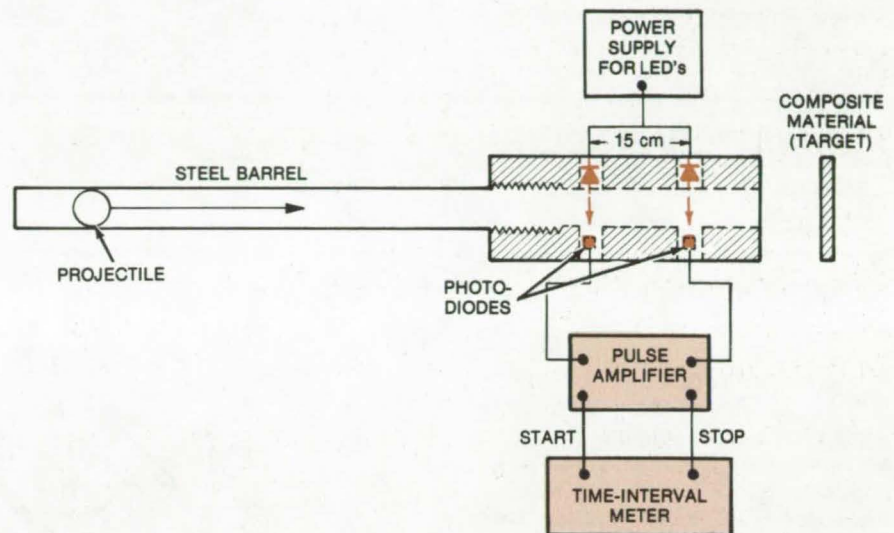


Figure 1. A Moving Projectile Triggers a Time-Interval Meter, once to start it and once to stop it, as the projectile passes through two light beams. The interrupted beams turn off a photodiode detector, delivering start and stop pulses to the timer.

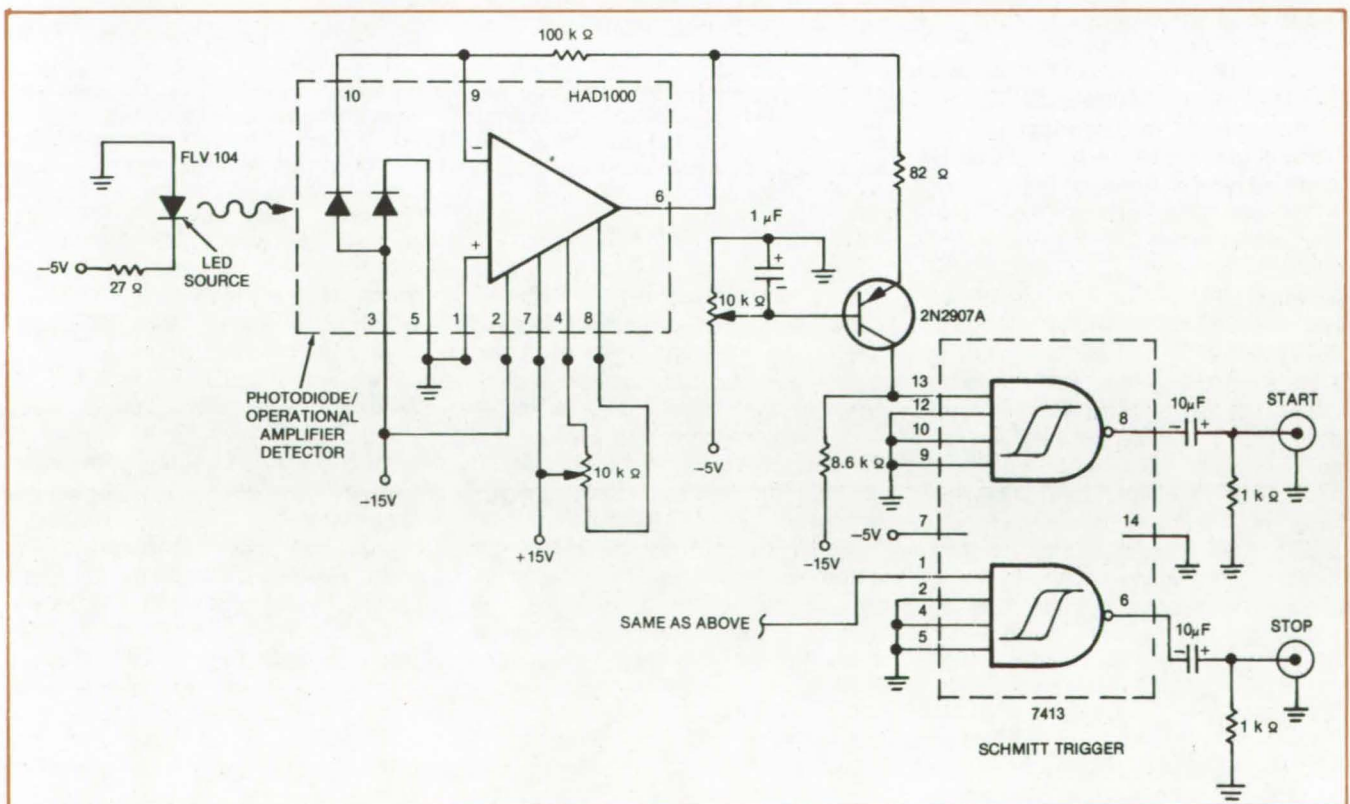


Figure 2. The Electronics of the projectile detector use three IC's, two transistors, and a few discrete components.

The sphere interrupts a light beam in each station, thereby triggering the start and stop signals. Each station contains a light-emitting diode source, a photodiode detector/operational amplifier, a bias transistor, and a Schmitt-trigger integrated circuit (see Figure 2).

The light from the LED induces a

current in the photodiode. When the sphere interrupts the beam, the photodiode current drops, and the operational amplifier produces a negative pulse. The bias transistor is adjusted so that it normally keeps the output circuit in its off state. When the negative pulse from the op amp alters the bias, a positive pulse appears at

the output to turn on the time-interval meter. An analogous sequence on the second channel turns off the time-interval counter.

This work was done by Johnny E. Jordan and Philip C. Kassel, Jr., of Langley Research Center. No further documentation is available. LAR-12387

Miniature Velocimeter

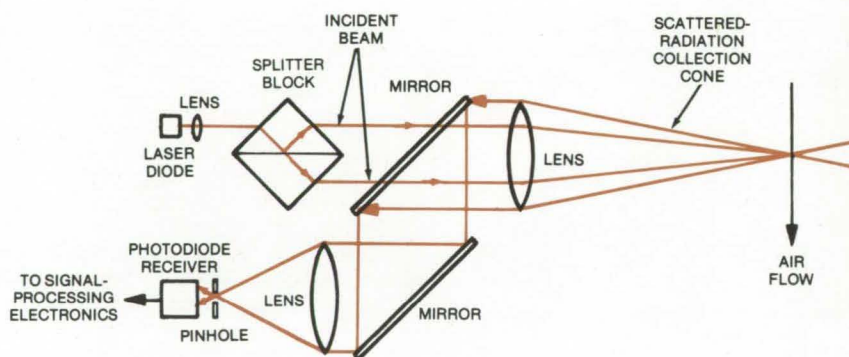
Laser diode makes a velocimeter small enough to fit inside wind-tunnel models.

Langley Research Center, Hampton, Virginia

A laser velocimeter (LV) designed to use a semiconductor-diode laser is 100 times smaller than continuous-wave gas-laser velocimeters — small enough to permit the miniature instruments to be mounted in previously inaccessible locations. The new semiconductor-laser velocimeter is compact enough to be mounted within wind-tunnel models, engine walls, or helicopter blades, where it can measure velocities in the boundary-layer gases flowing over it.

The mini-LV needs much less power than its gas-laser predecessor — 0.4 watt instead of 6.7 kilowatts. It is just as accurate as the conventional LV, measuring velocities with an accuracy of 98 percent or better.

The laser diode produces a continuous-wave beam at a wavelength of 820.0 nanometers and an output power of 10 milliwatts. Since the diode emits a beam with relatively wide divergence (20°), a collimating lens is placed in front of it to straighten the beam (see figure). In one configuration, the mini-LV samples a gas volume 3.66 millimeters long and about 0.197 millimeter in diameter — roughly the same as the conventional LV. The mini produces 20 interference fringes in this volume. The electronic circuits for processing the received laser signals are similar for both the conventional and new systems.



This **Miniature Laser Velocimeter** measures the speed of generally inaccessible flow fields of wind-tunnel models. Like larger devices, which use gas lasers, the mini can be operated as a forward-scatter dual-beam off- and on-axis velocimeter, as a backscatter dual-beam off-axis velocimeter, and as a coaxial-backscatter dual-beam velocimeter.

Two possible problems with semiconductor lasers — mode shifting and short coherence length — were found to be less serious than expected. Mode shifting from one electromagnetic radiation pattern to another is a common tendency in semiconductor diodes and would affect system accuracy. It is not a gradual process, however, but occurs in discrete jumps as current increases. Thus, it can be avoided by operating the laser at a stable current level. Experiments have shown that the spatial and

temporal coherence of the beam is adequate for the small volume measured in the LV application.

This work was done by John M. Franke, William W. Hunter, Jr., James F. Meyers, and Stewart L. Ocheltree of Langley Research Center. For further information, Circle 63 on the TSP Request Card.

Inquiries concerning rights for the commercial use of this invention should be addressed to the Patent Counsel, Langley Research Center [see page A8]. Refer to LAR-12281.

Multiple-Sample Holder for IC Testing

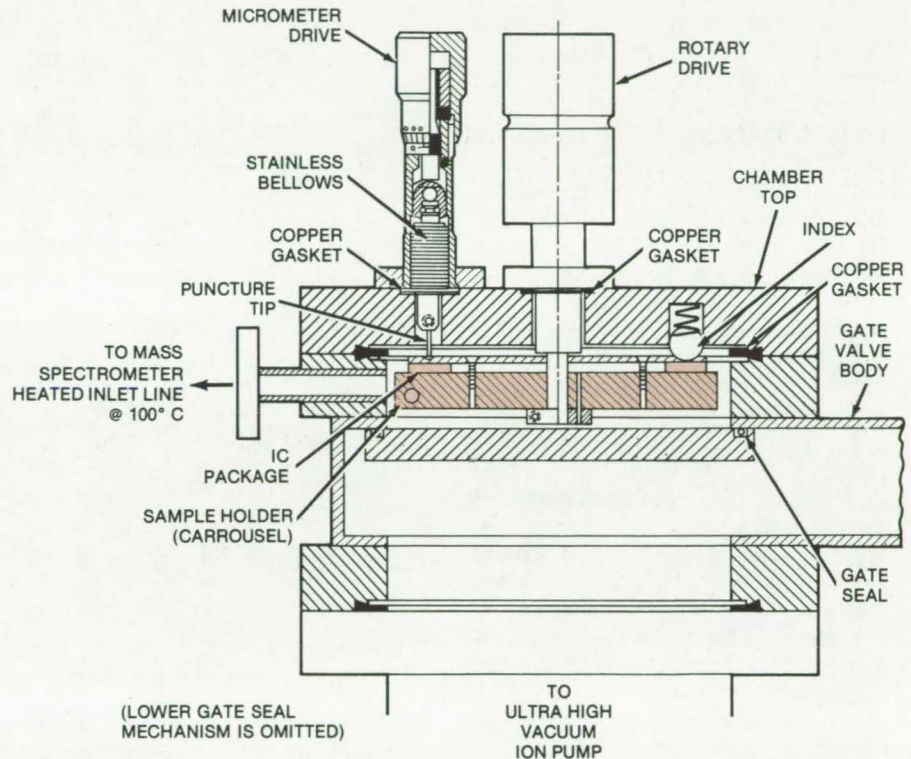
Carrousel tray speeds impurity analysis process.

NASA's Jet Propulsion Laboratory, Pasadena, California

Sealed integrated-circuit (IC) packages occasionally contain trapped impurities that reduce circuit reliability. These impurities are acquired during various stages of circuit fabrication and may erode materials making up the chips. Reliability is often determined by selecting a number of sample IC's and puncturing the packages under controlled conditions so that contaminants and total gas composition may be analyzed via mass spectrometer. Typical contaminants include chlorinated solvent vapors, excessive water, and acidic vapors picked up during various rinse operations. The test procedure is very time consuming.

A new carrousel tray speeds up the testing process by feeding the spectrometer with up to 12 samples in rapid succession. This effectively replaces a tedious procedure of testing one sample at a time. As before, the new system may be used to detect impurities carried over from fabrication rinse operations, or it can be used to test the hermetic integrity of the IC seal as a function of time. The new system (see figure) uses a simple, multiple-sample holder with detent elements on a carrousel tray and a means for rotating and puncturing the samples. The 12-sample batch can be analyzed without breaking external vacuum seals and introducing contamination. Copper gaskets assure stability at high temperatures and low pressures.

The method of running samples through the device is to load the holder with up to 12 sealed flat-pack or other IC sealed packages, positioning relative to the detents, transferring into the chamber, and tightening and torquing all flange screws (not shown). The temperature of the chamber is raised to 125° C and is held at that level for about 24 hours with the gate valve open and the high-vacuum ion pump in continuous operation. At the end of the 24-hour



The **Sample Chamber** consists of a suitable housing for the carrousel sample holder, the rotating holder with detents, a rotary drive element, and suitable gas inlet and outlet conduits. Up to 12 IC's can be tested in rapid succession to check for impurities.

period, the gate valve is closed, the temperature controller is reset to 100° C, and the system is allowed to stabilize, requiring up to 1 hour to reach 100° C. The mass spectrometer (diffusion vacuum pumping, liquid nitrogen cold baffle) is operated continuously on a 24-hour basis.

For analysis of the first sample, the micrometer puncture apparatus is slowly rotated until the first rush of captive heated gas is noted on the chamber capacitance manometer readout gage as having passed from the package to the chamber. Because a very fine needle is used, the lid of the puncture package will have only a small pinhole leak. The needle does not contact or damage the chip. The

micrometer so completely minimizes damage that in many cases it is also possible to carry out extensive electrical tests after removal of the test samples from the sample chamber.

Applications are not limited to IC packages with sealing metal or ceramic covers. For example, this system has also found application in routine analysis of small sealed heaters. With suitable modifications the total number of samples accommodated could be increased.

This work was done by Ray F. Haack of Caltech for **NASA's Jet Propulsion Laboratory**. For further information, Circle 64 on the TSP Request Card.
NPO-14314



SEM Probe of IC Radiation Sensitivity

A scanning electron microscope can localize "soft" areas to within 1 square mil.

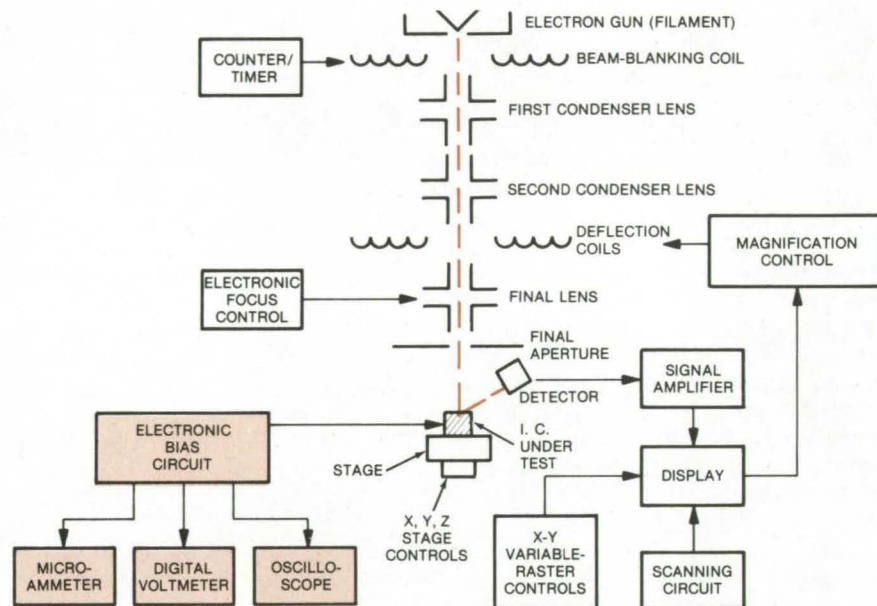
NASA's Jet Propulsion Laboratory, Pasadena, California

Integrated circuits can be tested for radiation sensitivity by applying an intense 30-keV beam from a scanning electron microscope (SEM). The SEM beam is narrow enough to irradiate a single IC subcomponent, such as a transistor. After each component is irradiated with a predetermined radiation dose [e.g., 10^6 rad (Si)], a device parameter is measured during the beam off period to determine the radiation sensitivity. By using the high magnification feature of a SEM, the irradiated region can be localized to within an area less than 1 by 1 mil (0.03 by 0.03 mm). Thus, it is possible to determine the exact location of the radiation-sensitive section within the IC.

A schematic of the scanning electron microscope is shown in the diagram. The radiation beam is directed onto the IC through a series of coils and condenser lenses. The decapped circuit is mounted on a stage that is modified to accept an electronic bias circuit. The bias parameters are monitored by a microammeter, a voltmeter, and an oscilloscope. The SEM also has a rastering feature that limits the electron-beam scan horizontally and vertically so that only a selected subcomponent or area of the IC is irradiated. In addition, the microscope includes a spot mode that permits the irradiation dot to be scanned manually over the area of interest.

Preliminary setup and raster adjustments are made at 2 keV to minimize radiation effects prior to the final, timed exposure. Then the electron energy is switched to 30 keV, which penetrates the metal and insulation layers. Magnification ranges between 100 and 500 are generally sufficient to cover single subcomponents and their isolation areas.

The test procedure is initiated by calibrating the absorbed electron-beam current at a fixed aperture setting, with the electron beam



A Scanning Electron Microscope irradiates an IC to test for radiation sensitivity. The microscope stage is modified for connection to the bias circuit.

confined to the chip area. The total absorbed current is measured by shorting all the terminals of the IC to ground through a microammeter. During the irradiation experiment, the same current is confined to the small region under investigation, and the flux rate is determined from the absorbed current.

Typical beam-current level for radiation-hardened (radiation-insensitive) devices is 12 pA; it is about 6 pA for unhardened devices. Because these low current levels create a noisy image on the microscope viewing screen, larger currents are used during the setup phase of the test. During the tests, the image detector is replaced when necessary to maintain the maximum signal-to-noise ratio.

Once the circuit is set up, all the subcomponents within a given section of a chip are irradiated in sequence, starting with the least sensitive and ending with the most sensitive. Typical exposure times are near 1 min

for a total dose of 10^6 rad (Si). Shorter exposures are used for unhardened devices. A digital counter/timer controls the exposure times through a beam-blanking coil.

When small sections are irradiated at magnification settings between 500 and 2,000, special compensation by the x, y, and z axes stage controls minimizes image offset. For these high magnification tests, exposures of between 10 and 100 s allow enough time to fine-tune the image and eliminate random offset errors.

This work was done by Michael K. Gauthier and Alan G. Stanley of Caltech for NASA's Jet Propulsion Laboratory. For further information, Circle 65 on the TSP Request Card.

This invention is owned by NASA, and a patent application has been filed. Inquiries concerning nonexclusive or exclusive license for its commercial development should be addressed to the Patent Counsel, NASA Resident Legal Office-JPL [see page A8]. Refer to NPO-14350.

Topping Pressures for Gas-Storage Cylinders

Easily read charts show the proper topping pressures for recharging cylinders.

Lyndon B. Johnson Space Center, Houston, Texas

While a gas-storage cylinder is being filled, compression heating inside the cylinder raises the gas temperature above the temperature of the supply gas. Several hours after the cylinder has been filled, however, it will have cooled to the surrounding temperature, and its pressure will have dropped. Thus, it normally is most efficient to charge the cylinder above its normal pressure to allow for the pressure drop when the cylinder cools.

With charts derived from a gas-storage system model, the required overpressure (or "topping" pressure) can be determined from the initial cylinder pressure and the temperature of the gas entering the cylinder. The charts account for heat transfer between the gas and the cylinder walls, and the charging gas is treated

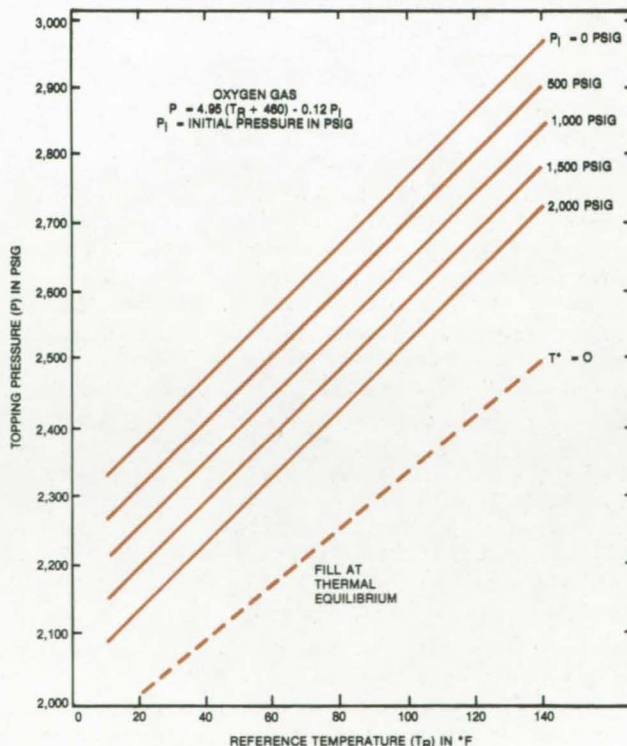
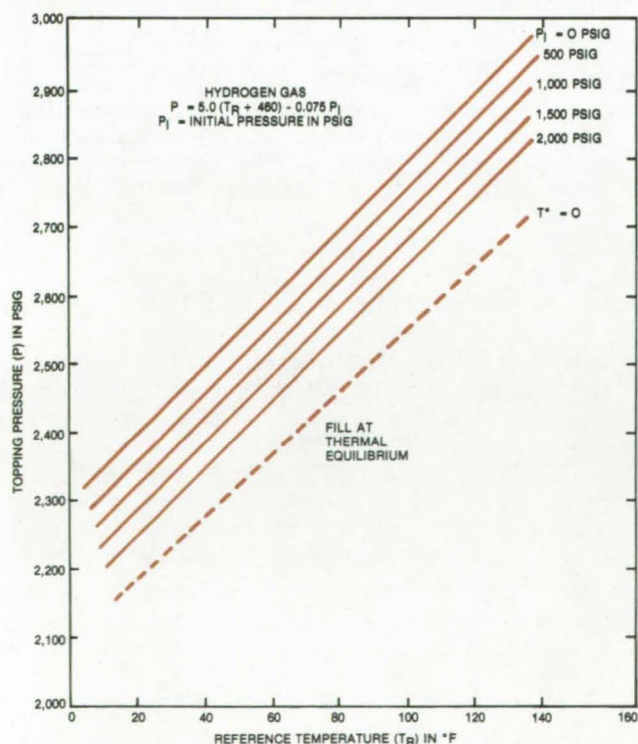
as a real gas that is subject to intermolecular forces. Previous methods for determining topping pressure required lengthy trial-and-error calculations, and they were based on the inaccurate assumptions that the charging process is adiabatic and that the filling gas behaves like an ideal gas.

Charts for two gases — hydrogen and oxygen — are available (see the figure), and charts for other important industrial gases can be developed from the model. The charts apply to high-pressure gas-storage cylinders conforming to the U.S. Department of Transportation Standard 3AA 2400. The hydrogen chart is calculated for a full load at 2,400 psig (16.5×10^6 N/m²) and 70° F (21.1° C), and the oxygen chart is for a full load at 2,200 psig (15.2×10^6 N/m²) and 70° F. The

plots are graphical representations of the equations shown as insets to the figure. The charts and equations are based on a filling time of 15 minutes. For a shorter filling time, the final equilibrium pressure will be lower than 2,400 psig (hydrogen) or 2,200 psig (oxygen), but the difference will not be more than 100 psi (0.689×10^6 N/m²).

The point at which the reference temperature (that is, the temperature of the gas entering the cylinder) is measured depends on the type of filling equipment. If the equipment is simply a direct line from a higher-pressure gas source to the storage cylinder, and if the temperature difference between the source gas and the environment is minimal, then the environment temperature can be used as the reference temperature.

(continued on next page)



Topping-Pressure Charts derived from a computer model indicate the pressure to which a cylinder should be charged so that it has the required final pressure at 70° F (2,400 psig for hydrogen, 2,200 psig for oxygen). For example, a cylinder containing hydrogen at 500 psig (3.45×10^6 N/m²) should be charged to 2,665 psig (18.37×10^6 N/m²) if the supply gas is at 80° F (26.6° C).

However, if the equipment includes pumps or compressors that add substantial heat to the gas during transfer, the reference temperature should be measured in the supply line, close to the receiving cylinder. If temperatures change during the fill, the reference temperature and the

topping pressure should be determined near the end of the fill, when the incoming gas temperature is relatively stable.

This work was done by Robert L. Haben of Rockwell International Corp. for **Johnson Space Center**. Documentation and/or the computer pro-

gram for the model from which the topping charts were developed ["High-Pressure Gas Storage System Blowdown Model" (MSC-19658)] can be purchased from COSMIC. For further information, Circle C on the COSMIC Request Card. MSC-18186

Dynamic Measurement of Bulk Modulus

A microwave technique measures changes in the bulk modulus of dielectric materials.

NASA's Jet Propulsion Laboratory, Pasadena, California

A microwave technique for determining changes in the bulk modulus of dielectric materials is based on measuring the phase difference between two microwave signals. One signal, a reference, is compared to a test signal that is transmitted through the specimen (and back-reflected). The change in specimen length is indicated by a change in the phase difference between the two signals. The method, which has been used to study the pressure variation of the bulk modulus of solid-fuel rocket propellants, should be useful in studying other materials as well.

A block diagram of the test apparatus is shown in Figure 1. A klystron, operating at 10 GHz and stabilized (to one part in 100 MHz) by an oscillator synchronizer, propagates a signal into an X-band waveguide. A 1-percent directional coupler picks up a reference signal, and the remainder of the signal enters the cylindrical test specimen, which behaves like a dielectric waveguide. A portion of the propagated wave is reflected from the top surface of the specimen, and another 1-percent coupler senses the reflected signal. The phase difference between the reference and reflected waves is a function of their respective path lengths. A microwave network analyzer monitors this phase differ-

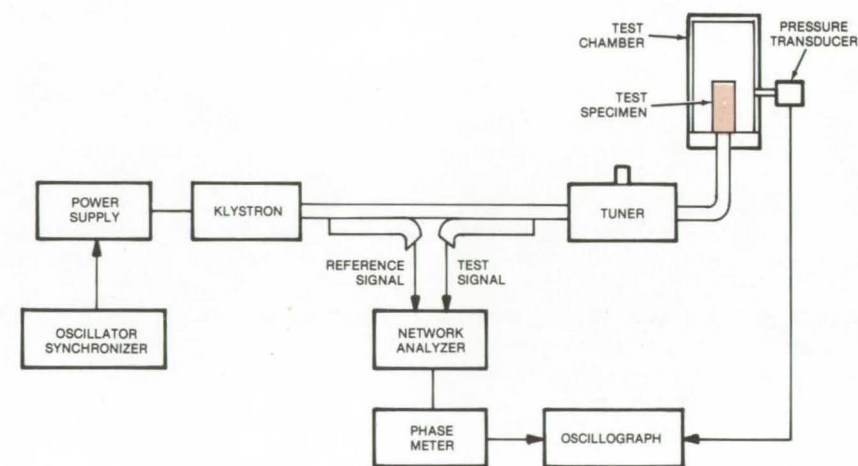


Figure 1. This **Apparatus for Measuring Changes in Bulk Modulus** utilizes a microwave test setup. Microwave signals are transmitted into a test specimen located in a pressurized test chamber. Changes in phase difference between the reference and test signals are directly proportional to changes in specimen length.

ence, providing a continuous measurement of any variation in the test material length. The test results are recorded on an oscillograph.

Tests were carried out with the specimen installed in a pressure-testing chamber (see Figure 2). The top surface of the specimen is coated with a metallic material to increase the magnitude of the reflected signal; the bottom of the specimen rests on a baseplate. A conical transition ele-

ment between the chamber and waveguide has the same dielectric constant as the test sample. This minimizes the discontinuity as the microwave signal propagates from the air-filled waveguide into the specimen. The chamber is constructed of dielectric material to prevent resonant modes from building up.

The chamber pressure is monitored by a pressure transducer. Continuous phase measurements are made as the

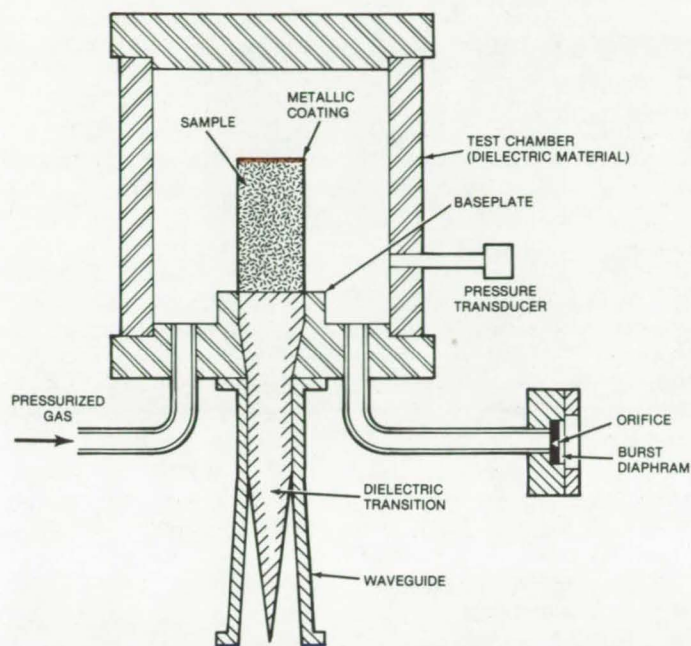


Figure 2. The **Test Chamber** for measuring bulk modulus is constructed of dielectric material. The pressure is vented through the burst diaphragm at the lower right, and the sample length is monitored by the microwave setup in Figure 1.

gas pressure is rapidly vented through a burst diaphragm and orifice. Both the phase angle and gas pressure information are displayed on the oscillograph.

This work was done by Warren L. Dowler and Leon D. Strand of Caltech for **NASA's Jet Propulsion Laboratory**. For further information, Circle 66 on the TSP Request Card. NPO-13226

Elastic Deformation of Ball Bearings, Gears, and Cams

Simplified model solution aids designers.

Lewis Research Center, Cleveland, Ohio

A simplified technique has been developed for calculating the elastic deformation at the center of the contact area for ball bearings, gears, cams, and similar components. The past procedure for solving the deformation variables required the tedious use of charts or a high-speed computer.

The contact geometry in ball bearings, gears, and cams can be depicted by two solids having different radii of curvature in a pair of principal planes (x and y) passing through a single-point contact between the solids with no applied load. Such a condition is called "point contact" and is shown in the figure where the radii of curvature are noted by r's.

It is assumed that for convex surfaces, the curvature is positive but that for concave surfaces, the curvature is negative. The curvature sum in the x and y directions can be written as:

$$\frac{1}{R} = \frac{1}{R_x} + \frac{1}{R_y} \quad (1)$$

where

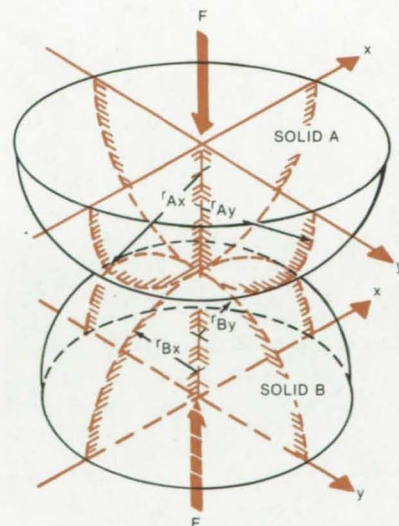
$$\frac{1}{R_x} = \frac{1}{r_{Ax}} + \frac{1}{r_{Bx}} \quad (2)$$

$$\frac{1}{R_y} = \frac{1}{r_{Ay}} + \frac{1}{r_{By}} \quad (3)$$

When a normal load (F) is applied to the ellipsoidal solids shown in the figure, the point contact expands to an ellipse with "a" as the semimajor axis and "b" as the semiminor axis.

The ellipticity parameter (k) is the semimajor axis divided by the semiminor axis ($k = a/b$). The ellipticity parameter (k) was obtained by an iterative numerical procedure. Thus for a given set of pairs of data, $\{ |k_i, (R_y/R_x) |, i = 1, 2, \dots, 39 \}$, a power fit using a linear regression by the method of least squares resulted in the following simplified expression for the ellipticity parameter

$$\bar{k} = 1.0339 \left(\frac{R_y}{R_x} \right)^{0.6360} \quad (4)$$



Point-Contacting Solids are used as a model in studying elastic deformation of ball bearings. The two solids have different radii of curvature in the x and y planes that pass through their single point of contact.

(continued on next page)

The expression for \bar{k} is valid in the range from 1 to 10. This covers applications ranging from circular contact to an application approximating a line contact.

Furthermore, it was found that the elliptical integrals of the first and second kind can be approximated by

$$\bar{F} = 1.5277 + 0.6023 \ln \frac{R_y}{R_x} \quad (5)$$

$$\bar{E} = 1.0003 + \frac{0.5968}{R_y/R_x} \quad (6)$$

The point contact deformation at the center of contact can be written as

$$\delta = \bar{F} \left[\frac{1}{2\bar{R}\bar{E}} \left(\frac{3F}{\pi k E'} \right)^2 \right]^{1/3} \quad (7)$$

where

$$E' = \frac{2}{\left[\frac{1 - \nu_A^2}{E_A} + \frac{1 - \nu_B^2}{E_B} \right]} \quad (8)$$

ν = Poisson's ratio

E = modulus of elasticity

Therefore, given the normal applied load (F), the material parameter (E'), and the geometry (r_{Ax} , r_{Bx} , r_{Ay} , and r_{By}) of the contacting solids, the elastic deformation at the center of the contact can be expressed by equation (7).

The importance of this technique is that the simplified expressions allow engineers to calculate deformation quickly from the material properties and geometry for ball bearings, gears, and cams.

[See related NASA Tech Briefs "Influence of Lubricant Starvation on Mechanical Parts" (LEW-12884) and "Determining Minimum Lubrication Film for Machine Parts" (LEW-12885) on pages 515 and 516, respectively, of NASA Tech Briefs, Vol. 2, No. 4 (Winter 1977).]

This work was done by Bernard J. Hamrock of **Lewis Research Center** and David E. Brewe of the U.S. Army Research & Technology Laboratories. Further information may be found in NASA TM-X-3407 [N76-26517], "Simplified Solution for Point Contact Deformation Between Two Elastic Solids," a copy of which may be obtained at cost from the New England Research Application Center [see page A7].

LEW-13076

Compact Turbidity Meter

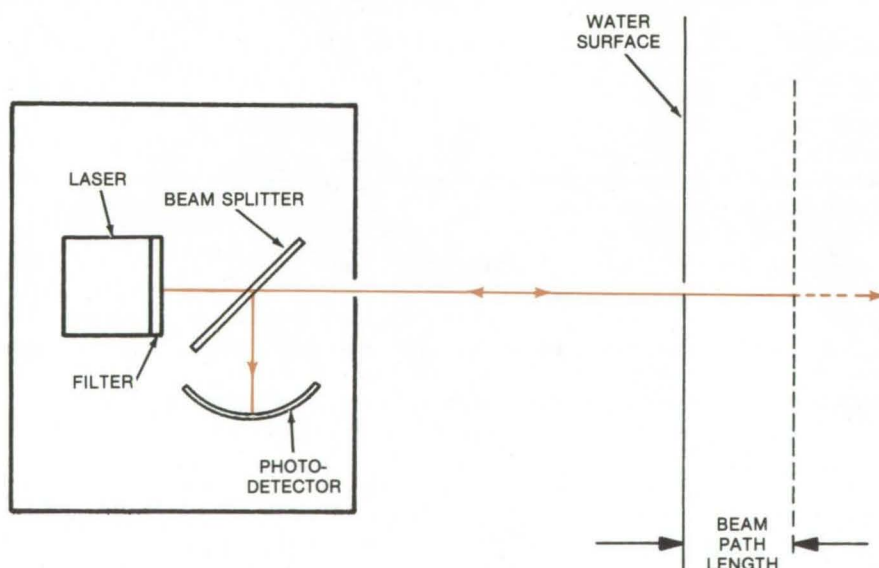
Infrared detector would make in situ measurements of the clarity of streams, lakes, and other bodies of water.

John F. Kennedy Space Center, Florida

The turbidity (lack of clarity) of lakes, streams, and other bodies of water could be measured relatively simply in situ with a proposed monitor that detects back-reflected infrared radiation. The monitor is compact, works as well in daylight as at night, and is easily operated, even in rough seas.

The use of infrared as the scattering radiation simplifies the apparatus because the path length of the near infrared in water is short. (Absorption reduces the path length to only about 20 cm.) This eliminates any background effects caused by radiation that might be backscattered from regions outside the volume being sampled. Effectively, the background is dark, just as if an absorbing target had been used; but, for this monitor, no target or support boom is required.

As shown in the figure, a solid-state laser (or several such lasers) would produce a collimated beam in the wavelength range from 700 to 950



This **Turbidity-Measuring Instrument** detects infrared radiation scattered at 180° from a volume near the water surface. It would be easy to use because no absorbing targets have to be placed around the sampled volume; the water has a short path length for infrared, and it absorbs the background radiation.

nanometers. The beam is scattered by particulates in a small region near the water surface. Radiation backscattered at 180° returns to the measuring instrument where it is deflected by a beam splitter to a photodetector.

The backscattered radiation intensity at 180° can be used as a measure of the turbidity of the water; or, em-

pirical curves relating scattered intensity to scattering angle can be extrapolated from the 180° measurement to determine the scattering coefficient at other angles. Such curves have been obtained for water, using conventional scattering detectors.

This work was done by Joseph G. Hirschberg of the University of Miami

for **Kennedy Space Center**. For further information, Circle 67 on the TSP Request Card.

Title to this invention has been waived under the provisions of the National Aeronautics and Space Act [42 U.S.C. 2457(f)], to the University of Miami, Coral Gables, FL 33124. KSC-11063

Automated Inspection of Wire-Frame Assemblies

An optical scanner could reduce inspection time and improve the accuracy of measurements.

Goddard Space Flight Center, Greenbelt, Maryland

A proposed instrument would sharply reduce the time needed to measure the spaces between wires in screen mesh and other wire-frame assemblies. The inspection would be done automatically and accurately by an optical scanner that gives a printout of the measured spacings.

As shown in the figure, a light source (such as a light-emitting diode) and a phototransistor light detector are mounted on platforms on opposite sides of the frame. The platforms ride on coupled lead screws. During the measurements, the source and detector are translated at the same speed parallel to the plane of the frame, and their positions are monitored by a laser reflectometer. The laser is mounted on the instrument chassis, and the reflector rides on the platform carrying the phototransistor.

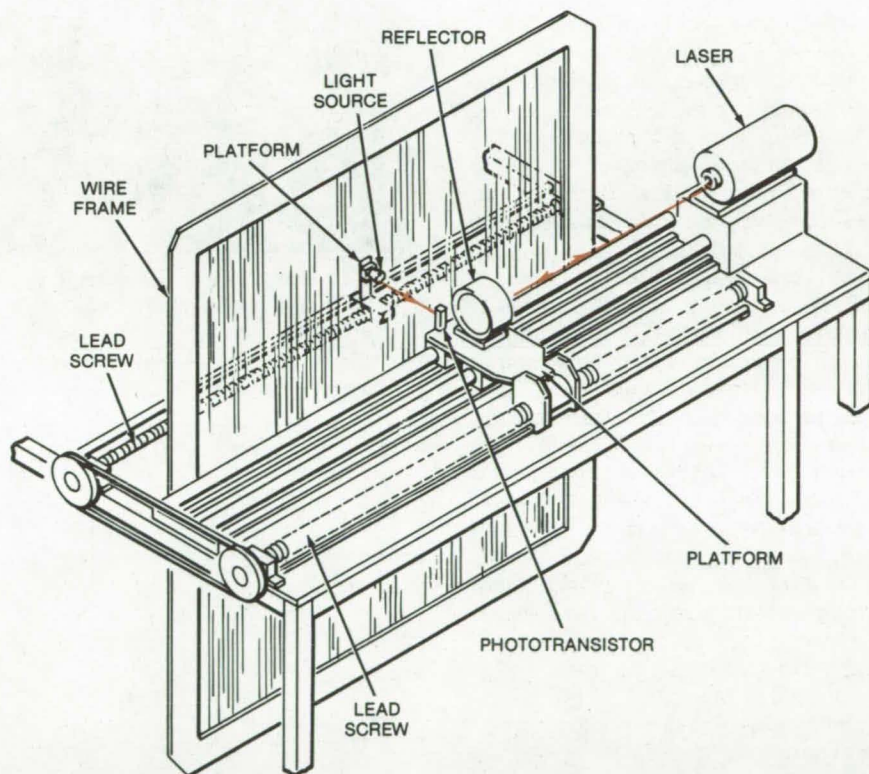
When the light path to the phototransistor is blocked by one of the wires of the frame, a trigger circuit activates the laser display unit to register the current position of the detector platform. The position signal is digitized and sent to a computer memory and a printer. The distance traveled between printouts, determined from the difference between the position measurements, is a measure of the spacings between the wires.

In one potential application, at Goddard Space Flight Center, it is estimated that the new instrument would

This Instrument for Inspecting Wire-Frame Assemblies includes a light source and phototransistor that ride on platforms on opposite sides of the frame. The wires intercept the light beam and trigger a measurement of the platform position by a laser reflectometer.

decrease the inspection time for wire frames from 50 hours (for manual inspection) to about 2 hours per frame. Measurement accuracy would be within ± 0.00025 in. (0.0064 mm) for wires spaced 0.032 in. (0.81 mm) apart.

This work was done by John G. Etzel and James A. Munford of Goddard Space Flight Center. For further information, Circle 68 on the TSP Request Card. GSC-12321



Detecting Surface Deformations Photographically

Simple technique brings out surface changes as small as 0.003 in. in opaque objects.

Lyndon B. Johnson Space Center, Houston, Texas

A simple photographic technique detects changes as small as 0.003 in. (0.08 mm) in the surface contours of opaque test specimens. The specimens are photographed before and after environmental or other testing. A negative transparency of the first image and a positive transparency of the second are overlaid in perfect register. Cracks and changes in shape appear as bright spots when the overlay is viewed on a light table.

The method was developed for evaluating the effect of environmental tests on ceramic tiles used in the Space Shuttle. It can also be used to detect surface changes in other objects (metal plates, for example) and to aid in accurately reassembling objects according to their original dimensional relationships.

Previously, strain gages and linear variable differential transformers (LVDT's) were used to detect surface changes in the ceramic tiles. This time-consuming procedure required some knowledge of where the changes might occur, and it gave no permanent record of the test results.

In the new technique, a point source of blue light illuminates the surface of the tile or other object through a grid transparency, as shown in Figure 1. The tile surface is photographed before a test. After the test, it is returned to its position on the photographic setup and is rephotographed. To ensure exact repositioning, the tile is mounted on a heavy plate, using index pins.

A negative transparency of the image taken before the test is overlaid with a positive transparency of the post-test image. The overlay is viewed on a light table. Changes in the surface, such as bulging, receding, hairline cracks, and pits show up as transparent areas visible through the overlay. Where there are no changes, the overlay is solid black. Bulges and depressions are seen as slight curvatures in the gridlines. To help register

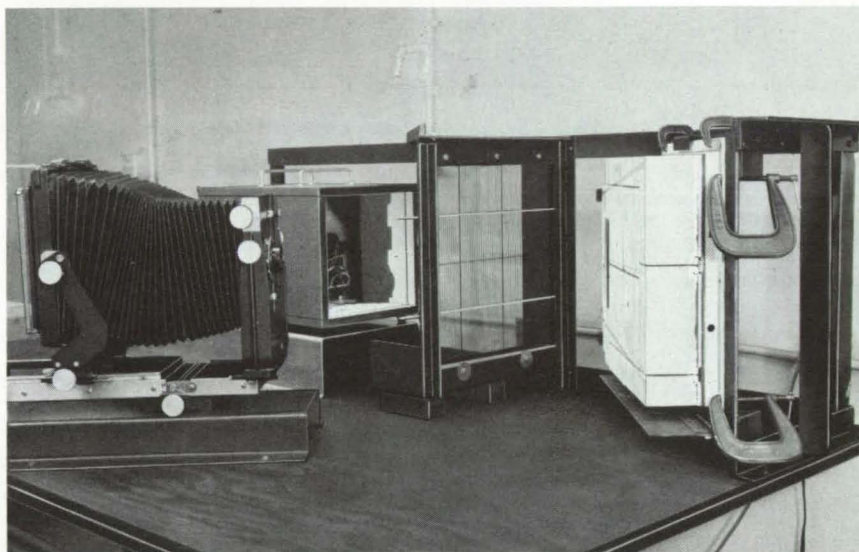


Figure 1. This **Photographic Setup** is used to make two image transparencies, one a negative and the second a positive, of a specimen surface. When the images are overlaid and viewed on a light table, changes (due to environmental tests) that occurred in the interval between photographs are made visible.

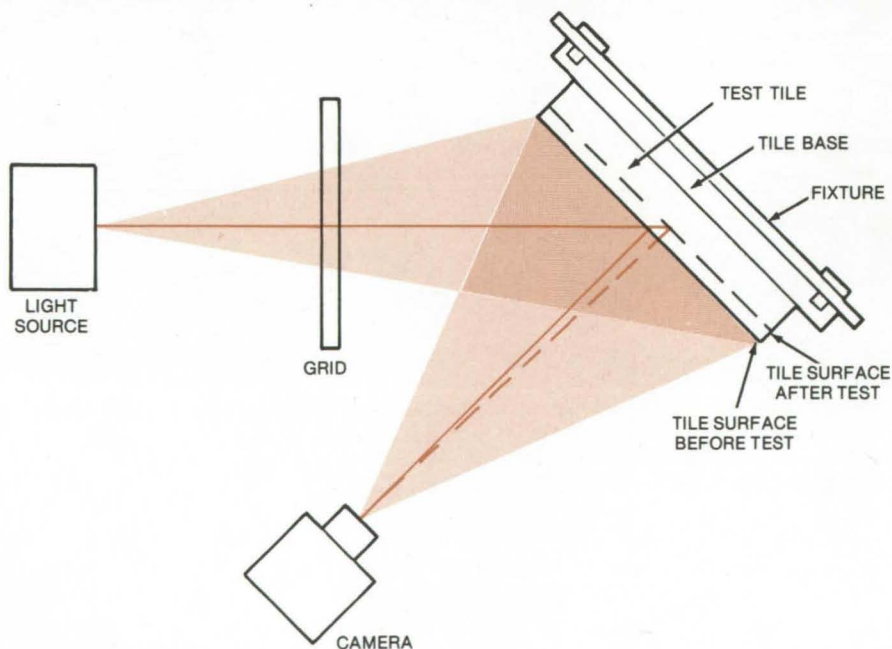


Figure 2. **Tiles for the Space Shuttle Were Tested** for surface deformation by the photographic technique, using this apparatus.

the photos, lighted index marks are affixed to the specimen support and are reproduced on the margin of the transparencies.

In the tile tests (see Figure 2), an 8-by 10-in. (20- by 25-cm) camera was

used. The distance from camera lens to the tile surface was 17 in. (43 cm), the lamp was 41 in. (114 cm) away from the filter, and the filter was 13-3/4 in. (34.9 cm) away from the center of the tile surface.

This work was done by Lloyd D. Beckerle and James R. Robson of Rockwell International Corp. for Johnson Space Center. No further documentation is available.
MSC-16156

Compression Testing of Flammable Liquids

A chamber subjects liquids to a rapid pressure rise to determine their compatibility with other materials.

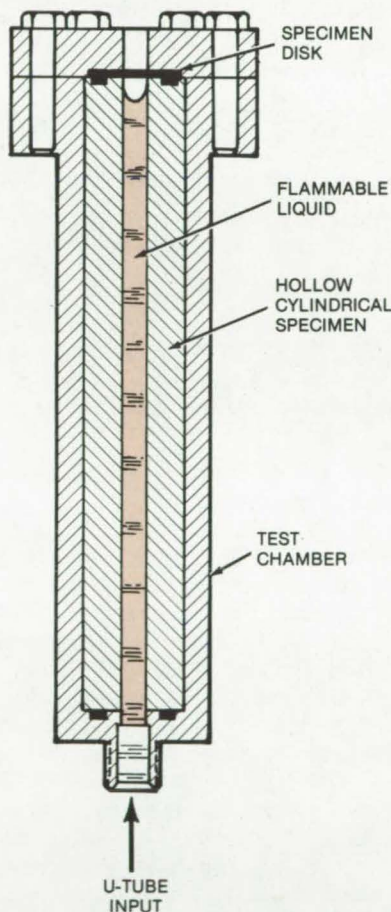
Lyndon B. Johnson Space Center, Houston, Texas

A small cylindrical test chamber can be used to determine the behavior of flammable liquids in combination with other materials under adiabatic compression. Experiments can be conducted to find out whether a given container material has a catalytic effect on a fuel that might contribute to accidental deflagration or detonation below the expected temperature.

The chamber has been used to determine the compatibility of hydrazine with various materials (stainless steels, aluminum alloys, tungsten carbide, and others) considered for the fuel system in the Space Shuttle. It should also be useful to producers and users of flammable liquids and to safety specialists.

Designed for use with a U-tube pressure system, the chamber holds a hollow cylindrical specimen of the material (see figure). An oil bath keeps the chamber at the required temperature. The U-tube applies pressure at a controlled rate until a predetermined compression ratio is reached.

Before a test, the specimen — with a bore that is drilled to match the inside diameter of the U-tube — is inserted in the chamber and U-tube assembly. A measured amount of the flammable liquid is poured in. Then, a flat disk of the specimen material, designed to rupture between 4,000 and 6,000 psi (27.6×10^6 and 41.4×10^6



Compression Chamber and U-Tube connect to a gas supply that provides fast, controlled rise to a predetermined compression ratio. The system is used to test the compatibility of flammable liquids (such as rocket fuels) with various materials.

N/m^2) and thereby indicate detonation, is placed over the bore. Last, the chamber cap is attached.

The U-tube is connected to the gas supply, and the chamber is immersed in oil until its temperature has stabilized. The oil is removed, and the bubble of vapor that has formed at the top of the chamber is suddenly compressed. The pressure rise is measured by a transducer and recorded on a strip chart. The chart (and the rupturable disk) gives evidence of any detonation.

In the hydrazine tests, the pressure was increased at a rate of 25,000 psi/s ($172.5 \times 10^6 \text{ N/m}^2/\text{s}$) to a 30:1 compression ratio at 80° F (26.7° C) and at 50,000 psi/s ($345 \times 10^6 \text{ N/m}^2/\text{s}$) to a 20:1 ratio at 275° F (135° C). No detonation was found with any of the materials tested.

The compression tester is a modification of an earlier version in which compression took place entirely in a U-tube made of the specimen material. The new chamber makes it possible to test materials that are not readily available in tube form.

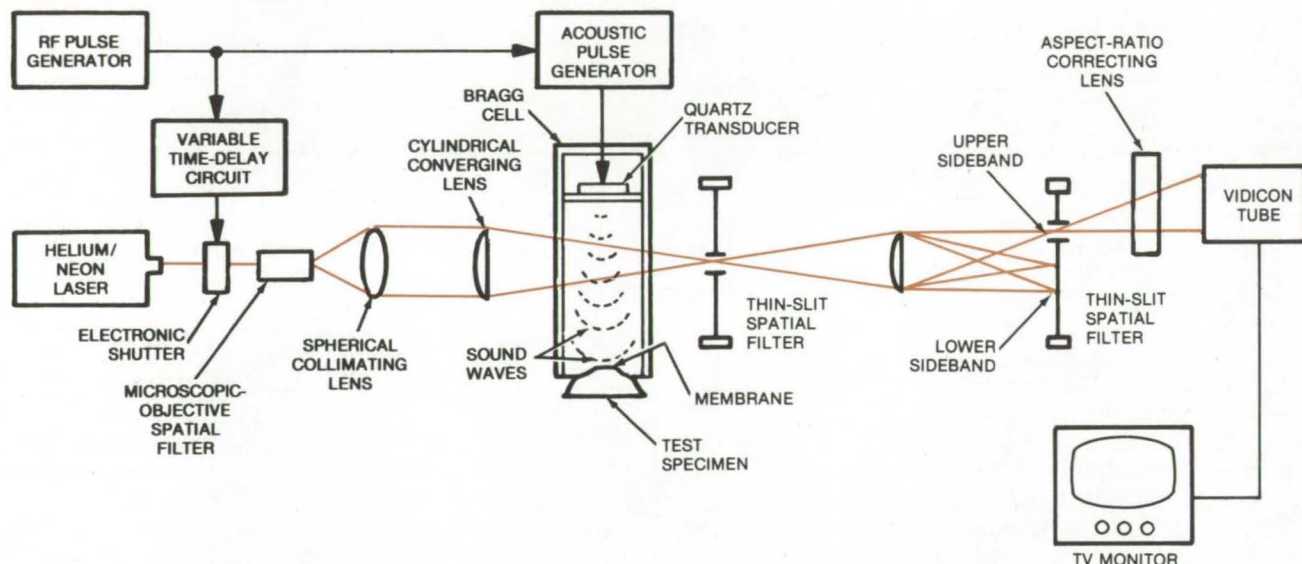
This work was done by Owen M. Briles and Richard P. Hollenbaugh of Sundstrand Advanced Technology Operations for Johnson Space Center. For further information, Circle 69 on the TSP Request Card.
MSC-16121



Acousto-optical Imaging Without Immersion

A membrane separates a test specimen from the acoustic transmission medium, making immersion of the specimen unnecessary.

Marshall Space Flight Center, Alabama



The **Interaction of Laser Light and Sound** reflected from a test specimen diffracts the laser beam and creates upper and lower sidebands. A vidicon and TV monitor display an image (of the upper sideband) that represents the internal structure of the specimen.

The immersion of a test specimen in water or other liquid is not necessary with a new acousto-optical imaging system for nondestructive testing. Instead, the specimen is placed in contact with a membrane that forms the end wall of a Bragg cell. Acoustic pulses are transmitted through the water-filled cell, through the membrane, and into the specimen. The pulses are reflected by the specimen back into the water, where they interact with pulses of laser light, diffracting part of the light into upper and lower sidebands (see figure). One of these sidebands is detected by a vidicon and is displayed on a TV monitor to image the internal structure of the specimen.

Light from the laser is collimated and converged into a wedge with a line of focus just outside the Bragg cell. The cell is an aluminum box measuring 40 by 20 by 20 centimeters. It is fitted with end windows that allow the laser light to enter and leave.

A quartz transducer is mounted on a panel at the top of the cell. The trans-

ducer fundamental frequency is 18.7 megahertz, but it can be driven at odd harmonics of the fundamental. Since the resolution of the system is directly proportional to the acoustic frequency, it is desirable to use the highest frequency practical, which in this case is about 56 megahertz.

The radio-frequency pulse that energizes the quartz transducer is also sent through a delay line to an electronic shutter that controls the laser light emission. The pulse synchronizes the acoustic and optical signals so that they appear simultaneously only at the time when the desired image can be formed. For example, after a sound burst has been generated, a laser pulse is generated to interact with reflected sound from a selected depth within the specimen. In this way, the structure of the specimen in a plane at the selected depth is imaged. This process is repeated with increasing delays between the emission of sound and the emission of light, so that the reflected sound represents increasing depths within the specimen.

The system operates in real time, does not require film developing, and uses readily-available optical components. One of its primary advantages is that it makes it possible to inspect objects that are too large to be immersed or might be damaged by direct contact with the liquid.

Unlike holographic imaging systems, the acousto-optical system does not demand exceptionally-high dimensional stability in its components, and thus it is easier to set up and maintain in production testing. Moreover, since the interpretation of interference fringes is not necessary, the system can be used by people without specific training in holography.

*This work was done by Hua-Kuang Liu of Lumin, Inc., for **Marshall Space Flight Center**. For further information, Circle 70 on the TSP Request Card.*

Inquiries concerning rights for the commercial use of this invention should be addressed to the Patent Counsel, Marshall Space Flight Center [see page A8]. Refer to MFS-23876.

Detecting Moisture in Composite Honeycomb Panels

X-rays reveal even minute amounts of liquid.

Lyndon B. Johnson Space Center, Houston, Texas

X-ray inspection can detect water in the cells of honeycomb composite panels. The water (and other trapped liquid) is often found in composites assembled with porous, fiber-reinforced plastic skins. Tests have found that the radiographic technique is sensitive to as little as 0.01 ml of liquid, and it has been suggested as a simple way of studying the effectiveness of drying procedures and the effects of water on the honeycomb structural quality and lifespan. The method may also have applications in production and quality-control tests.

To evaluate the procedure, representative honeycomb composite panels were injected with known, varied amounts of water. The panels

consisted of graphite-fiber-reinforced epoxy skins, an aluminum-powder-filled modified epoxy adhesive, and a fiber/phenolic-resin honeycomb core. The quantity of water varied from 0.3 milliliter (enough to fill a honeycomb cell completely) to 0.01 milliliter.

Just before and after the water was injected, the panel was X-rayed at low kilovoltage. The "before" and "after" films were compared, and areas where water had been injected were readily identifiable. Even without a "before" film for comparison, areas containing as little as 0.5 milliliter could be detected. Below that level, variations in the density of the adhesive film tended to mask the

water content unless a reference film was used for comparison.

The radiographic procedure is expected to be of use in the aerospace industry, where honeycomb composites are widely used in parts ranging from airframes to helicopter rotors. In addition, it may be of interest to makers of consumer products, such as automobile manufacturers, who are investigating honeycomb composites because of their high strength and light weight.

This work was done by John D. Culp and James W. Sapp, Jr., of McDonnell Douglas Corp. for **Johnson Space Center**. No further documentation is available.

MSC-16750

Refrigerant Leak Detector

Simple mechanical device
measures leakage rate.

Lyndon B. Johnson Space Center, Houston, Texas

A new quantitative leak detector is useful for testing large refrigeration systems where the precise location of a refrigerant leak of moderate size is not important. Determination of the rate of Freon 21 or similar fluid loss is made from a single test point with one measurement.

Other precise methods of leakage measurement depend on local "sniffing" at suspected test points. Some halogen leak detectors use a sensitive reactive electronic circuit that indicates leakage rate on a meter. Such units are very sensitive, detecting leaks as small as 0.0005 oz/year; however, they tend to drift as the circuits age and require precise adjustment and calibration plus periodic replacement of the filter and sensing elements.

The new unit, shown in Figure 1, visually demonstrates fluid loss from

(continued on next page)

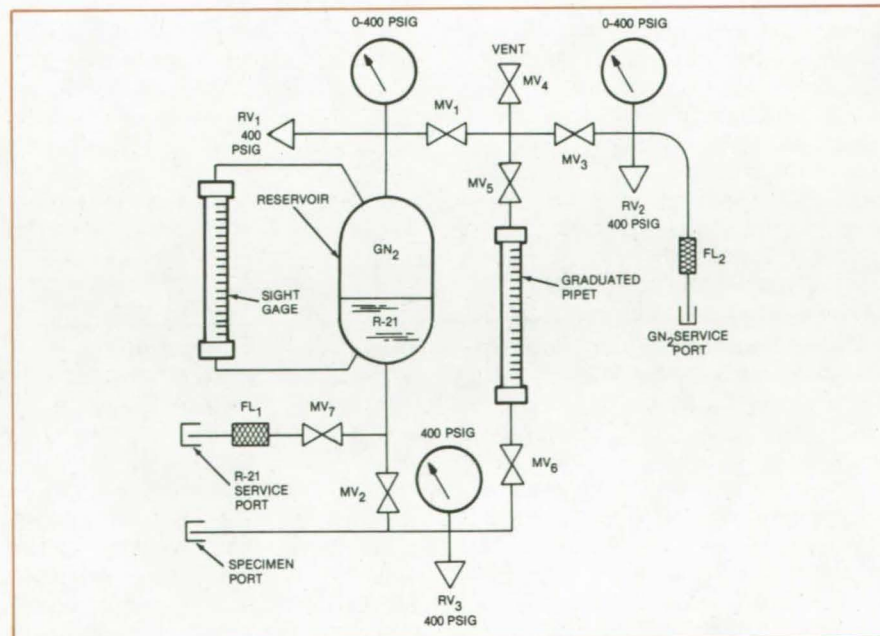


Figure 1. This **Mechanical Leak Detector** is simple to connect to refrigeration units and easy to calibrate.

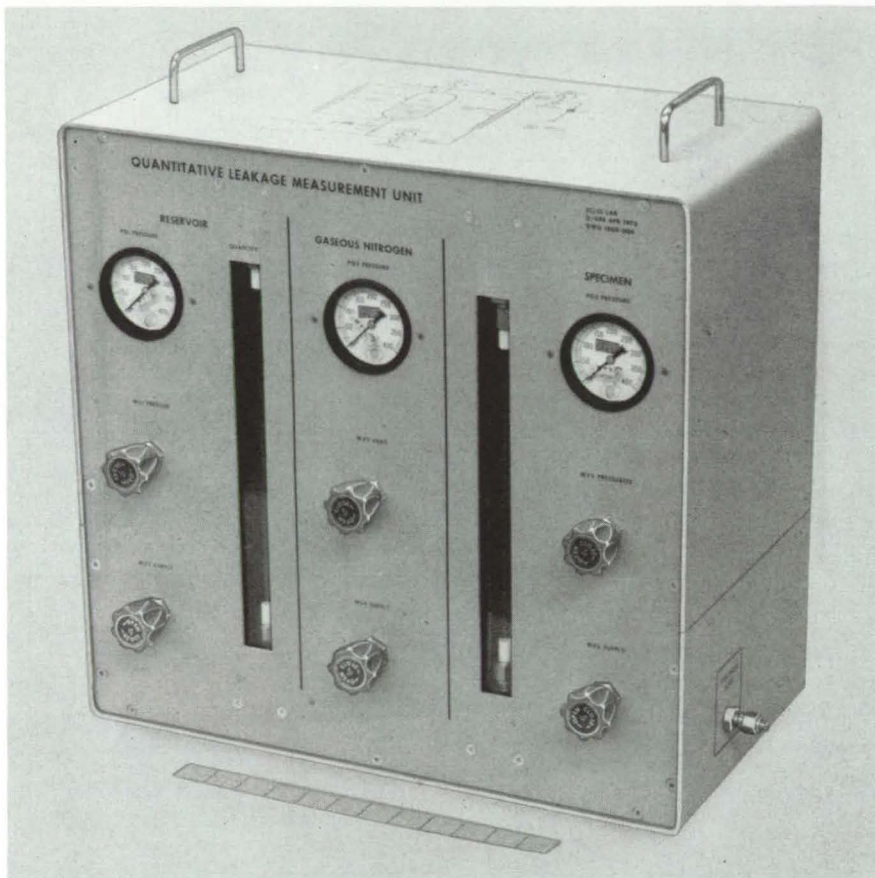


Figure 2. **Strictly Mechanical**, the leakage testing unit is portable and has no electrical parts that could be susceptible to drift.

Adjustable Gas-Flow Restrictor

Two mating threaded parts form the heart of a finely-adjustable flow restrictor and temperature controller for gases. A narrow helical path creates a sharp pressure drop over a short distance. Originally used to control oxygen flow for life support on spacecraft, the restrictor has many potential applications, including food and fuel processing. (See page 594.)

Infrared Scanners Detect Thermal Gradients in Building Walls

Thermal gradients in the walls of buildings and in other surfaces are detected by an infrared scanner and displayed as a televisionlike picture. Photographs can be made from the CRT image. The instrument responds to radiation from surfaces with temperatures from -20° to 800° C. Its resolution is better than 0.3° C. (See page 510.)

Ultrathin Films as Photomechanical Transducer

A stretched film can be a non-electrical substitute for a photocell. Tests on candidate films for the solar "sail" found a measurable change in strain when a film is illuminated. The response to intensity changes is rapid, and the film could therefore serve as the sensing element in an exposure meter. (See page 520.)

Testing Integrated Circuits by Photoexcitation

In a rapid pass/fail check for integrated circuits, a laser beam is scanned over the IC, and the photocurrent is displayed on a CRT. By superimposing the images of several digital states, the "signature" of the device is developed for comparison with a reference. The method is fast, nondestructive, and applicable to complex logic circuits. (See page 474.)

a precision volume over an established period of time. The unit is less costly than electronic "sniffers" and promises to be more reliable.

Operation of the unit can be followed in Figure 2. The reservoir is filled with R-21 or other test fluid, and the item to be tested is connected to the specimen port. The detector unit is then pressurized with gaseous nitrogen (GN_2), and valve MV_2 is opened. Valves MV_5 and MV_6 are adjusted until the test fluid is visible on the upper portion of the graduated pipet. Then MV_2 and MV_5 are closed, and MV_6 is opened. The pipet reading and time are noted at the beginning and end of the test period, and the data can be used to calculate volumetric loss per unit of time; e.g., standard cubic centimeters per second.

This work was done by Edward J. Byrne of Rockwell International Corp. for **Johnson Space Center**. No further documentation is available. MSC-18214

Flow-Compensating Pressure Regulator

A flow-compensating pressure regulator for eye surgery and other applications controls fluid pressure over a wide range of flow rates. Two diaphragms and a compound lever cooperate to compensate for changes in the infusion flow rate and maintain a constant outlet pressure. The gain of the regulator is variable. (See page 548.)

Measurement of Subcoat Thickness by Characteristic X-Rays

The thicknesses of ceramic topcoats and subcoats are determined by measuring characteristic X-rays emitted upon electron bombardment. The ceramic is analyzed by a scanning Bragg spectrometer. Within seconds the image appears on a CRT for viewing or photographing. The thicknesses of silica-based coatings for the Space Shuttle have been measured by this technique. (See page 530.)

"Gentle" Holder for Brittle Ceramics

Ceramic specimens are safely held by an inexpensive fixture.

Lyndon B. Johnson Space Center, Houston, Texas

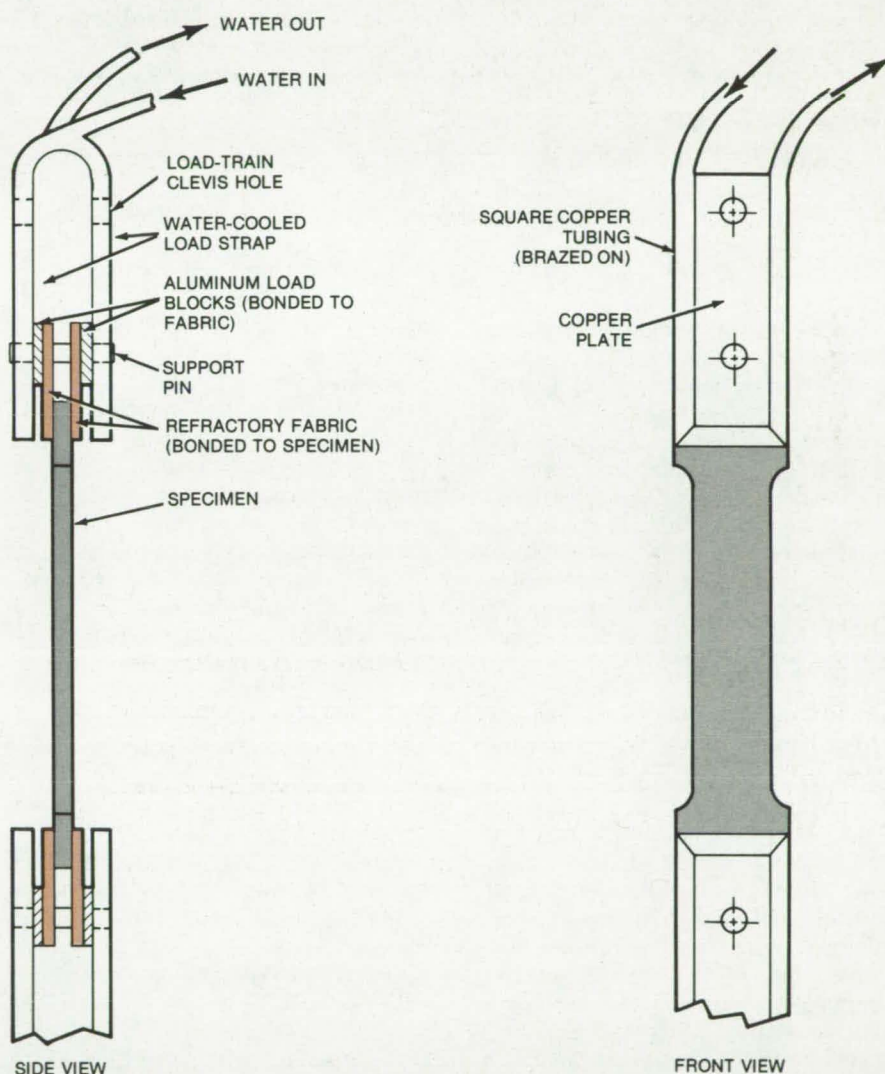
A new fixture (see figure) for gripping brittle ceramic specimens holds them "gently" during high-temperature tests and other applications. To use the fixture, a flexible refractory fabric is bonded to each side of the specimen and to adjacent aluminum blocks. The assembly is held at both ends by water-cooled copper straps that keep the bond areas cold during the high-temperature tests. The flexible fabric cushions the brittle surface and allows the specimen to be aligned without breaking.

A commercially available fiber such as Irish Refrasil (or equivalent) is used for the refractory fabric. It is bonded to the aluminum blocks and to the specimen with a silicone adhesive. In holders used to grip samples of reusable surface insulation for the Space Shuttle, there are two 1- by 4-in. (2.5- by 10-cm) fabric pieces on each side of the specimen. Each of the two aluminum blocks is 1 by 1.5 by 0.020 in. (2.5 by 3.8 by 0.050 cm).

Water circulates through a 1/4- by 1/8-in. (0.6- by 0.3-cm) copper tubing that is brazed onto the pure copper straps. The strap dimensions are 1/4 by 1/4 by 16 in. (0.6 by 0.6 by 40 cm). A load pin through each strap holds the assembly together.

The fixture is capable of withstanding high-temperature tests of up to 2,000° F (1,360 K) and above. The cooling water, pumped through the tubes, prevents damage to the adhesive bond and eliminates a need for expensive high-temperature adhesives.

This work was done by Everett G. Stevens of Rockwell International Corp. for **Johnson Space Center**. For further information, Circle 71 on the TSP Request Card.
MSC-19645



This **Fixture Holds Ceramic Insulation Specimens** for high-temperature tests. The brazed-on copper tubing carries water through the fixture to cool the adhesively bonded sections.

Computer Programs

These programs may be obtained at very reasonable cost from COSMIC, a facility sponsored by NASA to make new programs available to the public. For information on program price, size, and availability, circle the reference letter on the COSMIC Request Card in this issue.

Potential Flows in Propulsion System Inlets

Improved programs for VTOL and STOL aircraft

A collection of computer programs was developed as a set of procedures to aid in the design of propulsion system inlets, particularly for VTOL (Vertical Takeoff and Landing) and STOL (Short Takeoff and Landing) propulsion systems. The chief program is an axisymmetric potential-flow program, called EOD, which calculates the incompressible potential flow about arbitrary axisymmetric bodies.

Input for EOD, from various specified analytical shapes or sets of coordinate points for the inlet components, is generated by a program called SCIRCL. Basic solutions computed by the EOD program can be combined into solutions of interest by a program called COMBYN, which also applies compressibility corrections. Together, these programs can be used to calculate the compressible potential flow in an arbitrary axisymmetric inlet at any combination of operating conditions of inlet mass-flow rate, free-stream velocity, and inlet incidence angle. This package should prove to be a very useful tool for the development of a wide variety of propulsion system inlet designs.

Program SCIRCL prepares coordinate point input for efficient use by the potential-flow program. The inlet is assumed to be axisymmetric and is represented by its meridional profile. This profile is broken into segments at convenient tangent points. Each segment may be defined by an analytical expression or a set of points. SCIRCL prepares input for EOD and provides printed information, such as curvature, wall angles, and flow-area distribution, which can be

useful in the preliminary screening of proposed inlet shapes. Sets of points spanning the passage, like flow-measuring rakes, are defined at axial locations where velocity profiles or streamlines are desired. These rake points, with one specified as a control station, are passed as input to EOD along with the geometrical information. SCIRCL can provide plots of the inlet geometry, rake points, area distribution, and curvature distribution.

Program EOD, originally developed by the McDonnell Douglas Corporation, is used for calculating incompressible potential flow. The program applies an exact general method of solving the Neumann (or second boundary value) problem to the calculation of flows about or within axisymmetric bodies. The program utilizes a distribution of sources or sinks of initially unknown strength to represent the inlet profile. This representation results in a Fredholm integral equation of the second kind, which is exact for a continuous distribution of source strength. This continuous distribution is approximated by representing the inlet profile by a finite number of discrete elements characterized by a control point on each element. Each element may have the same type of source strength distribution (e.g., constant, linear, parabolic), and the element itself may be flat or curved. This approximation results in a set of linear algebraic equations that are solved by matrix methods for the source strength at the control points. Velocities at the control points and at specified off-body (rake) points are calculated from the source distribution. The program can calculate three basic solutions with the closed-duct solutions and shroud-vorticity solutions being used extensively. The closed-duct method uses a combination of a closed-duct inlet and an open duct, both in an axial free-stream flow, to obtain a static arbitrary mass flow. The shroud-vorticity method utilizes a distribution of unit vortices, in addition to the inlet profile distribution of sources, on the shroud surface to induce a static mass flow through the inlet. The basic solutions are output by EOD for use by program COMBYN.

Program COMBYN combines the basic solutions from EOD into any number of solutions of interest. A solution of interest is one having specified values for free-stream velocity, inlet incidence angle, and inlet weight flow. The average axial velocity at the control station may be input instead of inlet weight flow. Temperature and pressure may be specified if other than standard conditions are desired. The combined solution velocity, obtained from the basic incompressible solutions, includes the Lieblein-Stockman compressibility correction. Output from COMBYN includes a printout of the various parametric and calculated values and plots of the onbody static pressure ratio. When the velocity on the inlet surface becomes locally supersonic, the agreement, an optional supersonic correction based on local stream tube area, is included in COMBYN.

These programs are written in FORTRAN IV for execution in the batch or demand mode and have been implemented on a UNIVAC 1100/42 with a maximum central memory requirement of approximately 57K of 36-bit words. For plotted output, a CALCOMP plotting system is required.

This program was written by Charles A. Farrell, Jr., and Norbert O. Stockman of Lewis Research Center. For further information, Circle D on the COSMIC Request Card. LEW-13010

Orbital Heat Rate Package

Radiative heat analysis

The Lockheed Orbital Heat Rate Package (LOHARP) calculates the temperature distribution of an orbiting spacecraft. It is a valuable tool in the design and analysis of other structures that must function in complex thermal environments. LOHARP consists of three separate computer programs: the View Factor program (VUFACT), the Radiation Constant program (RADCON), and the Radiation Orbital Heating program (ROHEAT).

The VUFACT program calculates the diffuse radiation view factors between any system of surfaces and includes the effects of shading and semitransparent surfaces. The RADCON program calculates the radiant interchange factors between any system of surfaces, including the effects of absorptivity, emissivity, and reflectivity for multiple reflections. The ROHEAT program calculates the direct incident flux and total absorbed heat rates for complex vehicles in orbit about a planet.

Used as a system, these three programs can accurately predict the temperature distribution of a structure in planetary orbit. VUFACT and RADCON are very useful in the thermal analysis of any complex configuration where the effects of radiative interchange are important.

The VUFACT program calculates diffuse view factors based on geometry. The seven basic surface shapes available for modeling a complex vehicle are rectangular and trapezoidal plates, circular plates, cylinders, cones, spheres, and circular paraboloids. The view factor equation consists of a double-area integral evaluated over the two surfaces for which the view factor is to be calculated. VUFACT utilizes a double-summation numerical method for evaluating the integral equation.

This method utilizes an incremental area approach, in which each surface area is subdivided into incremental areas called elements. Assuming that the view factor over a given element area is constant, the view factors are calculated between elements and summed over the entire areas to yield the view factor between surfaces. Shading and semitransparent intervening surfaces are accounted for on the incremental level. VUFACT has a built-in restart capability so that completed calculations need not be repeated in the event of abnormal termination. VUFACT prepares an output tape containing necessary surface information and view factors to allow radiant interchange factors to be computed with RADCON.

The RADCON program computes the net radiant interchange between two surfaces as the difference between the radiant energy emitted by the first surface and absorbed by the second, and the energy emitted by the

second and absorbed by the first. This includes energy traveling directly from the first surface to the second and also the energy that impinges on other surfaces and is then reflected between several surfaces in the system until it is finally absorbed by the second.

RADCON employs the basic method of Hottel with the assumptions that all surfaces are perfectly diffuse emitters and reflectors, surface emissivities and absorptivities are constant (temperature-independent), all surfaces are gray (wavelength-independent), and infrared and solar transmissivities of each surface are constant (incident-angle-independent). Two sets of radiant interchange factors may be computed with one set based on the infrared emissivity of the surfaces and the other set based on the solar absorptivity. The interchange factors are output on magnetic tape for input to the ROHEAT program.

The ROHEAT program calculates the direct incident flux and total absorbed heat rates for vehicles in planetary orbit. An important consideration in the design of a spacecraft is the thermal environment the vehicle experiences in planetary orbit. The direct incident heat flux on a vehicle is the radiant energy flux that is available at the surface from the Sun (solar), the planet (planet shine), and that reflected from the planet atmosphere (albedo). The total absorbed heat rate is the energy rate that is absorbed by the surface and includes the energy reflected by other surfaces.

The vehicle to be analyzed may be in either a circular or an elliptic orbit and may be either planet- or Sun-oriented. A transfer orbit is available, and the vehicle is allowed to rotate about and to spin about the x-axis. The direct incident heat rates are calculated by classical methods. The total absorbed heat rates are calculated as functions of the direct incident fluxes, the radiant interchange factors from RADCON, the infrared absorptivity and transmissivity, the solar absorptivity and transmissivity, and the surface areas.

The programs are written in FORTRAN V and Assembler for batch execution and have been implemented on a UNIVAC 1108 under control of EXEC 8 with the largest program having a central memory requirement of approximately 64K of 36-bit words.

Program usage requires several tape drives (up to nine) and Fastran storage

This program was written by J. K. Lovin and L. W. Spradley of Lockheed Missiles & Space Co. for Marshall Space Flight Center. For further information, Circle E on the COSMIC Request Card.
MFS-23980

Tumbling-Vehicle Entry Heating

Program determines heating rates for vehicles as they tumble through the Earth's atmosphere.

The programs TEHEAT and BENTRY predict the heating rates at many points on vehicles of different geometry as they tumble and roll during reentry into the Earth's atmosphere. Heating rates can be computed rapidly for any point on the vehicle at any angle of attack or roll position. Thus, the heating environment for numerous points on the vehicle can be found accurately as a function of time for thermal protection systems or structural breakup studies. The programs calculate heating for free-molecular, rarefied, laminar, transitional, and turbulent-flow regimes.

The flow-field methods used for calculating tumbling-body entry heating are, in general, techniques used ultimately to compute boundary-layer edge conditions. The four major calculations made are: oblique shock, pressure distribution, recovery enthalpy, and specific vehicle geometry. Air thermodynamic and transport properties are used throughout. Real-gas thermodynamic and transport properties of air are obtained using the method of Hansen. Equilibrium thermodynamic properties of air are obtained in closed form from a set of approximate partition functions. The partition functions and thermodynamic relationships are programmed such that the total enthalpy, entropy, speed of sound, average molecular weight, heat capacity, and species concentration can be found for a given temperature and pressure.

(continued on next page)



Before the aerodynamic heating calculations are performed, the surface distance from the forward flying end to the axial location of interest is determined, the wall enthalpy is computed based on the specified wall temperatures, and the flight regime (e.g., free-molecular, rarefied, or boundary-layer) is determined. Regardless of the vehicle orientation, a zero-angle-of-attack flow-field and heating calculation is performed. If the angle of attack (plus the body angle) is greater than 1° , then a stagnation-line-angle-of-attack flow-field and heating calculation is also performed. A heating option for hemispherical geometry is available. The stagnation values are obtained using the method of Fay and Riddle, and the distribution values are obtained using a property-independent form of Lee's heating distribution for laminar flow.

The input is normally on cards and includes variables that describe the vehicle geometry, test conditions, trajectory, and number of body points to be computed. The printed program output contains free-stream variables, local heating rates, local total-heating load, heat-transfer coefficients, recovery enthalpy, and stagnation-line values.

These programs are written in FORTRAN IV for batch execution and have been implemented on a UNIVAC 1100-series computer under EXEC 8 with a central memory requirement of approximately 40K decimal of 36-bit words.

This program was written by Carl D. Engel of REMTECH Inc. for Marshall Space Flight Center. For further information, Circle F on the COSMIC Request Card.
MFS-23712

Flow in Axisymmetric Ducts With Struts

Finite-difference solution for turbulent swirling compressible flow

This computer program was developed to compute the turbulent swirling compressible flow in axisymmetric ducts. A continuing problem in the development of air-breathing propulsion systems is the design of efficient subsonic diffusers. Not only is the engineer faced with building an efficient diffuser but frequently he must tailor the exit flow within certain physical constraints imposed by the propulsion engine. This task has proved difficult in the past since the engineer was forced to rely on empirical design methods based on correlations of limited experimental data. The vast number of geometrical parameters involved, such as area ratio, length, wall curvature, and support struts, together with the physical flow parameters involved, such as mach number, Reynolds number, swirl angle, and inlet flow distribution, make the development of a sufficiently-generalized empirical method extremely difficult.

Analytical diffuser-design methods have generally not kept pace with empirical studies, with conventional analytical solutions dividing the flow field into an irrotational free-stream flow and a boundary-layer flow. The new method used in this program involves numerically solving the equations of motion for the entire flow in the diffuser, thereby insuring compatibility between the inviscid flow and the boundary-layer flow. The program provides an accurate analytical tool for the development of optimum diffuser designs for a wide range of applications.

This analysis method represents an extension to compressible flow of analysis methods previously developed for computing incompressible

swirling flows in axisymmetric ducts. The analysis solves for the entire flow across the duct at each station in the stream flow direction. The problems of matching solutions for the inviscid flow and boundary layer are eliminated, and no difficulties exist when boundary layers on the duct walls merge. The analysis supposes that the streamlines of the actual flow through the duct will not be appreciably different from the potential flow streamlines, an assumption that, from simple physical considerations, must remain valid for internal duct flows with only small regions of separation.

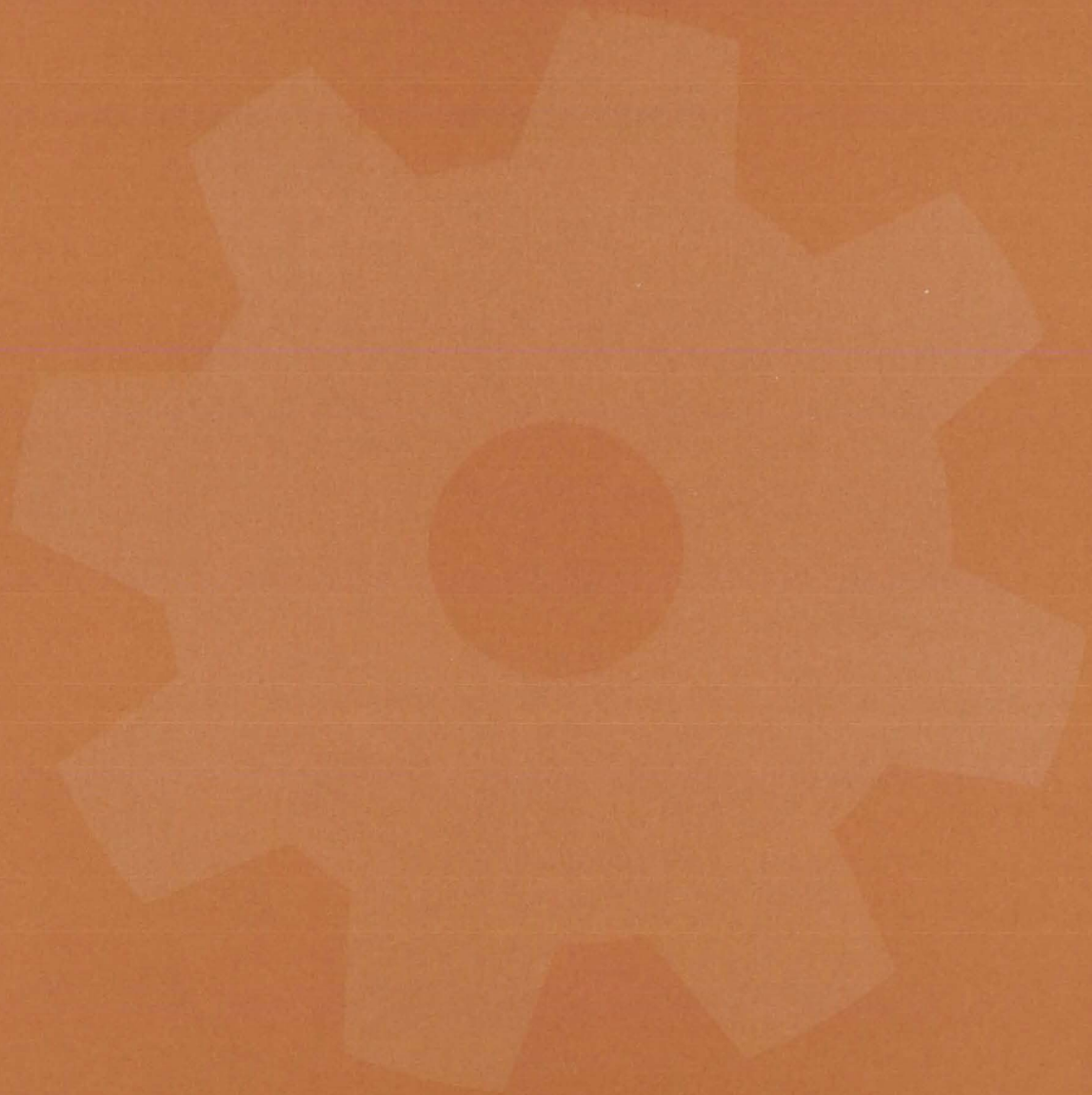
It is possible to make boundary-layer-type approximations in a coordinate system based upon the stream function and velocity potential of the potential flow. In this manner, the viscous effects can be treated as a perturbation upon the inviscid field and expressed as a parabolic partial differential equation. Elliptic properties of the flow are retained through selection of the potential flow streamlines as the coordinate system for the parabolic partial differential equation.

Included in the analysis are the capabilities for treating the effects of struts, inlet guide vanes, flow-straightening vanes, and distributed wall bleed. Input to the program consists of calculation control parameters, geometrical data, and physical data. Output includes calculated wall conditions, strut data, blade forces, and solutions for the flow variables across the duct at selected streamwise stations.

This program is written in FORTRAN IV for execution in the batch mode and has been implemented on a UNIVAC 1108 under control of EXEC 8 with a central memory requirement of approximately 47K of 36-bit words.

This program was written by O. L. Anderson of United Aircraft Corp. for Lewis Research Center. For further information, Circle G on the COSMIC Request Card.
LEW-12798

Machinery



Hardware, Techniques, and Processes

- 591 Two-Position Wax-Motor Rotary Actuator
- 592 Automatic Bypass Valve
- 593 Low Partial Discharge Vacuum Feedthrough
- 594 Adjustable Gas-Flow Restrictor
- 594 Transmitting Rotary Motion at an Angle
- 595 Coating for Hot Sliding Seals
- 596 Drag-Pump Rotating Filter
- 597 Compact Bypass-Flow Filter
- 597 Reducing Stickiness of Elastomer Valve Seals
- 598 Metallic Thermal Seal
- 599 Durable, Nonslip, Stainless-Steel Drivebelts
- 600 Two (or More) Rotary Outputs From One Input
- 601 Localized Cooling of Electronic Components
- 602 "Blind" Position Indicator
- 603 Fastener for Thermal Insulation Blankets
- 604 Combined Hinge and Latch
- 605 Gear-Tooth Fatigue-Strength Estimates
- 605 Rigid "Sling" for Topheavy Loads
- 606 Bend-Absorbing Clamp
- 607 Extension Handle for Spray Cans
- 607 Safe, Durable Soil Sampler
- 608 Dynamic Braking of Bidirectional Motors
- 609 Wrench for Thin-Walled Cylinders

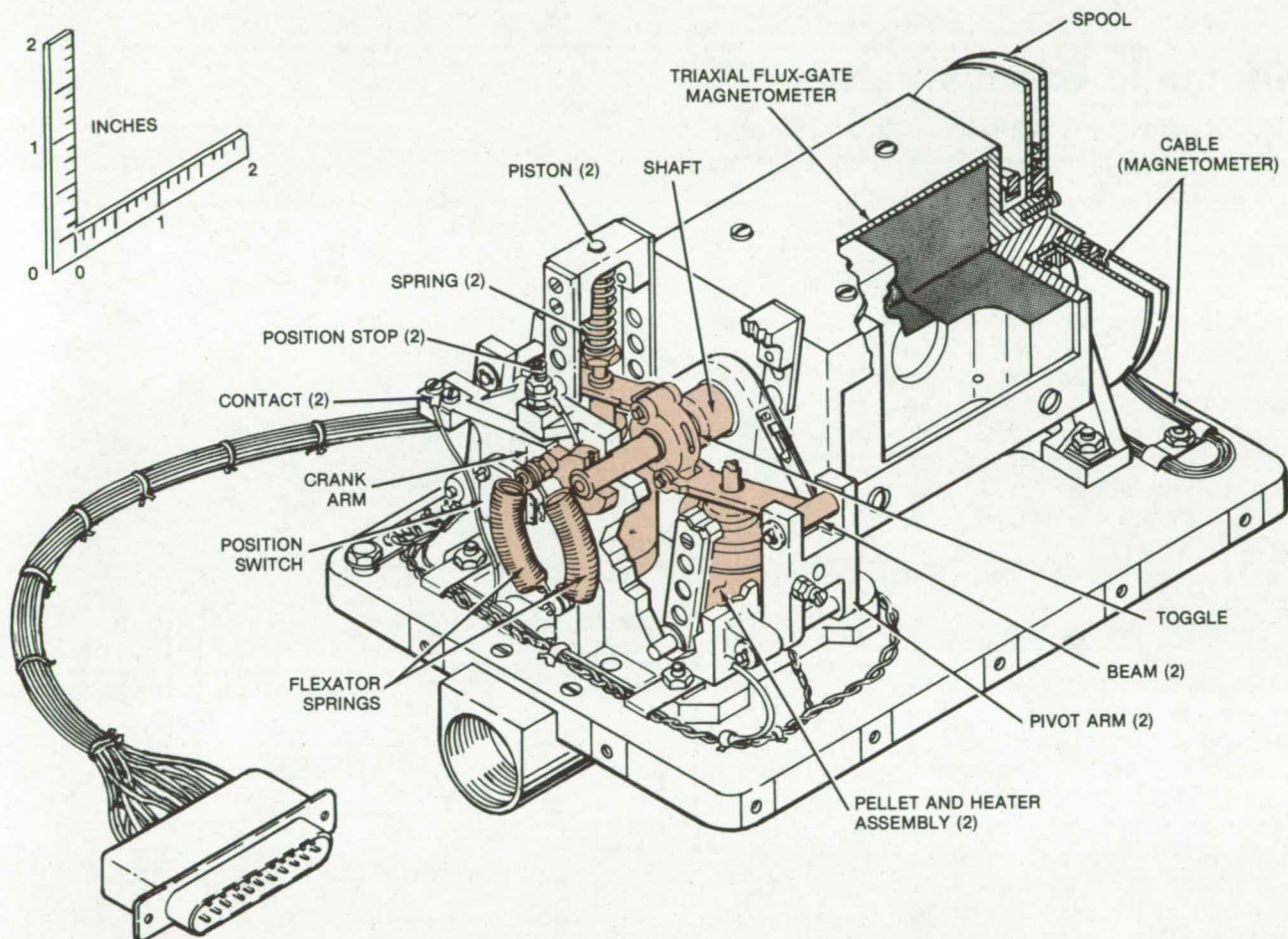
Books and Reports

- 610 Stirling-Engine Design Manual

Two-Position Wax-Motor Rotary Actuator

Heated wax motor (pellet) drives an actuator mechanism that controls two-position motion precisely.

Goddard Space Flight Center, Greenbelt, Maryland



A **Two-Position Rotary Actuator** can be used to flip a magnetometer for calibration in a magnetic field. A heated wax pellet produces the driving force to rotate the shaft by 100°. The final 80° of rotation are provided by the two springs that are compressed during the initial motion. Rotational tolerance is $\pm 1/4^\circ$; stray magnetic fields are less than 0.1 gamma.

Heated wax that expands against a piston drives a new two-position rotary actuator (see figure). The actuator rotates a shaft by precisely 180° and rotates it back on command. The mechanism weighs only 1/2 pound (0.23 kg), consumes 11 watts of power, and functions over a wide temperature range under high vacuum for long and unattended periods. It produces virtually no stray magnetic fields and may therefore be used to flip a magnetometer for calibration. The actuator is an improved version of a model described in a previous issue of

NASA Tech Briefs. [See "Cyclical Bidirectional Rotary Actuator" (GSC-11883, GSC-11974, and GSC-11975) on page 118 of Vol. 1, No. 1.]

When a heater bonded to the wax pellet is energized, the heated wax expands and forces the piston out from the pellet. A shoulder of the piston bears against the beam and rotates the toggle. The toggle is tied to the shaft through a pin that travels in the toggle slot. As the toggle rotates, it bears against the pin and rotates the shaft. This produces approximately 100° of rotation of the shaft. An

additional 80° are provided by the two flexator springs that were compressed during the initial motion.

Mechanical stops accurately limit the angle of rotation. A second heater-pellet and beam assembly rotates the shaft back to its original position. Two contact switches indicate whether rotation has been completed, and the position switch indicates whether the shaft is in the 0° or 180° orientation.

This mechanism possesses a number of advantages over other actuators, such as those that are driven by a bimetallic coiled spring.

(continued on next page)

The volume (less the magnetometer) is 35 in.³ (0.57×10⁻³ cm³). It requires no power other than that supplied to the heater during the actual rotation. It is therefore not susceptible to power fluctuations and is thermally stable. The actuator functions well from -45° to +65° C. Its rotational tolerance is

±1/4°. Stray magnetic fields are less than 0.1 gamma at 1/2 inch (1.3 cm), which makes it ideal for magnetometer applications.

This work was done by William C. Stange of **Goddard Space Flight Center**. For further information, Circle 72 on the TSP Request Card.

This invention is owned by NASA, and a patent application has been filed. Inquiries concerning nonexclusive or exclusive license for its commercial development should be addressed to the Patent Counsel, Goddard Space Flight Center [see page A8]. Refer to GSC-12521.

Automatic Bypass Valve

Regulator diverts air around a flow-rate-limited obstruction to maintain required total airflow.

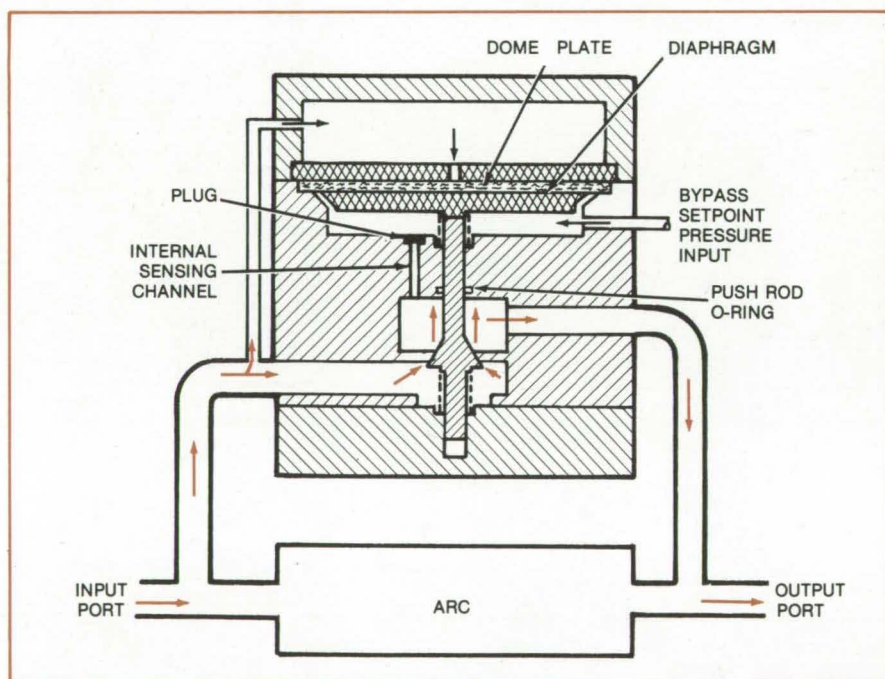
Langley Research Center, Hampton, Virginia

A standard pressure-regulator valve has been modified to divert extra gas flow automatically as required. The modified valve was developed for arc-powered wind tunnels that often require more air flow (in controlled amounts) than can pass safely through the arc. The valve injects the extra airflow into the tunnel downstream from the arc. The principle can be adapted to other equipment in which flow above a predetermined level must be diverted from time to time.

In the modification, a diaphragm pressure-reducing regulator is converted into a sensitive back-pressure regulator. The new version allows automatic, accurate, easily adjustable transfer of the excess airflow.

The modification consists of adding an O-ring seal to the pushrod and a plug to the internal sensing channel (see figure). The valve input port is connected by a tee to the airflow line at a point just upstream from the arc, and the valve output port is connected to the airflow line just downstream from the arc. The upstream pressure (the pressure at the input port) is connected to the dome side of the diaphragm, while the desired bypass setpoint pressure is applied under the diaphragm (through the normal external sensing port). An external surge volume of gas is inserted in the bypass setpoint pressure line to hold the setpoint.

The O-ring prevents bypass setpoint air from leaking along the push-



An **Excess-Flow Diverter Valve** is shown here with its pushrod in the fully closed position. The sensitivity of the valve is determined by the ratio of the diaphragm active area to the valve orifice area.

rod. The diaphragm side of the dome plate is lightly grooved to distribute the dome pressure over the entire surface of the diaphragm.

As long as the supply pressure (flow rate) is less than the preselected bypass pressure, the valve does not bypass any air — the entire flow enters the tunnel upstream of the arc. However, when the air flow to the arc drives the input pressure above the

bypass-setpoint pressure (maximum flow rate desired to the arc), the valve automatically adjusts to the proper opening by internal feedback and bypasses the excess flow to its discharge port and thence to the downstream airflow.

This work was done by Robert F. Mayo of **Langley Research Center**. No further documentation is available. LAR-12063

Low Partial Discharge Vacuum Feedthrough

A semiconducting sleeve on the inner conductor reduces partial discharge by a factor of 10^4 .

Goddard Space Flight Center, Greenbelt, Maryland

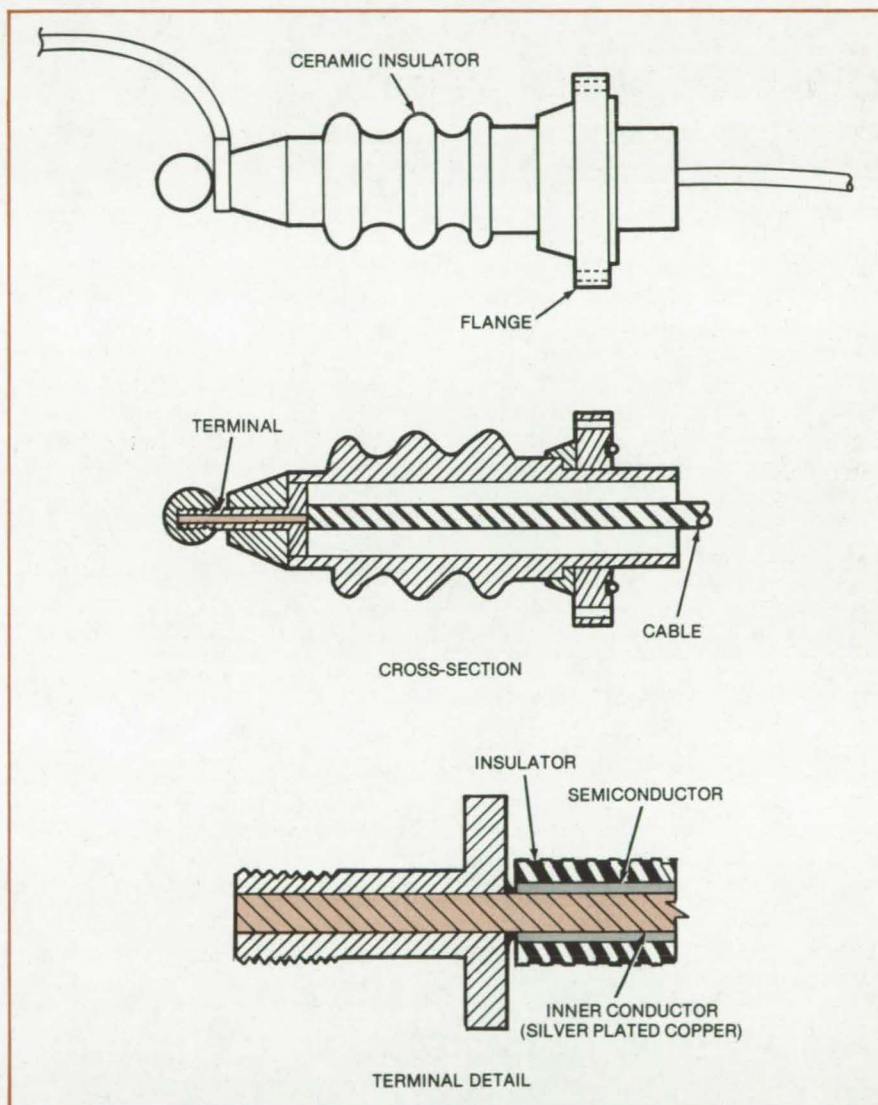
Partial discharges, troublesome momentary electrical breakdowns that occur near surface irregularities on high-voltage feedthroughs, are sharply reduced by a new feedthrough, shown in the figure. Its principal feature is a semiconducting sleeve around the inner conductor stranded wire that smooths out the equipotential surfaces and prevents intense local electric fields from building up.

Three of the new feedthroughs were tested at 20 kV dc and atmospheric pressure. In the tests, only 19, 20, and 83 partial discharges (for the respective models) at levels higher than 1.71 picocoulombs were detected during a 200-second acquisition time. This is a 4 orders-of-magnitude improvement over conventional feedthroughs, which were also tested. Additional tests below 10^{-5} torr showed only one partial discharge greater than 5 picocoulombs for the new design.

As shown in the figure, the feedthrough has a conducting terminal with a spherical screw-on knob. Silver-plated copper conductors are inserted through the axis of the terminal and are silver-soldered to a flange. To the right of the flange, the conductors are surrounded by a semiconducting sleeve, such as carbon-filled silicone, and by an outer flexible insulating sleeve.

Other components of the feedthrough include two metal (Kovar, or equivalent) sleeves and a ceramic insulating sleeve. The metal sleeve on the left is welded to the terminal, while on the one on the right is bonded to the ceramic material. The insulating sleeve is made of high-alumina ceramic; its inside diameter is larger than the outside diameter of the insulated conductors. A connecting flange on the end of the feedthrough is bolted to the vacuum-chamber wall and is sealed with a copper O-ring.

A cable can be secured to the feedthrough terminal by a spherical metal knob screwed on the threaded



A relatively **Discharge-Free Vacuum Feedthrough** uses silver-plated copper conductors jacketed by a carbon-filled silicone semiconductor. This reduces concentrated electric fields and minimizes the occurrence of partial discharges.

portion. The spherical shape reduces the electrical field at the terminal.

This work was done by Jeffrey W. Benham and Stephen R. Peck of General Electric Co. for **Goddard Space Flight Center**. For further information, Circle 73 on the TSP Request Card.

This invention is owned by NASA, and a patent application has been filed. Inquiries concerning nonexclusive or exclusive license for its commercial development should be addressed to the Patent Counsel, Goddard Space Flight Center [see page A8]. Refer to GSC-12347.

Adjustable Gas-Flow Restrictor

A flow path between mating threads reduces high pressures within a short axial distance.

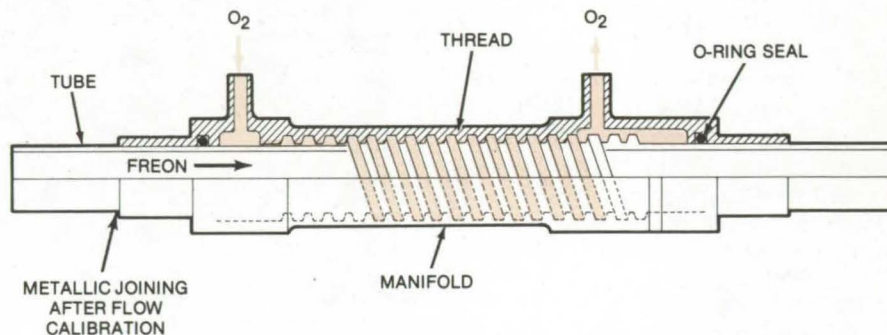
Lyndon B. Johnson Space Center, Houston, Texas

A new adjustable flow restrictor reduces the pressure of flowing gases and simultaneously heats them. The device consists essentially of two mating threads (see figure); the small space between the threads is a long narrow helical path for the flowing gas and reduces its original high pressure to a low value within a short axial distance. The pressure drop can be adjusted simply by screwing or unscrewing the threaded members to increase or decrease the length of the flow path.

Freon flowing through the hollow core of the restrictor heats the gas moving through the helical path. A spiral turbulator in the core prevents laminar flow of the Freon and thus ensures maximum heat transfer.

The flow restrictor was developed for the environmental-control and life-support subsystem of a space vehicle. It can be adapted to a variety of fluid-control applications — of liquids as well as gases — in petroleum processing and food processing, for example. If heat transfer is not necessary, the Freon flow can be eliminated.

In its original aerospace application, the flow restrictor converted



Because **Oxygen Flow Is Restricted** by its long spiral path through the mating threads, cryogenic high-pressure oxygen at the inlet becomes atmospheric-pressure, near-room-temperature oxygen at the outlet. The pressure drop can be adjusted simply by screwing or unscrewing the threaded parts to increase or decrease the flow path.

oxygen at an inlet pressure of 900 psi (6×10^6 N/m²) and a temperature of -150° F (-100° C) to an outlet pressure of 15 psi (10^5 N/m²) or less and a temperature of 0° F (-18° C). The maximum oxygen flow rate is 10 lb (4.5 kg) per hour. The Freon flow is 2,250 lb (1,020 kg) per hour at an inlet pressure of 200 psi (1.4×10^6 N/m²) and a temperature of 40° F (4° C). The pressure reduction and heating are accomplished in a device only about 6 inches (15 cm) long.

The equivalent diameter of the spiral gas-flow passage is 0.0175 inch (0.44 mm). This is large enough to make clogging with foreign particles unlikely, but if clogging does occur, the two halves can be unscrewed for cleaning.

This work was done by Jeffrey J. Brown and Angelo Carnevale of Rockwell International Corp. for Johnson Space Center. For further information, Circle 74 on the TSP Request Card.
MSC-19486

Transmitting Rotary Motion at an Angle

Bellows device transmits rotation at angles as great as 180° with minimal weight and complexity.

Lyndon B. Johnson Space Center, Houston, Texas

A flexible bellows transmits rotary motion around a corner, just as bevel gears do but with much less weight. The bellows can transmit torques in the range of 100 to 1,000 pound-inches (10 to 100 N-m) at corner angles as great as 180°.

Developed for opening and closing remotely operated doors on the Space

Shuttle Orbiter, this "transmission" might be useful in other situations where:

- light weight is desired,
- small motions or misalignments may occur between the two points of rotation,
- the passage of fluids or electric wires through the hollow interior

would save space and weight, •a hermetic seal between the two rotating members is required. Possible uses include marine or submerged mechanisms and food-processing or pharmaceutical machinery where a sealed drive line or a drive line without contaminating lubricants is required.

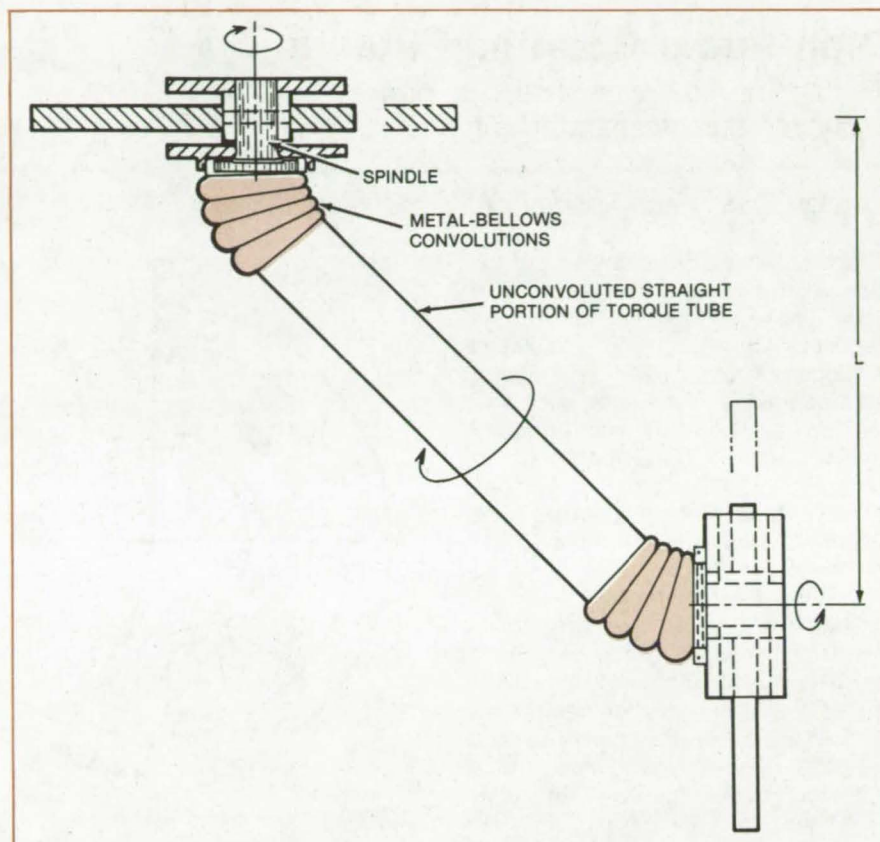
The transmission consists of a corrugated metal tube that can bend along its axis, but does not twist. Thus, rotation of one end of the bellows produces the same rotation at the other end. Both oscillating and continuous rotation can be transmitted. (However, if the arc is of small radius and large angle, the complete stress reversals of continuous rotations will shorten the life of the bellows.)

For distances greater than about 5 cm between the points of rotation, only the ends need be corrugated; the center portion can be a straight tube as in the figure. The bellows is welded or brazed to a spindle, which provides or accepts the rotational force.

If the torque is fairly high, the bellows has a tendency to undulate as it turns. This "squirming" motion can be prevented by encasing the bellows in a sheath. The sheath performs other useful functions as well: It supports an intermediate straight tube against vibration, and it protects the bellows against damage during handling and installation — particularly valuable if the bellows wall is thin.

If no sheath is used, the bellows linkage is essentially friction-free, and no lubrication is needed except that normally used at the main pivots. When a sheath is used, the relative motion between sheath and bellows causes a small amount of friction in the linkage.

If the application requires only limited rotation, the bellows may be shaped to an angle when it is fabrica-



Rotary Motion Is Transmitted from one shaft to another at an angle of 90° by this bellows device. Dimension L is 5 inches (12.7 cm) in this design.

ted. It will then be subjected to less flexure than if it were straight, and the allowable stiffness and strength may therefore be increased. In the example shown in the figure the total rotation is 60°. The bellows are rotated $\pm 30^\circ$, and each is preshaped

to a 45° curve.

This work was done by Walter T. Appleberry of Rockwell International Corp. for Johnson Space Center. For further information, Circle 75 on the TSP Request Card. MSC-19483

Coating for Hot Sliding Seals

Heat-resistant paint reduces friction, improves reliability.

Lyndon B. Johnson Space Center, Houston, Texas

A paint has been found to be an effective surface coating for a sliding seal that must operate at elevated temperatures. Unlike other coatings, the paint is easy and economical to apply and offers minimal friction. Ceramic coatings, for example, must be applied by plasma arc spraying; and unless such coatings are ground or lapped to a fine finish, they are abrasive in a sliding seal. Moreover, ceramic coatings can interfere with

subsequent manufacturing processes such as brazing.

High-emittance surfaces have been prepared on iron/cobalt/nickel heat- and corrosion-resistant alloy using Pyromark black refractory paint. (An equivalent paint could be used.) The paint is applied in successive 1-mil (0.025-mm) layers and is cured and vitrified at about 200° F (111° C) above the operating temperature. It can be used at temperatures as high as 2,000° F (1,093° C).

In rubbing tests against impregnated graphite at 5 psi (34.5×10^3 N/m²) loading, the coefficients of friction were 0.25 (static) and 0.1 (dynamic) at room temperature and at 900° F (482° C). Wear on paint and graphite surfaces was negligible.

This work was done by Julius Stock of Fairchild Industries Inc. for Johnson Space Center. No further documentation is available. MSC-16529



Drag-Pump Rotating Filter

Filter removes contamination to protect hydrogen pump-separator in fuel cell.

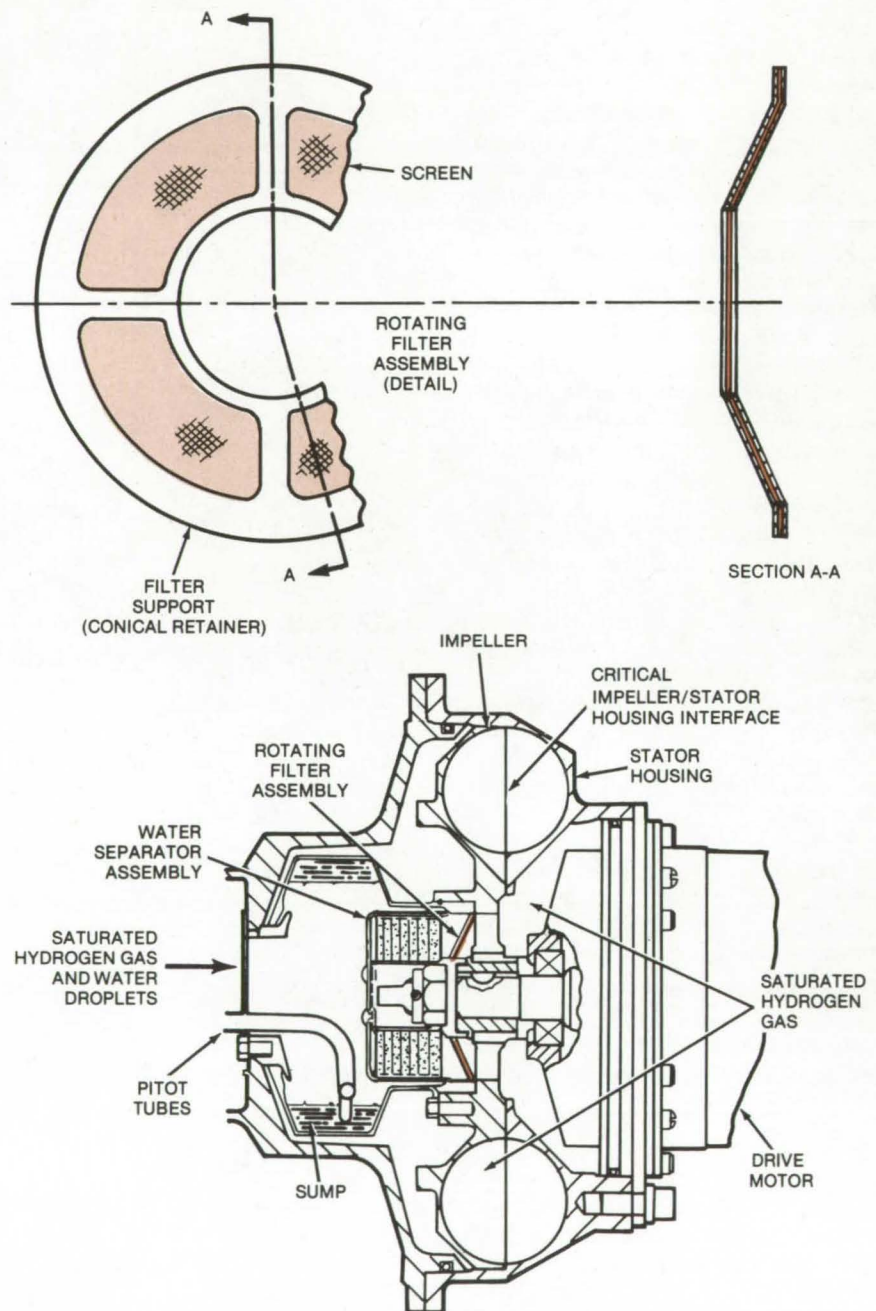
Lyndon B. Johnson Space Center, Houston, Texas

The fuel-cell powerplant aboard the Space Shuttle uses a drag pump with a liquid water separator to remove product water from the circulating hydrogen. A rotating filter (see figure) incorporated in the water separator section traps contaminants before they reach the critical impeller/stator-housing interface, thus preventing pump seizure or other damage. The filter is located as close as possible to the critical interface.

An important consideration in designing the filter is the close tolerances at the impeller face and at the impeller outside diameter. The tolerances are necessary for best pump performance with minimum size and weight. When the drag pump is in a vibration mode, the impeller/stator face gap normally closes, and the filter protects the face gap from contamination during the vibration-induced face closure.

As shown, the filter is a screen mesh on a conical retainer. It mounts on the water separator and is held in place by an interference fit. The centrifugal forces generated during the impeller/sump/separator rotation clear the screen of condensed water droplets that are deposited either during pump operation or following powerplant shutdown. Tests have shown that the screen clears itself after a normal fuel-cell shutdown and subsequent condensation of water vapor from the saturated hydrogen gas. The filter is located downstream of the point where the water droplets have been removed from the circulating hydrogen gas.

This work was done by George H. Davis and Thomas M. Doyle of United Technologies Corp. for **Johnson Space Center**. No further documentation is available.
MSC-16180



A **Rotating Filter** is placed very close to the drag-pump impeller/stator interface to prevent contamination of this critical region.

Compact Bypass-Flow Filter

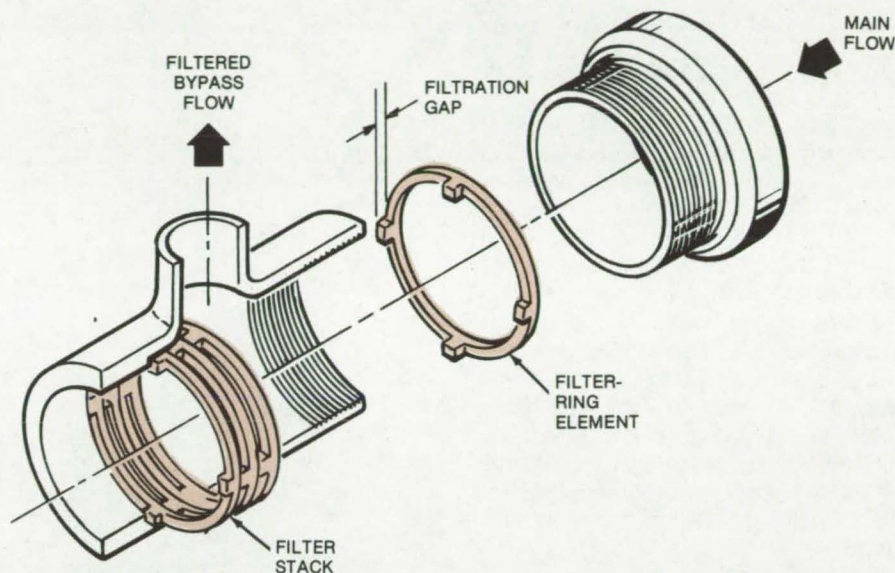
Stacking rings remove contamination from bypass flow without interfering with the main fluid flow.

Lyndon B. Johnson Space Center, Houston, Texas

An annular filter used in the Space Shuttle propellant system allows the unimpeded flow of fluid through its center but removes particles from fluid passing through it in a radial direction. The filter thus separates particulates from bypass fluid without slowing down the main flow (see figure). Possible applications include fluidized-bed reactors, equipment for catalyst operations, and water purification systems.

The filter consists of stacked rings containing precise, chemically milled gaps. The gaps allow bypass fluid to pass through the filter, but they retain particles. The gap depth corresponds to the maximum-size particle that can pass with the fluid. For example, rings with 3-micron gaps would retain particles larger than 3 microns.

The filter can withstand high differential pressures, and it can easily be disassembled for cleaning. It also takes up very little space, and it should therefore be useful in restricted geometries. When the ring elements are assembled, they exert a spring force against each other. Thus, a separate loading spring is not required.



Stacking-Ring Elements of a Bypass-Flow Filter cover the bypass orifice so that they collect particles that would otherwise enter the bypass stream. The filtration gaps are cut to the desired depth in the ring elements by chemical milling. (Gaps are exaggerated here to show detail.)

This work was done by William G. Swift and Jack M. Ulanovsky of Parker Hannifin Corp. for Johnson Space Center. No further documentation is available.

Inquiries concerning rights for the commercial use of this invention should be addressed to the Patent Counsel, Johnson Space Center [see page A8]. Refer to MSC-18311.

Reducing Stickiness of Elastomer Valve Seals

A special process partially removes a component that causes valve sticking.

Langley Research Center, Hampton, Virginia

Seals made of peroxide-cured elastomer (ethylene propylene and silicone) are used in special valves designed to open within a few milliseconds in response to an electrical signal. However, these seals tend to stick, particularly when the valves have been closed for a long time.

A close examination of the elastomer material revealed that a low-molecular-weight hydrocarbon oozes

out during heat exposure, forming a tough sticky film. This hydrocarbon, also called "tail," is present in all conventional polymer seals and constitutes about 3 percent by weight of the material. An additional tail is generated during peroxide-catalyzed cure as a result of free-radical-induced chain splitting. In both cases, the tail causes stickiness and promotes permanent deformation of seals that have been compressed.

A new process removes part of the tail from the elastomer. The elastomer (in this test NASEAL-411, or equivalent, based on Nordel 1635 formulation, or equivalent) is boiled in hexane at 150° F (65° C) for 1 hour. The elastomer then is dried for 1 hour at 320° F (160° C).

The process extracts 2.8 percent of the total weight from the finished elastomer, or approximately one-half
(continued on next page)



of the extractable tail. Complete extraction is not carried out because the elastomer may shrink and leak. The extraction efficiency is controlled by the diffusion rate and temperature.

Results from tests on finished elastomer seals showed that the valve opened in less than 5 milliseconds —

well within the duration of the electrical pulse initiating the action. The new seals showed less than 1 mil (0.03 mm) indentation as compared to indentations exceeding more than 3 mils (0.08 mm) on unprocessed seals.

This work was done by Troy V. Braswell and Jon W. Martin of TRW,

Inc., for Langley Research Center. No further documentation is available.

Inquiries concerning rights for the commercial use of this invention should be addressed to the Patent Counsel, Langley Research Center [see page A8]. Refer to LAR-11778.

Metallic Thermal Seal

An easy-to-install metal barrier prevents hot gas from leaking through small gaps.

Lyndon B. Johnson Space Center, Houston, Texas

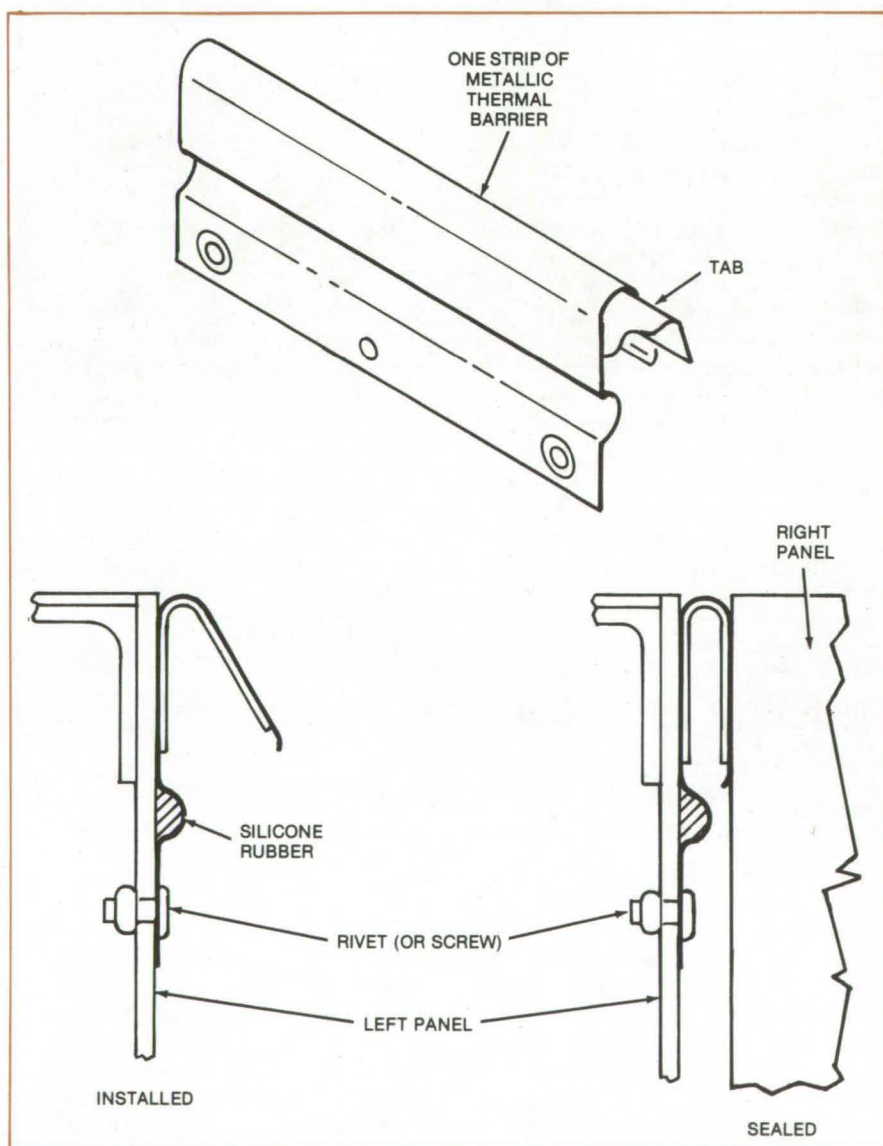
A simple metallic seal, originally designed to prevent hot gas from leaking through gaps between the split rudder and speed brake on the Space Shuttle, could be adapted for home and industrial use. It could, for example, be used to prevent heat from escaping through gaps around doors, windows, partitions, and similar structures.

The barrier consists of a series of U-shaped metal strips that are installed along the entire length of the gap. Each strip (see figure) is secured by rivets or screws to one side of the gap. This side also includes a channel filled with room-temperature-vulcanized (RTV) silicone rubber. The rubber lining prevents gas from leaking into the cavity on this side of the seal. The other side of the metallic barrier presses against the surface on the opposite side of the gap. Tabs are spot-welded to adjacent telescoping seal sections, forming a continuous barrier along the entire gap.

The new barrier is particularly effective in sealing small gaps [these were 0.25 to 0.32 in. (6.3 to 8.1 mm) on the Space Shuttle]. It is also effective at high temperatures at which nonmetallic seals cannot be used. In addition to its possible uses in homes, the thermal barrier might also be utilized by metal-processing industries to insulate part of a metal section during intermediate processing steps.

This work was done by John Bellavia and John O. Kane of Rockwell International Corp. for Johnson Space Center. For further information, Circle 76 on the TSP Request Card.

MSC-18135



This **Metallic Barrier** fits into gaps between panels to prevent hot gas from escaping. The barrier comprises U-shaped strips secured to one end of the gap by screws. The opposite end is spring-compressed for a flush fit. Tabs, spot-welded to adjacent barrier elements, form a continuous seal.

Durable, Nonslip, Stainless-Steel Drivebelts

Toothed drivebelts would have long lifespans in hostile environments.

Goddard Space Flight Center, Greenbelt, Maryland

Two toothed stainless-steel drivebelts originally proposed for use on spacecraft would retain their strength and flexibility in extreme heat or cold, intense radiation, or under high loading. The belts are particularly suited to use in machinery for which belt replacement is difficult or impossible, such as permanently encased equipment, machines used in tunnels or mine shafts, and machines that require elaborate disassembly before the belt is accessible. Unlike belts composed of plastic and polymeric fibers, the stainless-steel belts would not degrade in a harsh environment; and, unlike corrugated metal belts, the stainless-steel belts would not stretch or slip.

One design for an all-steel belt, shown in Figure 1, uses cylindrical rods that run transverse to the entire belt length and serve as teeth to mesh with wheel sprockets. The teeth/rods are held together by a number of steel wires that run along the length of the belt. The wires form loops around preselected rods; adjacent wires are looped around different rods, as shown, to prevent the rods from shifting position along the direction of belt travel (a common cause of belt failure).

To ensure correct spacing, wires are looped around rods according to the formula

$$M = K(N + 1)$$

where M is the number of rods making up the belt, N is the number of rods between consecutive loops, and K is an integer. For example, when N is 2 and K is 6, M is 18. A similar procedure is used when a spiraling single wire is wound around the periphery of the belt to form a multitude of adjacent wires. In this case

$$M = K(N + 1) \pm 1$$

(continued on next page)

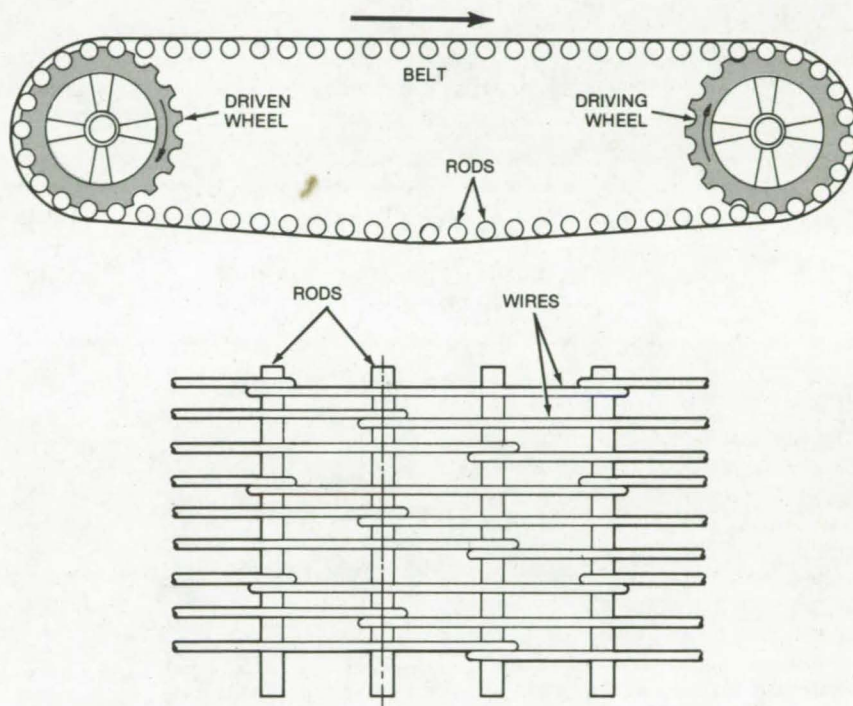


Figure 1. **Transverse Rods** form the teeth in this stainless-steel drivebelt. The rods are joined by wires that are looped around the rods in staggered fashion for flexibility without allowing the rods to shift longitudinally. The rods engage grooves in the wheels.

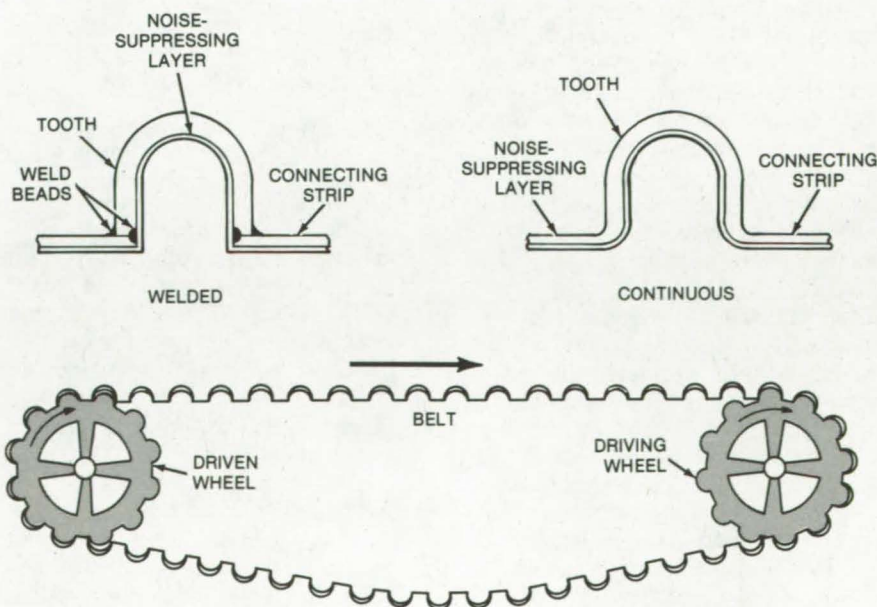


Figure 2. The **U-Shaped Teeth** of this stainless-steel belt flex as they fit over the sprocket wheels. Connecting strips between teeth are flexible for bending but do not stretch or slip. Welded or continuous construction may be used.

This belt may be encapsulated in a flexible rubber or plastic material to reduce any wear caused by the rods contacting the pulley sprockets. This measure also reduces noise generated by the metal-to-metal contact.

The second new belt consists of U-shaped teeth connected by flexible strips (see Figure 2) that engage sprockets on the wheels. The connecting strips between belt teeth resist stretching in their lengthwise

directions, but they are flexible enough to conform to the sprocket wheels. The teeth flex as they engage the wheel sprockets, but they do not stretch or slip.

As shown, the belt may be constructed by welding the ends of the U-shaped teeth to the connecting strips, or it may be formed from a continuous strip of stainless steel. To reduce noise, the inner surface of the belt may be coated with rubber or plastic.

This work was done by Hossein Bahman of **Goddard Space Flight Center**. For further information, Circle 77 on the TSP Request Card.

This invention is owned by NASA, and a patent application has been filed. Inquiries concerning nonexclusive or exclusive license for its commercial development should be addressed to the Patent Counsel, Goddard Space Flight Center [see page A8]. Refer to GSC-12276/12289.

Two [or More] Rotary Outputs From One Input

One input rotation is converted to several output rotations having independent arcs and periods.

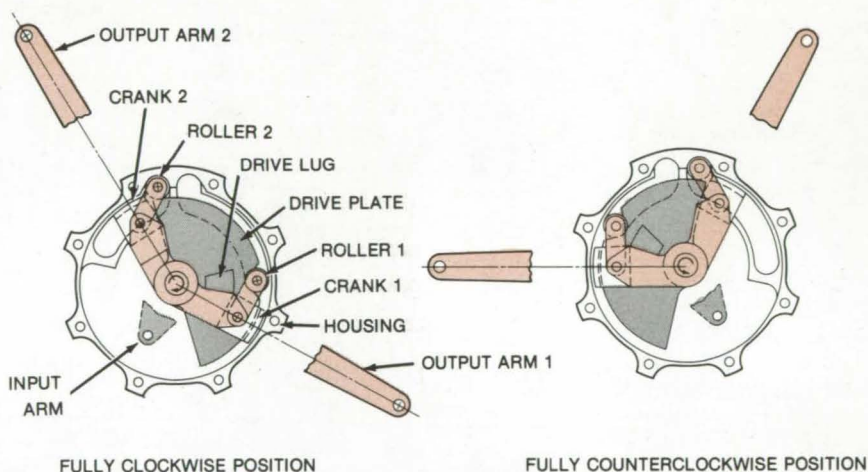
Lyndon B. Johnson Space Center, Houston, Texas

A proposed mechanical sequencing device would produce cyclic rotations of two outputs from a single cyclic rotary input. The device, which was originally conceived for remote unlatching of spacecraft doors, may also be useful in automatic assembly apparatus, in food-processing machinery and as a controller for sequentially operated valves.

The sequencer takes cyclic rotary motion (first clockwise, then counterclockwise over the same arc) and converts it to cyclic rotary motions, over smaller arcs, of two separate outputs.

As shown in the figure, an input arm moves a notched drive plate. The drive plate, in turn, moves two crank-and-roller assemblies, one for each output. In its neutral position (not shown in the figure), the drive-plate notch is centered at the top of the device, and the rollers rest above the drive plate in the housing.

When the drive plate turns clockwise, its drive lug engages crank 1, and the roller for crank 1 drops into the notch in the drive plate. The roller rides in a track as the lug pushes the crank, turning output arm 1 through an arc (90° in the figure). When the oscillating input changes direction and starts turning counterclockwise, output arm 1 is returned to its original neutral position (by a drive lug on the opposite face of the drive plate).



Proposed Rotary Sequencer engages and releases first one output shaft and then another. Each "roller" is actually a set of three rollers that turn about a common axle.

As the input continues its counterclockwise motion beyond the neutral point, crank 2 is engaged, and arm 2 is turned through an arc (of 60°) and then is returned to its neutral position during the next clockwise rotation of the input. One cycle of the input is thus converted to shorter cycles of output shafts 1 and 2.

Depending on the lengths of the roller tracks, the input shaft can rotate through up to 420°, and the output shafts can rotate through angles smaller or larger than 90°. Also,

output shafts 1 and 2 may or may not rotate through the same angles.

If the output angles are kept small, more than two outputs can be built into the device. The rotations of the output shafts can overlap, and the dwell (neutral position) period of each can be varied independently.

This work was done by Walter T. Appleberry of **Rockwell International Corp.** for **Johnson Space Center**. For further information, Circle 78 on the TSP Request Card. MSC-19450

Localized Cooling of Electronic Components

Dry nitrogen cools circuit components for quick tests at low temperatures.

Langley Research Center, Hampton, Virginia

Board-mounted electronic components can be cooled quickly and conveniently for troubleshooting with the aid of a device that produces a cold jet of dry nitrogen. The device can cool small areas [1 to 2 in. (2.5 to 5.0 cm) square] to -35°C in about 1 min.

Unlike mechanical cooling devices, the nitrogen-jet cooler can cool nonflat and hard-to-reach components. In addition, unlike aerosol-spray coolants, the nitrogen jet does not contaminate the circuit boards.

A dry-nitrogen source is connected via a noncontaminating plastic hose to a copper coil submerged in an insulated container (Figure 1). The container, which measures 4 by 4 by 4 in. (10 by 10 by 10 cm), is filled with dry ice and a Freon/alcohol mixture (use suitable safety precautions). The nitrogen flow is adjusted so that the pressure at the input to the plastic hose is 10 to 15 psig (170×10^3 to $205 \times 10^3 \text{ N/m}^2$).

The cooled gas flows through an insulated flexible hose and out of a nozzle. The nozzle is held about 1/2 inch (1 cm) away from the component to be cooled.

The gas temperature, which is measured by directing the nozzle at a thermocouple or thermometer, can be varied by adjusting the inlet valve to the cooling box. When moisture condensation around the cooled area must be avoided, the electronic equipment can be placed in a dry box in which the normal atmosphere has been displaced by dry nitrogen (Figure 2).

This work was done by the Aerospace Division of Honeywell Inc. for **Langley Research Center**. No further documentation is available. LAR-11955

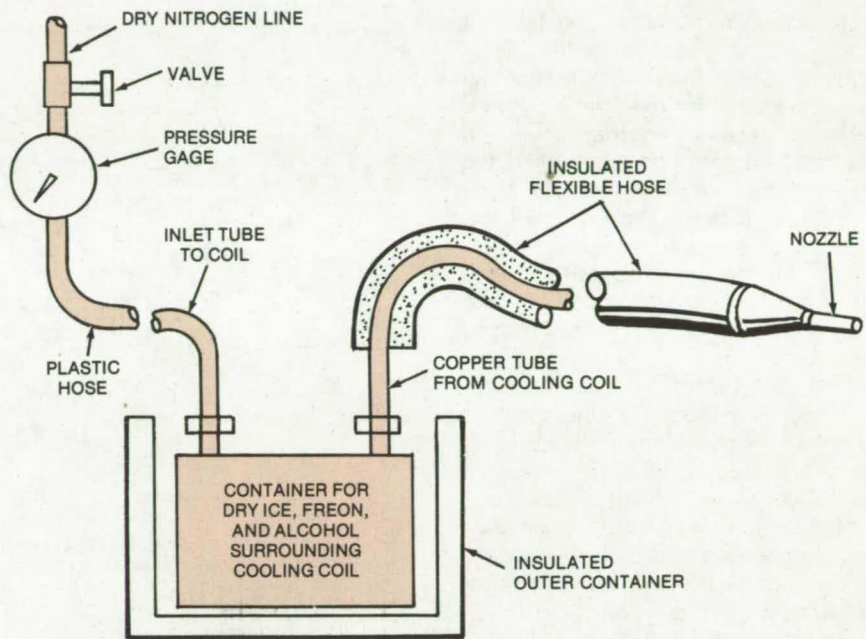


Figure 1. In a **Nitrogen-Jet Cooler**, dry nitrogen passes through a cooling coil submerged in a cooling container and emerges from a nozzle.

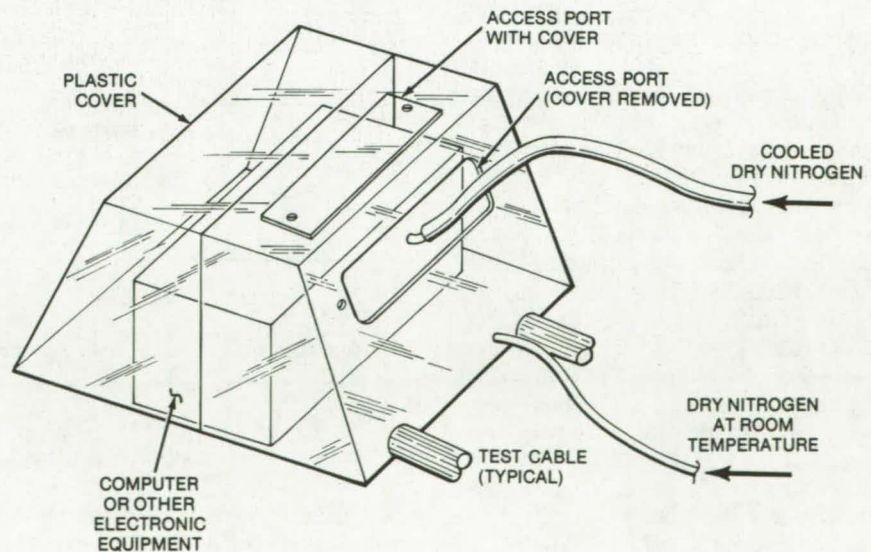


Figure 2. A **Dry Box** for the nitrogen-jet cooler prevents moisture from condensing on electronic equipment when its components are cooled.

"Blind" Position Indicator

Instrument helps to align and insert parts without "seeing" them.

Lyndon B. Johnson Space Center, Houston, Texas

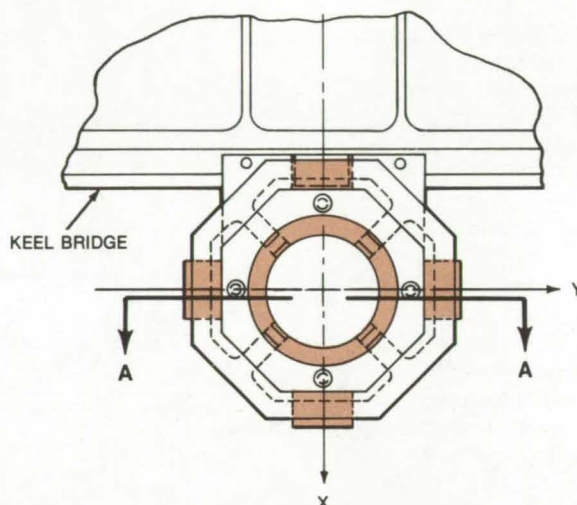
A position-indicating instrument helps an operator to align parts without seeing them. The instrument was developed for the Space Shuttle, where it is used to insert a trunnion on the payload keel into a fitting in the payload bay. A crewmember must insert the trunnion "blind." Without the aid of a position-sensing instrument, the operation is difficult and potentially dangerous, since the fitting can be pushed aside or missed entirely.

The new device visually indicates the relative positions of the trunnion and the fitting and shows when the two parts are lined up. It is also expected to be useful in industrial operations where parts must be blind-positioned accurately. One possible application is in the underwater assembly of rigs for offshore oil drilling.

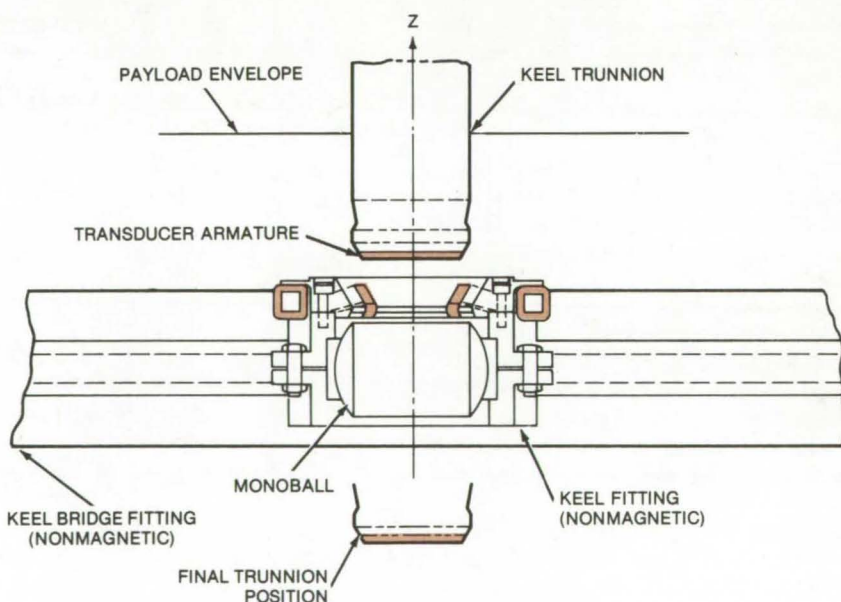
To install the indicator, two variable-reluctance transducers are mounted in a toroidal configuration on the Orbiter fitting, and an armature is added to the bottom of the keel trunnion (see figure). When the operator brings the trunnion close to the fitting, the armature alters the magnetic paths in the four segments of the transducer. If the reluctances of the four paths (including airgaps) are not equal, the differences in impedance are converted electronically to position error signals in the x and y axes. The errors are displayed on a meter readout.

The effective range of the transducer is ± 5 in. (12.5 cm) along the x and y axes (in the plane of the transducer) and 1 in. (2.5 cm) along the z axis (above the transducer). The accuracy of the position information increases as the z coordinate decreases and the trunnion approaches its final position. The accuracy is about 0.25 in. (0.65 cm) when the armature is 1 in. above the transducer and is about 0.02 in. (0.05 cm) when the armature is inside the transducer.

The transducer has a 60° entrance cone, and the trunnion has a corresponding taper to allow mating with a 0.60-in. (1.5-cm) offset between the



POSITION INDICATOR [TOP VIEW]



POSITION INDICATOR [SECTION VIEW]

A Centering Transducer for Alining Parts to be mated, shown in top and section views, includes an armature on one of the parts and variable-reluctance toroids on the other. Differences in the magnetic path impedances between the toroids measure the relative positions of the two parts.

parts. The keel-fitting monoball is restrained to 2.5° of rotation, and the trunnion edge is self-aligning to prevent jamming as it is inserted.

This work was done by Robert C.

Cruzan of Rockwell International Corp. for Johnson Space Center. For further information, Circle 79 on the TSP Request Card.
MSC-16972

Fastener for Thermal Insulation Blankets

A new fastener allows rapid attachment and detachment of insulating blankets.

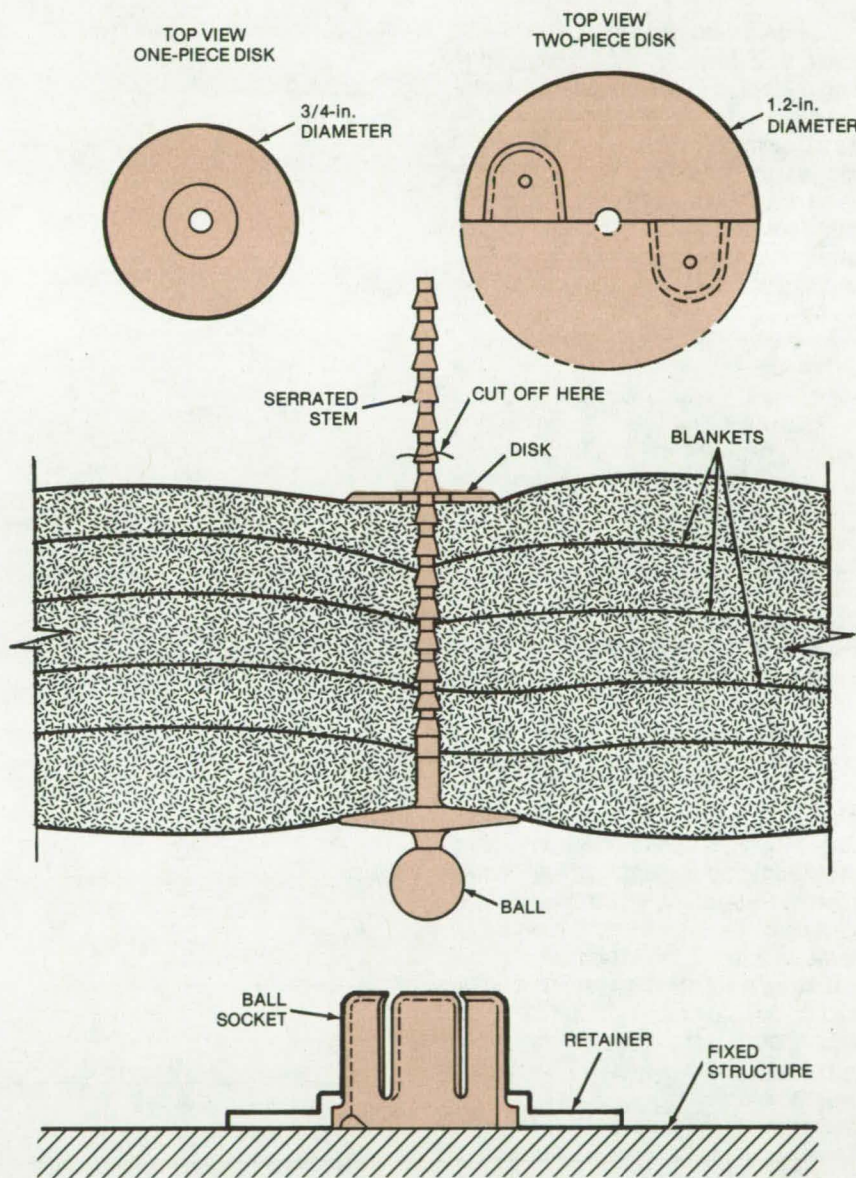
Lyndon B. Johnson Space Center, Houston, Texas

A serrated-stem fastener, similar to those that hold wire harnesses, has been adapted to a new application — attaching insulating blankets to supporting structures. The fastener (see figure) consists of a serrated stem and ball mount, a separable disk or washer, a ball socket, and a retainer. The stem and the disk hold the blankets, and the ball and socket allow the blankets to be attached to and detached from the support quickly.

The new fastener has advantages over several commercial fasteners that were originally considered for use on the Space Shuttle, including canvas snaps and string and tie buttons. The snaps were found to be difficult to install and align; and blankets held by string and tie buttons took too long to remove and replace for area maintenance.

Installation of the fastener begins by mounting several retainers and ball sockets on the supporting structure, using adhesive. An alternate version of the retainer is riveted to the structure. Next, the ball ends of the serrated fasteners are inserted into the ball sockets. The stem, ball, and disk are made out of Torlon, or equivalent material.

The insulation blankets are mounted by pressing them against the protruding serrated stems until the blankets are pierced. The pierced blankets are held in place by flexible (metallic or nonmetallic) disks that are snapped onto the stems. For applications above 350° F (177° C), a two-piece Torlon disk was designed. (A one-piece Torlon disk was found to be too brittle and inflexible to be snapped onto the stem.) These disks are inserted on the stems, and the two interlocking halves are snapped together. Disks can be installed on both the top and the bottom portions of the stems. Stem sections protruding above the disks are snipped off.



This **Fastener for Insulation Blankets** has a serrated stem and a ball mount. The ball is engaged by a socket that is held on a support by a retainer. The insulation blankets are held in place by disks on the serrated stem. Blankets are easily installed or removed by engaging or detaching the ball mounts.

This work was done by James D. Cole and Michael L. Marke of Rockwell International Corp. for

Johnson Space Center. For further information, Circle 80 on the TSP Request Card.
MSC-18253

Combined Hinge and Latch

One mechanism unlatches, opens, and locks open a door

Lyndon B. Johnson Space Center, Houston, Texas

In a proposed door mechanism, the hinge and latch are combined in a single four-part assembly. One continuous actuator stroke unlatches the door, swings it open, and finally it latches the door open at 180°. The assembly is simpler than the hardware found on most automatic doors, which generally have separate hinge and latch, each with their own actuating linkages.

As shown in Figure 1, the four parts of the device include the door, the doorframe, the actuator crank, and a curved drag link. As shown in the sequence, the curved link moves the door back to unlatch its edge from the jamb. Next, the actuator crank is rotated clockwise, which rotates the door through approximately 180° toward its fully open position. Further clockwise rotation of the crank locks the door open by pulling it over a hook extending from the wall or other structure adjacent to the door.

An alternate method of latching the door in the open position is illustrated in Figure 2. This design eliminates the extending hook. Instead, a spring-biased hook is added to the door; the hook engages a matching slot in the adjacent structure when the door is latched open. In this way the door can lie flush against the structure.

The new mechanism can be modified to lock the door in a 90° position. This is done with minor alterations in the shapes of the actuator link and the drag link.

This work was done by Walter T. Appleberry of Rockwell International Corp. for **Johnson Space Center**. For further information, Circle 81 on the TSP Request Card. MSC-19602

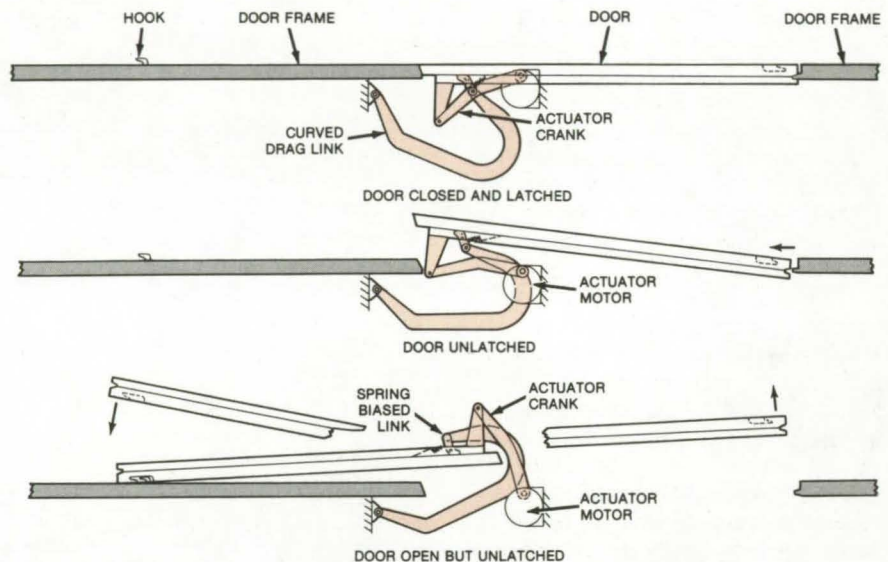


Figure 1. This **Latching Door Mechanism** operates as follows: (Top) the actuator crank is moved clockwise to unlatch the door; (center) the crank is moved clockwise to rotate the door to an open position; and (bottom) the door is latched to the hook to lock it in a 180° open position.

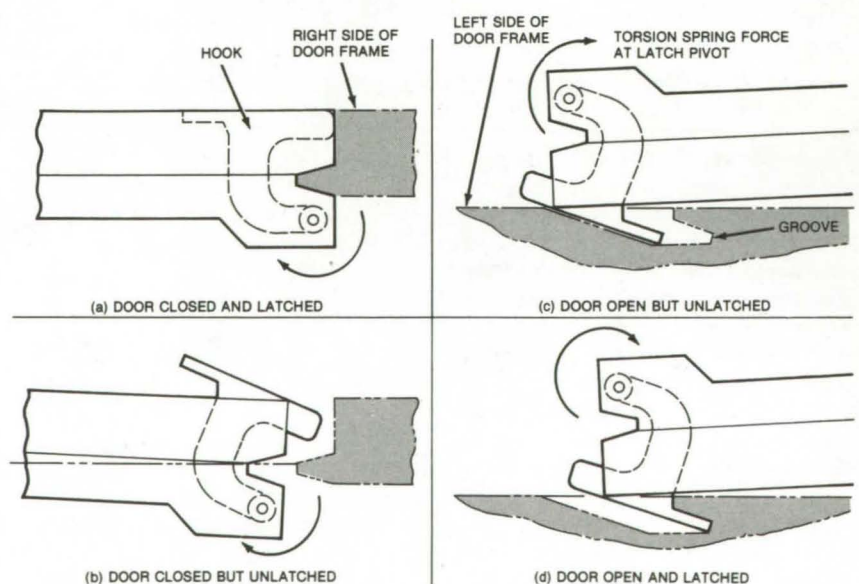
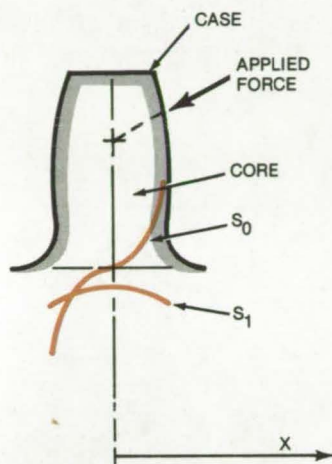


Figure 2. A **Modified Latch** eliminates the need for a protruding hook on the structure. The structure contains a slot to accept a hook on the door, locking the door in a 180° open position.

Gear-Tooth Fatigue-Strength Estimates

A new method helps to rapidly determine fatigue damage and safety margins for case-hardened gear teeth.

Lyndon B. Johnson Space Center, Houston, Texas



The Stresses in a Case-Hardened Gear Tooth vary with distance (x) along the base. The bending stress is S_0 ; the compression stress is S_1 . Equations for the stresses allow the fatigue behavior to be calculated for any point along the x axis.

A new method for determining the stresses in the base of a case-hardened gear tooth considers the entire base, not just the surface as in previous treatments. The method, which can be run on a desk calculator, can help designers to determine rapidly the gear fatigue life and the safety margin.

The outer portion of a case-hardened gear tooth is a thin hard layer (the case) that surrounds an inner core of softer, more ductile material (see figure). Although stress concentrations are largest in the case and diminish into the core, it is possible for the interior stresses to exceed the yield limit of the core material. The most critical region is the core/case interface, where the core is exposed to its greatest stress concentration.

In developing the method, the laws of statics were used to determine an equation for the total stress, including bending and compression contributions, at any point along the base. The stress at the core/case boundary is calculated by substituting known parameters, such as the case dimensions and the applied force, into the stress equation. The number of gear cycles to failure is then determined from the stress by using a modified Goodman diagram, which determines the cumulative damage. This number can be compared with the actual number of cycles to determine the suitability of the gear for the proposed application.

This work was done by Willis Brinkley of McDonnell Douglas Corp. for Johnson Space Center. For further information, Circle 82 on the TSP Request Card.
MSC-18167

Rigid "Sling" for Topheavy Loads

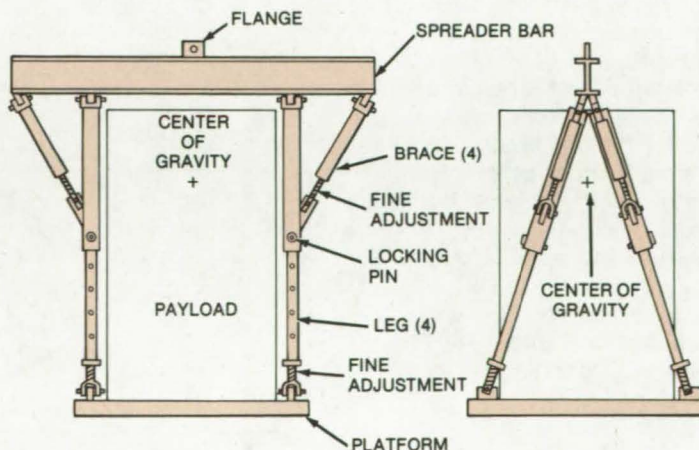
An easy-to-use gantry safely lifts topheavy loads.

Goddard Space Flight Center, Greenbelt, Maryland

Conventional flexible slings can be dangerous when lifting topheavy loads because even a slight misalignment can cause the load to slip through the slings. For applications in which the load center-of-gravity is above its midline, a new gantry that has a rigid platform and braces is a more stable, safer support. The gantry, which might be called a "rigid sling," is designed for quick assembly and adjustment around the payload.

As shown in the figure, the gantry has four bracing legs connected to an I-beam spreader bar. The bottoms of the legs support a platform. Additional rigidity is provided by braces between each leg and the spreader bar. The

(continued on next page)



This Rigid Sling has adjustable legs suspended from a spreader bar. The legs support a platform for lifting topheavy loads.

bar is equipped with a flange for hookup to a crane.

The entire assembly is adjustable in height to accommodate payloads of different sizes. The height is controlled by removing locking pins from the legs, adjusting the legs to the desired height, and reinserting the pins. Fine

height adjustment is provided by threaded sections on the bottoms of the legs.

To use the sling, the payload is centered on the platform, and the legs and braces are adjusted to position the hookup above the payload center-

of-gravity. A crane can then lift the entire structure.

This work was done by Richard D. Stewart of Goddard Space Flight Center. No further documentation is available.

GSC-12359

Bend-Absorbing Clamp

A compact, inexpensive clamp for flexible cables or rigid tubes absorbs vibrations and other motion.

Lyndon B. Johnson Space Center, Houston, Texas

A new clamp for cables or tubes consists of a slotted retainer enclosing a rolling ball. The ball, made out of Teflon (or equivalent) for low friction, is installed on the cable with a sliding fit. The retainer, placed over the ball and secured to a supporting structure, allows movement and bending of the cable without the need for bend-absorbing loops or "pigtailed." The clamp can safely support cables or rigid tubes that connect a fixed structure to vibrating or "floating" machinery.

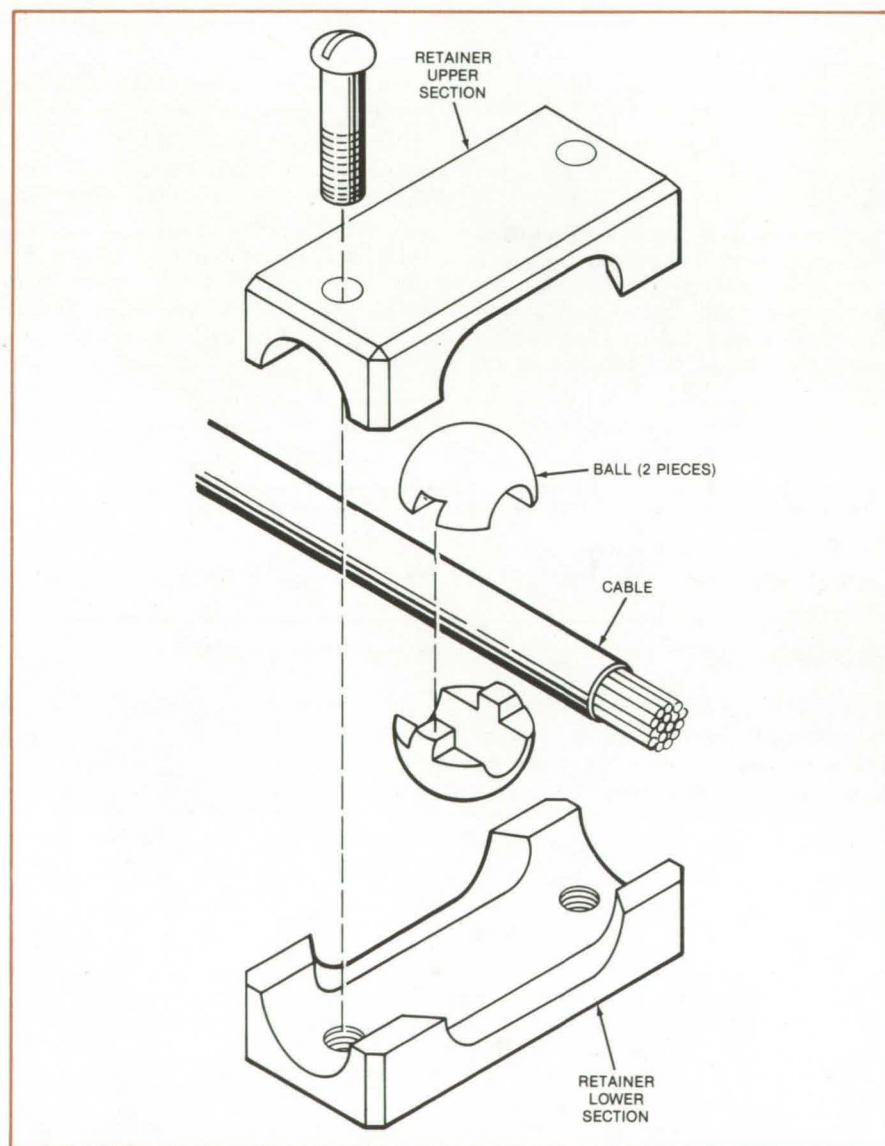
The configuration, as shown in the figure, includes a two-piece ball that fits over the cable in a tongue-and-groove arrangement. A hole through the center of the ball allows it to slide freely along the cable.

The ball is enclosed in a slotted retainer that is secured to a supporting structure, using a bracket and screws. Once the clamp is installed, the cable is free to slide inside the retainer along two orthogonal axes. In addition, the cable or tube can be rotated up to 20° around the third axis.

The clamp can be sized to accommodate a wide range of cable or tube dimensions. It saves space by eliminating the pigtailed or bellows that are commonly used to absorb linear movement or vibration.

This work was done by James R. Abbott and Ben Valencia, Jr., of Rockwell International Corp. for Johnson Space Center. For further information, Circle 83 on the TSP Request Card.

MSC-16971



A Bend-Absorbing Clamp comprises a ball and a slotted retainer. The ball surrounds a rigid tube or cable and slides in the retainer. This clamp is very effective on pipes or cables that connect fixed structures with vibrating machinery.

Extension Handle for Spray Cans

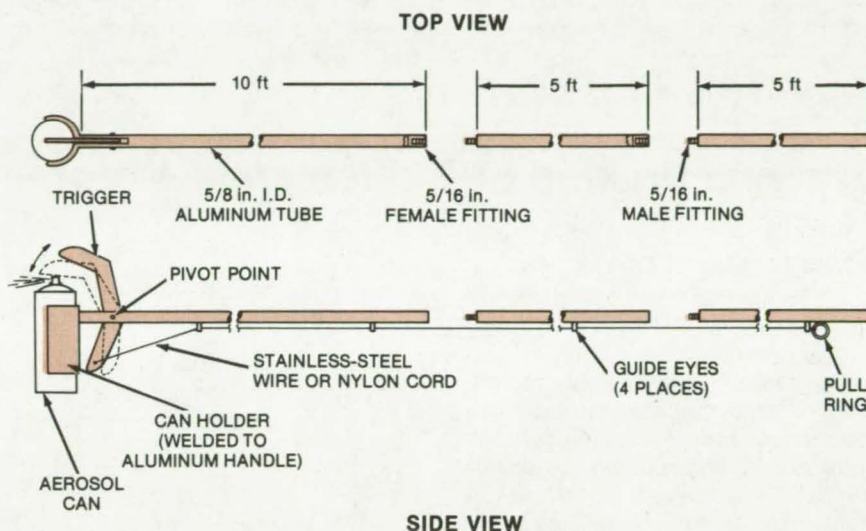
Tubing and trigger assembly directs aerosol spray into hard-to-reach areas.

John F. Kennedy Space Center, Florida

An extension handle and trigger mechanism for aerosol-spray cans allows hard-to-reach areas to be sprayed with touchup paint, lubricant, insecticide, and other materials. The aerosol can is fitted into a holder on the end of a 3-meter extender bar. In addition, there are two more 1.5-meter extenders that can be attached to make an even longer handle (see figure).

A stainless-steel wire or nylon cord, threaded through guide eyes on the sections, is pulled to operate the can. When the cord is pulled, a trigger presses the release button on the aerosol can. When the cord is released, the trigger is released, and the spray stops.

The tool was originally developed for applying oil to the operating mechanisms of large overhead doors located 6 meters above floor level. A moving platform had previously been used by maintenance people to climb up and reach the mechanisms; however, the platform could not be maneuvered into some of the areas where it was needed. A 20-foot ladder



Lightweight Handle for Spray Cans Extends to 20 Feet when three sections of aluminum tubing are assembled.

was also tried, but two people were needed to move and position it.

This work was done by William G. Lucas of The Boeing Aerospace Co.

for **Kennedy Space Center**. For further information, Circle 84 on the TSP Request Card. KSC-11083

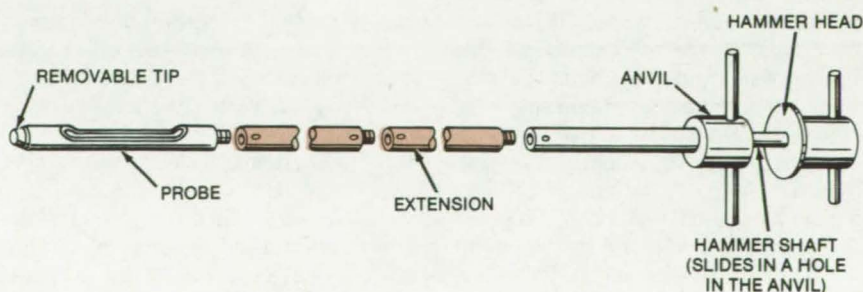
Safe, Durable Soil Sampler

Improved penetrometer protects the user from injury and resists the effects of weather and hard use.

Lyndon B. Johnson Space Center, Houston, Texas

A new soil-sampling tool is expected to be useful in construction, surveying, geological research, and other similar applications. Made of heavy-gage corrosion-resistant steel (CRES), the tool is rustproof and will not buckle (see figure). This modular sampler utilizes 12-inch (30.5-cm) extension sections that can be screwed together to make up a length appropriate for each particular sample. Each section is graduated in 6-inch (15.2-cm) intervals to give a

(continued on next page)



Modular Soil-Sampling Tool can be extended to any length by adding 12-inch sections.

On other penetrometers, recesses and protruding bolts tend to catch soil and hamper inserting and removing the tool. The internal threads on the new design eliminate this problem. Also, samples are easily removed from the specimen cavity, either with

Handles on the built-in hammer allow better control and greater force for insertion. A lip around the bottom of the hammer prevents injury by keeping the fingers away from the impact surface.

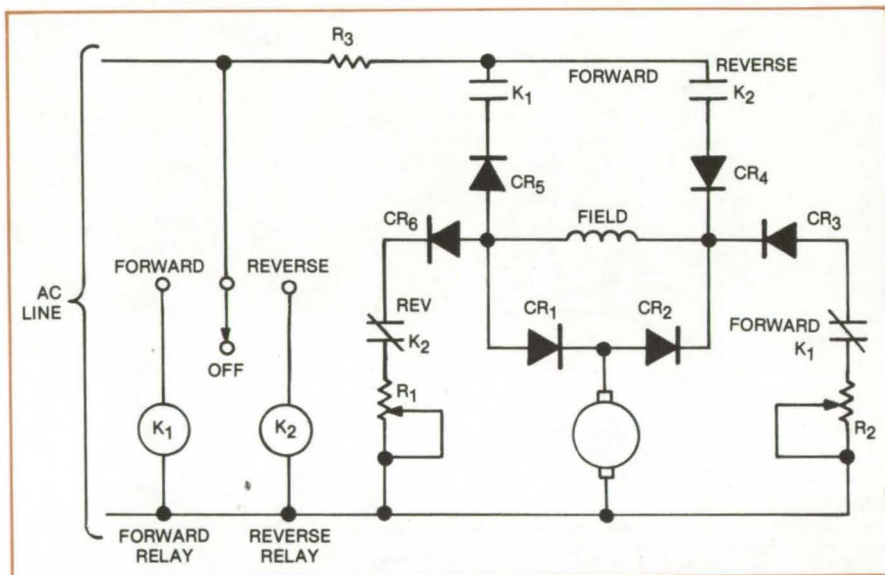
as conveniently for use. No special tools are needed; a screwdriver can be inserted into holes in the sections and used as a lever when joining or separating the parts.

This work was done by Ronald D. Durrant of Lockheed Electronics Co., Inc., for **Johnson Space Center**. For further information, Circle 85 on the TSP Request Card.

A circuit to control the switching of a bidirectional motor with dynamic braking

In an application at Ames Research Center, a bidirectional universal-motor drive for a remotely-operated switch mechanism coasted unpredictably and excessively. The motor would not regenerate for dynamic braking due to a total loss of current during switching from "run" to "brake" and due to a lack of consistent residual magnetism.

Switching for bidirectional motor operation with dynamic braking is simplified by half-wave dc operation of the motor. (However, dc operation cannot be tolerated in all cases since brush wear and commutation are adversely affected.) The circuit shown in the illustration was developed for remote control of a drive mechanism, using simple "forward," "off," and "reverse" switching. The field current direction is fixed and the motor is reversed by reversing the armature current. The current path in "forward" is through diodes CR₂ and CR₅; in "reverse" the current path is through diodes CR₄ and CR₁. Diodes CR₁ and CR₂ are in the field-current path during the transition of relay



contacts (K_1 or K_2) from the energized to the deenergized state. This sustains sufficient field excitation to start regeneration. The dc operation also provides residual magnetism in the field poles, which can start regeneration.

contacts of relays K_1 and K_2 are placed in the dynamic brake paths to avoid shunting the armature with a braking resistor during "run" conditions.

Dynamic braking may be independently adjusted for each direction by varying the value of the associated braking resistor (R_1 or R_2). If more speed or torque is available than is

required, resistor R_3 may be placed in series with the ac line to the motor, reducing motor current and improving brush and commutator life. Relay contacts can be substituted for two or more of the steering diodes. Interlocking relay contacts and travel limit

switches are common additions to this kind of motor control.

With this circuit, fast switching from forward to reverse can result in plugging the motor and may severely damage the gear units. Also, the usual caution should be observed in

applications involving high-inertia loads.

This work was done by Paul F. Dexter of Ames Research Center. No further documentation is available. ARC-11194

Wrench for Thin-Walled Cylinders

A torquing wrench holds thin-wall cylinders gently yet firmly.

Langley Research Center, Hampton, Virginia

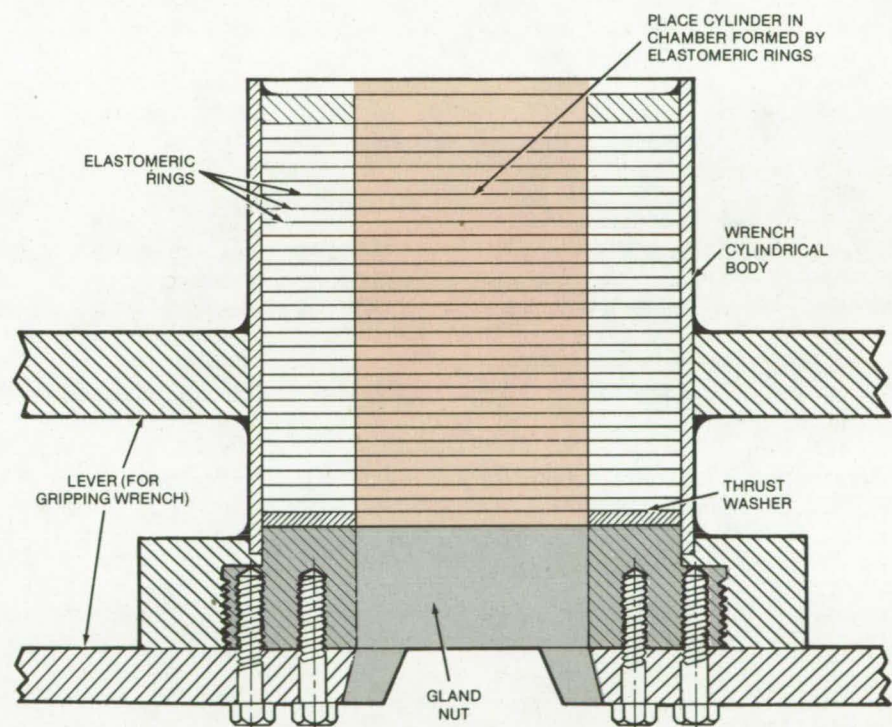
A new adjustable torquing wrench for thin-walled cylinders grips more-uniformly and strongly than conventional strap and pipe wrenches, yet it holds a part gently enough to prevent bending, denting, or otherwise marring of the surface. Moreover, no wrenching flats, slots, or holes need to be added to the cylinder.

The cylindrical wrench fits over a smaller cylinder, and the gap between the cylinders is filled with elastomeric rings. The elastomer is pressure-packed to create enough friction to lock the wrench body and cylinder into inseparable rotation.

As shown in the illustration, one end of the cylindrical body is threaded to accept a gland nut. The opposite end has an access hole with a diameter slightly larger than the cylinder to be manipulated. A lever for gripping the wrench is welded to the body.

To assemble the wrench, insert the elastomeric rings and the thrust washer into the wrench body, and then start the gland nut. Place the cylinder inside and tighten the gland nut for inseparable rotation.

This work was done by Wilbur C. Heier of Langley Research Center. No further documentation is available. LAR-12286



In this **Torquing Wrench for Thin-Wall Cylinders**, the gap between the wrench and the cylinder is filled with an elastomer that is pressure-packed to create a tight friction grip.



Books and Reports

These reports, studies, and handbooks are available from NASA as Technical Support Packages (TSP's) when a Request Card number is cited; otherwise they are available from one of NASA's Industrial Application Centers or the National Technical Information Service.

Stirling-Engine Design Manual

Theory, analyses, test data, and references

The Stirling engine offers the potential of high efficiency and low emissions along with inherent quietness and can use a variety of fuels and heat sources. For the Stirling engine to have widespread application and acceptance, the fundamental operation of the engine must be widely understood, and the analytic tools for simulation, design, evaluation, and optimization of Stirling-engine hardware should be readily available. To meet these objectives a Stirling-engine design manual has been written and published.

The manual discusses the variety of Stirling-cycle heat engines and their utility in comparison to other machines. The theory of Stirling engines is presented starting from simple cycle analysis.

Engine design methods are organized as first-order, second-order, and

third-order, in increasing complexity. First-order design methods employ the classical Schmidt equation and are principally useful in preliminary systems studies to evaluate how well-optimized engines may perform in given heat applications.

Second-order design methods may also utilize the Schmidt equation, but in addition, incorporate engine loss relationships that apply generally for the full engine cycle. This method assumes that the different processes going on in the engine interact very little, and is appropriate for engine performance optimization studies. Second-order engine-modeling relationships are given for several different types of Stirling engine. A method is presented in detail with worksheets for specific cases. One sample problem is presented using the worksheets.

Third-order design methods solve the equations expressing the conservation of energy, mass, and momentum using numerical methods. The engine is divided into many nodes, and short time steps are required for a stable solution. Due to the associated computer times required, third-order methods are usefully limited to engine R. & D. activities and to predicting the detailed performance of a specific engine configuration. Some third-order techniques assume a uniform pressure at each instant in time. This assumption greatly reduces computa-

tion time at some expense in accuracy. Both second- and third-order design methods must ultimately be validated by comparing the design predictions with actual performance of the engine.

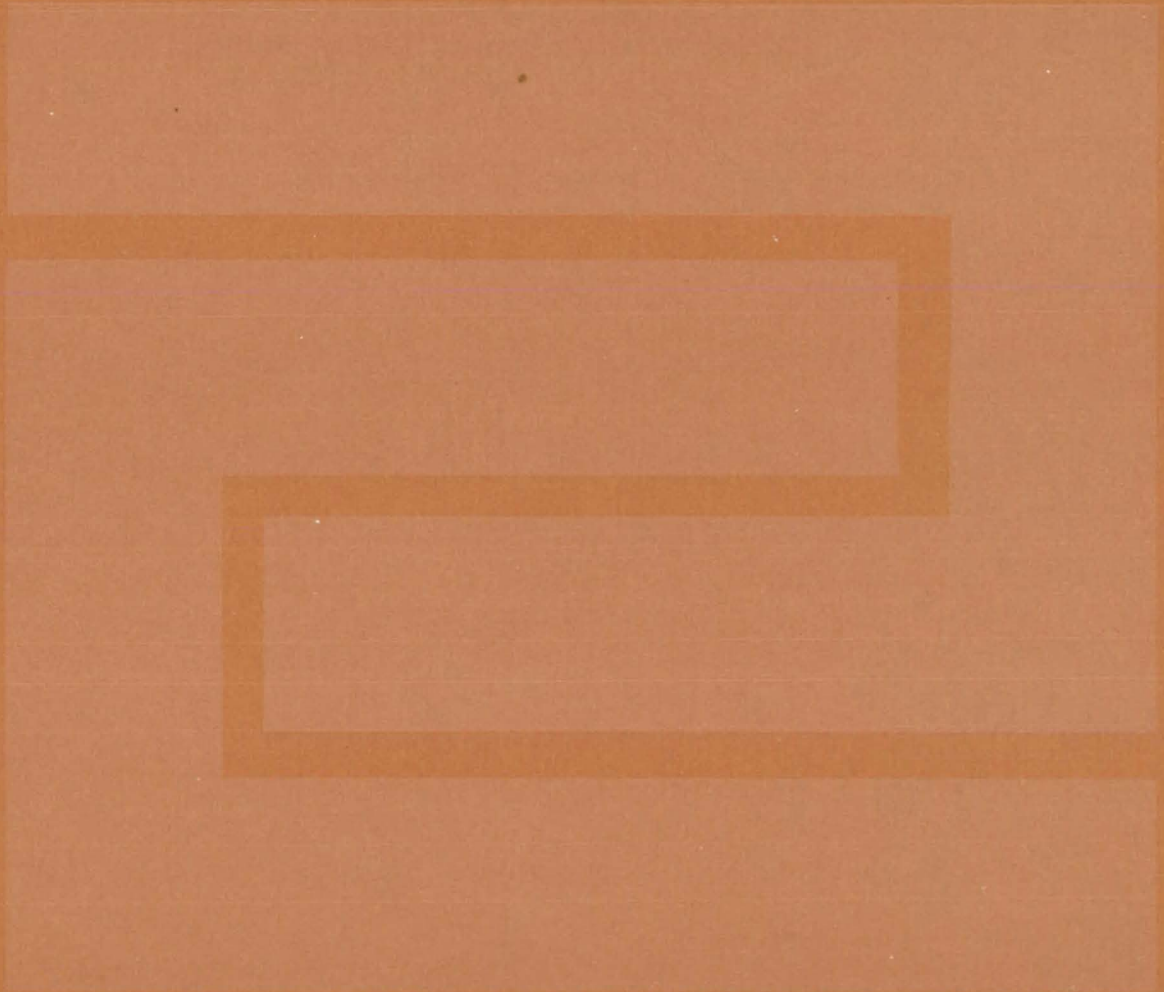
Current known development and testing programs for engines larger than 1 horsepower are summarized. The summary includes current engines by Philips, Ford, and United Stirling and a 10-year-old engine, the GPU-3 built by General Motors for the U.S. Army and now under test by the NASA Lewis Research Center.

The manual contains over 800 publicly available references on Stirling engines indexed according to year of publication (1807 through 1977), personal author, corporate author, and subject. A directory of individuals and organizations presently involved with Stirling engines is included.

This manual is the first step in making available comprehensive, economical, and verified analytical programs for Stirling engines.

This work was done by William R. Martini of the University of Washington for Lewis Research Center. Further information may be found in NASA CR-135382 [N78-23999], "Stirling Engine Design Manual," a copy of which may be obtained at cost from the New England Research Application Center [see page A7].
LEW-13098

Fabrication Technology



Hardware, Techniques, and Processes

- 613 Controlling the Growth of Silicon Sheets
- 614 Automated Control of Crystal-Growth
- 615 Applying Uniform Adhesive Coatings
- 616 Electroplated "Cold Patch" for Critical Parts
- 617 Accelerated Hybrid-Circuit Production
- 618 Detecting Overpenetration of Electron-Beam Welds
- 619 Brazing Dissimilar Aluminum Alloys
- 619 Contouring Pile-Brush Seals
- 620 Easily Installed Insulation for Steamfittings
- 621 All-Ion-Implantation Process for Integrated Circuits
- 621 Films for Adhesive Bonding

Books and Reports

- 622 Sealing Microcircuits With Adhesives

Controlling the Growth of Silicon Sheets

An automated system regulates sheet width, thickness, and composition.

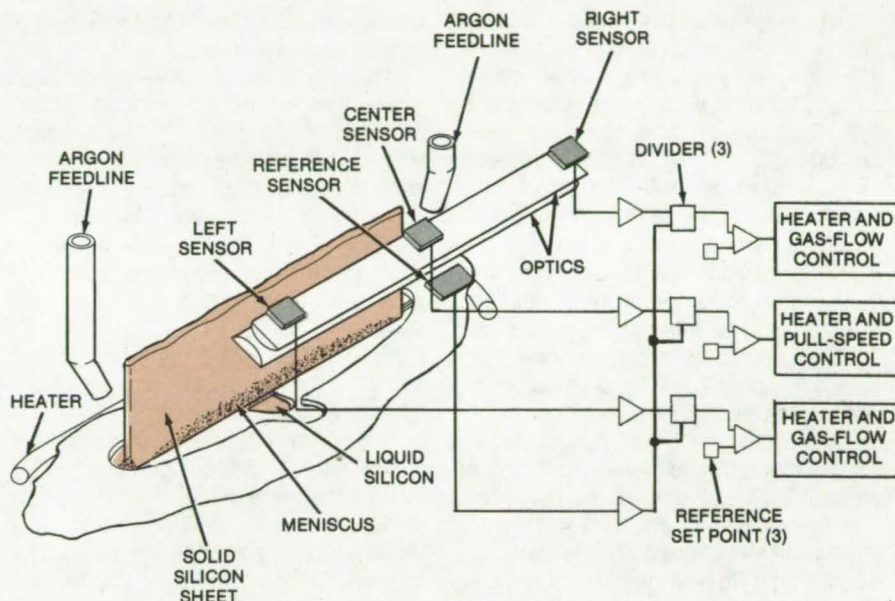
NASA's Jet Propulsion Laboratory, Pasadena, California

Careful process control is necessary to draw continuous, uniform single-crystal sheets from a silicon melt. The operating conditions must be precisely regulated to produce sheets of uniform width, thickness, and composition, such as those required for the manufacture of solar cells.

A new system that measures the brightness of the region where the solid sheet emerges from the molten silicon automatically regulates the growth of silicon ribbon sheets. The system responds to changes in the growth rate and makes compensations by altering the process parameters.

The emerging sheet is viewed at its left and right edges and at its center by photovoltaic sensors or vidicon tubes (see figure). The brightness level at each sensor is a composite of the brightness levels of the solid and liquid silicon that falls within the sensor field of view. Since the solid sheet appears much brighter than the liquid, a decrease in brightness implies that the area of liquid is increasing at the expense of solid. For example, a decrease in brightness at the left and right sensors implies that the area of solid is shrinking (i.e., the sheet is narrowing). A decrease in brightness at the left end only means that the left edge of the sheet is growing narrower. If the brightness decreased at the center, the liquid silicon meniscus is rising, and the sheet is becoming thinner.

Error signals from the left and right viewing devices control the flow of argon gas at the edges of the sheet. For example, a negative error signal from the right monitor (caused by a



The **Brightness of Sheet Silicon** as it leaves the melt is sensed at the left edge, middle, and right edge. Deviations from preset brightness levels create error signals that alter the gas flow, crystal-pulling speed, and melt temperature to produce uniform single-crystal sheets.

decrease in brightness at the right) increases the argon flow at the right. This, in turn, widens the sheet at the right. The left and right error signals also control the current in resistance heaters at the edges of the sheet.

Error signals from the monitor at the center are particularly important because they reflect not only thickness changes but also changes in growth stability and in silicon carbide particle density on the sheet surface. To maintain the meniscus height at a preset level, the middle error signal controls the sheet-pulling speed and the melt temperature. For example, a positive error signal from the middle

monitor increases the pull speed and decreases the temperature to decrease the sheet thickness and raise the meniscus height.

This work was done by Theodore F. Cizek of IBM Corp. for **NASA's Jet Propulsion Laboratory**. For further information, Circle 86 on the TSP Request Card.

This invention is owned by NASA, and a patent application has been filed. Inquiries concerning nonexclusive or exclusive license for its commercial development should be addressed to the Patent Counsel, NASA Resident Legal Office-JPL [see page A8]. Refer to NPO-14295.

Automated Control of Crystal-Growth

Optical sensors detect liquid/crystal-interface growth parameters.

NASA's Jet Propulsion Laboratory, Pasadena, California

The edgewise growth of silicon ribbon has been developed to reduce the costs of producing silicon solar cells. This process can be automated by using optical sensing with cold-cathode-discharge (CCD), linear imaging devices (LID) to determine the process status and to direct the growth process.

Ribbon crystal can be grown from a thin column of temperature-controlled liquid silicon, as seen in Figure 1. The liquid-column height is maintained by capillary action that is created in a slitlike channel in a die. The die is immersed in molten silicon. Critical factors in this process are the temperature of the metal die and the height of the meniscus at the crystal/liquid interface. Meniscus height is directly proportional to the thickness of the silicon crystal, and the die temperature is directly proportional to the meniscus width, provided the pull rate and width of the die slit are constant.

Previously crystal growth was either observed directly by the operator or monitored by some nonoptical means. Such methods did not lend themselves to automation or to close quality control.

An automated approach to controlling ribbon thickness and die temperature has been tested. It uses a CCD linear imaging device that senses light contrasts. The CCD device resembles a bar made up of many cells with a typical center-to-center spacing of 0.51 mil (0.013 mm); its resolution

compares favorably with more elaborate optical systems.

Two basic approaches have been developed to control silicon ribbon thickness: one measures the ribbon width, and the other measures meniscus height. Both of these parameters have an established mathematical relationship to the die temperature and thus the ribbon thickness. Figure 2 illustrates the ribbon-width sensing system.

The silicon ribbon appears bright against the dark background of the relatively-cool radiation shields surrounding the die. The output from the LID is a clocked series of pulses, each of which corresponds to an optical sensor in the array. The amplitude of each pulse is proportional to the photon flux that falls on the corresponding sensor. By the use of sampling techniques, a comparator, and a digital-to-analog converter, an analog representation of the position of the image of each edge of the ribbon is generated. Each edge position sensor independently controls the power applied to the respective end heater. Ribbon edge accuracy of ± 3 mils (± 0.08 mm) is possible, but the system is very susceptible to heater power variations.

The other approach to ribbon thickness control is the monitoring of the meniscus height. The CCD devices are positioned so that they can measure the height between the die top and the crystal-to-meniscus inter-

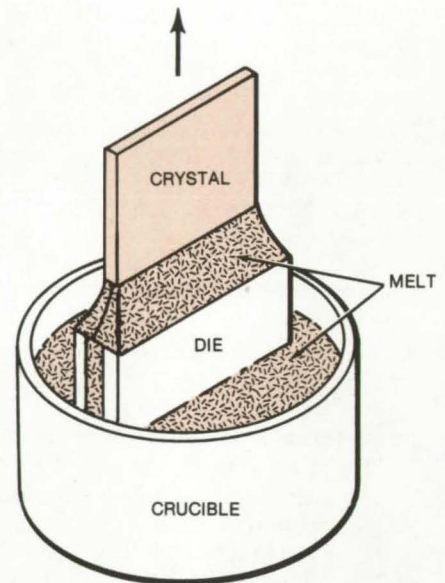


Figure 1. The **Basic Setup for Growing Silicon Ribbon** uses a die immersed in molten silicon. The ribbon is formed by pulling up a strip of molten silicon by capillary action.

face. While this system is potentially more accurate than the edge sensing approach, there is a tendency for large silicon carbide crystals to form near the meniscus. This, with the occasionally irregular border of the meniscus, introduces some inaccuracy to the control of the ribbon thickness. Future systems can avoid this by averaging the meniscus height over the entire ribbon width.

This work was done by Arthur Hatch and Douglas Yates of Mobile Tyco Solar Energy Corp. for **NASA's Jet Propulsion Laboratory**. For further information, Circle 87 on the TSP Request Card.
NPO-14420

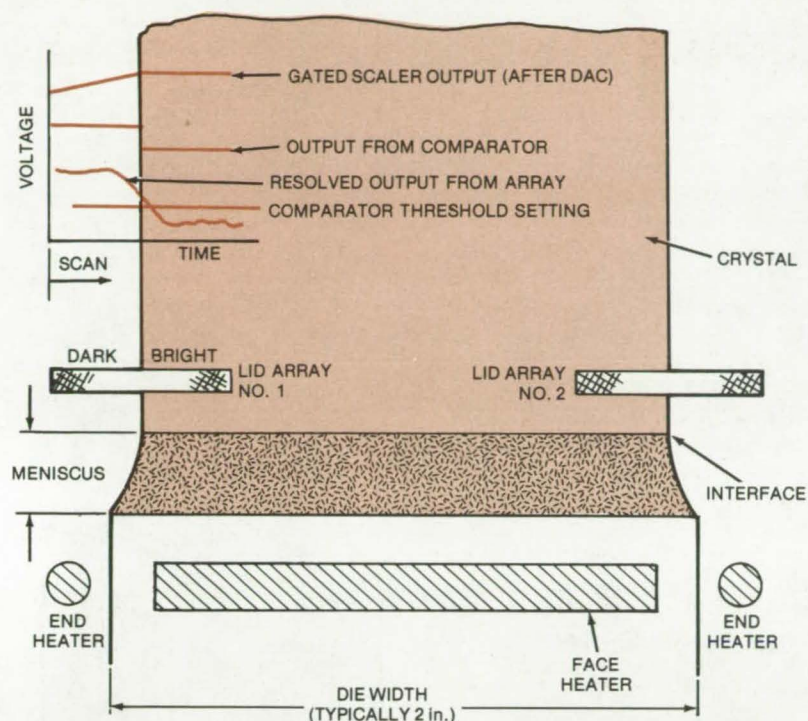


Figure 2. The **Ribbon-Width Control System** uses the LID array placed at the edge of the growing ribbon. The waveforms shown in the upper left reveal the electrical processes involved in detecting the ribbon edge.

Applying Uniform Adhesive Coatings

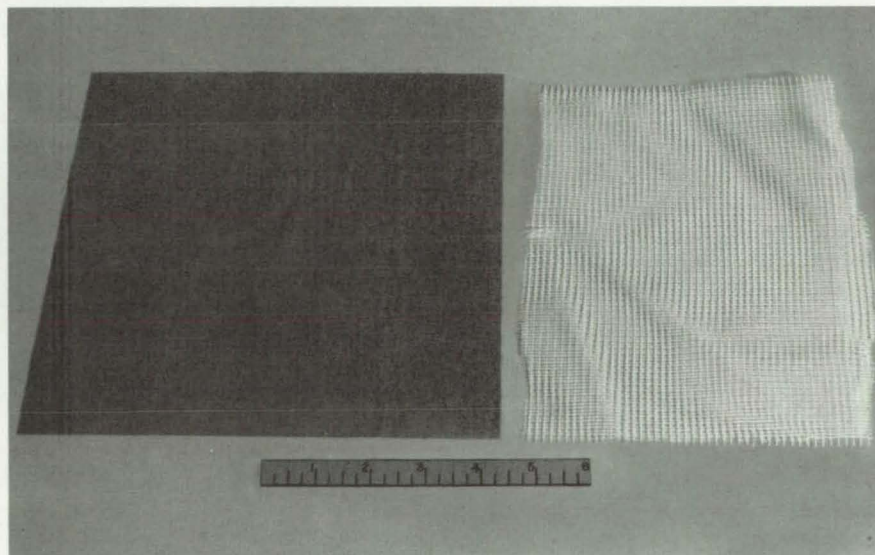
A removable overlay keeps thickness variations small, saving material and application time.

Lyndon B. Johnson Space Center, Houston, Texas

A simple technique for applying adhesive coatings to large surfaces keeps the coating thickness variations to less than ± 0.0005 in. (± 0.001 cm). In comparative tests against roller, brush, and spray application, thickness variations in the conventional techniques were at least three times greater.

The new method consists of placing a net fabric (such as nylon net) over the surface to be coated, applying the adhesive, evening it off with a squeegee blade, and then removing the net while the adhesive is still fluid. The adhesive settles into a smooth, uniform layer and is cured in the usual way.

Besides producing uniform thickness, the technique reduces application time by about one-half and saves roughly 30 percent in material, weight, and cost. On the Space Shuttle, for
(continued on next page)



Adhesive Is Applied through the nylon mesh shown at the right, then it is evened off with a squeegee; the resulting adhesive layer varies only a few ten-thousandths of an inch in thickness. The more densely woven fabric (left) used in conventional silk-screen application is shown for comparison.

example, where the method is used in bonding high-temperature surface tiles, it saves at least 500 pounds (226.5 kg) of a special low-volatility adhesive on each vehicle.

Various sizes and thicknesses of nylon, Teflon, or other plastic netting may be used, depending on the desired coating thickness. Any adhesive may be used, as long as it retains enough fluidity to level itself after the net is removed.

The new technique is similar to silk-screen application, but there are some basic differences between the processes. Silk screening uses finer-mesh

fabrics to apply patterns in small, delimited areas, and it requires expensive frames that must be cleaned after use. The new technique, on the other hand, applies a uniform coating over large areas by one-time use of inexpensive, commercially available netting.

In tests, a 6-mil (0.15-mm) nylon net (see figure) was stretched over a convex aluminum surface and held by adhesive tape. Room-temperature-vulcanized silicone adhesive was applied to the netting and then evened off with a squeegee blade. After the holding tape and netting were removed, the liquid coating settled to a

smooth, uniform layer that was allowed to cure at room temperature for 16 hours. The coating was then peeled away and measured. Its thickness variations were found to be no more than 0.0005 in. (0.013 mm) out of an average thickness of 0.0065 in. (0.17 mm). Similar tests on roller, brush, and spray coatings showed minimum thickness variations of ± 0.0015 in. (0.038 mm).

This work was done by David S. Wang of Rockwell International Corp. for Johnson Space Center. No further documentation is available.
MSC-19462

Electroplated "Cold Patch" for Critical Parts

Cracks in metal parts are filled by electrodeposition in a plating tank that conforms to the part to be repaired.

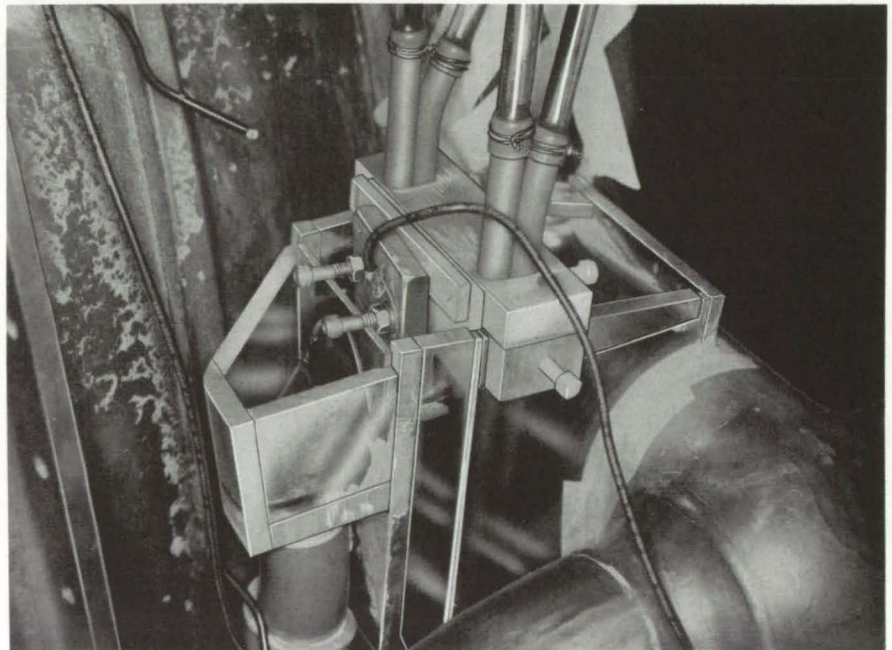
Marshall Space Flight Center, Alabama

Weakened or damaged metal parts can be "cold-patched" at ambient temperature by electroplating in a special tank in which the part becomes one of the tank walls. Since the part is not totally immersed, the plating solution contacts only the damaged area (see figure); other areas are isolated from the electrolyte. The principle could be applicable to the repair of cracks in the components of chemical reactors and other critical structures.

The method was developed to repair long cracks in the nickel-alloy mixer bowl of the Space Shuttle flight nozzle. Welding or brazing could not be used because these methods apply heat that can propagate the cracks. With the contoured plating tank, nickel is electrodeposited in the cracks, and the plated bowl surface is refinished to the design contours.

The plating tank contains four small spray nozzles to agitate the solution and also contains various electrodes for cleaning, activating, making the nickel strike, and electrodepositing the nickel.

A porous polypropylene membrane sections off the electrode portion of the tank to prevent sludge formed at the anode from dropping on the part. A weir dam and drain on the electrode



This **Electroplating Tank** matches the contour of a part to be plated (lower right) so that the plating solution contacts only the damaged surface that is to be plated. A weir dam and drain are shown at the left.

side of the tank maintain the solution level and provide a route for solution to return to the main reservoir. The reservoir is mounted on a cart, along with heating, circulation, and filtration equipment and a dc power supply.

This work was done by Harold A. Tripp of Rockwell International Corp. for Marshall Space Flight Center. For further information, Circle 88 on the TSP Request Card.
MFS-19401

Accelerated Hybrid-Circuit Production

A modified die-bonding machine speeds up hybrid-circuit production.

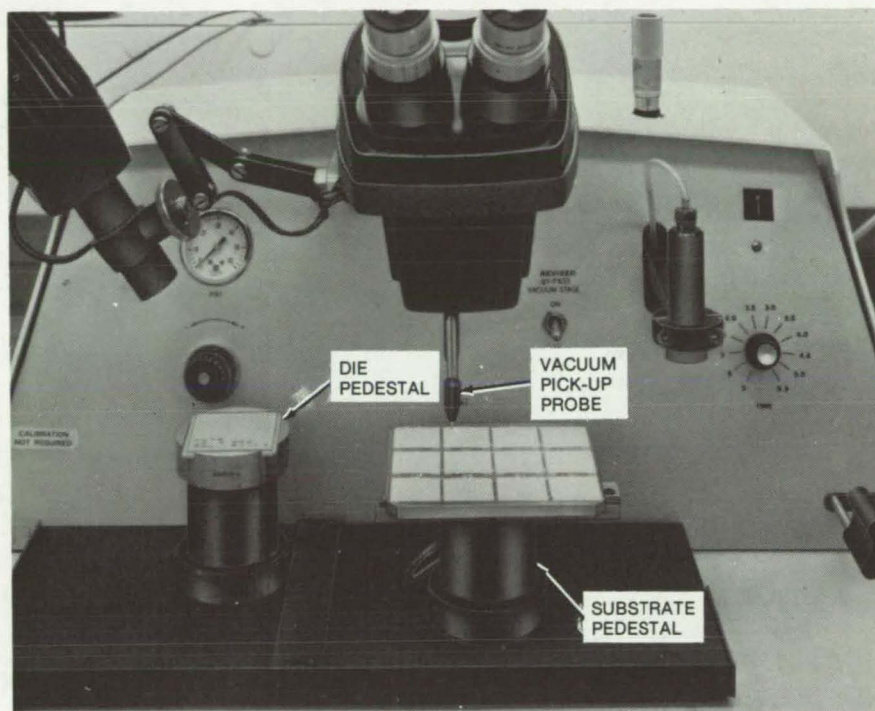
Lyndon B. Johnson Space Center, Houston, Texas

A modified die-bonding machine speeds the manufacture of hybrid electronic circuits. The machine incorporates a pedestal to hold a tray carrying a set of identical dice (IC chips). A second pedestal holds a set of substrates secured by a vacuum line. The dice are lifted from the tray by a vacuum probe and are placed at their proper locations on the epoxy-coated substrates. After a set of chips is installed, a tray with a different set is brought out, and the process is repeated until all the dice are installed.

The modified machine speeds up the process significantly because an earlier model could handle only one substrate at a time. It therefore required more handling of the substrates, more time to fabricate each hybrid, and a greater likelihood of damage and errors.

The new machine, shown in the illustration, incorporates two modified pedestals: one for the die tray and the other for the substrate tray. The first pedestal is equipped with a recessed adapter that secures the die tray. The second supports a tray holding a number of hybrid-circuit substrates (12 in this machine). The substrate tray is secured to the pedestal surface by a vacuum line.

The operating sequence begins when a tray of identical dice is placed in the proper orientation in the left pedestal. Then a tray with the hybrid-circuit substrates is placed on the right pedestal and is properly oriented by aligning pins. Next, the base table is moved to the right so that the pedestal with the die tray is underneath the vacuum probe, and the vacuum probe is lowered to lift a die (with the



This **Die-Bonding Machine** uses two modified pedestals: one supporting a die tray and the other holding a tray with substrates. The substrate tray could be modified to hold 20 substrates.

assistance of a binocular microscope).

The base table is then moved to the left so that the substrate tray is located underneath the probe (as shown), and the probe is lowered to deposit the die on the designated substrate location. These steps are repeated until all the dice are transferred to all the substrates on the pedestal.

Next, another tray with a different set of dice is brought out, and these are installed on the substrates. This process is continued until all the dice

required for the hybrid are mounted on the substrates on the pedestal.

Alternately, the operator may mount a particular type of die on the substrates; then he can replace this tray with another set of substrates, and so on, until that die type is mounted on all the substrates.

This work was done by James E. Berg and Michael A. Dassele of Sperry Rand Corp. for **Johnson Space Center**. For further information, Circle 89 on the TSP Request Card.

MSC-18272



Detecting Overpenetration of Electron-Beam Welds

Gold plate beneath the weldment reveals areas of excess penetration during X-ray inspection.

Marshall Space Flight Center, Alabama

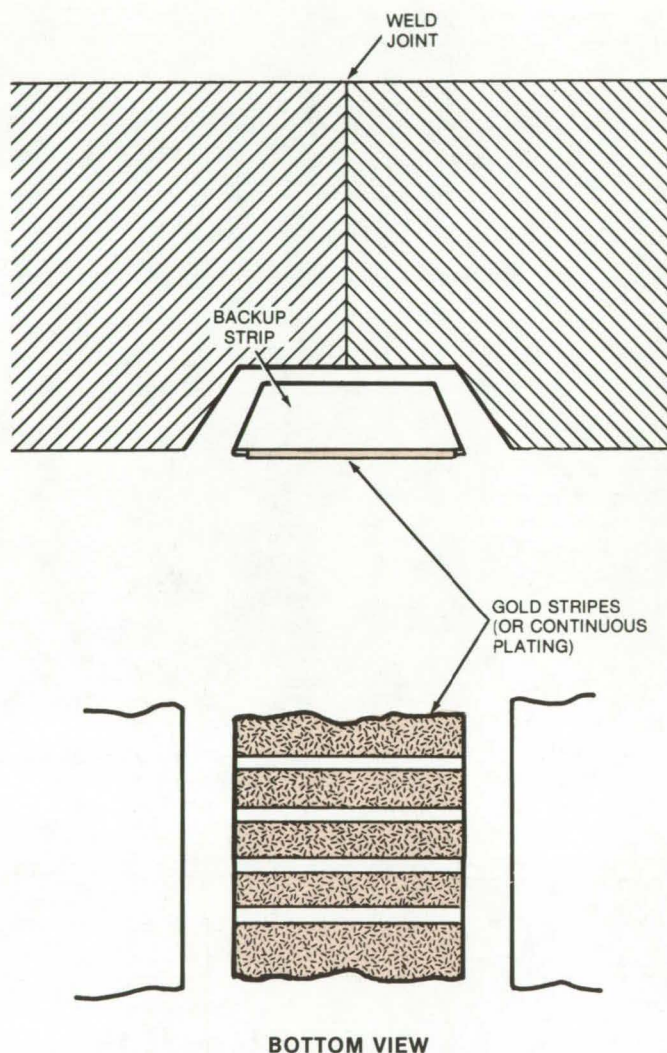
A simple, direct method of checking electron-beam welds for overpenetration can help avoid costly damage to welded assemblies during testing or while in service. The backup strip for an electron-beam-welded butt joint is plated with a thin layer of gold (see figure). After welding, the joint is inspected with X-rays. If there is no overpenetration, the gold appears as a light strip on the X-ray negative film. However, if the electron beam penetrates too far, it disturbs the gold plate and causes localized voids that show up as dark spots on the film.

The gold plate can be a continuous strip, or, to economize on the amount of gold needed, many short parallel stripes can be applied. Gold is used because it is highly opaque to X-rays and gives good contrast in the regions of weld overpenetration.

This overpenetration checking technique was originally developed for joints on the Space Shuttle main combustion chamber. It should also be applicable to other critical electron-beam welds, such as those in gas turbines and pressure vessels.

This work was done by D. I. Macfarlane and F. D. Young of Rockwell International Corp. for Marshall Space Flight Center. For further information, Circle 90 on the TSP Request Card.

MFS-19396



A Gold Film Is Applied to the electron-beam-weld backup strip. Any regions of excess penetration create voids in the gold that show up on X-ray images of the joint.

Ultrafine PBI Fibers and Yarns

An improved dry-jet/wet-spinning process fabricates ultrafine synthetic fibers for strong, lightweight textiles. The solution is extruded through a spinnerette, passed through a coagulating bath, and drawn to its final diameter through a tube furnace in which the entrance and exit speeds are precisely controlled. (See page 529.)

Testing Integrated Circuits by Photoexcitation

In a new technique for the production-screening of integrated circuits, a laser beam is rapidly scanned over the IC under test, and the photocurrent is displayed on a CRT. The method produces an IC "signature" that could be used to make a rapid accept/reject decision during the fabrication cycle. (See page 474.)

Coated-Felt Thermal Insulation

Commercially-available nylon felt coated with a pigmented elastomeric silicone is a lightweight replacement for silica insulating tiles. Suitable for use at temperatures up to 700° F, the coated-felt insulation is also water-proof and char resistant. The felt thickness can be from 0.16 to 0.4 in. as dictated by the local structural heat sink. (See page 535.)

Brazing Dissimilar Aluminum Alloys

A procedure for brazing dimensionally critical structures

Lyndon B. Johnson Space Center, Houston, Texas

A novel dip-brazing process joins aluminum castings to aluminum sheet made from a different aluminum alloy. The process includes careful cleaning, surface preparation, and temperature control.

The new process causes minimum distortion of the parts and is therefore superior to tack-welding in some cases. The method not only joins dissimilar alloys but also can join parts formed by different metallurgical techniques. For example, it has been used to bond a wrought part to a casting — a combination that complicates the already difficult task of brazing dissimilar metals.

The process was developed for fabricating a base for the inertial measurement unit on the Space Shuttle Orbiter. The base must be lightweight, stiff, and dimensionally stable. It is designed as a boxlike investment casting, measuring about 55 by 30 by 25 cm, and is made from 71A aluminum alloy. Because the casting is large and the material is

difficult to cast, the bottom is formed separately from a plate of 6061 aluminum alloy sheet; the plate is attached after casting.

Before the dip-brazing, the bottom edges of the casting are machined to form a plane seating surface for the plate. Both the plate and casting are heated to drive off oils. They are then dipped in a caustic solution to remove other foreign materials.

Aluminum brazing-alloy foil is placed on the inverted bottom edge of the casting, and the plate is seated on it. Then the plate is tack-welded to hold it in place during brazing, and the assembly is cleaned again.

As a last preparation for brazing, the assembly is heated in an oven from room temperature to 1,000° F (540° C), at a rate not exceeding 450° F (250° C) per hour. Finally, the assembly is immersed for 2 minutes in the brazing bath at 1,125° F (607° C). This temperature is only about 25° F (14° C) below the melting point of the casting; therefore it must

be carefully controlled.

The assembly is allowed to cool slightly so that the brazing salt residue can be flushed away. Then it is slowly cooled at a rate of no more than 180° F (100° C) per hour. The cooled brazed joint is inspected radiographically.

Heat-treatment and age-hardening complete the process. The heat treatment consists of heating the assembly to 775° F (415° C) at a controlled rate, holding it at that temperature for 5 hours, then cooling it according to the following schedule:

1. 775° to 650° F (415° to 343° C) in 2 h, minimum;
2. 650° to 450° F (343° to 232° C) in 1/2 h, maximum; and
3. 450° to 250° F (232° to 111° C) in still air.

For age-hardening, the assembly is held at 350° F (180° C) for 8 hours.

This work was done by H. Dalalian of The Singer Co. for Johnson Space Center. No further documentation is available.

MSC-16340

Contouring Pile-Brush Seals

A variety of shapes can be produced by simple flat machining.

Lyndon B. Johnson Space Center, Houston, Texas

Flexible pile materials can be trimmed to a precise contour by freeze-cutting. The pile material is mounted on a backup plate with a contour that is the reverse of the desired pile contour, and the pile is frozen (Figure 1). The curved pile, which has become rigid due to the freezing process, is then machined flat. When the pile is unfrozen and the backing is laid on a flat surface, the other surface of the pile assumes the required shape. Many pieces can be machined simultaneously.

(continued on next page)

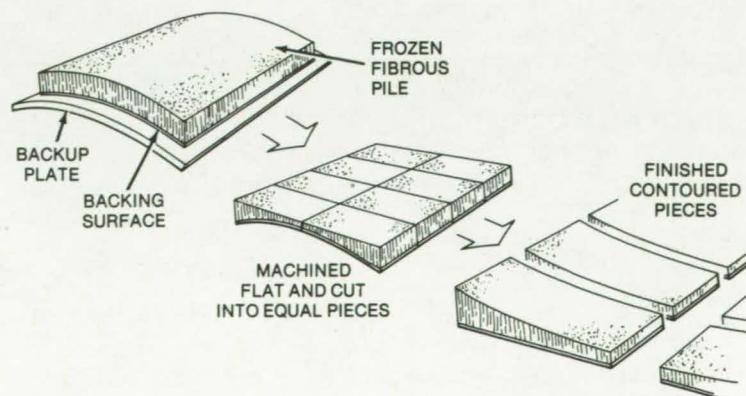


Figure 1. When **Pile Brushes** are bent and then frozen, they can be machined flat. When they are removed from the cutting fixture, they assume the required contour.

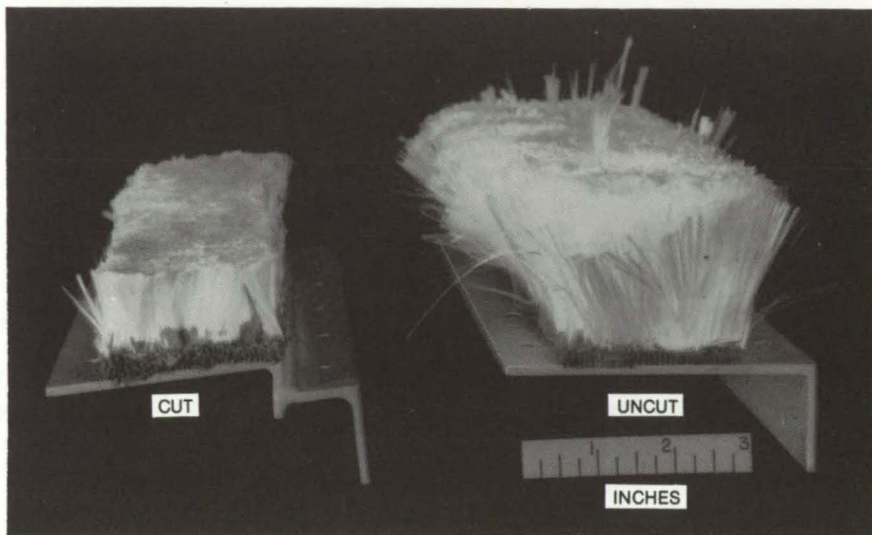


Figure 2. The **Glass-Fiber Pile** at left has been shaped by freeze-cutting. The pile at right is in original uncut condition.

The technique was developed for glass- and quartz-fiber piles (Figure 2), which are used in the Space Shuttle as high-temperature seals. The seals must mate with curved surfaces, hence the need for a contoured pile. Previously, a tracer or a numerically-controlled machine tool was used to cut the brushes individually. The new freeze-cut method is considerably less costly.

This work was done by Leland B. Norwood of Rockwell International Corp. for **Johnson Space Center**. No further documentation is available. MSC-16231

Easily Installed Insulation for Steamfittings

An insulating blanket trimmed by hook-and-loop fasteners adds safety and prevents heat loss.

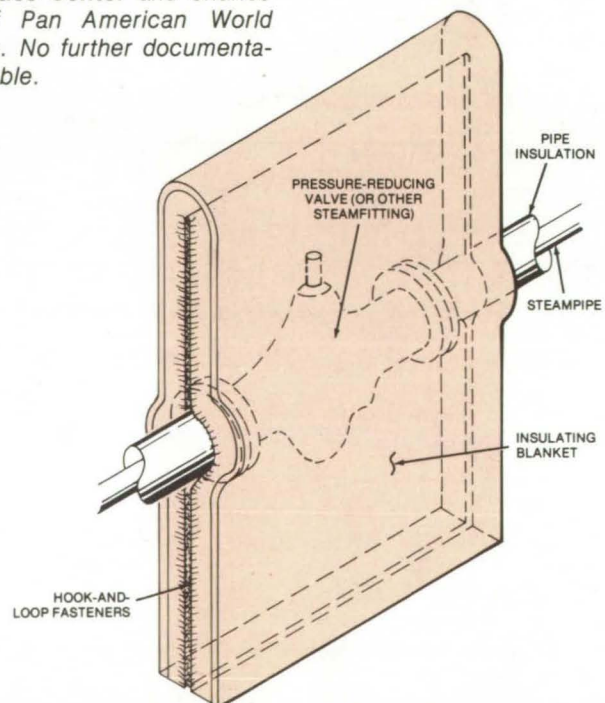
Lyndon B. Johnson Space Center, Houston, Texas

Conventional steampipes are usually heavily insulated from heat loss to the surrounding environment. However, other fittings, such as pressure-reducing valves, condensate traps, strainers, and the like, are often left uninsulated to allow easy access for maintenance and adjustments. This creates a safety hazard for people working near the hot exposed surfaces. The bare fittings also allow heat to escape, putting some extra load on the heating system and on any nearby air-conditioners or other cooling equipment.

A practical approach to insulating components in a steamplant is shown in the figure. The components are covered with a commercially-available insulating cloth such as Refrasil, or an equivalent material. The cloth borders are trimmed with hook-and-loop attachments, such as Velcro, Scotchmate, or similar fasteners.

The fabric is installed by slipping it over the component and fastening the hook-and-loop borders. For maintenance or adjustments, the borders can be quickly unfastened and the fabric slipped off.

This work was done by Graydon Owens and Joseph E. Pouzar of **Johnson Space Center** and Charles R. Peek of Pan American World Airways, Inc. No further documentation is available. MSC-18277

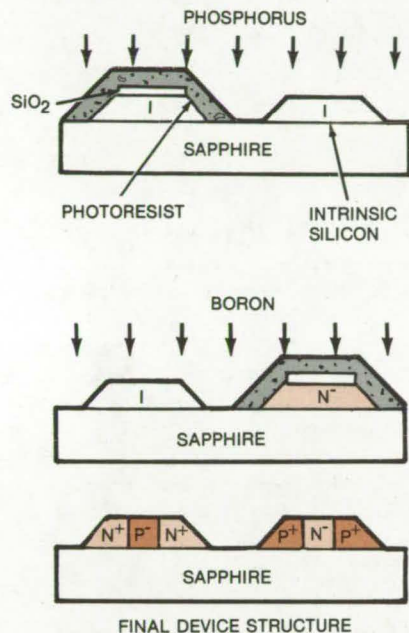


Insulating Cloth covers reducing valves, strainers, traps, and other components in a steamplant. The fabric borders are trimmed with hook-and-loop fasteners for quick installation and removal.

All-Ion-Implantation Process for Integrated Circuits

Simpler than diffusion fabrication, ion bombardment produces CMOS/SOS circuits that are one-third faster.

Marshall Space Flight Center, Alabama



Double Ion Implantation for complementary MOS on sapphire gives good control over both channels. After islands of intrinsic silicon (I) are formed by etching, half are shielded while phosphorous ions make the other half n-type; then the shielding is changed, and boron ions create p-type islands. Standard processing (not shown) is followed thereafter to complete fabrication of the device.

Introducing the dopants into a complementary-metal-oxide-semiconductor/silicon-on-sapphire (CMOS/SOS) integrated circuit by ion bombardment, instead of by diffusion from vapors or doped oxides, can increase the operating speed of the circuit by 33 percent. Moreover, ion implantation simplifies the IC fabrication procedure and produces circuits with more uniform characteristics.

Processes have been developed for all-ion-bombardment fabrication of an IC containing transistors, capacitors, a Zener diode, and a ring oscillator. The five ion-implantation steps used are:

- Phosphorus implantation in the silicon substrate;
- Boron implantation in the substrate;
- High-dosage boron implantation in the polycrystalline silicon gate;
- High-dosage phosphorus implantation in selected sources and drains (those for n-channel devices); and
- High-dosage boron implantation in the remaining sources and drains (those for p-type devices).

The equipment used for these steps includes a low-beam-current ion implanter for the first two (low-dosage)

steps and a high-beam-current machine for the last three steps. The range and spread of boron and phosphorus distributions in silicon were studied at various beam energies ranging from 10 to 1,000 keV, and experiments with a range of implantation doses and ion-activation treatments were carried out for each of the implantation steps.

Two basic processes for doping epitaxial substrate films were devised: single-ion implant (I^2 or II^2) and double-ion implant ($2I^2$). The reliability, radiation resistance, and threshold voltage are all greater with $2I^2$ processing. One version of this process is shown in the figure.

Threshold voltage, leakage current, source-drain breakdown voltage, channel-oxide breakdown voltage, channel conductance, and lateral diffusion were measured on the all-ion-implanted circuits. The values of these characteristics were then analyzed in terms of the implantation-process parameters.

This work was done by D. S. Woo of RCA Corp. for Marshall Space Flight Center. For further information, Circle 91 on the TSP Request Card. MFS-23995

Preparing Thin Aluminum Films for Adhesive Bonding

A carbonate pretreatment produces a highly bondable surface without harming the film.

NASA's Jet Propulsion Laboratory, Pasadena, California

Thin metal films that would be destroyed by conventional surface-preparation methods can be prepared for adhesive bonding by a simple new cleaning procedure. With the new procedure, vapor-deposited or ion-plated layers of aluminum or other metals on plastic or other substrates can be adhesive-bonded to other

materials. The procedure may also be applicable to electroplated surfaces.

Ordinarily, bulk aluminum surfaces are etched or anodized in an acid solution to remove the oxide layer and contamination that inevitably result from exposure to the atmosphere. Such pretreatment exposes a fresh surface that will bond securely to an

adhesive. However, this approach is too rough for very thin aluminum films since it can remove the film itself along with the contamination.

In the new procedure, the film is degreased with a standard solvent (such as benzene) that does not attack aluminum. It is then dipped in or swabbed with an aqueous carbonate (continued on next page)

solution for 1 minute. The carbonate solution reacts with aluminum to form a hydroxide layer a few hundred angstroms thick. This surface has been found to form strong bonds to adhesives.

In experiments with aluminum-coated Kapton films (candidates for the Solar Sail material), parts were bonded to the aluminum with epoxy

adhesive. The metallic layer was in the thickness range from 1,000 to 10,000 Å. Without the new treatment, the epoxy bond could be broken by pulling on the parts; but for the pretreated surfaces, the aluminum separated from the Kapton rather than the epoxy.

The new treatment should be useful in developing low-cost mirrors and solar concentrators fabricated from

metal-coated plastic films. The treatment should cost no more than standard degreasing and rinsing procedures.

*This work was done by Tennyson Smith of Rockwell International Corp. for **NASA's Jet Propulsion Laboratory**. For further information, Circle 92 on the TSP Request Card. NPO-14357*

Books and Reports

These reports, studies, and handbooks are available from NASA as Technical Support Packages (TSP's) when a Request Card number is cited; otherwise they are available from one of NASA's Industrial Application Centers or the National Technical Information Service.

Sealing Microcircuits With Adhesives

A study of adhesive-sealed packages under difficult temperature/humidity conditions

A new report describes a study of adhesive-sealed packages for hybrid microcircuits. Ten commercially available adhesives were used to seal metal and ceramic packages and were tested for moisture resistance at high humidity. Throughout the test program, gold-plated Kovar packages, sealed in the conventional way by seam welding, were used as controls.

The study was carried out in three phases:

- Ten selected adhesives were screened according to their ability to seal gold-plated Kovar "butterfly" packages. The test criterion was the retention of seal integrity after exposure to four increasingly-severe temperature/humidity environments: 10 days at 50° C/60 percent relative humidity (RH); 10 days at 60° C/90 percent RH; a 10-day moisture test according to method 1004.1 of MIL-STD-883A; and 10 days at 85° C/85 percent RH.
- The four adhesives that performed best in this initial screening were further screened for their ability to seal ceramic packages when subjected to thermal shock, temperature cycling, mechanical shock, constant acceleration, and temperature aging.
- The adhesive/package combination that best survived these environmental tests was exposed to 60° C/98-percent RH while its internal moisture content was monitored.

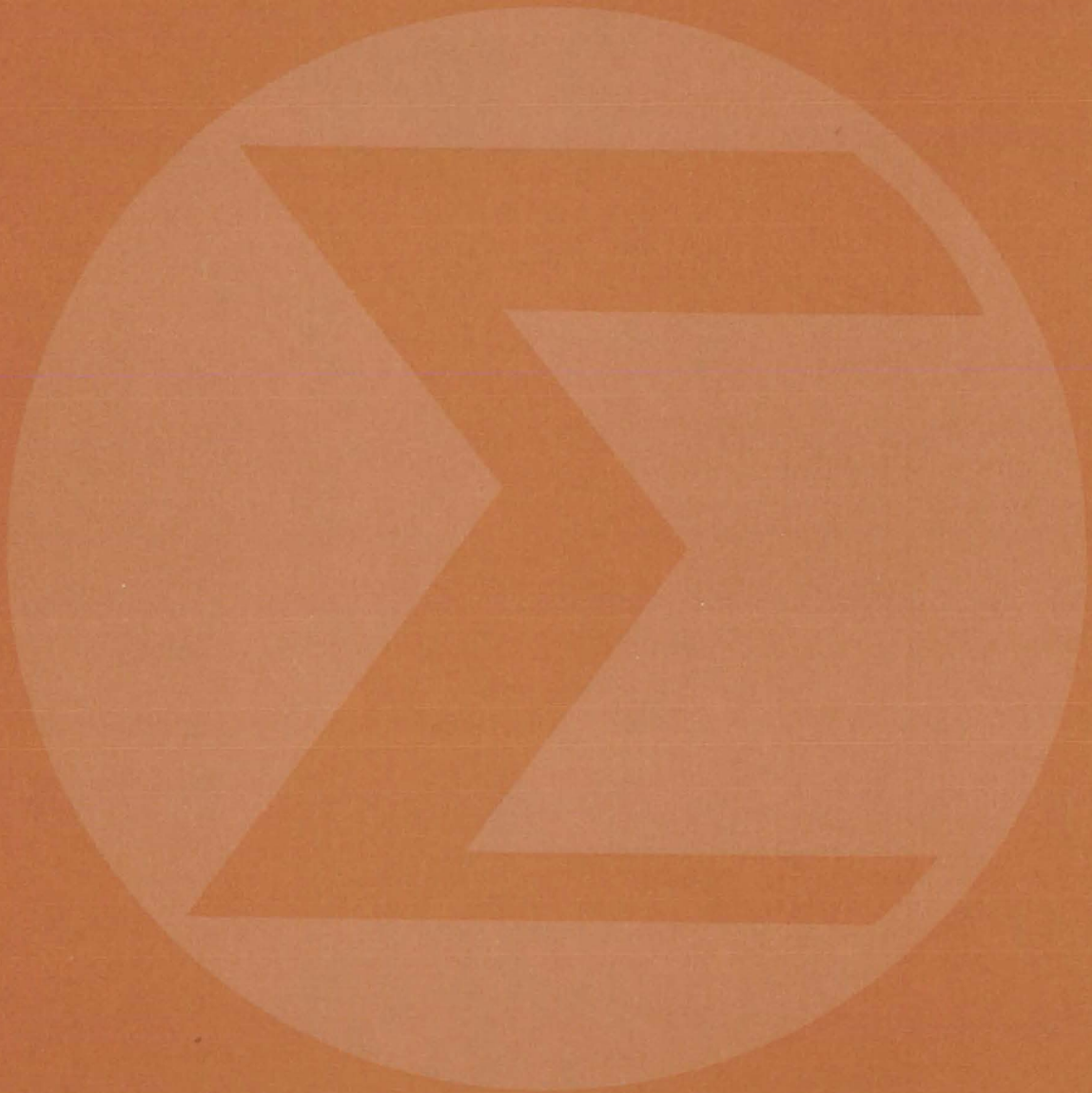
A useful byproduct resulted from the moisture-monitoring phase of the

study. It was found that commercially-available moisture sensors that base their measurements on the impedance of porous aluminum oxide sandwiched between aluminum and gold rapidly corroded at the humidity levels in the study. A new sensor structure was developed in which the aluminum oxide is contained between two layers of gold. When placed inside the test packages, this new device functioned without corroding.

*This work was done by J. J. Licari and K. L. Perkins of Rockwell International Corp. for **Marshall Space Flight Center**. Further information may be found in NASA CR-150420 [N77-33349], "Development of Low Cost, High Reliability Sealing Techniques for Hybrid Microcircuit Packages," a copy of which may be obtained at cost from the New England Research Application Center [see page A7].*

Inquiries concerning rights for the commercial use of this invention should be addressed to the Patent Counsel, Marshall Space Flight Center [see page A8]. Refer to MFS-23869.

Mathematics and Information Sciences



Hardware, Techniques, and Processes

- 625 Computation of Spare Parts Requirements
- 625 Resizing Algorithm for Loaded Structures
- 626 Predicting Crop Production From Satellite Data
- 627 Representation of Multivalued Logic Functions

Computer Programs

- 627 Plotting Max/Min Data Envelopes
- 628 Graphics Program for Charts
- 628 Price and Cost Estimation
- 629 Processor for the UNIVAC 1100 Series
- 629 Postprocessing Classification Images

Computation of Spare Parts Requirements

A statistical analysis determines the probability of failure for $N - 1$ spares.

Lyndon B. Johnson Space Center, Houston, Texas

A spares determination analysis, originally developed to compute redundancy requirements for space missions, could also help reduce downtime in industrial processes by determining the number of spare parts that must be stockpiled. The analysis can also be inverted so that it is possible to decide if the number of spares on hand is sufficient for the lifetime needs of a system.

In the analysis, the probability P that a mission (or system) will survive for a time T_m (if there is one installed component and $N - 1$ spares are on hand) is given by equation 1 in the figure. The parameter T_s in equation 1 is the cumulative lifetime of the component and its spares.

P can be expressed (in equation 2) in terms of a normalized "Z-score," familiar in probability theory; and Z_c , the minimum value of Z , can be obtained from the central-limit theorem. The result is given in equation 3. In equation 3, \bar{T}_s and σ_s are the mean and standard deviation of the cumulative lifetime of the unit plus its spares. Since the spares fail independently and it is assumed that they are identical, \bar{T}_s and σ_s can be expressed (as in equation 4) in terms of \bar{T} and σ , the mean and standard deviation of the lifetime of each unit.

To determine the probability of failure ($1 - P$) for a system, σ and \bar{T} for the component in question are determined

$$P = P\{T_m \leq T_s\} \quad (1)$$

$$P = P\{Z \geq Z_c\} \quad (2)$$

$$Z_c = \frac{T_m - \bar{T}_s}{\sigma_s} \quad (3)$$

$$Z_c = \frac{T_m - N\bar{T}}{\sigma\sqrt{N}} \quad (4)$$

$$\bar{T} \cong T_{0.50} + 0.185(T_{0.95} + T_{0.05} - 2T_{0.50}) \quad (5)$$

$$\sigma \cong \frac{T_{0.05} - T_{0.95}}{3.25} \quad (6)$$

A Generalized Analysis for Spare Parts is summarized in these equations and discussed in the text.

from reliability testing curves, and a value for Z_c is computed. Then, a table of Z-scores for a normally distributed variable is used to calculate P from equation 2.

Equation 4 can be inverted to obtain an expression for N in terms of Z_c . If a desired probability of success (non-failure in time T_m) is specified, Z_c can be determined from the standard table of Z-scores, and a value for N can be computed from the expression. A total of $N + 1$ units (of which one is installed and N are spares) would be required to insure the specified probability of success.

In determining the mean and standard deviation (\bar{T} and σ) of the reliability curve for each unit, it is possible to use approximations that require only three input points: the 0.95, 0.50, and 0.05 probability points on the normally-distributed reliability curve. The approximations are given in equations 5 and 6 in the figure. These estimates are valid to within about 1 percent.

This work was done by Michael A. Mezzacappa of Rockwell International Corp. for Johnson Space Center. For further information, Circle 93 on the TSP Request Card. MSC-16872

Resizing Algorithm for Loaded Structures

An algorithm for resizing structural members subjected to combined thermal and mechanical loading

Langley Research Center, Hampton, Virginia

Fully stressed design (FSD) is a widely used method for determining the correct size of mechanically and thermally loaded structures under

strength and minimum gage constraints. In this method, the sizes of the structural members are iterated, with the step size depending on the

ratio of the total stress to the allowable stress. Traditionally the FSD procedure has been used to minimize the weight of the final design.

(continued on next page)



Fully stressed design is usually satisfactory when the mechanical stresses dominate the thermal stresses. However, when the thermal and mechanical stresses are comparable, a thermal fully-stressed design (TFSD) computation may be advantageous in TFSD, the thermal and mechanical stresses are determined separately, and the thermal stress is subtracted from the allowable stress at each iterative step to form an effective allowable stress. The mechanical stress is driven toward the effective allowable value.

A new algorithm extends the TFSD approach to biaxial stress members (membranes). A previous algorithm was applicable only to uniaxial stress elements (rods). The TFSD algorithm converges in fewer iterations than does the FSD approach for problems where the thermal stresses are comparable to the mechanical stresses.

The resizing algorithms for uniaxial and biaxial stress members, using TFSD (and for comparison, FSD) are given in the accompanying table. The biaxial stress model is based on Von Mises' failure criterion for isotropic biaxial stress members.

In the uniaxial case, the rod cross section (A) is determined; for the

	TFSD	FSD
RODS	$A_{i+1} = \frac{\sigma_{Mi}}{\sigma_{a,M} - \sigma_{Ti}} A_i$	$A_{i+1} = \frac{\sigma_{Mi} + \sigma_{Ti}}{\sigma_a} A_i$
MEMBRANES	$t_{i+1} = \left[\frac{b_i}{2(\sigma_a^2 - V_{Ti}^2)} \pm \sqrt{\frac{b_i^2}{4(\sigma_a^2 - V_{Ti}^2)^2} + \frac{V_{Mi}^2}{\sigma_a^2 - V_{Ti}^2}} \right] t_i$	$t_{i+1} = \frac{V_i}{\sigma_a} t_i$

Resizing Algorithms for uniaxial (rod) and biaxial (membrane) stress members, using thermal fully stressed design (TFSD) and fully stressed design (FSD). The quantities σ_M , σ_T , and σ_a refer to the mechanical, thermal, and allowable stress components; V is Von Mises' stress measure; and b is the thermal/mechanical stress-coupling term.

biaxial problem, the membrane thickness (t) is calculated. Computer calculations have been carried out, using both procedures, for a simplified wing structure. Finite-element methods, using standard rod elements and triangular membrane elements, were used for the analysis.

Identical results for the final design were obtained using TFSD and FSD procedures. The FSD algorithm, however, required 18 iterations as compared to only a single iteration for TFSD. Calculations at lower temperatures also confirmed that TFSD is more rapidly convergent; however,

the efficiency of TFSD is most apparent when the thermal and the mechanical loadings are comparable.

This work was done by Howard M. Adelman of **Langley Research Center** and R. Narayanaswami of ODU Research Foundation. Further information may be found in NASA TM-X-72816 [N76-18530], "Resizing Procedure for Optimum Design of Structures Under Combined Mechanical and Thermal Loading," a copy of which may be obtained at cost from the New England Research Application Center [see page A7].
LAR-12064

Predicting Crop Production From Satellite Data

Crop area and yield for winter wheat can be found by an analysis of Landsat pictures.

Goddard Space Flight Center, Greenbelt, Maryland

Winter wheat production can be accurately determined from data furnished by Landsat satellites. In tests on a 21,000-km² area in Kansas, the Landsat estimate was within 2.8 percent of production reported by the Kansas Crop and Livestock Reporting Service.

The Landsat calculation is based on a "green-measure" criterion in which each picture element (pixel) in a Landsat image of the Earth below it is assigned a value according to the amount of green in its spectral signature. The method is not limited only to estimates of crop area, as were previous satellite measures. It also indi-

cates the yield of winter wheat by multiplying the area of each pixel by the yield for that pixel (determined from the green measure) and summing the products over the whole image.

In making the yield calculations, pixels containing water (e.g., lakes and rivers) are regarded as unavailable for crop production and are not included in the calculations. Areas containing clouds or cloud shadows, however, are assumed to have the same yield as the average yield of the crop-bearing pixels and are included in the estimate.

The correlation between green measure and yield is established from

measurements on known wheatfields with known yields. Pixels are identified as "wheat" or "nonwheat" according to whether the green measure exceeds a preset threshold. The correlation for a particular area could be made even more reliable by using data previously gathered over that area in the threshold level determination.

This work was done by J. E. Colwell, R. F. Nalepka, and D. P. Rice of the Environmental Research Institute of Michigan for **Goddard Space Flight Center**. For further information, Circle 94 on the TSP Request Card.
GSC-12379

Representation of Multivalued Logic Functions

A systematic method for representing multivariable finite Galois field functions can simplify the synthesis of multivalued logic elements.

NASA's Jet Propulsion Laboratory, Pasadena, California

Although Boolean algebra has been successfully applied to the analysis of binary switching circuits, progress in computer and LSI (large-scale-integrated) technology has advanced to where multivalued logic may be more appropriate for future circuit configurations. The Galois field is one promising approach to multivalued logic design. This branch of logic theory, a natural extension of the Boolean field, could be easily mapped onto digital hardware and implemented by LSI fabrication methods.

A new approach to Galois field representation systematically generates the coefficients of any multivariable Galois function directly from its truth table description. It thus forms a basis for synthesizing multivalued logic elements. The method is an extension to multivariable functions of the series expansion representation of single-variable Galois functions that has been used in the past. It should be useful for both binary and multivalued logic designs and in such areas as

data processing, coding, and switching networks.

The polynomial expansion for a multivariable Galois switching function, $F(x_1, x_2, \dots, x_m)$, is given by

$$F(x_1, x_2, \dots, x_m) = \sum_{k_1, \dots, k_m=0}^{p^n-1} f(k_1, \dots, k_m) x_1^{k_1} \dots x_m^{k_m}$$

$$k_1, \dots, k_m = 0$$

where p^n is the number of elements in the Galois field and p is any prime number. In the new approach, the functions f are expanded over the field in terms of generalized Boolean differences such as $F(0, \dots, 0) - F(y_1, \dots, 0)$ and $F(0, \dots, 0) - F(0, y_2, \dots, 0)$. The exact expansion, which involves rather lengthy expressions, can be obtained by requesting the Technical Support Package referenced at the end of this article. The expansion can be pro-

gramed on a computer or calculated by hand to determine the representation of the switching function.

When the method is applied to the synthesis of switching functions, using multioutput elements called "plus gates" and "times gates," economical representations of the functions are obtained. In testing the method on a specific six-input two-output binary function, only 5 "plus gates" and 8 "times gates" were needed, as compared to 22 AND gates and 2 OR gates using a standard Boolean representation. An efficient representation was also obtained for a four-input two-output truth table in which the variables can take on any of three signal levels represented by the integers 0, 1, and 2.

This work was done by Boonsieng Benjathrit of Caltech and Irving S. Reed of the University of Southern California for NASA's Jet Propulsion Laboratory. For further information, Circle 95 on the TSP Request Card. NPO-13760

Computer Programs

These programs may be obtained at very reasonable cost from COSMIC, a facility sponsored by NASA to make new programs available to the public. For information on program price, size, and availability, circle the reference letter on the COSMIC Request Card in this issue.

Plotting Max/Min Data Envelopes

Aids study of load distributions

The study of the maximum and minimum load distributions along a structural section can be greatly aided by the visual display of the load

distribution data. To this end, the maximum/minimum envelope plot program plots the maximum/minimum envelopes of the stresses and shear loads at selected points in a beam modeled by a series of finite elements. Digital output, for engineers and management, is presented such that the bulk of the data can be analyzed and understood quickly.

The program acts as a post-processor of finite-element structural analysis programs. The required inputs include coordinates, topology, and stress data in the COMBINE format. One can select the number of curves to be plotted, specific load cases, the finite elements that make up the beam section, and the number of stress or shear values desired. The program automatically reads the

stress or shear values and performs a maximum/minimum search. The program is limited to 120 nodes, 80 elements, and 250 load cases. The plotting limits are 12 elements per curve and 4 curves per plot. Input control cards are used to specify options, plot titles, and for care labeling. Printed envelope data are also generated.

This program is written in FORTRAN IV for batch or interactive execution and has been implemented on an IBM 360 with a central memory requirement of approximately 128K of 8-bit bytes. The program requires a load library that is supplied as an IBM IEHMOVE unloaded partitioned data set. A graphics CRT is required for plot display.

(continued on next page)



This program was written by Tetsuo Furuike and Jack C. Long of Rockwell International Corp. for Johnson Space Center. For further information, Circle H on the COSMIC Request Card.
MSC-18016

Graphics Program for Charts

Variety of thermophysical-property charts drawn economically

The program GASPLOT is a reliable, economical, and easy-to-use method of producing a variety of thermophysical-property charts. The program is designed so that any two of the following variables may be plotted as an ordinate-abscissa pair: the state variables of pressure, density, and temperature; the derived variables of enthalpy, entropy, specific heats, sonic velocity, and isentropic expansion coefficient; or the transport variables of thermal conductivity, viscosity, and surface tension. As many as five parametric variables, including temperature, pressure, density, enthalpy, and entropy, may be used. GASPLOT can be applied to (1) analysis of thermophysical data and trends of thermophysical-property parameters; (2) production of high-quality thermophysical-properties charts; (3) redrawing of charts to more useful scales; and (4) production of charts with SI units. A special feature of the program is the capability to enlarge or reduce any segment of a plot to produce the desired resolution.

GASPLOT currently uses the routine GASP ["Computer Program for Calculating Thermodynamic and Transport Properties of Fluids" — see NASA Tech Brief B75-10188 (LEW-12520)] that calculates thermophysical properties for 10 fluids: helium, methane, neon, nitrogen, carbon monoxide, oxygen, argon, carbon dioxide, fluorine, and parahydrogen. With minor modifications to GASLOT, one may replace GASP by WASP ["Computer Program for Calculating Water and Steam Properties" — see NASA

Tech Brief B74-10123 (LEW-12206)] to produce thermophysical plots for water and steam.

The program uses a geometric sequence of points for each line segment, giving closely spaced points near critical points and wider point spacing away from critical regions. A small region near the critical point is excluded from the plot. No points are calculated in the liquid to vapor transition region; instead points are calculated only on the saturation boundary. Thermophysical properties in the liquid to vapor transition region are assumed to make a smooth transition. A double three-point Lagrangian interpolation is used by all the subroutines in this program. Lines in the liquid and vapor regions do not use the geometric progression. In these regions the number of points is increased by dividing the lines into segments and using the geometric progression on each segment. Input is by means of a NAMELIST statement.

This program is written in FORTRAN V for UNIVAC 1100-series machines and has a central memory requirement of approximately 30K (decimal) of 36-bit words. The program uses a CALCOMP plotter and software package. Routines PLOT, SYMBOL, and NUMBER from the CALCOMP software are used.

This program was written by Robert C. Hendricks and Roger J. Trivisonno of Lewis Research Center. For further information, Circle J on the COSMIC Request Card.
LEW-12811

Price and Cost Estimation

Computer-assisted analysis of labor and materials costs

The PACE II, Price and Cost Estimating Program, was developed to prepare man-hour and material cost estimates. This versatile and flexible tool can significantly reduce computation time and errors and reduce the typing and reproduction time involved in the preparation of cost estimates.

PACE II performs all mathematical and clerical functions automatically once basic inputs are derived. This allows the time of estimators, estimate managers, office personnel, and engineers involved in the estimating and cost-analysis process to be devoted to the publication of ground rules and the collection, analysis, and adjustment of inputs and rationals. The current principal use of the PACE II system is the initial pricing and updating of Government estimates in support of Source Evaluation Board (SEB) proceedings. The system can also be used in tradeoff studies, change estimates, and budgetary studies.

The basic features of the PACE II system include: a uniform method of depicting and numbering a Work Breakdown Structure (WBS); a uniform labor rate structure; a uniform format for data input and output; and uniform methods for applying overhead, general and administrative costs, fees, and escalation. Use of the PACE II computer system is based on the development of man-hours and materials, travel, and other direct costs for the lowest level of each WBS being estimated. The application of PACE II is appropriate primarily where sufficient definition exists to define design and configuration parameters of hardware, man-loading, and time-phasing of engineering and support functions.

In a design-to-cost situation, a grounds-up estimate must be made first to develop a baseline. The design-to-cost factor is then applied to spread the reduction or increase to the lowest WBS level. The technique requires a detailed negotiation and rationalization of the adjusted man-hours of the work to be performed.

Input required by PACE II includes labor rates, dollar escalation rates, and WBS data. Input is edited for compliance to format specifications. Detected input errors are noted, and an error message is displayed for each. Output consists of a cost-estimate report showing the cost breakdown per fiscal year of the estimated project from the highest to the lowest levels of the WBS. An

escalation report is generated separately from the cost-estimate report.

This program is written in COBOL for batch execution and has been implemented on a UNIVAC 1108 with a central memory requirement of approximately 10K of 36-bit words.

This program was written by Rodney D. Stewart of Marshall Space Flight Center. For further information, Circle K on the COSMIC Request Card.

MFS-23812

Processor for the UNIVAC 1100 Series

Modified BASIC language reduces programing time.

MBASIC, an advanced version of the BASIC language developed at Dartmouth College, is a high-level interactive computer language designed to minimize the time required for a user to program a task for computer execution. With MBASIC, like BASIC and FORTRAN, one combines English and simple algebra to give instructions to the computer; however, MBASIC usually results in shorter and simpler programs that are easier to write and understand.

Practically all system commands needed for management-information processing are available in MBASIC. Thus MBASIC users need not learn new executive commands or rewrite MBASIC programs to accommodate system changes. MBASIC should serve as a powerful computing language for technical or management-information processing and for scientific and engineering applications.

The conversational nature of MBASIC allows the user to interact with the program as it is being developed. Each MBASIC statement is analyzed for errors as it is entered. Diagnostic error messages and versatile editing features enable one to make corrections quickly and easily. Any portion of a program may be executed before it is completely assembled. This feature

is one of the fundamental characteristics of MBASIC and is the principal reason that it has truly conversational capabilities. Although individual statements may be syntactically correct, improper cross-references between statements, variables, or expressions can interrupt a program during execution.

If an interruption occurs, a diagnostic message is printed, and control is returned to the user. If necessary, one may enter direct statements and execute them immediately. After program corrections have been made, execution can be resumed at any appropriate statement, including the statement in which the interruption occurred.

The power of MBASIC lies in its capacity to direct a computer to perform a large variety of complex tasks while requiring the user to supply a minimum number of simple English or algebraic instructions. The program instructions are written as sentences, resulting in a program that is easy to read and write. These instructions are combined into program modules that are written as paragraphs. Comments may be included to document module functions. The outstanding features that contribute to the power of MBASIC include:

- Multiple assignments in a single instruction;
- Conditional, assignment, and repetitive statement modifiers;
- Multiple modified statements in a single instruction;
- Excellent string-handling capabilities; and
- Excellent array-handling capabilities, including: assigning values while dimensioning, matrix algebra written like simple algebra, simple and array expressions in a single instruction, expressions to refer to statement numbers, and reading and writing tapes on terminal devices during program execution.

The availability of these and other features leads naturally to a simplification of the program design process.

This processor is written in Assembler for interactive execution and has been implemented on the UNIVAC 1108/1110 under control of EXEC 8 with a central memory requirement of

approximately 28K of 36-bit words. The processor is reentrant with each user requiring approximately 49K of data area. Installation of this processor will require a good understanding of system programming on the UNIVAC 1100-series computers.

This program was written by Franklin H. Bracher, Robert E. Holzman, Daniel I. Lewis, and R. C. Tausworthe of Caltech for NASA's Jet Propulsion Laboratory. For further information, Circle L on the COSMIC Request Card.
NPO-13469

Postprocessing Classification Images

Program cleans up remote-sensing maps.

The GETMEX/CLEAN computer program postprocesses classification images such as those derived from processing remotely-sensed Landsat data. The program remaps classification images, cleans up the salt-and-pepper appearance by forcing each object mapped in the image to have a minimum size specified by the user, and maps a special kind of mixed feature on the image. It can be used with existing image-processing software, such as LARSYS, CAMSP, and VICAR. The remapped images closely resemble the familiar resource information maps and can replace or supplement the classification images not postprocessed by GETMEX/CLEAN.

The program operates on binary classification maps, that is, maps having picture-element (pixel) values of "0" or "1." Connected sets in the map are searched and identified. The sizes of these connected sets are determined and checked against a prespecified threshold, which is controlled by the user. Connected sets smaller than threshold pixels are eliminated by changing their labels to the other type; that is, small sets of "1's" will be modified to "0" labels and "0's" to "1's." By such relabeling, a final image is produced in which every mapped object meets a minimum-threshold pixel-size

(continued on next page)



requirement. The program accepts as input multiclass single-channeled images formatted on computer-compatible tapes (CCT) in the Universal format for multispectral scanner (MSS) data storage. Output is in the form of

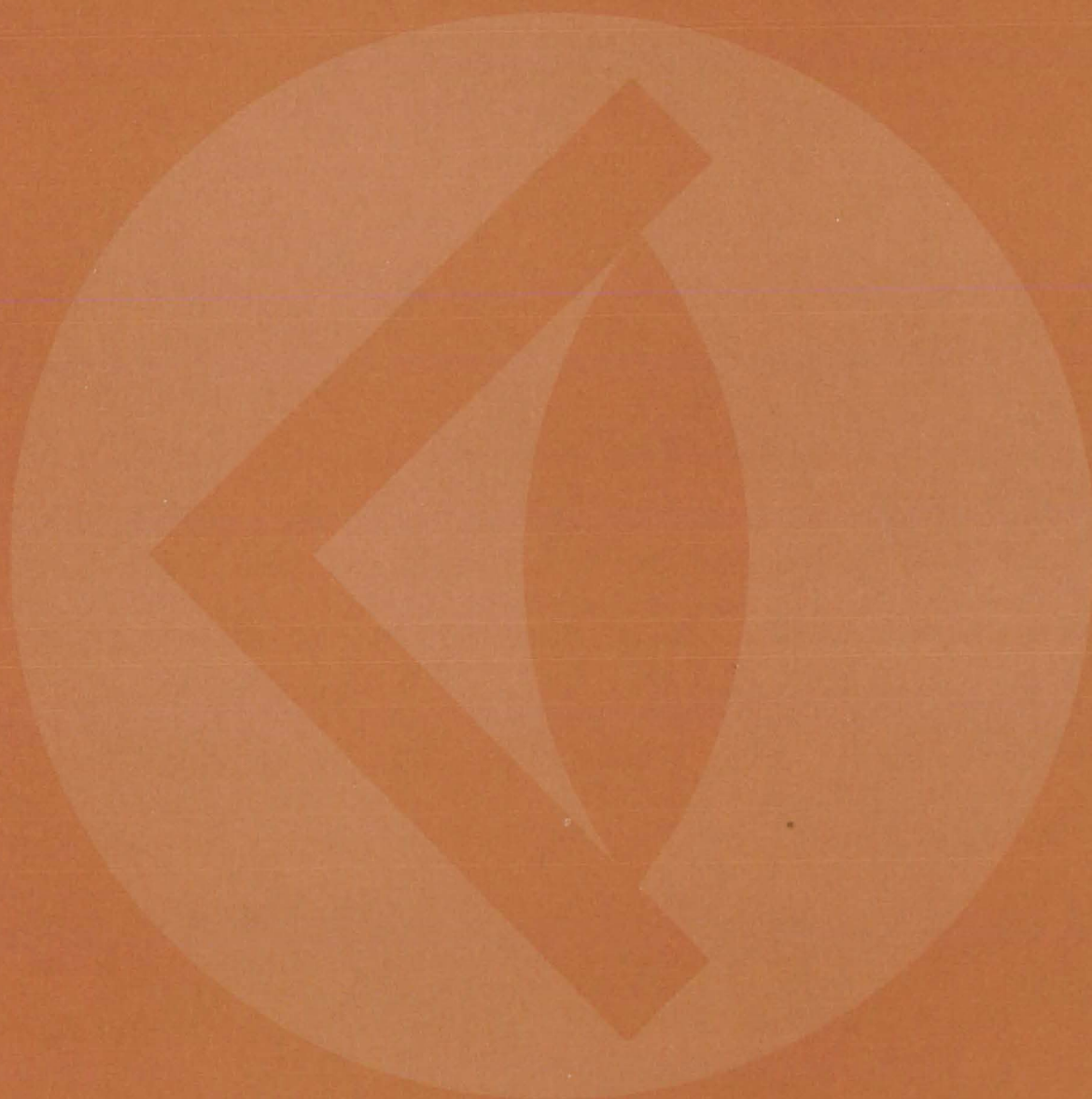
images on magnetic tape in the same format.

GETMEX/CLEAN is written in FORTRAN V for execution in batch mode and is implemented on a UNIVAC 1100-series computer operating under EXEC 8. The program requires two tape drives and a core requirement of

approximately 34K of 36-bit words for execution.

*This program was written by E. P. Kan of Lockheed Electronics Co., Inc., for **Johnson Space Center**. For further information, Circle M on the COSMIC Request Card.*
MSC-18238

SUBJECT INDEX



ABRASION RESISTANCE			ANTIREFLECTION COATINGS			BLOOD		
Scratch-resistant plastic lenses			Absorptive coating for aluminum solar panels			Automated electrophoresis apparatus		
page 543	ARC-11039		page 532	MFS-25033		page 540	MFS-23983	
ABSORBERS [MATERIALS]			ARC DISCHARGES			BLOOD PRESSURE		
Absorptive coating for aluminum solar panels			Arc detector uses fiber optics			Hand-held vital-signs monitor		
page 532	MFS-25033		page 472	NPO-13377		page 551	MSC-18232	
ACCESSORIES			ATTENUATORS			BODY TEMPERATURE		
Extension handle for spray cans			Pulse-width-modulated attenuator for AGC			Hand-held vital-signs monitor		
page 607	KSC-11083		page 483	NPO-14127		page 551	MSC-18232	
ACOUSTIC SCATTERING			AUTOMATIC CONTROL			Hybrid temperature-monitoring circuit		
Noncontacting electrokinetography system			Controlling the growth of silicon sheets			page 553	MSC-18231	
page 564	MSC-18162		page 613	NPO-14295		BOOLEAN ALGEBRA		
ACOUSTO-OPTICS			AUTOMATIC FREQUENCY CONTROL			Representation of multivalued logic functions		
Acousto-optical imaging without immersion			Multichannel VCO needs only one reference			page 627	NPO-13760	
page 582	MFS-23876		page 471	MSC-18225		BONDING		
ACRYLIC RESINS			AUTOMATIC GAIN CONTROL			Applying uniform adhesive coatings		
Antistatic coating for acrylics			Measuring radio-signal power accurately			page 615	MSC-19462	
page 534	NPO-13867		page 490	NPO-13373		Preparing thin aluminum films for adhesive		
ACTIONATORS			Pulse-width-modulated attenuator for AGC			bonding		
Two-position wax-motor rotary actuator			page 483	NPO-14127		page 621	NPO-14357	
page 591	GSC-12521		AUTOMATIC TEST EQUIPMENT			BOUNDARY LAYERS		
Two (or more) rotary outputs from one input			Multiplexed battery-bypass control system			Tumbling-vehicle entry heating		
page 600	MSC-19450		page 501	NPO-14414		page 587	MFS-23712	
ADDING CIRCUITS			Testing for microcircuit package impurities			BRAKING		
Digital correlator with fewer IC's			page 573	NPO-14314		Dynamic braking of bidirectional motors		
page 481	MSC-16743		Testing integrated circuits by photoexcitation			page 608	ARC-11194	
ADHESIVE BONDING			page 474	MFS-23943		BRAZING		
Applying uniform adhesive coatings			AUTOMOBILE ENGINES			Brazing dissimilar aluminum alloys		
page 615	MSC-19462		Real-time instrument averages 100 data sets			page 618	MSC-16340	
Preparing thin aluminum films for adhesive			page 567	LEW-13093		BRITTLE MATERIALS		
bonding			Stirling-engine design manual			"Gentle" holder for brittle ceramics		
page 621	NPO-14357		page 610	LEW-13098		page 585	MSC-19645	
ADHESIVES			AVALANCHE DIODES			BUDGETING		
Sealing microcircuits with adhesives			All-ion-implantation process for integrated circuits			Price and cost estimation		
page 622	MFS-23869		page 621	MFS-23995		page 628	MFS-23812	
AERATION			AVERAGE			BULK MODULUS		
Deaerating high-viscosity silicone rubber			Real-time instrument averages 100 data sets			Dynamic measurement of bulk modulus		
page 538	MSC-16694		page 567	LEW-13093		page 576	NPO-13226	
AEROSOLS			AXISYMMETRIC BODIES			BURNING TIME		
Extension handle for spray cans			Potential flows in propulsion system inlets			Fire-resistant wood products		
page 607	KSC-11083		page 586	LEW-13010		page 532	ARC-11174	
AIR CONDITIONING			AXISYMMETRIC FLOW			BUTT JOINTS		
Refrigerant leak detector			Flow in axisymmetric ducts with struts			Detecting overpenetration of electron-beam welds		
page 583	MSC-18214		page 588	LEW-12798		page 618	MFS-19396	
ALIGNMENT			BALL BEARINGS			BYPASSES		
"Blind" position indicator			Elastic deformation of ball bearings, gears, and			Automatic bypass valve		
page 602	MSC16972		cams			page 592	LAR-12063	
ALUMINUM ALLOYS			page 577	LEW-13076		Compact bypass-flow filter		
Absorptive coating for aluminum solar panels			BALLISTICS			page 597	MSC-18311	
page 532	MFS-25033		Measuring projectile speed			Multiplexed battery-bypass control system		
Brazing dissimilar aluminum alloys			page 571	LAR-12387		page 501	NPO-14414	
page 618	MSC-16340		BANDWIDTH			CALIBRATING		
ALUMINUM COATINGS			Determining the response of an FM receiver			High-sampling-rate pressure transducer has in		
Measurement of subcoat thickness by			page 491	MSC-16751		situ calibration		
characteristic X-rays			Narrow-bandwidth receiver			page 569	LAR-12230	
page 530	MSC-16718		page 489	GSC-12142		CAMS		
AMBIGUITY			BARRIER LAYERS			Elastic deformation of ball bearings, gears, and		
Eliminating ambiguity in digital signals			Metallic thermal seal			cams		
page 495	NPO-14289		page 598	MSC-18135		page 577	LEW-13076	
AMINES			BASIC [PROGRAMING LANGUAGE]			CANCER		
High-pressure liquid chromatography of aromatic			Processor for the UNIVAC 1100 series			Improved probe for rectal-cancer detection		
amines			page 629	NPO-13469		page 562	NPO-14247	
page 538	LAR-12163		BATTERY CHARGERS			CARBON DIOXIDE LASERS		
Porous bead packings for gas chromatography			Multiplexed battery-bypass control system			Low-power tuner for lasers		
page 542	ARC-11222		page 501	NPO-14414		page 515	MFS-23863	
ANTENNA ARRAYS			BEAMS [SUPPORTS]			CATALYSTS		
Efficient rectifying antenna			Plotting maximum/minimum data envelopes			Improved imide polymerization catalyst		
page 497	NPO-13884		page 627	MSC-18016		page 541	ARC-11107	
ANTENNAS			BELLOWS			CARRIER INJECTION		
Compact antenna has symmetrical radiation			Transmitting rotary motion at an angle			All-ion-implantation process for integrated circuits		
pattern			page 594	MSC-19483		page 621	MFS-23995	
page 500	ARC-11189		BENDING			CELLS [BIOLOGY]		
Lightweight conical antenna reflector			Bend-absorbing clamp			Separating biological cells		
page 499	NPO-13552		page 606	MSC-16971		page 547	MFS-23883	
More efficient microwave-power transmission								
page 492	NPO-13885							



CERAMIC COATINGS

Measurement of subcoat thickness by characteristic X-rays
page 530 MSC-16718

CERAMICS

"Gentle" holder for brittle ceramics
page 585 MSC-19645

CENTRIFUGAL PUMPS

Drag-pump rotating filter
page 596 MSC-16180

CHEMICAL ATTACK

Corrosion inhibitors for solar-heating and cooling systems
page 525 MFS-25023

CHEMICAL REACTORS

Model of silicon production in a fluidized-bed reactor
page 544 NPO-14404

CHROMATOGRAPHY

High-pressure liquid chromatography of aromatic amines
page 538 LAR-12163
Porous bead packings for gas chromatography
page 542 ARC-11222

CIRCUIT BOARDS

Localized cooling of components
page 601 LAR-11955

CIRCUIT PROTECTION

Electrical/ground monitor
page 620 MSC-18281
Load balancing in multimodule power converters
page 485 NPO-13832
Overload protection system
page 484 NPO-13872
Voltage regulator for solar panels
page 508 NPO-13895

CIRCULATORS [PHASE SHIFT CIRCUITS]

More efficient microwave-power transmission
page 492 NPO-13885

CLAMPS

Bend-absorbing clamp
page 606 MSC-16971
Fastener for thermal insulation blankets
page 603 MSC-18253

CLASSIFICATIONS

Postprocessing classification images
page 629 MSC-18238

CLIPS

Fastener for thermal insulation blankets
page 603 MSC-18253

CLOCKS

Hybrid clock generator
page 560 MSC-18228

COAL

Low-temperature refining of coal
page 535 NPO-14210

COATINGS

Antistatic coating for acrylics
page 534 NPO-13867
Applying uniform adhesive coating
page 615 MSC-19462
Coating for hot sliding seals
page 595 MSC-16529
Forming "dynamic" membranes on stainless steel
page 537 MSC-18172
Measurement of subcoat thickness by characteristic X-rays
page 530 MSC-16718
Scratch-resistant plastic lenses
page 543 ARC-11039
CODING
Efficient digital encoding scheme
page 493 MSC-18267
Eliminating ambiguity in digital signals
page 495 NPO-14289

COLLOIDS

Accelerated purification of colloidal silica sols
page 536 MSC-16793

COMBUSTION EFFICIENCY

Stirling-engine design manual
page 610 LEW-13098

COMMUNICATION CABLES

Splicing shielded cables
page 476 MSC-18297

COMPATIBILITY

Compression testing flammable liquids
page 581 MSC-16121

COMPOSITE MATERIALS

Fire-resistant wood products
page 532 ARC-11174

COMPOSITE STRUCTURES

Detecting moisture in composite honeycomb panels
page 583 MSC-16750

COMPRESSED GAS

Topping pressures for gas-storage cylinders
page 575 MSC-18186

COMPRESSIBILITY

Dynamic measurement of bulk modulus
page 576 NPO-13226

COMPRESSIBLE FLOW

Flow in axisymmetric ducts with struts
page 588 LEW-12798

COMPRESSION TESTS

Compression testing flammable liquids
page 581 MSC-16121

COMPUTER STORAGE DEVICES

One-third selection for matrix-addressing ferroelectrics
page 479 LAR-11993

CONCENTRATORS

Concentrating solar collector — installation package
page 524 MFS-25068

CONNECTORS

Miniature thermocouple disconnect
page 568 LAR-12013
Modular ground-wire connector
page 477 MSC-16633

CONTOURS

Contouring pile-brush seals
page 619 MSC-16231

COOLING

Localized cooling of components
page 601 LAR-11955
Orbital heat rate package
page 586 MFS-23980

COPPER OXIDES

Absorptive coating for aluminum solar panels
page 532 MFS-25033

CORRELATION DETECTION

Digital correlator with fewer IC's
page 481 MSC-16743

CORROSION PREVENTION

Corrosion inhibitors for solar-heating and cooling systems
page 525 MFS-25023
Eliminating gold migration in microcircuits
page 486 MSC-18213

COST ESTIMATES

Price and cost estimation
page 628 MFS-23812

COST REDUCTION

Telecommunications network optimization
page 504 NPO-14486

CROP GROWTH

Predicting crop production from satellite data
page 626 GSC-12379

CRYSTAL GROWTH

Automated crystal-growth control system
page 614 NPO-14420

Controlling the growth of silicon sheets
page 613 NPO-14295

CRYSTAL OSCILLATORS

Multichannel VCO needs only one reference
page 471 MSC-18225

CURVE FITTING

Real-time instrument averages 100 data sets
page 567 LEW-13093

CYLINDRICAL CHAMBERS

Topping pressures for gas-storage cylinders
page 575 MSC-18186

CYLINDRICAL SHELLS

Wrench for thin-wall cylinders
page 609 LAR-12286

DATA CORRELATION

Digital correlator with fewer IC's
page 481 MSC-16743

DATA REDUCTION

Data reformatting with less hardware
page 496 NPO-13676

DATA TRANSMISSION

Eliminating ambiguity in digital signals
page 495 NPO-14289

DEEP SCATTERING LAYERS

Acousto-optical imaging without immersion
page 582 MFS-23876

DEFORMATION

Detecting surface deformations photographically
page 580 MSC-16156
Elastic deformation of ball bearings, gears, and cams
page 577 LEW-13076

DEGASSING

Deaerating high-viscosity silicone rubber
page 538 MSC-16694

DEMODULATORS

Miniature K_u-band down converter
page 473 MSC-18313
Narrow-bandwidth receiver
page 489 GSC-12142
Simplified phase detector
page 480 NPO-13395

DESULFURIZING

Low-temperature refining of coal
page 535 NPO-14210

DIFFRACTION

Diffraction X-ray focusing
page 516 GSC-12357
Measurement of subcoat thickness by characteristic X-rays
page 530 MSC-16718

DIODES

Precise matching of diodes
page 475 NPO-14293

DIPOLE ANTENNAS

Efficient rectifying antenna
page 497 NPO-13884

DISCONNECT DEVICES

Miniature thermocouple disconnect
page 568 LAR-12013

DISPLAY DEVICES

Hybrid LCD driver
page 559 MSC-18229

DOORS

Latching door mechanism
page 604 MSC-19602

DRIVE BELTS

Durable nonslip, stainless-steel drive belts
page 599 GSC-12276/12289

DUCTED BODIES

Flow in axisymmetric ducts with struts
page 588 LEW-12798

DYES

High-pressure liquid chromatography of aromatic amines
page 538 LAR-12163

EARTH RESOURCES

Multidimensional histograms
page 526 MFS-23855

ELASTIC DEFORMATION

Elastic deformation of ball bearings, gears, and
cams
page 577 LEW-13076

ELASTOMERS

Reducing stickiness of elastomer valve seals
page 597 LAR-11778

ELECTRIC ARCS

Arc detector uses fiber optics
page 472 NPO-13377

Low-discharge vacuum feedthrough
page 593 GSC-12347

ELECTRIC BATTERIES

Multiplexed battery-bypass control system
page 501 NPO-14414

ELECTRIC CONNECTORS

Modular ground-wire connector
page 477 MSC-16633

ELECTRIC GENERATORS

Wind/water energy converter
page 513 GSC-12361

ELECTRIC MOTORS

Dynamic braking of bidirectional motors
page 608 ARC-11194

ELECTRIC POWER PLANTS

Ocean thermal plant
page 512 KSC-11034

ELECTRIC WIRE

Modular ground-wire connector
page 477 MSC-16633

ELECTRICAL GROUNDING

Electrical/ground monitor
page 620 MSC-18281

ELECTROCARDIOGRAPHY

Hybrid ECG signal conditioner
page 554 MSC-18230

Hybrid respiration-signal conditioner
page 556 MSC-18226

Noncontacting electrokinetography system
page 564 MSC-18162

ELECTROPHORESIS

Automated electrophoresis apparatus
page 540 MFS-23983

Separating biological cells
page 547 MFS-23883

ELECTROPLATING

Electroplated "cold patch" for critical parts
page 616 MFS-19401

ELECTROSTATIC CHARGE

Antistatic coating for acrylics
page 534 NPO-13867

ELECTRON BEAM WELDING

Detecting overpenetration of electron-beam welds
page 618 MFS-19396

ELECTRON EMISSION

Ion-beam-textured graphite
page 530 LEW-12724

ELECTRON MICROSCOPES

SEM probe of IC radiation sensitivity
page 574 NPO-14350

EMERGENCY LIFE SUSTAINING SYSTEMS

Hybrid respiration-signal conditioner
page 556 MSC-18226

ENCODING

Efficient digital encoding scheme
page 493 MSC-18267

ENDOSCOPES

Improved probe for rectal-cancer detection
page 562 NPO-14247

ENERGY CONVERSION EFFICIENCY

Stirling-engine design manual
page 610 LEW-13098

ENGINE DESIGN

Stirling-engine design manual
page 610 LEW-13098

ENGINE TESTS

Real-time instrument averages 100 data sets
page 567 LEW-13093

EXTENSIONS

Extension handle for spray cans
page 607 KSC-11083

EYE DISEASES

Intraocular pressure reduction and regulation
page 549 LEW-12723

FARM CROPS

Predicting crop production from satellite data
page 626 GSC-12379

FAST FOURIER TRANSFORMATIONS

Wideband digital spectrum analyzer
page 494 NPO-14394

FASTENERS

Bend-absorbing clamp
page 606 MSC-16971

Fastener for thermal insulation blankets
page 603 MSC-18253

Latching door mechanism
page 604 MSC-19602

FATIGUE [MATERIALS]

Gear-tooth fatigue-strength estimates
page 605 MSC-18167

FEEDTHROUGHS

Low-discharge vacuum feedthrough
page 593 GSC-12347

FEEDBACK CONTROL

Improved servo for a Michelson interferometer
page 517 NPO-14093

Ferroelectricity

One-third selection for matrix-addressing
ferroelectrics
page 479 LAR-11993

FIBERS

Ultrafine PBI fibers and yarns
page 529 ARC-11221

FILLERS

Fire-resistant wood products
page 532 ARC-11174

FINANCIAL MANAGEMENT

Price and cost estimation
page 628 MFS-23812

FIRE PREVENTION

Fire-resistant wood products
page 532 ARC-11174

FLAMMABILITY

Compression testing flammable liquids
page 581 MSC-16121

FLOW MEASUREMENT

Miniature velocimeter
page 572 LAR-12281

FLOW REGULATORS

Adjustable gas-flow restrictor
page 594 MSC-19486

Automatic bypass valve
page 592 LAR-12063

Flow-compensating pressure regulator
page 548 LEW-12718

FLOW VELOCITY

Flow-compensating pressure regulator
page 548 LEW-12718

FLUID FILTERS

Compact bypass-flow filter
page 597 MSC-18311

Drag-pump rotating filter
page 596 MSC-16180

FLUIDIZED BED PROCESSORS

Model of silicon production in a fluidized-bed
reactor
page 544 NPO-14404

FOAMS

Improved imide polymerization catalyst
page 541 ARC-11107

FOCUSING

Diffraction X-ray focusing
page 516 GSC-12357

FOURIER ANALYSIS

Improved Fourier interference spectrometer
page 515 NPO-14025

FREON

Refrigerant leak detector
page 583 MSC-18214

FREQUENCY ANALYZERS

Wideband digital spectrum analyzer
page 494 NPO-14394

FREQUENCY CONVERTERS

More efficient microwave-power transmission
page 492 NPO-13885

FREQUENCY MODULATION

Determining the response of an FM receiver
page 491 MSC-16751

FREQUENCY STANDARDS

Hydrogen-maser frequency standard
page 519 GSC-12334

GALLIUM ARSENIDES

More-efficient GaAs solar cells
page 509 LAR-12216

GANTRY CRANES

Rigid "sling" for topheavy loads
page 605 GSC-12359

GAS COOLING

Localized cooling of components
page 601 LAR-11955

GAS FLOW

Adjustable gas-flow restrictor
page 594 MSC-19486

Automatic bypass valve
page 592 LAR-12063

GAS MASERS

Hydrogen-maser frequency standard
page 519 GSC-12334

GAS PRESSURE

Topping pressures for gas-storage cylinders
page 575 MSC-18186

GASKETS

Metallic thermal seal
page 598 MSC-18135

GEARS

Elastic deformation of ball bearings, gears, and
cams
page 577 LEW-13076

Gear-tooth fatigue-strength estimates
page 605 MSC-18167

GLASS FIBERS

Contouring pile-brush seals
page 619 MSC-16231

GLAUCOMA

Intraocular pressure reduction and regulation
page 549 LEW-12723

GOLD COATINGS

Eliminating gold migration in microcircuits
page 486 MSC-18213

GONIOMETERS

Instrument measures many optical properties in
visible and IR
page 518 LAR-12285

GRAPHITE

Ion-beam-textured graphite
page 530 LEW-12724

GRAPHS [CHARTS]

Graphics program for charts
page 628 LEW-12811

GUNN DIODES

Multichannel VCO needs only one reference
page 471 MSC-18225



HANDLES

Extension handle for spray cans
page 607 KSC-11083

HARDNESS

Scratch-resistant plastic lenses
page 543 ARC-11039

HEART FUNCTION

Hand-held vital-signs monitor
page 551 MSC-18232

Hybrid ECG signal conditioner
page 554 MSC-18230

Hybrid heart/breath-rate processor
page 557 MSC-18227

Noncontacting electrokinetography system
page 564 MSC-18162

HEAT RATE

Orbital heat rate package
page 586 MFS-23980

HEAT SHIELDING

Contouring pile-brush seals
page 619 MSC-16231

Metallic thermal seal
page 598 MSC-18135

HEATING EQUIPMENT

Concentrating solar collector — installation
package
page 524 MFS-25068

Corrosion inhibitors for solar-heating and cooling
systems
page 525 MFS-25023

Design and installation of a flat-plate collector
page 523 MFS-25010

Development, testing, and certification of a hot-air
solar collector
page 523 MFS-23997

Easily installed insulation for steamfittings
page 620 MSC-18277

Residential solar-heating system — design
package
page 523 MFS-25071

Solar-heating system
page 522 MFS-25022

Solar-heating system — design data brochure
page 521 MFS-23977

Solar-heating system — performance tests
page 522 MFS-25021

Solar hot-water system
page 522 MFS-25043

Solar-powered hot-air system
page 511 MFS-23976

HERMETIC SEALS

Transmitting rotary motion at an angle
page 594 MSC-19483

HELICAL ANTENNAS

Compact antenna has symmetrical radiation
pattern
page 500 ARC-11189

HIGH PRESSURE OXYGEN

Topping pressures for gas-storage cylinders
page 575 MSC-18186

HIGH VOLTAGES

Low-discharge vacuum feedthrough
page 593 GSC-12347

HISTOGRAMS

Multidimensional histograms
page 526 MFS-23855

HOLDERS

Fastener for thermal insulation blankets
page 603 MSC-18253

"Gentle" holder for brittle ceramics
page 585 MSC-19645

HONEYCOMB STRUCTURES

Detecting moisture in composite honeycomb
panels
page 583 MSC-16750

HYBRID CIRCUITS

Accelerated hybrid-circuit production
page 617 MSC-18272

Hand-held vital-signs monitor
page 551 MSC-18232

Eliminating gold migration in microcircuits
page 486 MSC-18213

Hybrid clock generator
page 560 MSC-18228

Hybrid ECG signal conditioner
page 554 MSC-18230

Hybrid LCD driver
page 559 MSC-18229

Hybrid temperature-monitoring circuit
page 553 MSC-18231

Miniature K_u -band down converter
page 473 MSC-18313

HYDROGEN

Hydrogen-maser frequency standard
page 519 GSC-12334

HYSTERESIS

One-third selection for matrix-addressing
ferroelectrics
page 479 LAR-11993

IMAGE ENHANCEMENT

Postprocessing classification images
page 629 MSC-18238

IMAGERY

Data reformatting with less hardware
page 496 NPO-13676

Multidimensional histograms
page 526 MFS-23855

IMAGING TECHNIQUES

Acousto-optical imaging without immersion
page 582 MFS-23876

Automated crystal-growth control system
page 614 NPO-14420

Predicting crop production from satellite data
page 626 GSC-12379

IMIDES

Improved imide polymerization catalyst
page 541 ARC-11107

IMPURITIES

Testing for microcircuit package impurities
page 573 NPO-14314

INDICATING INSTRUMENTS

"Blind" position indicator
page 602 MSC-16972

INDUSTRIAL SAFETY

High-pressure liquid chromatography of aromatic
amines
page 538 LAR-12163

INFORMATION THEORY

Eliminating ambiguity in digital signals
page 495 NPO-14289

INFRARED DETECTORS

Instrument measures many optical properties in
visible and IR
page 518 LAR-12285

INSPECTION

Automated inspection of wire-frame assemblies
page 579 GSC-12321

Detecting moisture in composite honeycomb
panels
page 583 MSC-16750

INSULATION

Contouring pile-brush seals
page 619 MSC-16231

Easily installed insulation for steamfittings
page 620 MSC-18277

Fastener for thermal insulation blankets
page 603 MSC-18253

Metallic thermal seal
page 598 MSC-18135

INTEGRATED CIRCUITS

Accelerated hybrid-circuit production
page 617 MSC-18272

All-ion-implantation process for integrated circuits
page 621 MFS-23995

Eliminating gold migration in microcircuits
page 486 MSC-18213

Sealing microcircuits with adhesives
page 622 MFS-23869

SEM probe of IC radiation sensitivity
page 574 NPO-14350

Testing for microcircuit package impurities
page 573 NPO-14314

Testing integrated circuits by photoexcitation
page 474 MFS-23943

INTERFEROMETERS

Improved Fourier interference spectrometer
page 515 NPO-14025

Improved servo for a Michaelson interferometer
page 517 NPO-14093

INTERNAL-COMBUSTION ENGINES

Real-time instrument averages 100 data sets
page 567 LEW-13093

INTESTINES

Self-propelling, self-locating colonoscope
page 563 NPO-14092

Improved probe for rectal-cancer detection
page 562 NPO-14247

INTRAOCULAR PRESSURE

Intraocular pressure reduction and regulation
page 549 LEW-12723

Flow-compensating pressure regulator
page 548 LEW-12718

INVENTORY MANAGEMENT

Computation of spare parts requirements
page 625 MSC-16872

INVERTED CONVERTERS [DC TO AC]

Load balancing in multimodule power converters
page 485 NPO-13832

Overload protection system
page 484 NPO-13872

ION BEAMS

Ion-beam-textured graphite
page 530 LEW-12724

ION EXCHANGE MEMBRANE ELECTROLYTES

Forming "dynamic" membranes on stainless steel
page 537 MSC-18172

ION IMPLANTATION

All-ion-implantation process for integrated circuits
page 621 MFS-23995

JACKETS

Easily installed insulation for steamfittings
page 620 MSC-18277

JIGS

"Gentle" holder for brittle ceramics
page 585 MSC-19645

Ku BAND

Miniature K_u -band down converter
page 473 MSC-18313

LANDSAT DATA SATELLITES

Postprocessing classification images
page 629 MSC-18238

LANDSAT SATELLITES

Predicting crop production from satellite data
page 626 GSC-12379

Multidimensional histograms
page 526 MFS-23855

LASER APPLICATIONS

Acousto-optical imaging without immersion
page 582 MFS-23876

LASER DOPPLER VELOCIMETERS

Miniature velocimeter
page 572 LAR-12281

LASERS

Low-power tuner for lasers
page 515 MFS-23863

LATCHES

Latching door mechanism
page 604 MSC-19602

LEAK DETECTORS

Refrigerant leak detector
page 583 MSC-18214

LENSES

Scratch-resistant plastic lenses
page 543 ARC-11039

LIGHT TRANSMISSION

Compact turbidity meter
page 578 KSC-11063

LIGHTNING

System for monitoring lightning strikes
page 502 KSC-11018

LIMITER CIRCUITS

Overload protection system
page 484 NPO-13872

LIQUID CRYSTALS

Hybrid LCD driver
page 559 MSC-18229

LOAD DISTRIBUTION (FORCES)

Plotting maximum/minimum data envelopes
page 627 MSC-18016

Resizing algorithm for loaded structures
page 625 LAR-12064

Rigid "sling" for topeavy loads
page 605 GSC-12359

LOADS (FORCES)

Resizing algorithm for loaded structures
page 625 LAR-12064

LOCKS (FASTENERS)

Latching door mechanism
page 604 MSC-19602

LOGIC DESIGN

Representation of multivalued logic functions
page 627 NPO-13760

LOW TEMPERATURE TESTS

Thermoelectrically-cooled variable-temperature
probe
page 514 MSC-18192

MACH NUMBER

Shock-swallowing air sensor
page 570 FRC-10107

MAGNETIC TRANSDUCERS

Low-power tuner for lasers
page 515 MFS-23863

MAGNETOMETERS

Two-position wax-motor rotary actuator
page 591 GSC-12521

MAGNETRONS

More efficient microwave-power transmission
page 492 NPO-13885

MAJORITY CARRIERS

More-efficient GaAs solar cells
page 509 LAR-12216

MANAGEMENT INFORMATION SYSTEMS

Processor for the UNIVAC 1100 series
page 629 NPO-13469

MANAGEMENT PLANNING

Price and cost estimation
page 628 MFS-23812

MAPPING

Postprocessing classification images
page 629 MSC-18238

MASERS

Hydrogen-maser frequency standard
page 519 GSC-12334

MATCHING

Precise matching of diodes
page 475 NPO-14293

MECHANICAL DRIVES

Durable, nonslip, stainless-steel drive belts
page 599 GSC-12276/12289

Gear-tooth fatigue-strength estimates
page 605 MSC-18167

Two-position wax-motor rotary actuator
page 591 GSC-12521

Two (or more) rotary outputs from one input
page 600 MSC-19450

MEMBRANES

Forming "dynamic" membranes on stainless steel
page 537 MSC-18172

METAL FILMS

Preparing thin aluminum films for adhesive
bonding
page 621 NPO-14357

METAL OXIDE SEMICONDUCTORS

All-ion-implantation process for integrated circuits
page 621 MFS-23995

MICHAELSON INTERFEROMETERS

Improve Fourier interference spectrometer
page 515 NPO-14025

Improved servo for a Michaelson interferometer
page 517 NPO-14093

MICROCIRCUITS

Eliminating gold migration in microcircuits
page 486 MSC-18213

Sealing microcircuits with adhesives
page 622 MFS-23869

Testing for microcircuit package impurities
page 573 NPO-14314

MICROWAVE ANTENNAS

Compact antenna has symmetrical radiation
pattern
page 500 ARC-11189

Efficient rectifying antenna
page 497 NPO-13884

MICROWAVE REFLECTOMETERS

Dynamic measurement of bulk modulus
page 576 NPO-13226

MICROWAVE TRANSMISSION

Arc detector uses fiber optics
page 472 NPO-13377

MINORITY CARRIERS

More-efficient GaAs solar cells
page 509 LAR-12216

MIXING CIRCUITS

Pulse-width-modulated attenuator for AGC
page 483 NPO-14127

MODULATORS

Pulse-width-modulated attenuator for AGC
page 483 NPO-14127

MOISTURE CONTENT

Detecting moisture in composite honeycomb
panels
page 583 MSC-16750

Sealing microcircuits with adhesives
page 622 MFS-23869

MONITORS

Electrical/ground monitor
page 620 MSC-18281

Multiplexed battery-bypass control system
page 501 NPO-14414

MOTORS

Dynamic braking of bidirectional motors
page 608 ARC-11194

MULTICHANNEL COMMUNICATION

Multichannel VCO needs only one reference
page 471 MSC-18225

MULTILAYER INSULATION

Fastener for thermal insulation blankets
page 603 MSC-18253

MULTIPLEXING

Multiplexed battery-bypass control system
page 501 NPO-14414

MULTISPECTRAL PHOTOGRAPHY

Multidimensional histograms
page 526 MFS-23855

Predicting crop production from satellite data
page 626 GSC-12379

NETWORK ANALYSIS

Telecommunications network optimization
page 504 NPO-14486

NONDESTRUCTIVE TESTS

Acousto-optical imaging without immersion
page 582 MFS-23876

Automated inspection of wire-frame assemblies
page 579 GSC-12321

Detecting moisture in composite honeycomb
panels
page 583 MSC-16750

Detecting overpenetration of electron-beam welds
page 618 MFS-19396

OCEAN ENERGY

Ocean thermal plant
page 512 KSC-11034

OPACITY

Compact turbidity meter
page 578 KSC-11063

OPHTHALMOLOGY

Intraocular pressure reduction and regulation
page 549 LEW-12723

OSCILLATORS

Multichannel VCO needs only one reference
page 471 MSC-18225

OSMOSIS

Forming "dynamic" membranes on stainless steel
page 537 MSC-18172

OVERLOAD PROTECTION

Overload protection system
page 484 NPO-13872

OXYGEN REGULATORS

Adjustable gas-flow restrictor
page 594 MSC-19486

PAINTS

Coating for hot sliding seals
page 595 MSC-16529

PARTICLE MOTION

Automated electrophoresis apparatus
page 540 MFS-23983

Separating biological cells
page 547 MFS-23883

PAYLOADS

Rigid "sling" for topeavy loads
page 605 GSC-12359

PERFORMANCE TESTS

Development, testing, and certification of a hot-air
solar collector
page 523 MFS-23997

Solar-heating system — performance tests
page 522 MFS-25021

Solar simulator test facility
page 507 MFS-23972

PHASE DETECTORS

Narrow-bandwidth receiver
page 489 GSC-12142

Simplified phase detector
page 480 NPO-13395



PHASE MODULATION

Determining the response of an FM receiver
page 491 MSC-16751

PHASE SHIFT KEYING

Eliminating ambiguity in digital signals
page 495 NPO-14289

PHONOCARDIOGRAPHY

Noncontacting electrokinetography system
page 564 MSC-18162

PHOTOELECTRIC CELLS

More-efficient GaAs solar cells
page 509 LAR-12216

Plastic film as photomechanical transducer
page 520 NPO-14363

PHOTOELECTRIC EMISSION

Testing integrated circuits by photoexcitation
page 474 MFS-23943

PHOTOGRAPHIC MEASUREMENT

Detecting surface deformations photographically
page 580 MSC-16156

PHOTOMECHANICAL EFFECT

Plastic film as photomechanical transducer
page 520 NPO-14363

PHOTOEXCITATION

Testing integrated circuits by photoexcitation
page 474 MFS-23943

PHYSIOLOGICAL RESPONSES

Hand-held vital-signs monitor
page 551 MSC-18232

Hybrid clock generator
page 560 MSC-18228

Hybrid ECG signal conditioner
page 554 MSC-18230

Hybrid LCD driver
page 559 MSC-18229

Hybrid temperature-monitoring circuit
page 553 MSC-18231

PLATING

Electroplated "cold patch" for critical parts
page 616 MFS-19401

PLOTTING

Plotting maximum/minimum data envelopes
page 627 MSC-18016

POLYBENZIMIDAZOL

Ultrafine PBI fibers and yarns
page 529 ARC-11221

POLYMERIZATION

Improved imide polymerization catalyst
page 541 ARC-11107

POLYMER CHEMISTRY

Antistatic coating for acrylics
page 534 NPO-13867

High-pressure liquid chromatography of aromatic amines
page 538 LAR-12163

Porous bead packings for gas chromatography
page 542 ARC-11222

Separating biological cells
page 547 MFS-23883

POSITION INDICATORS

"Blind" position indicator
page 602 MSC-16972

POTENTIAL FLOW

Potential flows in propulsion system inlets
page 586 LEW-13010

POWER CONVERTERS

Load balancing in multimodule power converters
page 485 NPO-13832

POWER SPECTRA

Measuring radio-signal power accurately
page 490 NPO-13373

POWER SUPPLY CIRCUITS

Voltage regulator for solar panels
page 508 NPO-13895

PRESSURE CHAMBERS

Compression testing flammable liquids
page 581 MSC-16121

PRESSURE MEASUREMENTS

Dynamic measurement of bulk modulus
page 576 NPO-13226

Shock-swallowing air sensor
page 570 FRC-10107

PRESSURE REGULATORS

Adjustable gas-flow restrictor
page 594 MSC-19486

Automatic bypass valve
page 592 LAR-12063

Flow-compensating pressure regulator
page 548 LEW-12718

Intraocular pressure reduction and regulation
page 549 LEW-12723

PRESSURE SENSORS

High-sampling-rate pressure transducer has in situ calibration
page 569 LAR-12230

PROGRAMING LANGUAGES

Processor for the UNIVAC 1100 series
page 629 NPO-13469

PROJECT PLANNING

Price and cost estimation
page 628 MFS-23812

PROJECTILES

Measuring projectile speed
page 571 LAR-12387

PROPULSION SYSTEM CONFIGURATIONS

Potential flows in propulsion system inlets
page 586 LEW-13010

PULLEYS

Durable, nonslip, stainless-steel drivebelts
page 599 GSC-12276/12289

PULSE DURATION MODULATION

Pulse-width-modulated attenuator for AGC
page 483 NPO-14127

PUMPS

Drag-pump rotating filter
page 596 MSC-16180

PYROLYSIS

Chemical-vapor deposition of silicon from silane
page 525 NPO-14403

PYROMETALLURGY

Model of silicon production in a fluidized-bed reactor
page 544 NPO-14404

RADIOGRAPHY

Detecting moisture in composite honeycomb panels
page 583 MSC-16750

Detecting overpenetration of electron-beam welds
page 618 MFS-19396

RADOMES

Efficient rectifying antenna
page 497 NPO-13884

REACTION KINETICS

Model of silicon production in a fluidized-bed reactor
page 544 NPO-14404

RECEIVERS

Determining the response of an FM receiver
page 491 MSC-16751

Miniature K_u-band down converter
page 473 MSC-18313

Narrow-bandwidth receiver
page 489 GSC-12142

Wideband digital spectrum analyzer
page 494 NPO-14394

RECTIFIERS

Efficient rectifying antenna
page 497 NPO-13884

Precise matching of diodes
page 475 NFO-14293

RECTUM

Improved probe for rectal-cancer detection
page 562 NPO-14247

Self-propelling, self-locating colonoscope
page 563 NPO-14092

REFINING

Accelerated purification of colloidal silica sols
page 536 MSC-16793

Low-temperature refining of coal
page 535 NPO-14210

Model of silicon production in a fluidized-bed reactor
page 544 NPO-14404

REFLECTOMETERS

Instrument measures many optical properties in visible and IR
page 518 LAR-12285

REFLECTORS

Lightweight conical antenna reflector
page 499 NPO-13552

REFORMATTING

Data reformatting with less hardware
page 496 NPO-13676

REFRIGERATING MACHINERY

Refrigerant leak detector
page 583 MSC-18214

REGENERATORS

Dynamic braking of bidirectional motors
page 608 ARC-11194

REGULATORS

Voltage regulator for solar panels
page 508 NPO-13895

REINFORCING FIBERS

Ultrafine PBI fibers and yarns
page 529 ARC-11221

RESONATORS

Low-power tuner for lasers
page 515 MFS-23863

RESPIRATION

Hand-held vital-signs monitor
page 551 MSC-18232

Hybrid heart/breath-rate processor
page 557 MSC-18227

Hybrid respiration-signal conditioner
page 556 MSC-18226

ROTATING SHAFTS

Two (or more) rotary outputs from one input
page 600 MSC-19450

ROTATION

Transmitting rotary motion at an angle
page 594 MSC-19483

RUSTING

Corrosion inhibitors for solar-heating and cooling
systems
page 525 MFS-25023

SAMPLERS

Safe, durable soil sampler
page 607 MSC-18171

SAMPLING

High-sampling-rate pressure transducer has in
situ calibration
page 569 LAR-12230

SEALING

Sealing microcircuits with adhesives
page 622 MFS-23869

SEALS (STOPPERS)

Coating for hot sliding seals
page 595 MSC-16529

Metallic thermal seal
page 598 MSC-18135

Reducing stickiness of elastomer valve seals
page 597 LAR-11778

Testing for microcircuit package impurities
page 573 NPO-14314

SERVOCONTROL

Improved servo for a Michaelson interferometer
page 517 NPO-14093

SHAFTS (MACHINE ELEMENTS)

Two (or more) rotary outputs from one input
page 600 MSC-19450

Two-position wax-motor rotary actuator
page 591 GSC-12521

SHIELDING

Splicing shielded cables
page 476 MSC-18297

SHIFT REGISTERS

Data reformatting with less hardware
page 496 NPO-13676

SHOCK ABSORBERS

Bend-absorbing clamp
page 606 MSC-16971

SHOCK WAVES

Shock-swallowing air sensor
page 570 FRC-10107

SHORT CIRCUITS

Electrical/ground monitor
page 620 MSC-18281

SIGNAL ANALYSIS

Wideband digital spectrum analyzer
page 494 NPO-14394

SIGNAL DETECTION

Hybrid heart/breath-rate processor
page 557 MSC-18227

Narrow-bandwidth receiver
page 489 GSC-12142

Simplified phase detector
page 480 NPO-13395

SIGNAL ENCODING

Efficient digital encoding scheme
page 493 MSC-18267

SIGNAL MEASUREMENT

Measuring radio-signal power accurately
page 490 NPO-13373

SIGNAL PROCESSING

Hybrid ECG signal conditioner
page 554 MSC-18230

SIGNAL TO NOISE RATIOS

Measuring radio-signal power accurately
page 490 NPO-13373

SIGNAL TRANSMISSION

Eliminating ambiguity in digital signals
page 495 NPO-14289

SILANES

Chemical-vapor deposition of silicon from silane
page 525 NPO-14403

Model of silicon production in a fluidized-bed
reactor
page 544 NPO-14404

SILICON

Automated crystal-growth control system
page 614 NPO-14420

Chemical-vapor deposition of silicon from silane
page 525 NPO-14403

Controlling the growth of silicon sheets
page 613 NPO-14295

Model of silicon production in a fluidized-bed
reactor
page 544 NPO-14404

SILICON DIOXIDE

Accelerated purification of colloidal silica sols
page 536 MSC-16793

SILICONE RUBBER

Deaerating high-viscosity silicone rubber
page 538 MSC-16694

SIMULATORS

Solar simulator test facility
page 507 MFS-23972

SIZE DETERMINATION

Resizing algorithm for loaded structures
page 625 LAR-12064

SIZE SEPARATION

Compact bypass-flow filter
page 597 MSC-18311

SOILS

Safe, durable soil sampler
page 607 MSC-18171

SOLAR CELLS

Automated crystal-growth control system
page 614 NPO-14420

Chemical-vapor deposition of silicon from silane
page 525 NPO-14403

More-efficient GaAs solar cells
page 509 LAR-12216

SOLAR ENERGY

Absorptive coating for aluminum solar panels
page 532 MFS-25033

Concentrating solar collector — installation
package
page 524 MFS-25068

Corrosion inhibitors for solar-heating and cooling
systems
page 525 MFS-25023

Design and installation of a flat-plate collector
page 523 MFS-25010

Development, testing, and certification of a hot-air
solar collector
page 523 MFS-23997

More-efficient GaAs solar cells
page 509 LAR-12216

Residential solar-heating system — design
package
page 523 MFS-25071

Solar-heating system
page 522 MFS-25022

Solar-heating system — design data brochure
page 521 MFS-23977

Solar-heating system — performance tests
page 522 MFS-25021

Solar hot-water system
page 522 MFS-25043

Solar-powered hot-air system
page 511 MFS-23976

Solar simulator test facility
page 507 MFS-23972

Solidification
page 613 NPO-14295

SOLIDIFICATION

Controlling the growth of silicon sheets
page 613 NPO-14295

SPARE PARTS

Computation of spare parts requirements
page 625 MSC-16872

SPECTROMETERS

Improved Fourier interference spectrometer
page 515 NPO-14025

SPECTROPHOTOMETRY

Instrument measures many optical properties in
visible and IR
page 518 LAR-12285

SPECTRUM ANALYSIS

Improved Fourier interference spectrometer
page 515 NPO-14025

Wideband digital spectrum analyzer
page 494 NPO-14394

SPEED INDICATORS

Measuring projectile speed
page 571 LAR-12387

Miniature velocimeter
page 572 LAR-12281

Shock-swallowing air sensor
page 570 FRC-10107

SPLICING

Splicing shielded cables
page 476 MSC-18297

SPRAYERS

Extension handle for spray cans
page 607 KSC-11083

STATIC ELECTRICITY

Antistatic coating for acrylics
page 534 NPO-13867

STATISTICAL TESTS

Real-time instrument averages 100 data sets
page 567 LEW-13093

STEAM FITTINGS

Easily installed insulation for steamfittings
page 620 MSC-18277

STIRLING ENGINES

Stirling-engine design manual
page 610 LEW-13098

STRAIN GAUGES

Plastic film as photomechanical transducer
page 520 NPO-14363

STRAPS

Bend-absorbing clamp
page 606 MSC-16971

SUPPORTS

Rigid "sling" for topheavy loads
page 605 GSC-12359

SURFACE DISTORTION

Detecting surface deformations photographically
page 580 MSC-16156

SURFACE LAYERS

Applying uniform adhesive coatings
page 615 MSC-19462

SURFACE PREPARATION

Preparing thin aluminum films for adhesive
bonding
page 621 NPO-14357

SURFACE TEMPERATURE

Orbital heat rate package
page 586 MFS-23980

SURGERY

Intraocular pressure reduction and regulation
page 549 LEW-12723

SWITCHING CIRCUITS

Dynamic braking of bidirectional motors
page 608 ARC-11194

One-third selection for matrix-addressing
ferroelectrics
page 479 LAR-11993

SWITCHING THEORY

Representation of multivalued logic functions
page 627 NPO-13760

SYMMETRY

Compact antenna has symmetrical radiation
pattern
page 500 ARC-11189



SYNCHRONISM

Simplified phase detector
page 480 NPO-13395

SYNTHETIC FIBERS

Ultrafine PBI fibers and yarns
page 529 ARC-11221

TELECOMMUNICATION

Telecommunications network optimization
page 504 NPO-14486

TEMPERATURE DISTRIBUTION

Orbital heat rate package
page 586 MFS-23980

TEMPERATURE MEASUREMENT

Hybrid temperature-monitoring circuit
page 553 MSC-18231

TEMPERATURE MEASURING INSTRUMENTS

Miniature thermocouple disconnect
page 568 LAR-12013

TEST FACILITIES

Solar simulator test facility
page 507 MFS-23972

Testing integrated circuits by photoexcitation
page 474 MFS-23943

TEXTURES

Ion-beam-textured graphite
page 530 LEW-12724

THERMAL INSULATION

Contouring pile-brush seals
page 619 MSC-16231

Easily installed insulation for steamfittings
page 620 MSC-18277

Fastener for thermal insulation blankets
page 603 MSC-18253

Metallic thermal seal
page 598 MSC-18135

THERMOCOUPLES

Miniature thermocouple disconnect
page 568 LAR-12013

THERMOELECTRIC COOLING

Thermoelectrically-cooled variable-temperature
probe
page 514 MSC-18192

THICKNESS

Measurement of subcoat thickness by
characteristic X-rays
page 530 MSC-16718

THIN FILMS

Preparing thin aluminum films for adhesive
bonding
page 621 NPO-14357

THIN WALLED SHELLS

Wrench for thin-wall cylinders
page 609 LAR-12286

THUNDERSTORMS

System for monitoring lightning strikes
page 502 KSC-11018

TIDE POWERED GENERATORS

Wind/water energy converter
page 513 GSC-12361

TRANSDUCERS

High-sampling-rate pressure transducer has in
situ calibration
page 569 LAR-12230

Plastic film as photomechanical transducer
page 520 NPO-14363

TUMBLING MOTION

Tumbling-vehicle entry heating
page 587 MFS-23712

TUNERS

Low-power tuner for lasers
page 515 MFS-23863

TURBIDITY

Compact turbidity meter
page 578 KSC-11063

ULTRASONIC TESTS

Noncontacting electrokinetography system
page 564 MSC-18162

ULTRAVIOLET RADIATION

Diffraction X-ray focusing
page 516 GSC-12357

V/STOL AIRCRAFT

Potential flows in propulsion system inlets
page 586 LEW-13010

VACUUM TESTS

Low-discharge vacuum feedthrough
page 593 GSC-12347

VALVES

Automatic bypass valve
page 592 LAR-12063

Reducing stickiness of elastomer valve seals
page 597 LAR-11778

VAPOR DEPOSITION

Chemical-vapor deposition of silicon from silane
page 525 NPO-14403

VELOCITY MEASUREMENT

Measuring projectile speed
page 571 LAR-12387

Miniature velocimeter
page 572 LAR-12281

Shock-swallowing air sensor
page 570 FRC-10107

VITAL SIGNS

Hand-held vital-signs monitor
page 551 MSC-18232

VOLTAGE CONTROLLED CRYSTAL OSCILLATOR

Multichannel VCO needs only one reference
page 471 MSC-18225

VOLTAGE REGULATORS

Voltage regulator for solar panels
page 508 NPO-13895

WATERWAVE ENERGY CONVERSION

Wind/water energy converter
page 513 GSC-12361

WELDED JOINTS

Detecting overpenetration of electron-beam welds
page 618 MFS-19396

WELDING

Brazing dissimilar aluminum alloys
page 618 MSC-16340

WHEAT

Predicting crop production from satellite data
page 626 GSC-12379

WIND TUNNEL APPARATUS

High-sampling-rate pressure transducer has in
situ calibration
page 569 LAR-12230

WIND TUNNEL DRIVES

Automatic bypass valve
page 592 LAR-12063

WIND TUNNELS

Miniature thermocouple disconnect
page 568 LAR-12013

WINDPOWERED GENERATORS

Wind/water energy converter
page 513 GSC-12361

WIRE

Modular ground-wire connector
page 477 MSC-16633

WIRE CLOTH

Automated inspection of wire-frame assemblies
page 579 GSC-12321

WIRING

Splicing shielded cables
page 476 MSC-18297

WOODEN STRUCTURES

Fire-resistant wood products
page 532 ARC-11174

WRENCHES

Wrench for thin-wall cylinders
page 609 LAR-12286

X-RAY DIFFRACTION

Diffraction X-ray focusing
page 516 GSC-12357

X-RAY INSPECTION

Detecting moisture in composite honeycomb
panels
page 583 MSC-16750

Detecting overpenetration of electron-beam welds
page 618 MFS-19396

Measurement of subcoat thickness by
characteristic X-rays
page 530 MSC-16718

YARNS

Ultrafine PBI fibers and yarns
page 529 ARC-11221

ZIRCONIUM OXIDES

Forming "dynamic" membranes or stainless steel
page 537 MSC-18172

National Aeronautics and
Space Administration

Washington, D.C.
20546

Official Business
Penalty for Private Use \$300

SPECIAL FOURTH-CLASS RATE
BOOK

FOURTH-CLASS MAIL
POSTAGE & FEES PAID
NASA
WASHINGTON, D.C.
PERMIT No. G 27

NASA

A laser sighting system designed at Goddard Space Flight Center and later refined for commercial production greatly speeds up many surveying tasks. Accurate headings can be taken over substantial distances even though terrain blocks a direct "line of sight."

